Investigation of decay properties of the Pygmy Dipole Resonance and photon strength functions on excited states in $(\vec{\gamma}, \gamma'\gamma'')$ reactions

Dissertation
zur Erlangung des Grades
"Doktor der Naturwissenschaften"
im Promotionsfach Physik

am Fachbereich Physik, Mathematik und Informatik
der Johannes Gutenberg-Universität Mainz

JOHANNES GUTENBERG
UNIVERSITÄT MAINZ

Johann Isaak
geboren in Krasikowo, Russische Föderation

Darmstadt, 2016

Datum der mündlichen Prüfung: 26.08.2016

Abstract

In the scope of this work, the decay properties of ^{128}Te and ^{130}Te are studied via photon-induced reactions exploiting the γ^3-setup at the High Intensity γ-ray Source (HIγS) at Duke University. The unique combination of γ-γ coincidence measurements and linearly-polarized and quasi-monochromatic photon beams allows for the investigation of the decay behavior of the Pygmy Dipole Resonance (PDR) in $(\vec{\gamma}, \gamma'\gamma'')$ reactions. Properties of individual excited states as well as average decay quantities are extracted, such as $B(E1)\uparrow$ strength distributions and average branching ratios. The novel experimental technique enables the determination of the photon strength function build on the ground state and, in particular, for the first time on the first excited state $2+_1$ state of ^{128}Te in a model-independent way below the neutron emission threshold. The comparison of the experimental data to calculations within the quasi-particle phonon model (QPM) and the statistical model allows for the interpretation of the measured decay behavior from a microscopic point of view and from the point of an average approach, respectively. The analysis hints to a group of excited states around 6 MeV with a different underlying structure compared to the rest of the investigated energy region. Furthermore, an indication for the violation of the Brink-Axel hypothesis below an excitation energy of 8 MeV is found for both tellurium isotopes.

Zusammenfassung

Im Rahmen dieser Arbeit werden Zerfallseigenschaften von ^{128}Te und ^{130}Te mit Hilfe von Photonen induzierten Reaktionen am γ^3 Aufbau an der High Intensity γ-ray Source (HIγS) an der Duke University untersucht. Die einzigartige Kombination von γ-γ Koinzidenzmessungen mit linear polarisierten und quasi-monochromatischen Photonenstrahlen ermöglicht die Untersuchung des Zerfallsverhaltens der Pygmy Dipole Resonance (PDR) in $(\vec{\gamma}, \gamma'\gamma'')$ Reaktionen. Eigenschaften einzelner angeregter Zustände als auch gemittelte Zerfallsgrößen werden extrahiert, wie zum Beispiel $B(E1) \uparrow$ Stärkeverteilungen und gemittelte Verzweigungsverhältnisse. Der neue experimentelle Aufbau erlaubt die modellunabhängige Bestimmung der photon strength function auf dem Grundzustand und insbesondere zum ersten Mal auf dem ersten angeregten 2_1^+ Zustand in ^{128}Te unterhalb der Neutronenseparationsschwelle. Die experimentellen Daten werden mit Rechnungen im quasi-particle phonon model (QPM) und dem statistischen Model verglichen, um Aussagen über das gemessene Zerfallsverhalten aus mikroskopischer Sicht sowie aus Sicht gemittelter Größen machen zu können. Die Analyse deutet auf eine Gruppe angeregter Zustände um 6 MeV herum, die eine andere Struktur aufweisen im Vergleich zum restlichen untersuchten Energiebereich. Über dies hinaus, gibt es Hinweise darauf, dass die Brink-Axel Hypothese unterhalb von 8 MeV für beide Telluriumisotope nicht gültig ist.

Contents

1 Introduction

"It's a warm summer evening in ancient greece" [1]:
First attempts have been made to provide rational explanations for the mechanisms observed in nature and what the world is made of. Famous greek philosophers have dedicated their life to study the composition of matter. Two opposing theories existed at that time. On one hand, philosophers such as Empedocles ($\sim$ 450 B.C.) and Aristotle (384-322 B.C.) believed that all substances are composed of four primordial elements: earth, water, air and fire. According to their philosophy all objects are created by the mixture and segregation of these primordial elements. The subdivision of a substance can be repeated an infinite number of times leading to the conclusion that something like a "smallest" corpuscle does not exist. On the contrary, Leucipuus ($\sim$ 440 B.C.) and Democritus ($\sim$ 420 B.C.) have postulated that all objects in our world are composed of tiny indivisible units. Following their theory, no object can be divided endlessly into smaller and smaller parts. These "smallest" particles were called atoms (*greek*: $\alpha\tau o\mu o\varsigma$, indivisible). In their imagination these atoms exist in different shapes, size and weight. However, the following centuries have been strongly influenced by the philosophy of Aristotle, while the atomistic school sank into oblivion. It was not until the 18th century, that a huge progress in chemistry achieved by the natural scientists Antoine Laurent de Lavoisier, Joseph Louis Proust and John Dalton who discovered new chemical elements and put the *four elements theory* of Aristotle into doubt. In his book *A New System Of Chemical Philosophy* Dalton initiated the renaissance of the atomistic view of our world. He stated that the new scientific findings can be explained if matter is composed of indivisible spherical atoms that can form chemical compounds, which can be rearranged or separated. Dalton's model was successful in explaining the *law of multiple proportions* of chemical compounds, but not able to describe the electrophysical nor the electrochemical properties of atoms. It was Joseph John Thomson who discovered in 1897 the first subatomic particle, the electron [1]. Based on this he proposed a new atomic model in which *"the atoms of the elements consist of a number of negatively electrified corpuscles enclosed in a sphere of uniform positive electrification"* [2].

In 1896, only one year before the discovery of the electron, Henri Becquerel initiated the era of nuclear physics. In experiments with phosphorent materials he observed that uranium emits some kind of radiations [3] that later will be identified as α- and β-radiation, respectively. Furthermore, Pierre and Marie Curie discovered more chemical elements to be radioactive [4] what already indicated that atoms might not be that indivisible as expected until then. In 1909,

[1] Dr. Dr. Sheldon Lee Cooper - *The Big Bang Theory, The Gorilla Experiment (Season 3, Episode 10, CBS), December 7, 2009.*

an important milestone towards modern nuclear physics were the famous α-scattering experiments on thin gold foils [5] performed by Hans Geiger and Eugene Marsden, both students of Ernest Rutherford. According to the *Thomson atomic model* the α-particles were expected to pass the gold foil without any deflection or only with very small deflection angles, what indeed was observed for most of the projectiles. However, a small fraction of the α-particles was also detected at scattering angles larger than 90°. Rutherford correctly concluded in 1911 that the atom consists essentially of empty space filled with electrons and a tiny, incredibly dense, positively charged nucleus in the center [6]. Nevertheless, the *Rutherford atomic model* still lacked the explanation for the stability of atoms and the characteristic emission and absorption lines of hydrogen atoms. It was later revised by Niels Bohr postulating that atomic electrons can only circulate stably on *stationary orbits* which have fixed distances to the nucleus [7]. In that way, the discrete emission spectrum of hydrogen was interpreted as a *jump* of an electron from one orbit to the other. The energy difference between two orbits is consequently emitted as electromagnetic radiation. Due to the advance in quantum mechanics by Erwin Schrödinger and Werner Heisenberg, among others, the nowadays accepted *modern quantum cloud model* was developed, where electrons are not orbiting on fixed tracks around the nucleus, but are represented by an *electron cloud* [8, 9] resulting from the *Heisenberg uncertainty principle*. The history of the different pictures used to describe the atom is briefly summarized in Fig. 1.1.

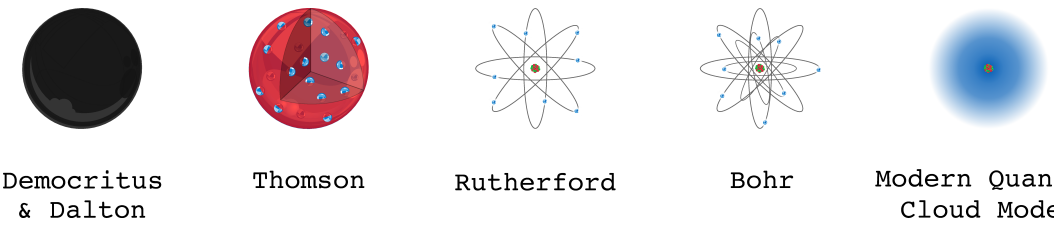

Figure 1.1: Models of the atomic nucleus throughout history.

Almost the complete atomic weight is concentrated in one point, the nucleus, which is about four order of magnitudes smaller than the total size of the atom. This finding gave birth to the new field of nuclear physics. It was once again Rutherford who managed to make the next step. In 1919, he conducted α scattering experiments on nitrogen producing a proton and an oxygen nucleus and thus discovered the proton to be a constituent of the atomic nucleus [10]. About a decade later James Chadwick, one of his students, discovered an additional constituent of the nucleus, the neutron [11]. Today, we know that protons and neutrons are composed of even smaller particles: quarks and gluons. It is part of recent research if they are elementary particles or if future experiments will reveal a substructure inside of them as well.

Throughout history, mankind is seeking to understand *"whatever holds the world together in its inmost folds"*[2]. From greek philosophers to modern scientists, the deeper they looked into the composition of matter, the more and smaller substructures have been discovered. Figure 1.2 illustrates the different sizes, energy scales and components of matter that are known up to now without attempting to be comprehensive. Various specialized fields of physics arose from the investigation of the different levels of matter.

[2] Johann Wolfgang von Goethe, *Faust: Eine Tragödie - Kapitel 4, translation from German to English by the author.*

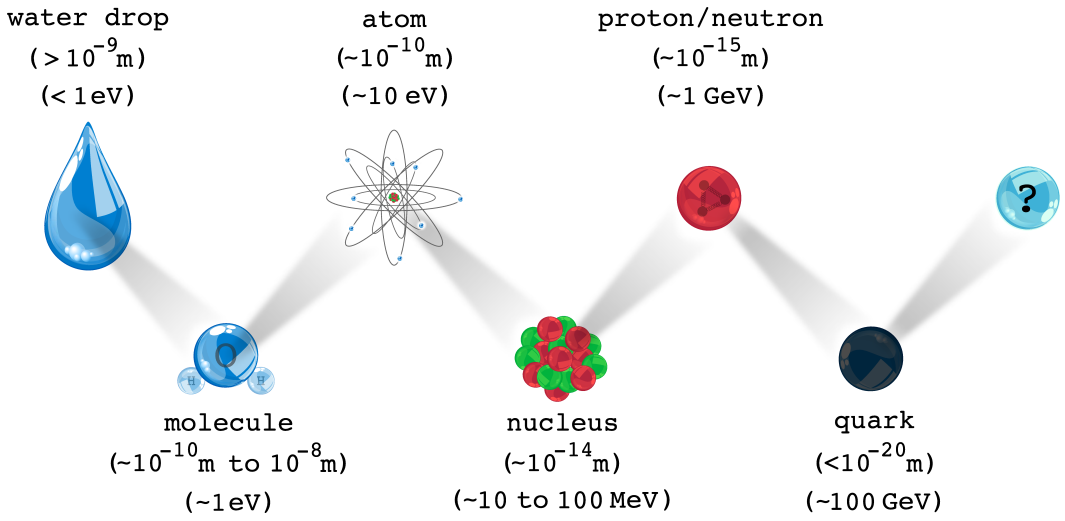

Figure 1.2: The scales of matter. The dimensions and energy regimes are schematically illustrated from macroscopic objects such as a water drop down to the constituents of nucleons, such as quarks.

Nuclear structure physics deals with the study of the atomic nucleus as a whole. The nucleus is a complex system of neutrons and protons that is governed by the weak, strong, and the electromagnetic interaction. The overall objective of nuclear structure physics is to describe and understand the mechanisms and properties of nuclei all over the nuclear chart (see Fig. 1.3). About 6000 nuclei are expected to exist as energetically bound systems in the universe. So far, approximately 300 stable and 2500 unstable nuclei are experimentally known, respectively.

It is a challenging task for both, theory and experiment, to study the characteristics of atomic nuclei. The nucleus represents a many-body problem ranging from a few up to several hundred nucleons that interact with each other. Hence, the nucleus is a fascinating system; complex enough to study collective phenomena and symmetries, but still sufficiently fundamental to be a quantum system with well-defined or approximate quantum numbers. From a theoretical point of view, these characteristics and the complexity of the interactions involved, such as the strong interaction, make it difficult, if not impossible, to describe the nucleus with one universal model. Depending on different aspects such as nuclear-mass regions and excitation-energy regions, among other things, different theoretical models are more suitable to describe nuclear properties than others. Obviously, nuclear structure theory tries to describe and explain the phenomena observed in nature and nuclear physics experiments, respectively. Its impact ranges from understanding the nucleosynthesis of the elements right after the big bang to applications in daily life, such as tumor therapy using ion beams.

The outstanding success of Rutherford has shown that scattering experiments are a fundamental tool to study various properties of nuclei. One common feature of atomic nuclei are nuclear excitation modes, such as giant resonances (GR) [13]. In a macroscopic picture, GR's are usually described as collective motions of many if not all nucleons. The investigation of their properties, e.g. excitation strength and energy, offer a connection of experimental observables to the bulk properties of nuclear matter, such as the number of particles participating in the excitation and the size of the nuclear system. In modern nuclear physics, many different kinds of probes are used for systematic investigations. One excellent and commonly used probe are photons. The wavelength of high-energy photons (typically $\sim$ MeV to 100 MeV) is in the order

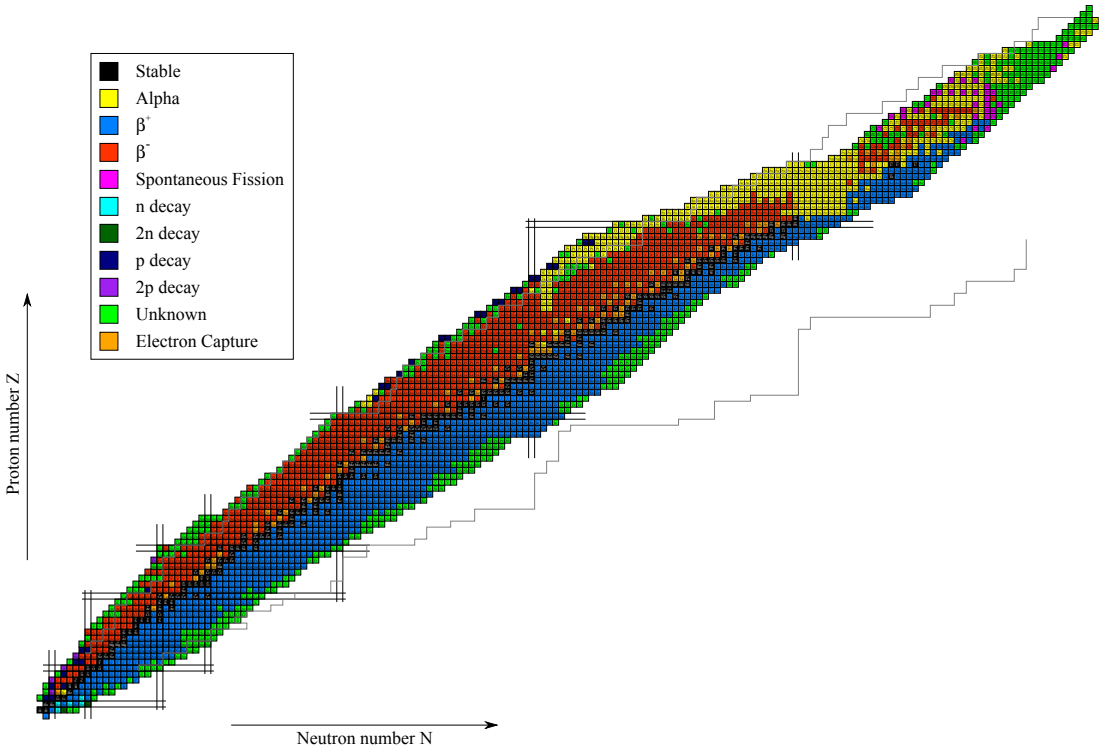

Figure 1.3: Nuclear chart. Stable nuclei are marked in black, while unstable isotopes are shown in different colors depending on the dominant decay channel. Shell closures in the nuclear shell model, also referred to as magic numbers, are given by vertical and horizontal double lines for neutrons and protons, respectively. The grey line above and mainly below the colored part of the nuclear chart indicate limits for extremely exotic, but still bound isotopes predicted by theoretical calculations. These are the so-called proton and neutron drip lines, respectively. Figure is generated with *inch* [12].

of the size of the nucleus ($\sim$ fm) and, thus, is sensitive to its internal structure. Furthermore, the interaction mechanism is given by the electromagnetic interaction alone, which can be exactly described by basic theory.

One of the prominent excitation modes that have been first investigated with the means of photons is the well-known Isovector Giant Dipole Resonance (IVGDR) [13]. The IVGDR was observed for the first time by Bothe and Gentner [14] in 1937 using γ radiation obtained from the ^{7}Li(p,γ) reaction and systematically investigated by Baldwin and Klaiber [15]. It can be macroscopically interpreted as an out-of-phase dipole oscillation of all protons against all neutrons [16]. Figure 1.4 gives a schematical overview of the electric dipole ($E1$) strength observed in typical medium and heavy mass, spherical atomic nuclei. The integrated cross section of the IVGDR (located around 15-20 MeV) exhausts about 100% of the so-called Thomas-Reiche-Kuhn (TRK) sum rule [17, 18]. The TRK sum rule gives an estimation of the total strength for a given excitation mode based on first principles, in the present case for $E1$ excitations:

$$\int_0^\infty \sigma(E)\mathrm{d}E = \frac{2\pi^2 e^2 \hbar}{mc}\frac{NZ}{A} = 60\frac{NZ}{A}\,\mathrm{MeVmb}\,, \tag{1.1}$$

where N, Z and A are the neutron, proton and atomic mass number. The IVGDR was the first giant resonance to be discovered and triggered enormous experimental and theoretical interest

to study resonance phenomena in atomic nuclei. Photons as probes in many reactions such as (γ,n), $(\gamma,2n)$, (γ,x) and so on, have proven to be very successful for nuclear structure studies.

This thesis focuses on photon-scattering experiments with real photons which is called nuclear resonance fluorescence (NRF) [19, 20]. In this reaction the nucleus is excited by resonant photoabsorption while the de-excitation takes place by the subsequent emission of photons. The first attempt for an NRF experiment has been conducted by Kuhn in 1929 [21]. He used the 2.614 MeV γ-ray from *Thorium C"* to irradiate lead with natural abundance. This γ-ray is characteristic for the end product of the thorium decay chain, historically called *Thorium D* and nowadays referred to as ^{208}Pb. This means that he used a photon emitted by ^{208}Pb to induce photoabsorption of another ^{208}Pb nucleus. Until that time, this concept was successfully applied in atomic resonance fluorescence (see, e.g. Ref. [22]). However, the typical natural line width of nuclear resonances ($\sim 10^{-3}$ eV) is much narrower than the recoil energy loss $E_\gamma/2Mc^2$ ($\sim$ eV) due to the emission and absorption process. Due to the total recoil energy loss the resulting photon energy was off-resonance and, hence, was not resonantly re-absorbed leading to a negative experimental result. It took more than two decades until the first successful NRF experiment was performed by Moon [23]. He used a radioactive ^{198}Au source ($^{198}\mathrm{Au} \rightarrow {}^{198}\mathrm{Hg} + e^- + \overline{\nu}_{e^-}$) which was carried by a high-speed rotor with a velocity of about 7×10^4 cm/s and liquid mercury as scattering target (scatterer). Exploiting the Doppler effect, the velocity was high enough to compensate for the recoil energy loss of the emitted 411 keV line in ^{198}Hg. Consequently, nuclear resonance fluorescence was observed for the first time.

With the advent of electron accelerators the first continuous-energy bremsstrahlung sources were available which bypassed the difficulties caused by the nuclear recoil process. After the first proposal by Schiff in 1946 to use bremsstrahlung as photon source for NRF experiments [24] it was not until 1957 that Hayward and Fuller successfully performed a photon-scattering experiment on ^{12}C with a 19 MeV bremsstrahlung beam [25]. In the 1960's additional photon sources such as quasi-monochromatic "tagged photon" beams became available for NRF experiments [26, 27]. Furthermore, the development of high-resolution germanium detectors in the late 1970s triggered an increased interest in the NRF technique to study the fine structure of collective excitations in atomic nuclei.

A prominent example is the scissors mode, a magnetic-dipole ($M1$) excitation, which was predicted by Lo Iudice and Palumbo [28, 29] in 1978. A few years later, it was observed for the first time by Richter *et al.* in (e,e') reactions [30, 31]. The fine structure of the $M1$ scissors mode, that is described in a macroscopic picture as a rotational vibration of the neutrons versus the protons, was studied in numerous NRF experiments [32–37] which provided a wealth of data to understand the nature of this resonance [20]. For comprehensive reviews on collective $M1$ excitations see Refs. [38, 39].

Moreover, the NRF method was and is extensively used to study low-energy two-phonon excitations. Of particular interest is the energetically low-lying 1^- state of the negative-parity quintuplet originating from the coupling of the quadrupole and octupole collective phonons $[2^+_1 \otimes 3^-_1]_{1^-}$. Figure 1.4 shows a schematic view of the $E1$ strength typically observed in spherical nuclei. The two-phonon 1^- state is usually located at low excitation energies in the region of the sum energy of the 2^+_1 and 3^-_1 states. To identify possible candidates for the two-phonon 1^- state, NRF measurements serve as a useful tool [20] being highly selective to dipole excitations. Systematic studies of the collectivity and the fragmentation of two-phonon 1^- states were performed in many photon scattering experiments throughout the nuclear chart [20, 40–43].

Proceeding to higher excitation energies, a resonance-like accumulation of $E1$ strength in

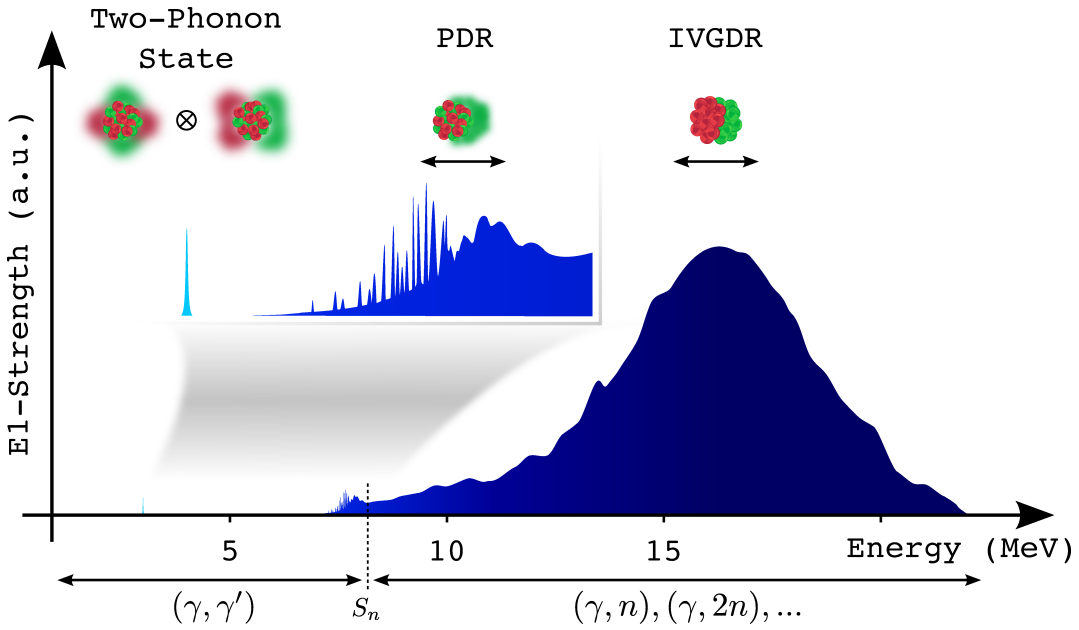

Figure 1.4: Schematic distribution of the electric dipole strength in spherical medium and medium-heavy nuclei. The coupling of the lowest quadrupole and octupole phonons results in the two-phonon 1^- state, which is usually located at a few MeV excitation energy. The dominant part of the $E1$ strength is located in the Isovector Giant Dipole Resonance (IVGDR) at excitation energies of about $\sim$ 15 MeV. On top of the low-energy tail of the IVGDR, in the vicinity of the neutron separation threshold S_n, an accumulation of $E1$ strength was observed in numerous nuclei, which is often denoted as Pygmy Dipole Resonance (PDR).

the vicinity of the neutron threshold and on top of the low-energy tail of the IVGDR, respectively, is observed in numerous nuclei. This low-lying $E1$ strength is often denoted as Pygmy Dipole Resonance (PDR) [44]. The content of this dissertation concentrates on NRF experiments in the region of the PDR, wherefore a more detailed discussion of this phenomenon is given in the following section.

1.1 The Pygmy Dipole Resonance

In the early 1960's, neutron-capture experiments lead to the first observation of a concentration of multipole strength on top of the low-energy tail of the IVGDR [45, 46]. Roughly ten years later, Mohan *et al.* interpreted this low-lying strength in a three-fluid hydrodynamical model [47] as extension of the two-fluid model that was introduced to describe the IVGDR. Two of these fluids are composed of the same amount of protons and neutrons, respectively, while the third fluid is given by the remaining excess neutrons. In this model two independent electric dipole modes are automatically generated. One strong out-of-phase oscillation of all protons against all neutrons, the IVGDR, and a much weaker electric dipole excitation at lower energy where the excess neutron oscillates versus the isospin-satured (N=Z) proton-neutron core. The term "pygmy" was established in the comparison of the total $E1$ strength of this low-lying resonance-like structure to the well-pronounced IVGDR. In contrast to the IVGDR, the PDR exhausts only a few percent of the TRK sum rule depending on the nucleus. The scales in

Fig. 1.4 give a rough picture of the difference in total $E1$ strength of the PDR relative to the IVGDR.

Further photo-induced reactions using tagged photons [48–50] extended the amount of experimental data pointing to an enhancement of the $E1$ strength in the vicinity of the neutron threshold for many nuclei.

The availability of high-resolution Germanium detectors made it feasible to study the fine structure of the PDR, i.e., performing a state-to-state analysis below the neutron separation threshold. One of the first high-resolution NRF experiments to investigate the dipole strength distribution was conducted by Herzberg *et al.* on ^{140}Ce [51] and ^{138}Ba [52], while Govaert *et al.* studied the tin isotopes ^{116}Sn and ^{124}Sn [53]. These experiments, using continuous-energy bremsstrahlung as photon source, showed in all nuclei a concentration of strong dipole excitations with electric character in accordance to results from the previously mentioned tagged photon experiments [48–50]. First systematic studies of the fragmentation of the PDR in the stable $N = 82$ isotones were published in Refs. [54–56] and compared to calculations within the quasi-particle phonon model (QPM) [57]. Figure 1.5 shows a compilation of the $N = 82$ data given in Ref. [56]. The overall strength distribution is reasonably well reproduced, while the position is shifted to slightly higher excitation energies in the QPM calculations.

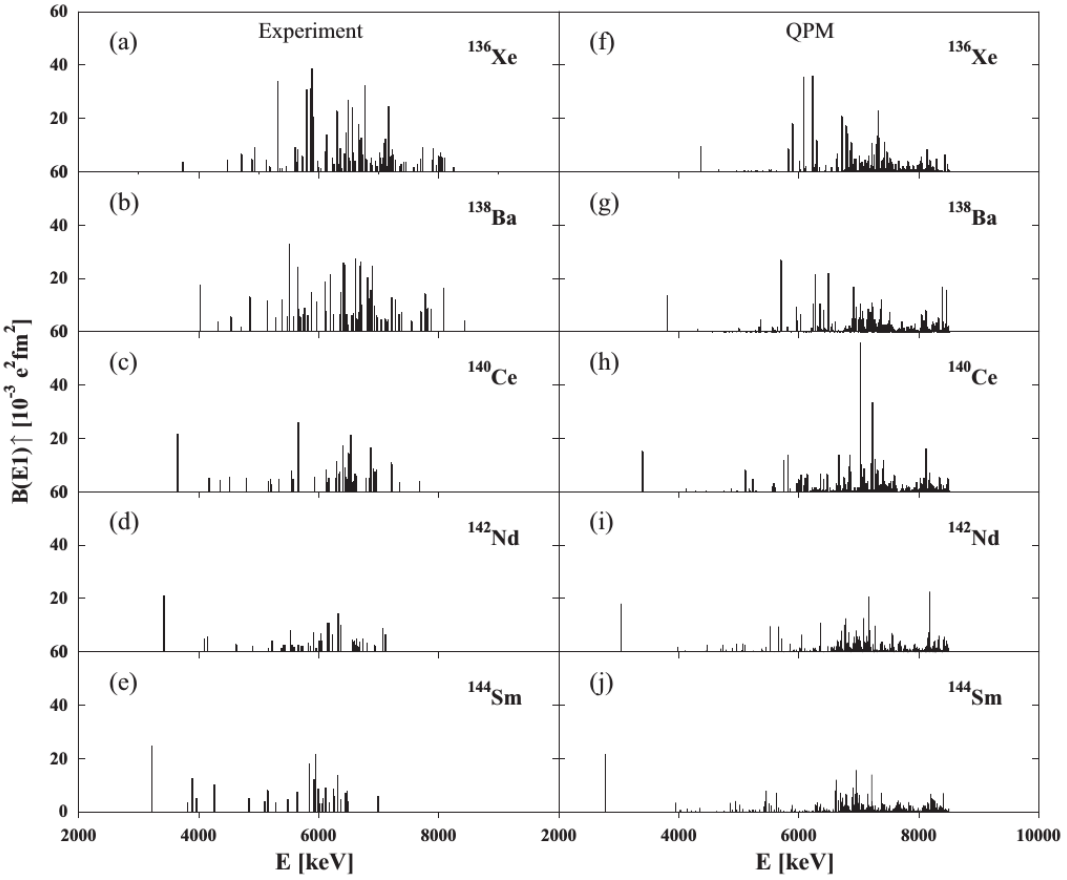

Figure 1.5: $B(E1)$ strength distribution for $N = 82$ isotones. The experimental results are shown in panels (a)-(e), while the corresponding QPM calculations are given in panels (f)-(j).
Source: Reprinted figure with permission from [56]. Copyright 2011 by the American Physical Society.

In the past two decades, a large amount of high-resolution NRF experiments at different research facilities have been conducted to investigate the dipole strength distribution and the de-excitation properties of photo-excited states in the vicinity of the neutron separation threshold. As a result, stable nuclei throughout the nuclear chart were systematically investigated, ranging from the medium mass region around calcium, nickel and germanium [58–65] up to the N=50 [66–69] and N=82 mass region [54–56, 70–74], respectively.

Real-photon scattering experiments, however, are limited to stable nuclei. The extension of the PDR investigations to exotic unstable isotopes became possible with research facilities that are able to produce radioactive ion beams. In 2005, first results on the low-lying $E1$ strength in neutron-rich tin and antimon isotopes [75, 76] (see Fig. 1.6) were gained from Coulomb excitation experiments in inverse kinematics. A few years later, studies on the unstable neutron-rich isotope ^{68}Ni [77, 78] were published. For ^{132}Sn and ^{68}Ni the low-lying dipole strength attributed to the PDR exhausts about 5% of the TRK sum rule. In comparison to that, stable isotopes investigated by NRF experiments exhaust around 1% of the TRK sum rule depending on whether a state-to-state analysis was performed or an analysis of the complete strength including the unresolved strength hidden in the background (see, e.g., Refs.[66, 79, 80] and references therein). The latter two analysis methods are discussed, among other things, in more detail in the review of Savran *et al.* [44].

For a complete picture of the nature of the PDR it is crucial to conduct different kind of experiments using complementary probes. Hadronic probes, such as α-particles [81–84] or ^{17}O [85, 86] were used to study the isoscalar component of the electric dipole strength in the PDR region. These experiments lead to surprising and interesting results. The comparison of NRF results to differential cross sections obtained from $(\alpha, \alpha'\gamma)$ experiments at KVI Groningen revealed a so-called "isospin-splitting" of the PDR strength [81]. The results for three $N = 82$ isotones are shown in Fig. 1.7. It can be clearly seen that in the $(\alpha, \alpha'\gamma)$ reactions dipole-excited states above a certain energy are not or with suppressed probability excited compared to the (γ, γ') data. This points to different underlying isospin structures of the excited states. While photons are predominantly sensitive to the isovector part of nuclear wavefunctions, hadrons probe at the given kinematical conditions the isoscalar components. These findings were later

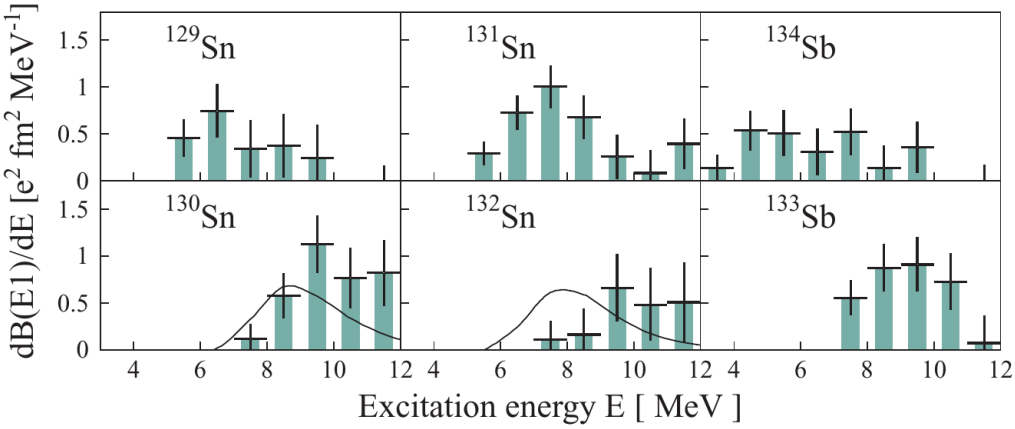

Figure 1.6: Electric dipole strength distribution for unstable Sn and Sb obtained from Coulomb excitation experiments in inverse kinematics.
Source: Reprinted figure with permission from [76]. Copyright 2007 by the American Physical Society.

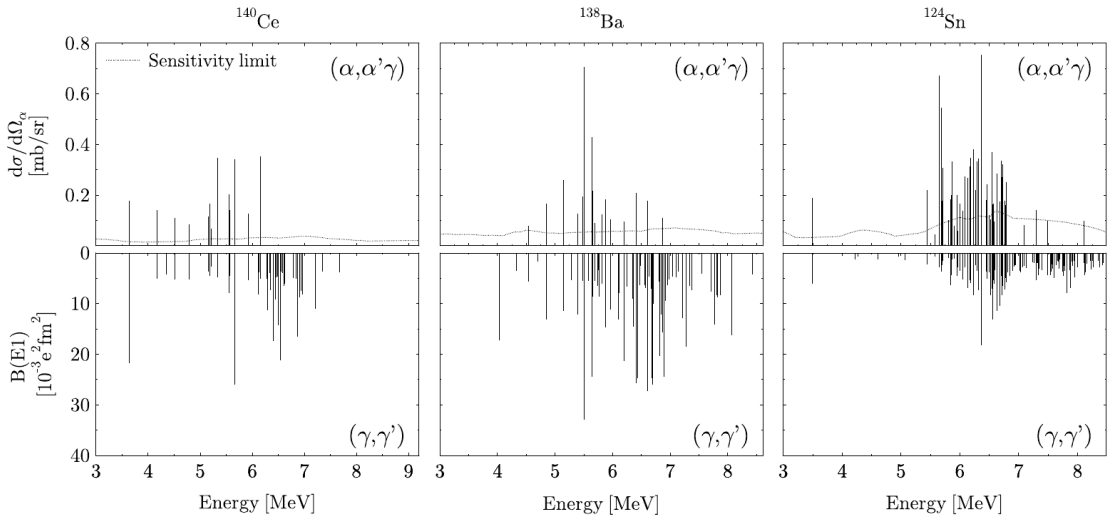

Figure 1.7: Comparison of the $E1$ strength in ^{140}Ce, ^{138}Ba and ^{124}Sn extracted from $(\alpha,\alpha'\gamma)$ experiments and (γ,γ') measurements [53, 54, 81–83]. *Source*: Reprinted from Ref. [88] with permission from IOP Publishing.

confirmed in (^{17}O,^{17}O'γ) experiments for ^{124}Sn [86], ^{208}Pb [85] and ^{140}Ce [87].

A lot of effort has been put into the experimental and theoretical investigation of the PDR, however, its nature is still unclear. So-called transition densities from microscopic model calculations in the relativistic quasi-particle random-phase approximation (RQRPA) [89] support the interpretation of the PDR as a neutron-skin oscillation. The upper panel of Fig. 1.8 illustrates the dipole-strength functions $S(E)$ for the tin isotopes ^{116}Sn and ^{140}Sn [89]. The proton neutron transition densities for the pronounced peaks are given in the lower panel. For the peak at 8.94 MeV in ^{116}Sn, the neutron component of the transition densities is dominating on the surface of the nucleus, while the inner part is governed by a mixture of protons and neutrons. Proceeding to higher excitation energies, this feature diminishes and the transition densities indicate an out-of-phase oscillation of protons and neutrons in the IVGDR region. The macroscopic view of the IVGDR excitation mechanism is in agreement with previous extensive studies [13]. A similar evolution is observed in ^{140}Sn. Hence, the RQRPA calculations support the picture of an neutron-skin oscillation of the nucleus in the PDR region as it is the case for many other calculations (see, e.g. Ref. [90]). However, other excitation modes that might explain the origin of the low-lying $E1$ strength on top of the low-energy tail of the IVGDR are also considered, e.g., the toroidal dipole mode [92, 93]. A comprehensive review on theoretical approaches to the PDR, among other excitation modes, can be found in the review by Paar *et al.* [90].

Following the macroscopic picture of an oscillating neutron skin, microscopic models predict a connection between the PDR strength and the neutron-skin thickness (see, e.g. [94–98] and references therein). The neutron-skin thickness itself is linked to the symmetry energy of the equation of state (EoS) of nuclear matter [99, 100] that describes dense astrophysical objects, such as neutron stars (see, e.g. [101]). An observable that might be well-suited to study the neutron-skin thickness and parameters of the EoS [97, 101–103] is the so-called dipole polarizability:

$$\alpha_D = \frac{\hbar c}{2\pi^2 e^2} \int_0^\infty \frac{\sigma_\gamma}{E^2} \mathrm{d}E \ . \tag{1.2}$$

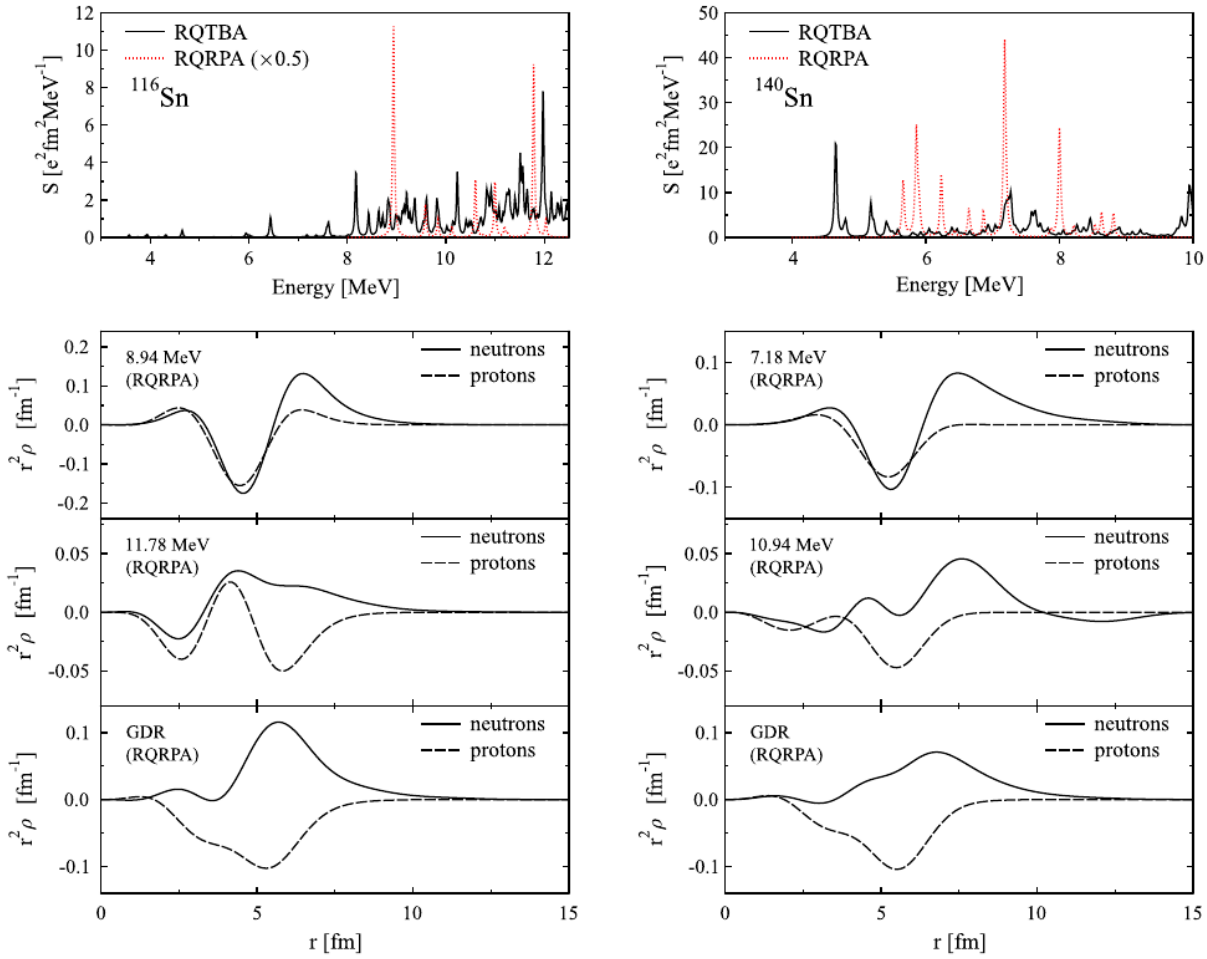

Figure 1.8: $E1$ strength distribution in ^{116}Sn (upper left) and ^{140}Sn (upper right) calculated in RQRPA and RQTBA. Lower panels: Proton and neutron transition densities for the most pronounced peaks at low excitation energies. In addition, the transition densities in the IVGDR region are shown.
Source: Reprinted from [44], Copyright 2013, with permission from Elsevier. Data originally taken from [89, 91].

It corresponds to the inverse energy-weighted photoabsorption cross section. It has to be emphasized, that the correlation between the neutron-skin thickness and α_D is established if the full photoabsorption cross section is known. Hence, the complete energy-dependent $E1$ strength distribution has to be determined experimentally. This is a challenging task that has been conducted for ^{208}Pb [104, 105] and ^{120}Sn [106] in (p, p') experiments. Furthermore, Coulomb excitation experiments in inverse kinematics provided results for α_D in the neutron-rich nickel isotope ^{68}Ni [78]. It should be noted, that even though the PDR exhausts only about 1 % to 5 % of the TRK sum rule of the electric dipole strength, its contribution to the dipole polarizability is not negligible due to the inverse-energy weighting and ranges from 3 % up to 15 %.

Different kinds of complementary approaches were used to learn more about the origin of the low-lying electric dipole strength observed in numerous nuclei on top of the low-energy tail of the IVGDR . However, the nature of the PDR is still widely discussed and a hot topic in modern nuclear structure physics. This section presented a brief overview of the state-of-the-art on the investigation of the PDR without attempting to be comprehensive. For a detailed and

comprehensive discussion on experimental studies of the PDR, the review by Savran *et al.* [44] is highly recommended.

1.2 Photon strength functions: Present status

Impact on nucleosynthesis calculations

Even though the contribution of the PDR to the total $E1$ response in the nucleus is small compared to the IVGDR, it has important impacts on astrophysical scenarios. The rapid neutron-capture process (r-process) is responsible for the nucleosynthesis of about half of the medium-heavy to heavy nuclei. The calculations for the corresponding neutron-capture rate in (n,γ) reactions, are usually performed in the statistical Hauser-Feshbach model [107]. The statistical decay properties rely, among other things, on the so-called photon strength function (PSF), which is connected to the average photoabsorption cross section σ_γ (for more details, see Section 2.1). Consequently, the additional electric dipole strength of the PDR has an influence on the PSF in this energy region. Since the PDR is usually located in the vicinity of the neutron separation threshold, its contribution to the total PSF may have a significant impact on astrophysical reaction rate calculations. Therefore, a detailed knowledge of the absolute scale and energy dependence of the PSF is crucial for reliable calculations. In particular, very neutron-rich nuclei play an important role in the r-process. However, their PSF cannot be easily studied, if at all, with current experimental techniques. Thus, statistical model calculations rely on extrapolations of the PSF from available experimental data to very neutron-rich isotopes using microscopic model calculations [108–110]. Furthermore, the p-process [111, 112], generally describing photo-disintegration reactions in stellar environments, strongly depend on the PSF as well. When speaking about photon strength functions, it is usually referred to the PSF on top of the ground state of the atomic nucleus. However, in hot stellar environments, temperatures in the $\sim 10^9$ K scale increase the probability for nuclei to be in excited states rather than the ground state. Thus, photoabsorption and photo-disintegration take place on excited states of these nuclei. It is not trivial to determine the photoabsorption cross section on excited states. For theoretical calculations, it is assumed, that the PSF on top of excited states is equivalent to the one on the ground state. This assumption is in accordance to the so-called Brink-Axel hypothesis [113, 114]. An overview of astrophysical reaction rate calculations and their dependence on the corresponding photon strength functions can be found, e.g., in Ref. [115].

Experimental approaches

Different experimental methods and approaches have been used to study the photon strength function, especially the $E1$-PSF in several atomic nuclei. Above the neutron separation threshold, photo-disintegration reactions, such as (γ,n) and $(\gamma,2n)$ are used to measure the photoabsorption cross section (see, e.g., [116]). However, below the neutron binding energy, other methods have to be applied to investigate the PSF.

The Oslo method

The Oslo Cyclotron group has developed a procedure to determine the PSF from $(^3He,\alpha\gamma)$ and $(^3He,^3He'\gamma)$ reactions. In the so-called Oslo method [117–121], primary γ-ray spectra are extracted via particle-γ coincidences for various excitation energies. In an iterative procedure,

the product of level densities and the total PSF can be determined from these primary spectra even for low γ-ray energies ($\leq$ 3 MeV). Figure 1.9 shows examplarily results for several tin isotopes [120] using the Oslo method. However, these reactions induce many types of multipole transitions making it difficult to disentangle the different components of the measured total PSF. In addition, the product of level density and PSF is determined. This leads to a level density model-dependent extraction of the corresponding PSF.

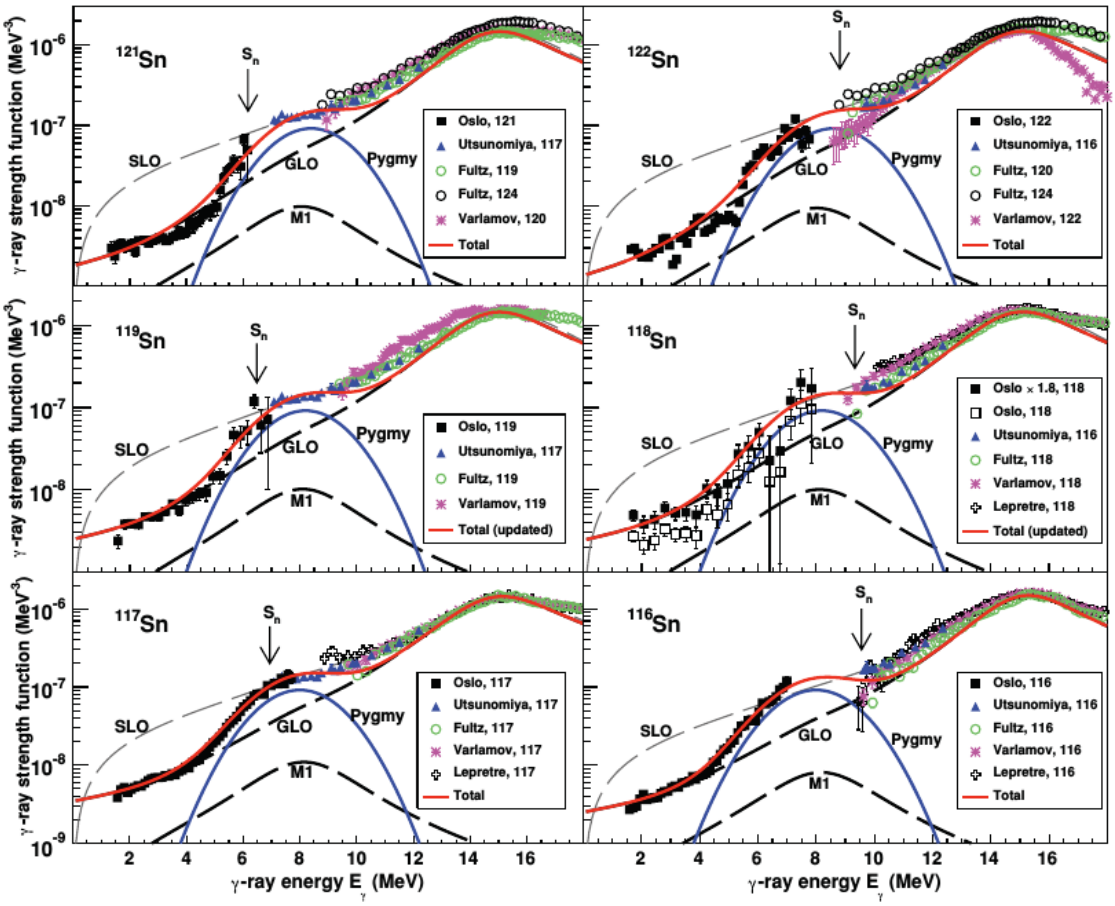

Figure 1.9: Experimental results for the total photon strength function in the tin isotopes ^{116,117,118,119,121,122}Sn extracted with the Oslo method.

Source: Reprinted figure with permission from [120]. Copyright 2011 by the American Physical Society.

p-γ-γ correlations

A model-independent measurement of the energy dependence of the PSF was conducted in Ref. [122] using p-γ-γ correlations in ^{94}Mo$(d,p)^{95}$Mo reactions (see Fig. 1.10). Furthermore, a detailed discussion on the consistency of a number of PSF models with the experimental data was very recently published [123]. The (d,p) reaction, however, suffers from the same lack of sensitivity for different multipole transitions as pointed out earlier. Particle-induced reactions populate a large variety of states with different quantum numbers. The separation of dipole excitations and in particular the selection of states that are attributed to the PDR is therefore not a trivial task.

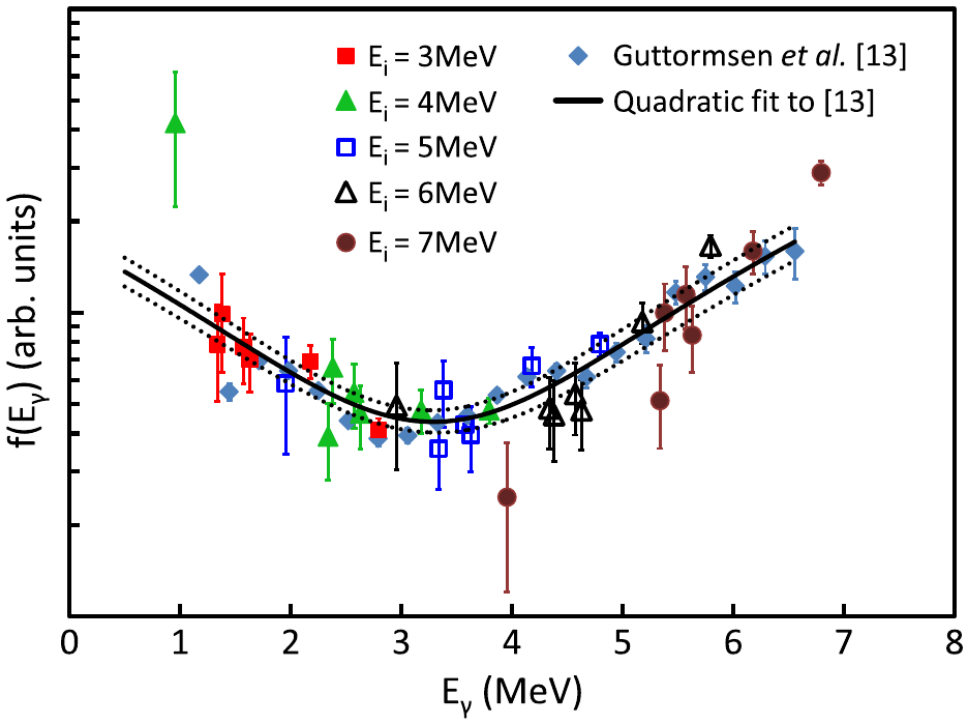

Figure 1.10: Experimental results for the relative shape of the photon strength function determined from p-γ-γ correlations in ^{94}Mo$(d,p)^{95}$Mo reactions.
Source: Reprinted figure with permission from [122]. Copyright 2012 by the American Physical Society.

Photon scattering: Continuous spectrum analysis

This is where the advantage of photon scattering experiments compared to particle-induced reactions comes into play. Due to the low momentum transfer of real photons, mainly dipole transitions are induced selecting a definite set of excited states. Moreover, the extraction of intrinsic properties is conducted in a model-independent way. Transition probabilities, e.g., are directly linked to experimental reaction cross sections via the electromagnetic interaction. Consequently, photon scattering is well-suited to study the $E1$ and $M1$ part of the total dipole photon strength function below the neutron separation threshold. The corresponding reaction mechanism is denoted as nuclear resonance fluorescence (NRF) [19, 20, 124] and will be discussed in detail in Chapter 2.2. After the excitation by resonant photoabsorption, the nucleus either decays directly to the ground state or to lower-lying intermediate states via photon emission. In order to extract the photoabsorption cross section for a given excitation energy, it is crucial to determine the complete dipole response.

The Dresden-Rossendorf group developed an analysis method to determine the full dipole strength from NRF experiments using bremsstrahlung as photon source (see, e.g., Refs. [67, 72] and references therein). Figure 1.11 illustrates the procedure. The experimental γ-ray spectrum is corrected for natural background radiation (black) as well as the detector response (red). Furthermore, the beam-induced non-resonant background (blue) is simulated and subtracted. The resulting spectrum (green) contains γ-rays from nuclear transitions, only. Peaks stemming from transitions between excited states within the nucleus are apparent. The continuum below the pronounced peaks is the so-called "unresolved strength", which arises due to the in-

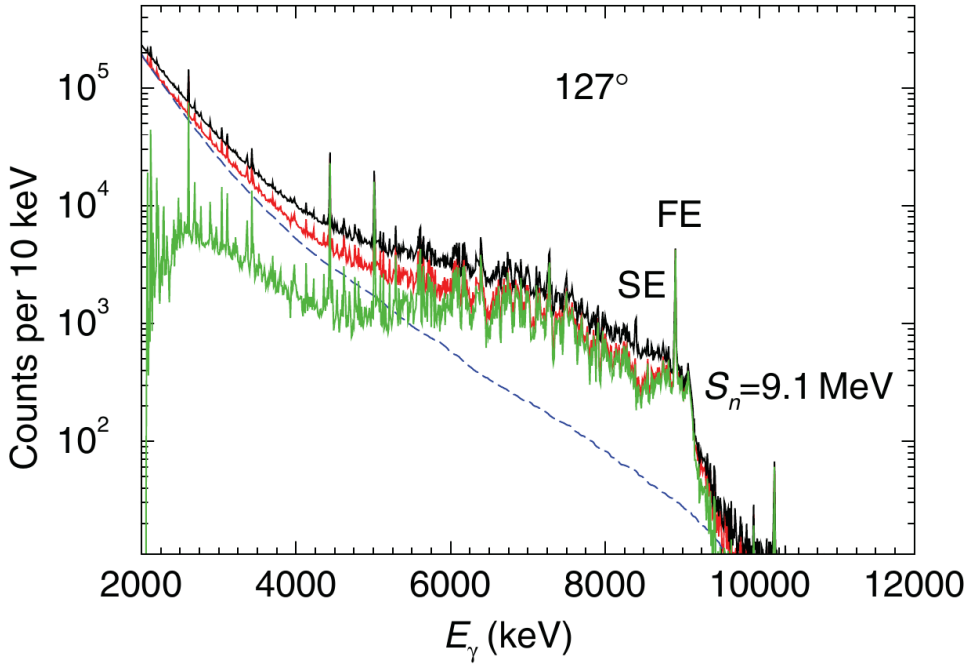

Figure 1.11: Extraction of the total dipole strength from an analysis of the complete γ-ray spectrum, i.e. including the strength located in isolated peaks as well as the unresolved strength hidden in the continuum below the peaks. For details see text or [72].
Source: Reprinted figure with permission from [72]. Copyright 2012 by the American Physical Society.

creasing nuclear level density. Furthermore, the spectrum includes ground-state and feeding transitions, respectively. Eventually, for the extraction of the photoabsorption cross section, the spectrum has to be corrected for feeding and subsequently for the ground-state branching ratio of the remaining intensity. This is done using statistical model calculations. Even though NRF experiments provide, in general, model-independent observables, the designated photoabsorption cross section extracted with this kind of analysis is, therefore, not model-independent at all. Many model-dependent simulations and corrections have been applied to the experimental spectra before the dipole response was extracted. Furthermore, the concept of the statistical model is not applicable at all excitation energies, but is limited to regions with sufficiently high nuclear level densities.

Photon scattering: Experiments with quasi-monochromatic photon beams

A model-independent way to measure the photoabsorption cross section with the NRF method was proposed by Tonchev *et al.* [71]. Instead of using continuous-energy bremsstrahlung, the quasi-monochromatic photon beam at the High Intensity γ-ray Source (HIγS) [125] is exploited. Due to the tunable beam energy, it is possible to study the level scheme and the photoabsorption cross section for energy bins of a few hundreds of keV. Figure 1.12.a) shows exemplarily for ^{130}Te a typical spectrum (blue) recorded in single γ-ray spectroscopy using High Purity Germanium detectors (HPGe). The spectral distribution of the incoming photon beam with a mean energy of 7.85 MeV is displayed in grey. In Fig. 1.12.b) an expansion of the excitation region is given, showing individual resolved peaks stemming from ground-state transitions in ^{130}Te. The

summed background-corrected intensity in this energy range is connected to the elastic cross section $\sigma_{\gamma\gamma}$, which will be discussed in Section 4.6.1.

Investigating the low-energy part of the spectrum, de-excitations of low-lying excited states are observed (see Fig. 1.12.c)). Due to the quasi-monochromatic photon beam, these states cannot be excited directly. Following the idea of Tonchev *et al.* [71], these levels must have been populated by cascade transitions from excited states around the beam energy of 7.85 MeV. Primary transitions to these states are often too weak to be observed in single γ-ray spectroscopy due to the comparatively high beam-induced background radiation at energies below the beam energy. Nevertheless, it is usually assumed that the vast majority of the cascading events decay via one of the first 2^+ states. The collected intensities observed for these states serve as an estimation for the inelastic cross section $\sigma_{\gamma\gamma'}$. For a more detailed discussion of the technique see Section 4.6.1. Exploiting this approach, photoabsorption cross sections ($\sigma_\gamma = \sigma_{\gamma\gamma} + \sigma_{\gamma\gamma'}$) for a few nuclei have been determined in the past years (see, e.g., Refs. [69, 71, 73]).

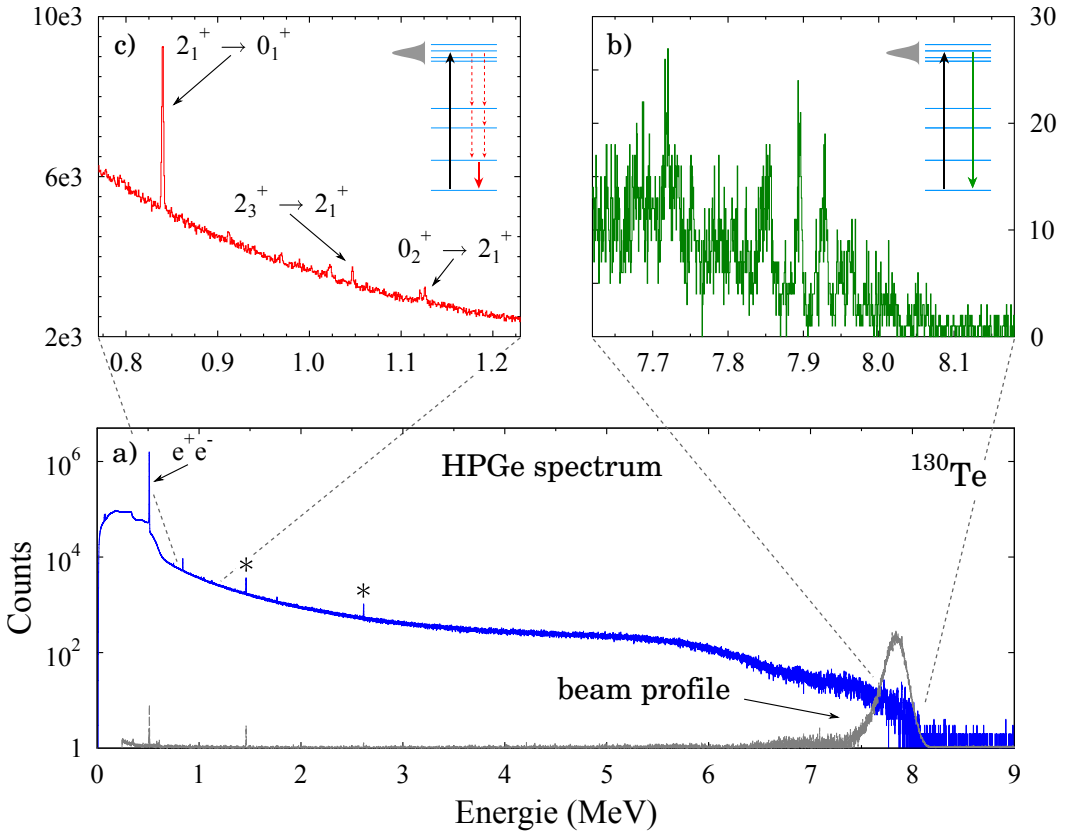

Figure 1.12: a) Measured HPGe spectrum of ^{130}Te (blue) together with the beam profile (grey). b) Spectrum at 7.85 MeV. Resolved peaks stemming from ground-state transitions in the excitation energy region. c) Low-energy part of the spectrum. Transitions from low-lying excited states can be observed that have been populated by cascade transitions initially excited states around 7.85 MeV.

1.3 Objective of this work

The methods discussed in the end of the previous Chapter provided a brief overview of complementary strategies currently applied to measure the photoabsorption cross section and connected to it the PSF build on the ground state. However, several challenges in this context have still to be met:

- Validity of the Brink-Axel hypothesis
- Experimental determination of photon strength functions build on excited states
- Photon strength functions for $E_\gamma < 4$ MeV

An important open question related to PSF's is whether the so-called Brink-Axel hypothesis [113, 114] is universally valid and in which excitation energy regions it is applicable. The Brink-Axel hypothesis states, that the PSF's build on top of excited states are equivalent to the ones on the ground state. This means, the PSF is independent of the internal structure of excited states, but a function of the energy of the γ-rays involved in the corresponding reactions, only. It is one of the major assumptions applied in nearly all model calculations for astrophysical reaction rates. However, it is difficult to measure the PSF on excited states in actual photoabsorption experiments, since atomic nuclei are usually found in their ground state in the laboratory. Hence, γ-ray spectroscopy of excited states decaying to a lower-lying excited state can be used to extract information on the PSF build on this nuclear level. This would yield crucial data to study and test the Brink-Axel hypothesis in a model-independent manner exploiting real photon scattering experiments.

Due to its high selectivity for dipole-excitations, real photon scattering is the method of choice to study dipole PSF's in atomic nuclei. Up to now, NRF experiments were mainly performed in single γ-ray spectroscopy mode. The associated sensitivity is usually too low to observe primary transitions from excited levels to lower-lying levels. One way to improve the sensitivity is the use of the γ-γ coincidence method. For that reason, the novel γ^3-setup [126] was installed at HIγS in 2012 to perform coincidence experiments exploiting the provided quasi-monochromatic photon beam. It has to be emphasized, that the unique combination of the γ-γ coincidence setup with the incoming quasi-monochromatic photon beam enables $(\gamma, \gamma'\gamma'')$ reactions with known excitation energy and, thus, is equivalent to particle-γ-γ measurements. As a result, the sensitivity for the measurement of relatively weak transitions is strongly improved. The decay behavior of photo-excited states and in particular average quantities such as the PSF can be studied in greater detail than in any NRF experiment before. First results using the γ-γ coincidence mode of the γ^3-setup have been published on ^{40}Ca and ^{140}Ce investigating quadrupole-octupole 1^- states [127]. Furthermore, the average decay pattern of the PDR in ^{140}Ce has been successfully studied as well [128].

An additional crucial point is, that the connection between the photoabsorption cross section and the photon strength function is assumed to be valid at excitation energies with a sufficient amount of nuclear levels available. At lower energies, nuclear structure effects play a major role in the description of the nucleus. Thus, information on the PSF for very low excitation energies ($\lesssim$ 3-4 MeV) is not easily accessible. In statistical model calculations, the low-energy part of the PSF has a particular influence on the correction for unobserved branching transitions, for instance in the procedure introduced in the previous Chapter for the analysis of the continuum in γ-ray spectra.

Therefore, a new approach using the quasi-monochromatic photon beam provided at HIγS is introduced to overcome this task. As discussed before and shown in Fig. 1.12, after photo-excitation not only the ground state, but also low-lying excited states are populated by cascade transitions, in particular 2^+ states. How strong each of these states has been populated can be deduced from an analysis of their decay intensities. Figure 1.13 illustrates this idea. A comparison of the measured population intensities to calculations within the statistical model proves to be sensitive to the PSF for γ-ray energies below $\sim$ 4 MeV. A brief description of the procedure can be found in Ref. [73], while a more detailed discussion follows in Section 4.7.

The main objective of this doctoral thesis is to study the dipole response and the decay behavior of photo-excited states in ^{128}Te and ^{130}Te from low excitation energies up to the region of the PDR in the vicinity of the respective neutron separation threshold. The tellurium isotopes ^{122,126,130}Te were investigated in NRF measurements up to excitation energies of $\sim$ 5.5 MeV by Schwengner *et al.* [129]. However, their focus was to study low-lying two-phonon $J = 1$ states. The first (γ, γ') experiment in the energy regime of the PDR in a tellurium isotope was performed on ^{130}Te [73]. In order to extend the systematic analysis of the PDR strength in the isotopic chain, ^{128}Te proves to be an excellent candidate. Decreasing the neutron number from N=78 to N=76, ^{128}Te is additional two neutrons off the magic shell closure at N=82 than ^{130}Te. The low-lying dipole strength and the photon strength function, respectively, have been mainly investigated in magic nuclei, such as the Ca isotopes [60, 61], the N=82 isotones [54, 55, 70], ^{88}Sr [66] and ^{208}Pb [93], just to mention of few. However, NRF data in the PDR energy region on nuclei apart from magic shell closures are still scarce. In recent years, measurements on the Ge isotopes [58], ^{76}Se [65, 130] as well as on the Mo isotopic chain [69, 131] were conducted. The tellurium isotopes allow for the extention of the available data set for non-magic nuclei

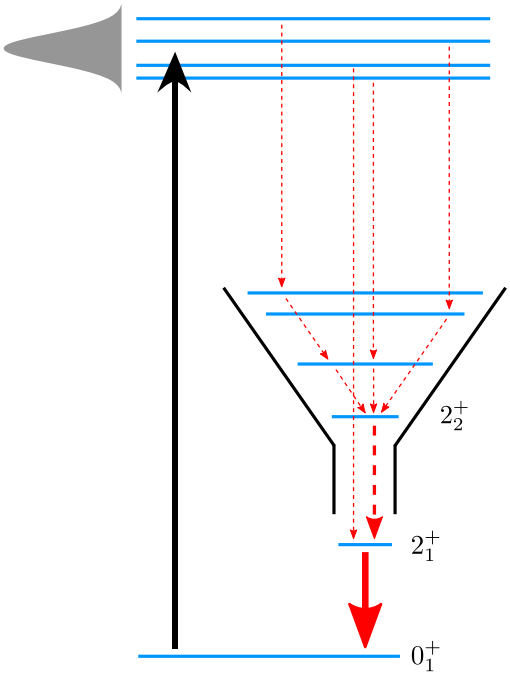

Figure 1.13: Scheme illustrating how the first excited 2^+ states collect the majority of the intensity decaying via intermediate states rather than directly back to the ground state.

from medium-mass to $A \sim 130$ mass nuclei. The similar natural abundances of ^{128}Te (31.74 %) and ^{130}Te (34.08 %) makes them a natural choice for further NRF studies in this mass regime.

In the scope of this work, photon-scattering experiments were performed on ^{128}Te and ^{130}Te at two nuclear physics facilities. One experiment was conducted at the Darmstadt High Intensity Photon Setup (DHIPS) [132] using continuous-energy bremsstrahlung as photon source. Here, a state-to-state analysis is performed to determine integrated cross sections of individual resolved dipole-excited states. Secondly, NRF experiments were realized at the HIγS facility. Single γ-ray spectroscopy was performed with ^{130}Te in 2011 using four High Purity Germanium (HPGe) detectors. The γ^3-setup [126] was installed at HIγS in 2012 and was used for the experiments with ^{128}Te. The possibility for γ-γ coincidence measurements enables the extraction of direct information on the de-excitation pattern of photo-excited states. In particular, it is possible to observe direct populations of the first excited 2^+ states and to determine average cross sections for these transitions, which are directly connected to the photon strength functions build on these excited states. Moreover, the linear polarization of the photon beam allows for the distinction between $E1$ and $M1$ strength of the total dipole response observed below the neutron binding energy. This feature is applied to resolved transitions as well as to averaged decay intensities. As a consequence, it is possible to study the PSF and, in particular, the $E1$-PSF in a detailed fashion.

2 Theoretical basics

2.1 The statistical model

Nuclear physics and in particular nuclear structure physics deal with the properties of the nucleus as a whole. Level energies, spin quantum numbers, excitation strengths and many more characteristica are typical quantities that are investigated. One objective is to understand the structure and distinctive properties of individual nuclear states, in many cases from a microscopic point of view. A schematic level scheme of an atomic nucleus is shown on the left-hand side of Fig. 2.1. Investigations of individual excited states are, in general, limited to low excitation-energy regions where the spacing between two neighboring levels is much larger than their resonance width.

Going to higher excitation energies, the average spacing between succeeding levels decreases strongly (see level scheme in Fig. 2.1). Hence, it becomes more suitable to describe the number of excited levels in a certain energy region with an average quantity, the nuclear level density (NLD). Furthermore, it is assumed in this regime, that the overall excitation and decay behavior of the nucleus is described well enough by averaging the individual transition strengths of an ensemble of all nuclear states in a particular energy region. Therefore, the so-called photon strength function (PSF) is introduced, which is directly linked to the average reduced radiation width of a given ensemble of states. Both, the nuclear level density and the photon strength function describe the properties of the nucleus in a statistical manner leading to the concept denoted as statistical model. Calculations within the statistical model are important for astrophysical predictions, especially in describing stellar reaction rates and the nucleosynthesis of the elements (see e.g. Refs. [108, 133–136] and for a more recent review Ref. [137]). Therefore, it is crucial to study both quantities in great detail. It should be noted, that a description of the excitation and decay properties of the nucleus with averaged quantities is a strong simplification. In which energy regions and under which conditions this approximation is sufficient in the description is a matter of ongoing discussions and cannot be answered easily.

In the following section, the idea of the nuclear level density and the photon strength function will be presented. In connection to this the so-called *Brink-Axel hypothesis* will be introduced, which plays an important role in the interpretation and application of photon strength functions in statistical model calculations.

2.1.1 The nuclear level density

Statistical properties of nuclei have been studied for many years. One of the basic properties is the average spacing $D(E)$ between individual states. While it is possible to determine the average spacing at low excitation energies simply by analyzing the discrete spectrum, as shown in Fig. 2.1, it becomes more difficult with increasing energy. At excitation energies above several MeV, depending on the mass of the nucleus, the level spacing is decreasing rapidely and it is no more possible to distinguish experimentally between individual states. Below and in the vicinity of the neutron separation threshold, respectively, the level scheme is often referred to as quasi-continuum (see Fig. 2.1). Far beyond the neutron binding energy, $D(E)$ becomes much smaller than the natural line width of the excited states resulting in the overlapping of many nuclear resonances. Thus, a continuum of nuclear levels is formed.

Consequently, the idea of counting each level separately is replaced by the concept of an average description: the nuclear level density (NLD). The NLD $\rho(E)$ is inversely proportional to $D(E)$ and is defined as the number of levels N per unit energy at a certain excitation energy E:

$$\mathrm{d}N/\mathrm{d}E = \rho(E,J) = f(J)\rho(E)\ . \tag{2.1}$$

Usually, the NLD is factorized into a total level density $\rho(E)$ that is increasing exponentially with the excitation energy E, and a spin distribution function $f(J)$ (see, e.g., [138]):

$$f(J) = \mathrm{e}^{-J^2/2\sigma^2} - \mathrm{e}^{-(J+1)^2/2\sigma^2}\ , \tag{2.2}$$

with σ being the spin-cutoff parameter. In general, the NLD may also depend on the parity quantum number π of the states, which is neglected in the following.

Two models for $\rho(E)$ are widely used: the back-shifted Fermi gas model (BSFG) [139, 140] and the constant temperature model (CT) [140, 141]. The BSFG is based on the assumption that the nucleus can be treated as a Fermi gas composed of two types of particles and was later refined including shell structure effects:

$$\rho_{\mathrm{BSFG}}(E) = \frac{\mathrm{e}^{2\sqrt{a(E-E_1)}}}{12\sqrt{2}\sigma a^{1/4}(E-E_1)^{5/4}}\ , \tag{2.3}$$

where a and the excitation-energy shift E_1 are free parameters that are adjusted to experimental data. The corresponding spin-cutoff parameter σ is defined as:

$$\sigma^2 = 0.0146A^{5/3}\frac{1+\sqrt{1+4a(E-E_1)}}{2a}\ . \tag{2.4}$$

The CT model is simply given by an exponential shifted by E_0:

$$\rho_{\mathrm{CT}}(E) = \frac{1}{T}\mathrm{e}^{(E-E_0)/T}\ , \tag{2.5}$$

with T being the temperature of the nucleus. A different parametrization for $\sigma = 0.98A^{0.29}$ was suggested for the CT model in Ref. [142].

Both are semi-empirical models depending on a small set of parameters that are adjusted to experimentally determined level spacings for nuclei in different mass regions (see, e.g., Refs. [138, 143]). One experimental approach to determine $\rho(E)$ directly at low excitation energies is simply done by counting the number of levels, e.g., using spectroscopy measurements. At excitation energies slightly above the neutron separation threshold neutron resonances in

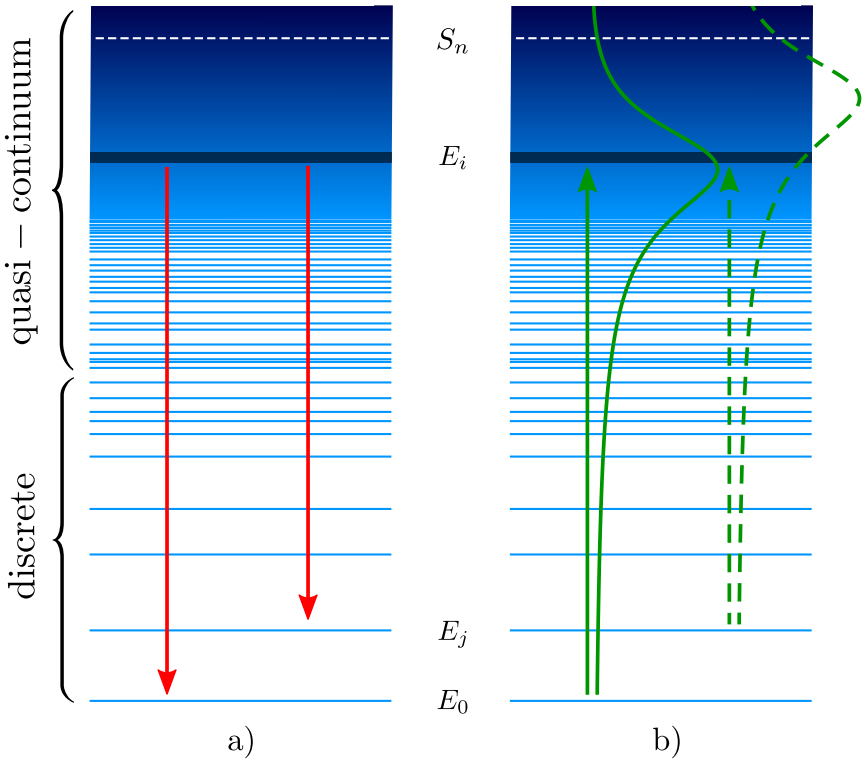

Figure 2.1: Concept of the photon strength function (PSF). a) The probability for the decay from a set of excited states at E_i to another group of states at E_j is related to the photon strength function. b) According to the Brink-Axel hypothesis, the PSF build on the ground state is equivalent to the one build on top of excited states E_j. For details see text.

neutron-capture reactions are counted to get the local level density (see, e.g., Ref. [144] for an overview), while another approach uses fluctuation analysis of experimental spectra from (p, p') experiments to extract level densities in the IVGDR region [145–148]. However, these methods deliver NLD values only for local and very restricted energy regions. Still, information below the neutron threshold, in particular in the PDR region, is very scarce or not possible to obtain with current experimental techniques. Therefore, reliable theoretical models are highly required to interpolate the NLD in this energy regime.

For a detailed discussion and recent systematic studies of the parameters for the BSFG and CT models throughout the nuclear chart see e.g. Refs. [138, 143] and references therein.

2.1.2 The photon strength function

As already pointed out in the previous section, the spectroscopy of individual nuclear levels is not feasible at sufficiently high excitation energies. Even HPGe detectors, which have currently the best energy resolution for γ-detection in the MeV region, do not have a sufficient resolving power to resolve all individual states. In a similar way as for the introduction of a continuous level density it is possible to treat the possibility for γ-emission in an average and statistical fashion, respectively. In that case, average decay properties of an ensemble of states are considered rather than features of individual levels. The decay probability $\mathscr{P}(E_\gamma)$ from an excitation

energy E_i to a set of states at energy E_j (see Fig. 2.1.a)) is linked to the γ-transmission coefficient $\mathscr{T}(E_\gamma)$ and the number of available states at E_j expressed by the corresponding NLD $\rho(E_j)$:

$$\mathscr{P}(E_\gamma) \propto \mathscr{T}(E_\gamma) \cdot \rho(E_j) \,, \tag{2.6}$$

with $E_\gamma = E_i - E_j$ being the γ-ray energy of the emitted photon. Historically, the "strength" for a certain type of electromagnetic transition λL is often denoted as the (downward) photon strength function (PSF, $f_{\lambda L}$)[4] [149]:

$$f_{\lambda L}(E_\gamma) = \frac{1}{2\pi} \cdot \frac{\mathscr{T}_{\lambda L}(E_\gamma)}{E_\gamma^{2L+1}} \,. \tag{2.7}$$

Following Eq. (3.1) in Ref. [150], $f_{\lambda L}(E_\gamma)$ can be expressed in terms of average reduced transition widths $\langle \Gamma^{ij}_{\lambda L} \rangle$:

$$f_{\lambda L}(E_\gamma) = \frac{\langle \Gamma^{ij}_{\lambda L} \rangle \cdot \rho(E_i)}{E_\gamma^{2L+1}} \,, \tag{2.8}$$

where $\rho(E_i)$ is the NLD at the initial excitation energy. Due to the principle of detailed balance in reaction theory, the PSF for photon emission and photoabsorption are equivalent. Photoabsorption is generally considered with the nucleus being initially in the ground state. Relating the average reduced ground-state transition width $\langle \Gamma^{0j}_{\lambda L} \rangle$ to the average photoabsorption cross section $\langle \sigma_{\gamma,\lambda L} \rangle$, Eq. (2.8) can be transformed into the (upward) photon strength function:

$$f_{\lambda L}(E_\gamma) = \frac{1}{(\pi\hbar c)^2} \cdot \frac{\langle \sigma_{\gamma,\lambda L} \rangle}{g \cdot E_\gamma^{2L-1}} \,, \tag{2.9}$$

with $g = \frac{2J_j+1}{2J_0+1}$ expressed by the ground-state spin quantum number J_0 and the spin J_j of the ensemble of states that are populated. The definition of $f_{\lambda L}(E_\gamma)$ is in line with the so-called Brink-Axel hypothesis [113, 114] assuming its independence from the excitation energy. In 1955, Brink postulated in his doctoral thesis, that if *"we assume that the energy dependence of the photo effect is independent of the detailed structure of the initial state so that, if it were possible to perform the photo effect on an excited state, the cross section for absorption of a photon of energy E would still have an energy dependence"* [113] as measured for the ground state. This idea is illustrated in Fig. 2.1.b). The photoabsorption cross section measured on top of the excited state j has the same shape as for the ground state, but is shifted in energy by E_j. While Brink considered only the energy dependence of the IVGDR, his assumption was later refined and generalized for any transition between resonant states [46, 114].

The relations for the PSF in Eqs. (2.8) and (2.9) give rise to two ways to extract $f_{\lambda L}(E_\gamma)$ experimentally: analyzing the decay transitions from excited states and/or measuring the photoabsorption cross section on the ground state. Most of the experimental data on the photoabsorption cross section are derived from (γ,γ') and (γ,n) reactions investigating the IVGDR (see, e.g., Refs. [13, 116]). In the region of the IVGDR, $\langle \sigma_{\gamma,E1} \rangle$ is usually described by a Lorentzian curve:

[4] In the literature, the terms photon strength function, γ-ray strength function, and radiative strength function are used interchangeably.

$$\langle \sigma_{\gamma,E1} \rangle = \sigma_0 \frac{\Gamma^2 E_\gamma^2}{(E_0^2 - E_\gamma^2)^2 + \Gamma^2 E_\gamma^2} \,, \tag{2.10}$$

with the resonance maximum σ_0 at E_0 and a resonance width Γ. To compute the PSF also for γ-ray energies below the neutron separation threshold, the Lorentzian model is usually extrapolated to low energies or modified to fit to experimental data in this region, resulting in adapted models (see, e.g., Ref. [150]). Below the neutron threshold, several NRF experiments were performed using a statistical analysis approach to extract the total photoabsorption cross section, see, e.g., Refs. [66, 67]. However, in photo-induced reactions, the connection between $\langle \sigma_{\gamma,\lambda L} \rangle$ and $f_{\lambda L}$ is valid only for excitation energies with sufficiently high level densities. This is usually the case in the regime of the quasi-continuum and above the neutron binding energy. At lower energies, this approach is no longer applicable, even though it is not well defined below which point the statistical model loses its validity.

Nevertheless, to obtain a complete picture, it is crucial to determine the PSF also for low γ-ray energies. In that case, the measurement of photon emission intensities from excitation energy regions where a statistical treatment is reasonable becomes very useful. Many attemps have been made to study the PSF and test the *Brink-Axel hypothesis* in particle-induced reactions (see e.g. Refs. [121, 150–156] and references therein). However, these reactions induce many types of multipole transitions making it difficult to disentangle the different components λL of the measured total PSF: $f_{tot}(E_\gamma) = \sum_{\lambda L} f_{\lambda L}(E_\gamma)$. In addition, in most of these experiments the product $f(E_\gamma) \cdot \rho(E_j)$ is measured leading to a level density dependent extraction of the PSF. A model-independent measurement of the energy dependence of the PSF was conducted in Ref. [122] using p-γ-γ correlations in ^{94}Mo$(d,p)^{95}$Mo reactions. Exploiting the relation in Eq. (2.8), ratios of the PSF for different γ-ray energies were extracted:

$$R = \frac{f(E_{\gamma_1})}{f(E_{\gamma_2})} = \frac{\langle \Gamma^{ij}_{\lambda L} \rangle}{\langle \Gamma^{i0}_{\lambda L} \rangle} \cdot \left(\frac{E_{\gamma_2}}{E_{\gamma_1}} \right)^{2L+1} \,. \tag{2.11}$$

Taking Fig. 2.1.a) as an illustrative example, the intensity ratio between both transitions starting at E_i is proportional to the ratio of the PSF at the corresponding photon energies $E_{\gamma_1} = E_i - E_j$ and $E_{\gamma_2} = E_i - E_0$, respectively. Applying this method to different excitation energies E_i, the γ-ray energies for the decays to the states E_j and E_0 change and, hence, the shape of the PSF can be extracted even for small γ-ray energies. The corresponding results from Ref. [122] were already shown in Fig. **??**. The PSF can be measured for E_γ down to $\sim$ 1 MeV. Furthermore, the changing of the initial excitation energy E_i provides overlapping results from different measurements, which are useful cross checks. The (d,p) reaction, however, suffers from the same lack of sensitivity for different multipole transitions as already pointed out. Particle-induced reactions populate a wide range of states with different quantum numbers. In addition, approximations of theoretical models describing the reaction mechanism have to be applied to connect measured reaction cross sections to intrinsic properties such as transition probabilities. This is where the great advantage of photon scattering experiments comes into play. Due to the low momentum transfer of real photons, mainly dipole transitions are induced selecting a definite set of excited states. Moreover, the extraction of nuclear structure properties is conducted in a model-independent way. Consequently, this method is extremely suited to study the PSF for $E1$ and $M1$ transitions.

2.2 Nuclear resonance fluorescence

In the previous chapters, the nuclear resonance fluorescence (NRF) technique [19, 20, 124] was already briefly introduced. Since the main focus of this doctoral thesis lies on NRF experiments, the data analysis, and the interpretation of the corresponding results, this section is devoted to a more detailed description of the method and the general formalism.

Nuclear resonance fluorescence is also often referred to as real-photon scattering. It is a widely used method to investigate properties of excited low-spin states in atomic nuclei. On one hand nuclear levels are characterized by their spin (J) and parity (π) quantum number, respectively. On the other hand the life time τ of an excited state is usually one of the common and important observables in nuclear physics experiments and is inversely proportional to the natural line width Γ.

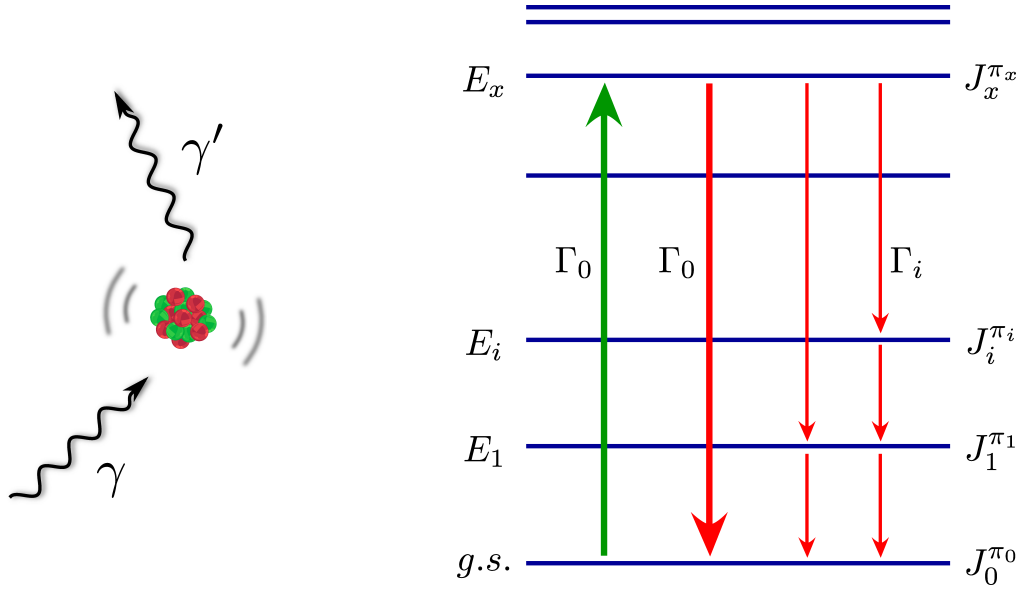

Figure 2.2: Schematic overview of the NRF method. By resonant photoabsorption the nucleus is excited from the ground state with spin-parity quantum numbers $J_0^{\pi_0}$ to an excited state with spin-parity $J_x^{\pi_x}$. The corresponding excitation probability is proportional to the ground-state transition width Γ_0. Subsequently, the nucleus can either decay directly back to the ground state (thick red arrow) or cascade via intermediate levels (thin red arrows). The transition width Γ_i is directly linked to the probability for the transition between two states $J_x^{\pi_x}$ and $J_i^{\pi_i}$.

In the (γ,γ') reaction, a real photon is resonantly absorbed by the nucleus, which subsequently de-excites via the emission of another photon. This process is schematically illustrated in Fig. 2.2. In this manner, the nucleus is excited from the ground state with spin-parity quantum number $J_0^{\pi_0}$ to a state with $J_x^{\pi_x}$ and excitation energy E_x. The corresponding excitation probability is expressed by the ground-state transition width Γ_0. In the de-excitation channel usually two different outcomes are considered. Either the nucleus releases its total excitation energy in one transition and decays directly back to the ground state or it emits the energy step-by-step via cascacade transitions. The ground-state transition is commonly connected to the term *elastic*. In a classical picture, however, this term is not correct, since the emitted photon is not the same as the absorbed one. In analogy to that, the transition from a photo-excited state to

a lower-lying level other than the ground state is denoted as *inelastic*. In this case, the transition probabilities are connected to the transition widths Γ_i (see Fig. 2.2).

The excitation and the de-excitation process is governed by the electromagnetic interaction, which is one of the best understood phenomena in physics. Thus, the extraction of intrinsic properties of individual excited levels accessible from observables can be performed in a model-independent way. Such quantities are, e.g., excitation energies, spin and parity quantum numbers, as well as transition strengths. The corresponding theoretical framework has been developed as early as 1937 by Bethe and Placzek [157] and has been comprehensively adapted for the particular case of NRF in the review of Metzger in 1959 [19]. Recent reviews of experimental nuclear structure studies using the NRF technique can be found in Ref. [20, 124].

In the following sections, a compilation of the essential formalism used in NRF experiments and analysis is provided. In the first part, the quantum-mechanical selection rules are briefly introduced while the second part is devoted to the description of the photon-scattering cross section. Finally, a more detailed analysis of angular distribution and correlation between several γ-rays is given in the third section.

2.2.1 Selection rules

In quantum systems, observables are always connected to quantum-mechanical operators. Symmetry transformation of these operators result in quantum numbers which represent invariant quantities of motion.

The invariance under rotation is the consequence of the isotropy of the three-dimensional space. The corresponding angular momentum quantum numbers lead to the following selection rule:

$$\left|J_i - J_f\right| \leq L \leq J_i + J_f \ . \tag{2.12}$$

It defines allowed multipole orders L for electromagnetic transitions between two nuclear states i and f. The triangle inequality is based on the spin quantum numbers J_i and J_f of the involved levels, while L can take integer values successively incremented by one.

The spatial inversion of the coordinates of an operator is called parity transformation. Even though it has been shown that the weak interaction is violating the parity invariance [158], this effect can be neglected in normal electromagnetic interactions. The application of the parity transformation on electromagnetic multipole operators result in additional selection rules:

$$\begin{aligned} \pi_i \cdot \pi_f = (-1)^L \quad &\longrightarrow \quad \text{for electric transitions } (\lambda = E) \\ \pi_i \cdot \pi_f = (-1)^{L+1} \quad &\longrightarrow \quad \text{for magnetic transitions } (\lambda = M) \ , \end{aligned} \tag{2.13}$$

where π_i and π_f are the parity quantum numbers of the states involved in the transition. Depending on which relation is valid, the transition character λ can be determined for every possible electromagnetic transition between two nuclear states: either an *electric* (E) or a *magnetic* (M) transition can take place. Using the introduced selection rules, the emitted and absorbed electromagnetic radiation, respectively, is characterized by its transition character and multipole order: λL.

Due to the low momentum transfer of real photons, NRF reactions induce mainly $E1$ and $M1$ transitions, while $E2$ transitions occur with a strongly suppressed probability. Higher order radiations (such as $M2$, $E3$, ...) are usually not observed in standard NRF experiments. They are restricted to rather rare cases where no transitions of lower multipole orders are possible.

2.2.2 Cross sections

The cross section of a physical process is a measure for the probability of a certain interaction between particles. One of the main focal points of this thesis is the determination of photoabsorption cross sections. The following description of the general formalism for resonant absorption of photons by an atomic nucleus is mainly adopted from Refs. [19] and [159].

Individual nuclear levels

As previously mentioned, NRF is about the resonant absorption of real photons by atomic nuclei and the subsequent emission of other photons. It is a nuclear resonance within the complex quantum system of the nucleus that is excited by photoabsorption. The terms nuclear resonance, nuclear state or level are used interchangeably, if not otherwise stated. The partial cross section $\sigma^0_{x,i}(E_\gamma)$ for photoabsorption from the ground state to an excited state x with resonance energy E_x followed by the de-excitation to a state i is given by a Breit-Wigner distribution

$$\sigma^0_{x,i}(E_\gamma) = \frac{\pi}{2} \cdot \left(\frac{\hbar c}{E_\gamma}\right)^2 \cdot g \cdot \frac{\Gamma_0 \Gamma_i}{(E_\gamma - E_x)^2 + (\Gamma/2)^2} \,, \tag{2.14}$$

which is a function of the photon energy E_γ. The involved levels are in general degenerated. Therefore, the statistical factor $g = \frac{2J_x+1}{2J_0+1}$ accounts for the different magnetic substates and contains the spin quantum number of the ground state J_0 and the excited state J_x, respectively. The transition widths to the ground state and to the state i are given by Γ_0 and Γ_i, respectively, while Γ corresponds to the total width of the excited state:

$$\Gamma = \sum_i \Gamma_i = \Gamma_0 + \Gamma_1 + \Gamma_2 + \dots \,, \tag{2.15}$$

which is defined as the sum of all possible transition widths originating from the state x. Furthermore, $\Gamma = \hbar/\tau$ is connected to the lifetime τ of the excited state.

After the photoabsorption, de-excitations to different levels can take place. Consequently, the photoabsorption cross section $\sigma^0_{abs}(E_\gamma)$ into a single resonance is deduced by summing over all possible de-excitation channels i:

$$\sigma^0_{abs}(E_\gamma) = \sum_i \sigma^0_{x,i}(E_\gamma) = \frac{\pi}{2} \cdot \left(\frac{\hbar c}{E_\gamma}\right)^2 \cdot g \cdot \frac{\Gamma_0 \Gamma}{(E_\gamma - E_x)^2 + (\Gamma/2)^2} \,. \tag{2.16}$$

Equations (2.14) and (2.16) describe the ideal case of a static nucleus, i.e., thermal motion is neglected. However, taking this effect into account, the actual width of the resonance is affected by the Doppler effect and, thus, is much wider than expected from the simple assumption. A detailed study of the influence of the Doppler broadening on the resonance width can be found, e.g., in Ref. [19]. Nevertheless, it can be shown that the integrated photoabsorption cross section is independent of any width-broadening effects. Relations (2.14) and (2.16) can be written in the form

$$\sigma^0_{abs}(E_\gamma) = \sigma^0_{max} \cdot \frac{1}{1 + \left(\frac{2(E_\gamma - E_x)}{\Gamma}\right)^2} \,, \tag{2.17}$$

where σ^0_{max} is the maximum value of the resonance, i.e., at $E_\gamma = E_x$. The integration over all energies results in

$$\int_{-\infty}^{\infty} \sigma_{abs}^{0}(E'_\gamma)\,\mathrm{d}E'_\gamma = \sigma_{max}^{0} \cdot \int_{-\infty}^{\infty} \frac{\mathrm{d}E'_\gamma}{1+\left(\frac{2(E'_\gamma - E_x)}{\Gamma}\right)^2} = \sigma_{max}^{0} \cdot \frac{\pi}{2} \cdot \Gamma \tag{2.18}$$

Substituting σ_{max}^{0} by the corresponding expression from Eq. (2.16) the total integrated photoabsorption cross section is

$$I_{0\to x} = \pi^2 \cdot \left(\frac{\hbar c}{E_x}\right)^2 \cdot g \cdot \Gamma_0 \,. \tag{2.19}$$

The integrated cross section for a particular transition sequence $J_0 \to J_x \to J_i$ can be determined by accounting for the branching ratio Γ_i/Γ from the excited state x to state i

$$I_{0\to x\to i} = \pi^2 \cdot \left(\frac{\hbar c}{E_x}\right)^2 \cdot g \cdot \Gamma_0 \cdot \frac{\Gamma_i}{\Gamma} \,. \tag{2.20}$$

The transition between two nuclear states is described by the reduced transition probability $B(\lambda L)$, which is directly linked to the associated transition width Γ_i. For ground-state transitions it is expressed by

$$\Gamma_0 = 8\pi \sum_{\lambda L} \left(\frac{E_\gamma}{\hbar c}\right)^{2L+1} \cdot \frac{L+1}{L[(2L+1)!!]^2} \cdot B(\lambda L)\downarrow \,, \tag{2.21}$$

where $B(\lambda L)\downarrow$ corresponds to the reduced de-excitation probability, while

$$B(\lambda L)\uparrow = g \cdot B(\lambda L)\downarrow \tag{2.22}$$

is connected to the excitation process. The transitions dominantly induced in NRF reactions are $E1$, $M1$ and $E2$ transitions. The associated reduced transition probabilities are derived from Eq. (2.21)

$$\frac{B(E1)\uparrow}{\mathrm{e}^2\mathrm{fm}^2} = 9.554 \cdot 10^{-4} \cdot g \cdot \frac{\Gamma_0}{\mathrm{meV}} \cdot \left(\frac{\mathrm{MeV}}{E_x}\right)^3 \,, \tag{2.23}$$

$$\frac{B(M1)\uparrow}{\mu_N^2} = 8.641 \cdot 10^{-2} \cdot g \cdot \frac{\Gamma_0}{\mathrm{meV}} \cdot \left(\frac{\mathrm{MeV}}{E_x}\right)^3 \,, \tag{2.24}$$

$$\frac{B(E2)\uparrow}{\mathrm{e}^2\mathrm{fm}^4} = 1.245 \cdot 10^{3} \cdot g \cdot \frac{\Gamma_0}{\mathrm{meV}} \cdot \left(\frac{\mathrm{MeV}}{E_x}\right)^5 \,. \tag{2.25}$$

Average cross section

So far, the formalism was dedicated to individual nuclear levels. Under certain circumstances, this approach is not feasible anymore. Either the energy resolution of the γ-ray detectors is not sufficient to resolve single transitions or the nuclear level densities are high enough, such that neighboring nuclear resonances overlap. With increasing level density the measured photoabsorption cross section is smoothed due to the superposition of many discrete levels. It should

be noted, that in the latter case, the separation of individual states is not hindered by the lack of energy resolution of current experimental techniques, but is physically impossible due to the strongly overlapping resonances.

In the analysis in later chapters, the averaged photoabsorption cross section is extracted from the experimental data. The photoabsorption cross section for one nuclear level can be written as

$$I_{0\to x} = I_{0\to x\to 0} + \sum_{i\neq 0} I_{0\to x\to i} \,. \tag{2.26}$$

In general, the averaged photoabsorption cross section σ_γ can be expressed as the sum of photoabsorption cross sections of many levels averaged over the corresponding energy bin ΔE

$$\sigma_\gamma \quad = \quad \sigma_{\gamma\gamma} \quad + \quad \sigma_{\gamma\gamma'}$$

$$\frac{\sum_x I_{0\to x}}{\Delta E} = \frac{\sum_x I_{0\to x\to 0}}{\Delta E} + \frac{\sum_x \sum_{i\neq 0} I_{0\to x\to i}}{\Delta E} \,. \tag{2.27}$$

The first term $\sigma_{\gamma\gamma}$ corresponds to the direct decay back to the ground state via photon emission and is denoted as *elastic* cross section. The second term $\sigma_{\gamma\gamma'}$ is called *inelastic* cross section, which is the sum running over all possible direct transitions to lower-lying levels i, except for the ground state.

The definition of σ_γ given in Eq. (2.27) is accurate for photoabsorption measurements in (γ,γ') experiments below the neutron separation threshold, which is covered in this thesis. For completeness, it is noted that above this threshold, additional reaction channels have to be considered to determine the complete photoabsorption cross section, such as (γ,n) and $(\gamma,2n)$ reactions:

$$\sigma_\gamma = \sigma_{\gamma\gamma} + \sigma_{\gamma\gamma'} + \sigma_{\gamma n} + \sigma_{\gamma 2n} + ... \tag{2.28}$$

2.2.3 Angular distribution and correlation of γ-rays

At the end of the present chapter, an introduction to the correlation of photons is given, since they are crucially important for the data analysis and the interpretation of the resulting outcomes presented in later chapters. The concepts, introduced in the following part reflect a condensed summary adopted from Refs. [160] and [161], respectively, and adapted for the cases needed in this thesis.

Measurements of angular distributions and correlations of γ-rays in nuclear reactions are very useful and frequently applied in nuclear structure physics. They provide a great tool to assign spin and parity quantum numbers to nuclear states or to determine multipole components of nuclear transitions. The derivation and computation of the angular distribution of γ radiation emitted from an ensemble of atomic nuclei can be wrapped up in three basic quantities:

- orientation of the ensemble,
- direction of the observed photons,
- polarization of the involved radiation.

The term "orientation" is referred to the orientation of a nuclear state with angular momentum J with respect to a given axis. A state is called *oriented* if the magnetic substates m_J are not equally populated[3]. The angular distribution of photons emitted from *oriented* nuclear states is, in general, anisotropic and depends on intrinsic quantum numbers of the system. A definite orientation of a nuclear ensemble, e.g., target material, can be achieved by defining a specified orientation axis $\vec{z}$ that corresponds to the propagation direction of the incoming radiation. The according quantum-mechanical expression is given by the *radiation orientation parameter* $B_\nu(\gamma_0)$:

$$B_\nu(\gamma_0) = (2J_1+1)^{1/2} \cdot \sum_{m_J} (-1)^{J_1+m_J} \cdot \langle J_1 - m_J J_1 m_J | \, \nu 0 \rangle \cdot P(m_J) \,. \tag{2.29}$$

It is a function of the spin quantum number J_1 and magnetic substates m_J of the *oriented* state, respectively, that is populated by the incoming photon γ_0. The relative population of the magnetic substates is denoted as $P(m_J)$.

Unpolarized photons

For the case of an unpolarized impinging photon beam, $B_\nu(\gamma_0)$ can be explicitly written as:

$$\begin{aligned} B_\nu(\gamma_0) &= \sum_{\lambda L \lambda' L'} (-1)^{L+L'} \cdot F_\nu(LL'J_0J_1) \cdot \gamma(\lambda L)\gamma^*(\lambda' L') \Big/ \sum_{\lambda L} |\gamma(\lambda L)|^2 \\ &= \frac{1}{1+\delta_0^2} \cdot [F_\nu(LLJ_0J_1) - 2\delta_0 \cdot F_\nu(LL'J_0J_1) + \delta_0^2 \cdot F_\nu(L'L'J_0J_1)] \,. \end{aligned} \tag{2.30}$$

The *ordinary* F_ν*-coefficients* are defined by the two leading multipole orders L and $L' = L+1$ for the transition from the initial state with spin J_0 to the final state with spin J_1. The term $\gamma(\lambda L)$ represents the reduced matrix element for the λL transition, while the mixing ratio δ_0 is defined as $\delta_0 = \gamma(\lambda' L')/\gamma(\lambda L)$ using the phase convention of Krane, Steffen and Wheeler [160]. For the sake of completeness, the *ordinary* F_ν*-coefficients* are calculated by:

$$\begin{aligned} F_\nu(LL'J_0J_1) = (-1)^{J_0+J_1+1} \cdot [(2\nu+1)(2L+1)(2L'+1)(2J_1+1)]^{1/2} \times \\ \times \begin{pmatrix} L & L' & \nu \\ 1 & -1 & 0 \end{pmatrix} \begin{Bmatrix} L & L' & \nu \\ J_1 & J_1 & J_0 \end{Bmatrix} . \end{aligned} \tag{2.31}$$

The last two terms in brackets are $3j$- and $6j$-symbols, respectively. Note, that in this definition the spin J_1 of the *oriented* state is always at the end of the parameter input. Tabulated values can be found, e.g., in Ref. [161].

After the orientation axis $\vec{z}$ is defined by the absorption of γ_0, the angular distribution of subsequently emitted photons γ_1 relative to $\vec{z}$ is given by:

$$W(\vartheta) = \sum_{\nu=0,2,4} B_\nu(\gamma_0) A_\nu(\gamma_1) P_\nu(\cos\vartheta) \,, \tag{2.32}$$

[3] An example for an *unoriented* system is a radioactive source. This ensemble of unstable nuclei is on average randomly oriented and, therefore, the emission of radiation is isotropic in space.

where $P_\nu(\cos\vartheta)$ is the Legendre polynomial with ϑ being the polar angle between the incident photon γ_0 and the emitted photon γ_1. The *angular distribution coefficient* $A_\nu(\gamma_1)$ is defined in a similar way as $B_\nu(\gamma_0)$:

$$\begin{aligned} A_\nu(\gamma_1) &= \sum_{\lambda L \lambda' L'} F_\nu(LL'J_2J_1)\cdot\gamma(\lambda L)\gamma^*(\lambda' L') \Big/ \sum_{\lambda L}|\gamma(\lambda L)|^2 \\ &= \frac{1}{1+\delta_1^2}\cdot\left[F_\nu(LLJ_2J_1) + 2\delta_1\cdot F_\nu(LL'J_2J_1) + \delta_1^2\cdot F_\nu(L'L'J_2J_1)\right]. \end{aligned} \tag{2.33}$$

The spin quantum number J_2 is attributed to the final state that is populated from the *oriented* state J_1.

Polarized photons

In the following, the angular correlation for the case of an impinging linearly polarized photon $\vec{\gamma}_0$ and the angular distribution of the subsequently emitted photon γ_1 is introduced. To account for the linear polarization of the initial photon, the angular distribution function for unpolarized γ-ray beams in Eq. (2.32) has to be modified by a polarization term. Without going into detail, a substitution of $P_\nu(\cos\vartheta) \to P_\nu(\cos\vartheta) + (-1)^{\sigma(\lambda')}\cdot\kappa_\nu(LL')\cdot P_\nu^{(2)}(\cos\vartheta)\cdot\cos(2\varphi)$ has to be performed as suggested in Ref. [162]:

$$\begin{aligned} W(\vartheta,\varphi) &= \sum_{\nu=0,2,4} B_\nu(\vec{\gamma}_0)A_\nu(\gamma_1)\times \\ &\qquad \times\left[P_\nu(\cos\vartheta) + (-1)^{\sigma(\lambda')}\kappa_\nu(LL')P_\nu^{(2)}(\cos\vartheta)\cos(2\varphi)\right] \\ &= \sum_{\nu=0,2,4} B_\nu(\vec{\gamma}_0)A_\nu(\gamma_1)P_\nu(\cos\vartheta) + \\ &\qquad + B_\nu(\vec{\gamma}_0)(-1)^{\sigma(\lambda')}\kappa_\nu(LL')\cdot A_\nu(\gamma_1)P_\nu^{(2)}(\cos\vartheta)\cos(2\varphi) \\ &= W(\vartheta) + \sum_{\nu=0,2,4} B'_\nu(\vec{\gamma}_0)A_\nu(\gamma_1)P_\nu^{(2)}(\cos\vartheta)\cos(2\varphi)\,, \end{aligned} \tag{2.34}$$

where $W(\vartheta)$ is defined in Eq. (2.32), while φ is the azimuthal angle between the polarization plane and the scattering plane (see Fig. 2.3). The polarization plane is spanned by the direction of the incoming photons and their electric field vector, i.e., the direction of the linear polarization. The scattering plane is spanned by the propagation direction of the incoming photons and the direction of the scattered photons. The quantity $P_\nu^{(2)}(\cos\vartheta)$ is the unnormalized associated Legendre function, while the *linear-polarization orientation parameter* $B'_\nu(\vec{\gamma}_0) = B_\nu(\vec{\gamma}_0)(-1)^{\sigma(\lambda')}\kappa_\nu(LL')$ is defined as

$$\begin{aligned} B'_\nu(\vec{\gamma}_0) &= \frac{\sum_{\lambda L\lambda' L'}(-1)^{L+L'}\cdot(-1)^{\sigma(\lambda')}\cdot\kappa_\nu(LL')\cdot F_\nu(LL'J_0J_1)\cdot\gamma(\lambda L)\gamma^*(\lambda' L')}{\sum_{\lambda L}|\gamma(\lambda L)|^2} \\ &= \frac{(-1)^{\sigma(\lambda)}}{1+\delta_0^2}\cdot\left[\kappa_\nu(LL)\cdot F_\nu(LLJ_0J_1) + \right. \\ &\qquad \left. 2\delta_0\cdot\kappa_\nu(LL)\cdot F_\nu(LL'J_0J_1) - \delta_0^2\cdot\kappa_\nu(LL)\cdot F_\nu(L'L'J_0J_1)\right] \end{aligned} \tag{2.35}$$

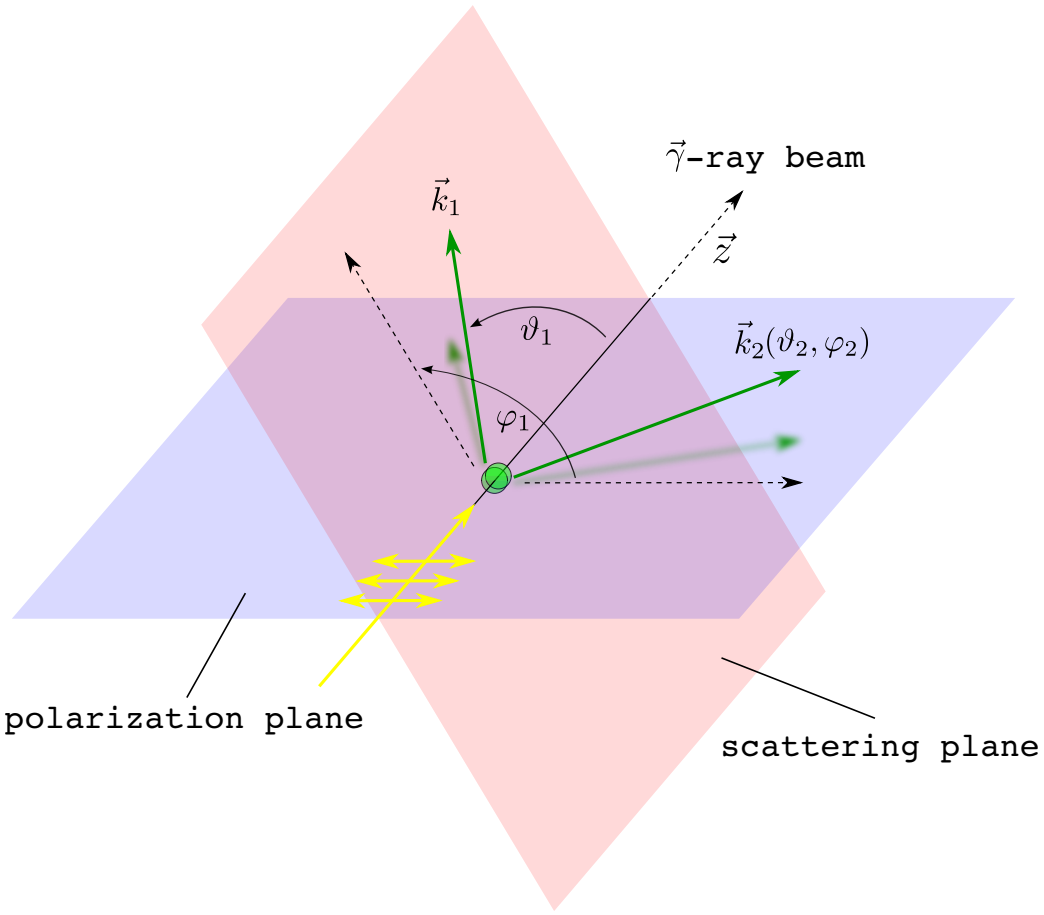

Figure 2.3: Illustration of the coordinate system for the γ-γ correlation of two photons (green arrows) emitted in the decay of a nuclear level, that is excited via a linearly polarized photon beam (yellow arrow). A more detailed description is given in the text.

where $\sigma(\lambda)$ is a function of the transition character λ associated to the λL transition. It takes the value $\sigma(E) = 0$ for an electric transition and $\sigma(M) = 1$ for a magnetic transition, respectively. The coefficient κ_ν is given by

$$\kappa_\nu(LL') = -\left[\frac{(\nu-2)!}{(\nu+2)!}\right]^{1/2} \cdot \frac{C(LL'\nu,11)}{C(LL'\nu,1-1)}\,, \tag{2.36}$$

with $C(LL'\nu,11)$ and $C(LL'\nu,1-1)$ being the corresponding Clebsch-Gordon coefficients. The values for κ_ν that are relevant for photon-scattering experiments are:

$$\kappa_2(11) = -\frac{1}{2}, \qquad \kappa_2(12) = -\frac{1}{6}, \qquad \kappa_2(22) = \frac{1}{2}, \qquad \kappa_4(22) = -\frac{1}{12}\,. \tag{2.37}$$

Considering dipole transitions in an even-even nucleus ($0^+ \xrightarrow{\vec{\gamma}_0} 1^{\pi_1} \xrightarrow{\gamma_1} 0^+$), the resulting angular distribution for an excitation from the ground state, and subsequent decay to the ground state is derived as:

$$W(\vartheta,\varphi) = \frac{3}{4} \cdot [1 + \cos^2\vartheta + \pi_1 \cdot \cos(2\varphi) \cdot \sin^2\vartheta]\,, \tag{2.38}$$

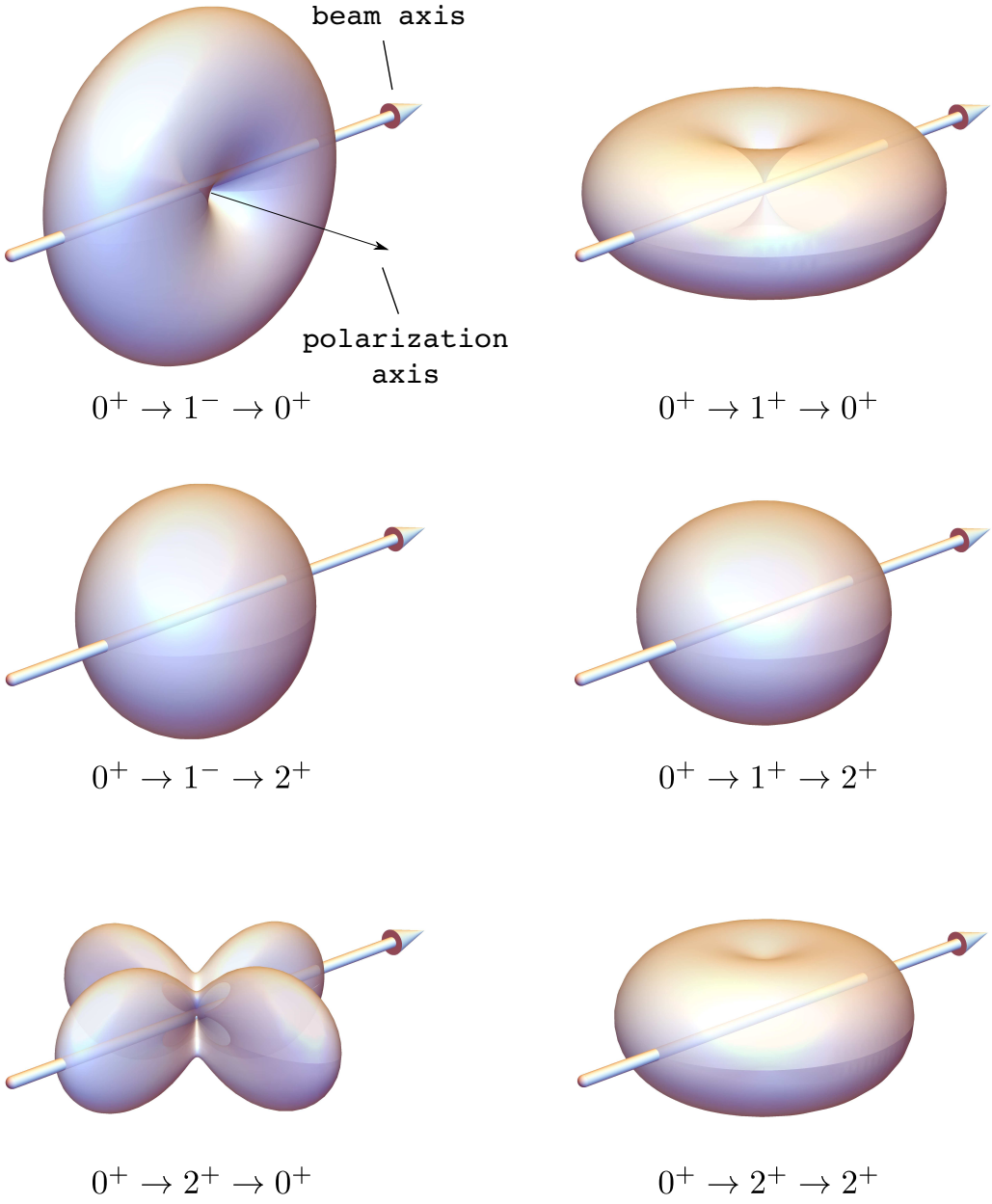

Figure 2.4: Angular distributions for the spin sequences relevant for NRF measurements with even-even nuclei, such as ^{128}Te, using linearly polarized photon beams. In particular, the angular distributions for ground-state transitions differ substantially for 1^-, 1^+ and 2^+ states. This observation will be used in Section 4.5.2 for an unambiguous determination of spin-parity quantum numbers J^π of excited states. As a further example, distributions for the decay to 2^+ states are shown.

where π_1 corresponds to the parity quantum number of the excited state. If the excited 1^{π_1} state populates directly a low-lying excited state instead of the ground-state, e.g., $0^+ \xrightarrow{\vec{\gamma}_0} 1^{\pi_1} \xrightarrow{\gamma_1} 2^+$, the angular distribution for the emitted photon is not as pronounced as for the case in Eq. (2.38), but still relevant for NRF studies:

$$W(\vartheta,\varphi) = \frac{3}{40} \cdot [13 + \cos^2\vartheta + \pi_1 \cdot \cos(2\varphi) \cdot \sin^2\vartheta] \,. \tag{2.39}$$

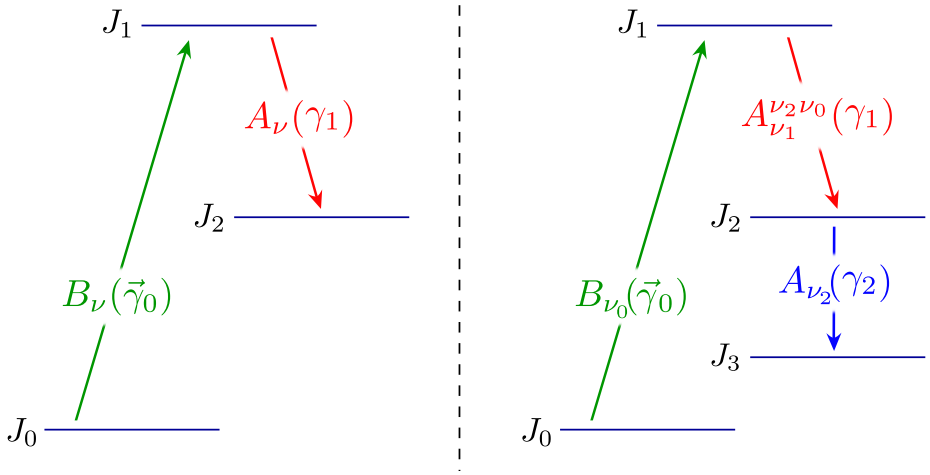

Figure 2.5: Left part: Scheme illustrating the connection of the coefficients $B_\nu(\vec{\gamma}_0)$ and $A_\nu(\gamma_1)$ to the transitions between excited states with spin quantum numbers J_0, J_1 and J_2. Right part: The case of two successively emitted photons. Similar to the left part of this figure, but introducing the generalized directional distribution coefficient $A^{\nu_2\nu_0}_{\nu_1}(\gamma_1)$ for the intermediate transition from J_1 to J_2.

For the sake of completeness, the analytical expression for the spin sequence $0^+ \xrightarrow{\vec{\gamma}_0} 2^+ \xrightarrow{\gamma_1} 0^+$ is given by:

$$W(\vartheta,\varphi) = \frac{5}{8}\cdot[2+\cos(2\vartheta)+\cos(4\vartheta)-(1+2\cos(2\vartheta))\cdot 2\cos(2\varphi)\cdot\sin^2\vartheta]\,. \tag{2.40}$$

In Fig. 2.4, the three-dimensional angular distributions are illustrated for different spin sequences relative to the beam and polarization axis, respectively.

So far, the case was considered where a γ-ray was absorbed by an atomic nucleus and defined the *orientation axis* that corresponds to the propagation direction of the same. Then, the angular distribution for the first emitted photon relative to this *orientation axis* was computed. The left-hand side of Fig. 2.5 illustrates this concept referring to the different *orientation* and *angular distribution coefficients* that take part in this process.

Angular correlation of two photons emitted in succession

In the following part, the angular correlation of two successively emitted photons from an *oriented state* J_1 is discussed, i.e. after excitation via a polarized photon (see right part of Fig. 2.5). A two-step cascade is considered with the focus being on the directional correlation between the two γ-rays γ_1 and γ_2.

For this purpose, the angular correlation function has to be extended and modified in a similar fashion as in Eq. (2.34). A detailed derivation can be found in Ref. [161], but would not improve the comprehensibility here, thus, only the final result is given:

$$W(\vartheta_1\,\varphi_1,\vartheta_2\,\varphi_2) = \sum_{\substack{\nu_0 q_0,\nu_1 q_1,\nu_2 q_2\\ \nu_0,\nu_1,\nu_2=0,2,4}} (-1)^{\nu_1+\nu_2} B_{\nu_0 q_0}(\vec{\gamma}_0) A_{\nu_1}^{\nu_2\nu_0}(\gamma_1) A_{\nu_2}(\gamma_2) \times$$
$$\times \begin{pmatrix} \nu_2 & \nu_1 & \nu_0 \\ q_2 & q_1 & q_0 \end{pmatrix} (2\nu_2+1)^{-1/2} Y_{\nu_1 q_1}(\vartheta_1\,\varphi_1) Y_{\nu_2 q_2}(\vartheta_2\,\varphi_2)\,. \qquad (2.41)$$

Here, $Y_{\nu_i q_i}(\vartheta_i\,\varphi_i)$ are the spherical harmonics of degree ν_i and order $q_i \in [-\nu_i,\nu_i]$ as a function of the direction of the emitted γ-ray. The angles are defined in Fig. 2.3. Parameter $B_{\nu_0 q_0}(\vec{\gamma}_0)$ is defined as follows:

$$B_{\nu_0 0}(\vec{\gamma}_0) \;=\; B_\nu(\vec{\gamma}_0)\,, \qquad (2.42)$$
$$B_{\nu_0 \pm 2}(\vec{\gamma}_0) = \; B_\nu(\vec{\gamma}_0)\cdot(-1)^{\sigma(\lambda')}\cdot\frac{C(LL'\nu,11)}{C(LL'\nu,1-1)}\,, \qquad (2.43)$$
$$B_{\nu_0 q_0}(\vec{\gamma}_0) \;=\; 0 \qquad \text{for} \qquad q_0 \neq 0,\pm 2\,. \qquad (2.44)$$

The coefficients $B_\nu(\vec{\gamma}_0)$ and $A_{\nu_2}(\gamma_2)$ are given in Eqs. (2.30) and (2.33), respectively. Note, that the parameters in definition (2.33) have to be adapted to the present set of quantum numbers. The *generalized directional distribution coefficient* $A_{\nu_1}^{\nu_2\nu_0}(\gamma_1)$ has a similar form as $A_{\nu_2}(\gamma_2)$:

$$A_{\nu_1}^{\nu_2\nu_0}(\gamma_1) = \sum_{\lambda L\lambda' L'} F_{\nu_1}^{\nu_2\nu_0}(LL'J_2J_1)\cdot\gamma(\lambda L)\gamma^*(\lambda' L') \Big/ \sum_{\lambda L}|\gamma(\lambda L)|^2$$
$$= \frac{1}{1+\delta_1^2}\cdot[F_{\nu_1}^{\nu_2\nu_0}(LLJ_2J_1) + 2\delta_1\cdot F_{\nu_1}^{\nu_2\nu_0}(LL'J_2J_1) + \delta_1^2\cdot F_{\nu_1}^{\nu_2\nu_0}(L'L'J_2J_1)]\,, \qquad (2.45)$$

with the difference that the *ordinary F_ν-coefficients* are substituted by the *generalized $F_{\nu_1}^{\nu_2\nu_0}$-coefficients*:

$$F_{\nu_1}^{\nu_2\nu_0}(LL'J_2J_1) = (-1)^{L'+\nu_2+\nu_0+1}\cdot[(2\nu_0+1)(2\nu_1+1)(2\nu_2+1)$$
$$\times(2J_1+1)(2J_2+1)(2L+1)(2L'+1)]^{1/2}$$
$$\times \begin{pmatrix} L & L' & \nu_1 \\ 1 & -1 & 0 \end{pmatrix} \begin{Bmatrix} J_2 & L & J_1 \\ J_2 & L' & J_1 \\ \nu_2 & \nu_1 & \nu_0 \end{Bmatrix}\,. \qquad (2.46)$$

The parameter with braces is the so-called $9j$-symbol. Using the generic formalism introduced in Eq. (2.41) it is feasible to calculate the angular distribution of γ_1 relative to the coincident observation of γ_2 and vice versa. Figure 2.6 shows exemplarily angular correlations between γ_1 and γ_2 for different spin sequences and for the case that γ_2 was observed either at $(\vartheta,\varphi) = (\pi/2,\pi/2)$ (left side) or at $(\vartheta,\varphi) = (\pi/2,0)$ (right side).

Beside the involved spins, the angular distribution depends on the mixing ratio δ for the leading multipole transitions. For electromagnetic transitions, the mixing between $M1$ and $E2$ transition have to be considered, while for $E1/M2$ mixing $E1$ is dominant. As mentioned before even higher order transitions can be neglected. Figure 2.7 shows an evolution

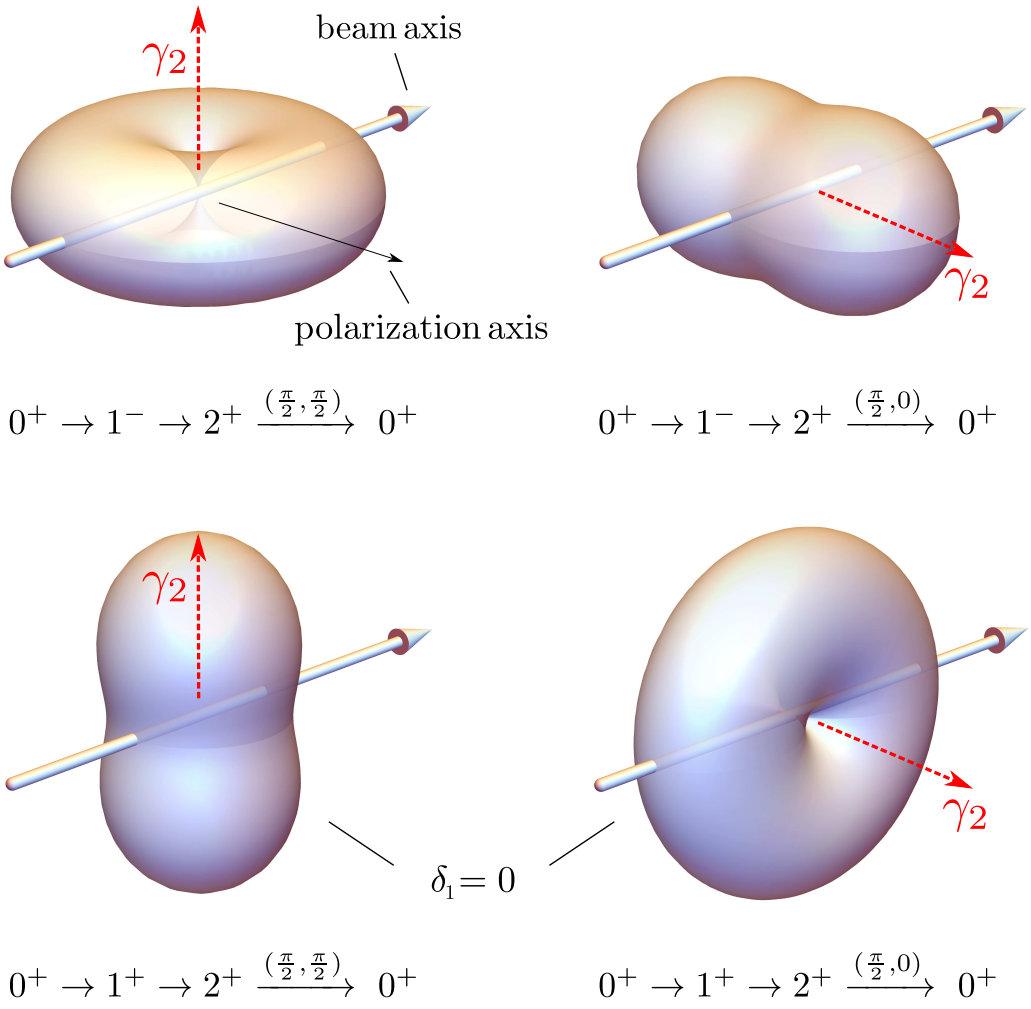

Figure 2.6: Angular correlation between two successively emitted photons γ_1 and γ_2 for the examples of $0^+ \rightarrow 1^- \xrightarrow{\gamma_1} 2^+ \xrightarrow{\gamma_2} 0^+$ and $0^+ \rightarrow 1^+ \xrightarrow{\gamma_1,\delta_1=0} 2^+ \xrightarrow{\gamma_2} 0^+$. The angular directional correlation of γ_1 changes depending on the observation direction (ϑ, φ) of γ_2 (red dashed arrow). This can be used to determine the quantum numbers of excited states that directly populate a lower-lying level, such as the first excited 2_1^+ state. A detailed analysis for the case of ^{128}Te is given in Section 4.8.4.

of the angular distribution of γ_1 as a function of the mixing ratio for the transition cascade $0^+ \rightarrow 1^+ \xrightarrow{\delta_1} 2^+ \xrightarrow{(\vartheta,\varphi)} 0^+$:

As will be discussed in more detail in chapter 4.8, the γ-γ correlation between the photons emitted from an *oriented* state provides useful evidence about the transition character λ and multipole order L of the involved transitions.

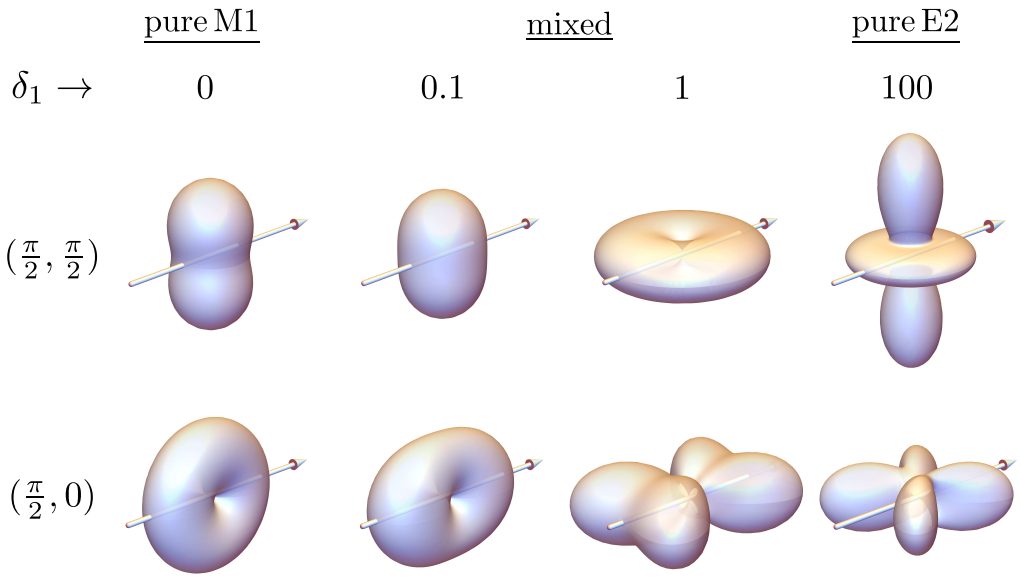

Figure 2.7: Evolution of the angular directional correlation of γ_1 relative to the observation direction (ϑ, φ) of γ_2 as a function of the mixing ratio δ_1 in the spin sequence $0^+ \rightarrow 1^+ \xrightarrow{\delta_1} 2^+ \xrightarrow{(\vartheta,\varphi)} 0^+$.

3 Experimental setup

The focus of the experimental part lies on the performance and analysis of two separate photon-scattering experiments to investigate the low-lying dipole strength in ^{128}Te. The first NRF experiment was performed at the Darmstadt High Intensity Photon Setup (DHIPS) [132] with continuous-energy bremsstrahlung. The electrons for the bremsstrahlung production were provided by the Superconducting Darmstadt Electron Linear Accelerator (S-DALINAC) [163]. In the second experiment, quasi-monochromatic photon beams were used. These are generated by intracavity laser Compton backscattering of laser photons at the High Intensity γ-ray Source (HIγS) [125]. At HIγS, the γ^3-setup [126] was exploited to perform γ-γ coincidence measurements.

In the following two sections, both nuclear physics facilities and the corresponding NRF setups are introduced.

3.1 S-DALINAC

Figure 3.1 gives a schematic overview of the S-DALINAC. Two electron sources are available: a thermionic gun and a polarized source which provides spin-polarized electrons [165], which have in both cases a kinetic energy of about 250 keV. The succeeding chopper-prebuncher sys-

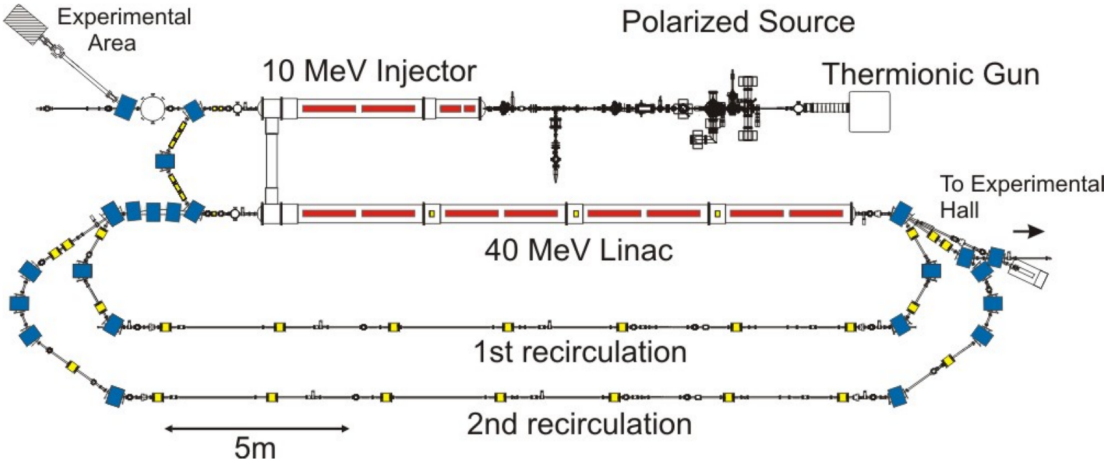

Figure 3.1: Schematic view of the S-DALINAC. Figure adopted from Ref. [164].

tem generates an electron beam with a 3 GHz time structure. In the subsequent superconducting niobium cavities of the injector, it is possible to accelerate the electron beam up to an energy of about 10 MeV with beam currents of approximately 60 μA during the ^{128}Te experiment in 2013. Right behind the injector, the electron beam can either be used for the production of bremsstrahlung to perform experiments at the NRF measuremental site or it can be injected into the main linear accelerator (Linac). The design value of the Linac induces an electron energy increment of 40 MeV per pass. Due to two recirculation paths a total beam energy of 130 MeV can be achieved in theory. However, in practice a total energy of about 90 MeV is reached since the niobium cavities do not exhibit their nominal efficiencies. Behind the Linac, the electron beam can be provided to several experimental setups to perform on one hand electron-scattering experiments at the QCLAM [166] and Lintott spectrometers [167], respectively, and on the other hand experiments with tagged photons at NEPTUN [168].

3.1.1 DHIPS

Directly behind the injector of the S-DALINAC, the experimental site for photon-scattering experiments is located: the Darmstadt High Intensity Photon Setup (DHIPS) [132]. In Fig. 3.2 the setup is shown schematically. The electrons from the injector hit a segmented radiator target and interact with the Coulomb field of the nuclei in the material. Whenever a charged particle is accelerated it emits radiation, which is what happens when the electrons are deflected due to the Coulomb field. The energy loss for the radiative process increases with the electron energy and the proton number of the radiator material. Thus, the material of the radiator at DHIPS can be chosen according to individual experimental requirements and constraints. Typical spectral distributions of bremsstrahlung simulated with GEANT4 [169] are shown in Fig. 3.3 for electron energies of E_{e^-} = 6.0 MeV and E_{e^-} = 9.13 MeV using Au and Ag radiator targets, respectively. In both simulations the same number of impinging electrons is used. The spectra have a continuous energy distribution up to an endpoint energy corresponding to the electron energy E_{e^-}. Bremsstrahlung as photon source is well suited to simultaneously study properties of excited states in atomic nuclei over a wide energy range.

The photon beam can either be used for activation experiments at position T0 or for NRF experiments at target positions T1 and T2, that are located right behind the copper collimator. Due to the collimator, a well-defined beam spot with a diameter of about 25 mm and 30 mm is available at T1 and T2, respectively. The typical size of an NRF target is chosen in a way to be completely illuminated by the beam (Ø $\sim$ 20 mm). The target placed at T1 is surrounded by two High Purity Germanium (HPGe) detectors at 130° and one detector at 90° with respect to the beam direction. Each detector is equipped with a bismuth germanate (BGO) shield for active Compton suppression, that considerably improves the peak-to-background ratio in the experimental spectra and strongly reduces single and double escape peaks [170]. The single γ-ray spectroscopy measurements are recorded by an analog data acquisition. A typical NRF target is composed of a few grams of enriched material, wherefore most of the impinging photons cross the target T1 without any interaction, such that the beam can be further used at T2 to perform, e.g., parity measurements of photo-excited states using a polarization-sensitive Clover detector [171].

In conclusion, DHIPS is a multifunctional NRF setup where several experiments with photons from bremsstrahlung can be performed simultaneously. A detailed description of the current status of DHIPS can be found in Ref. [132].

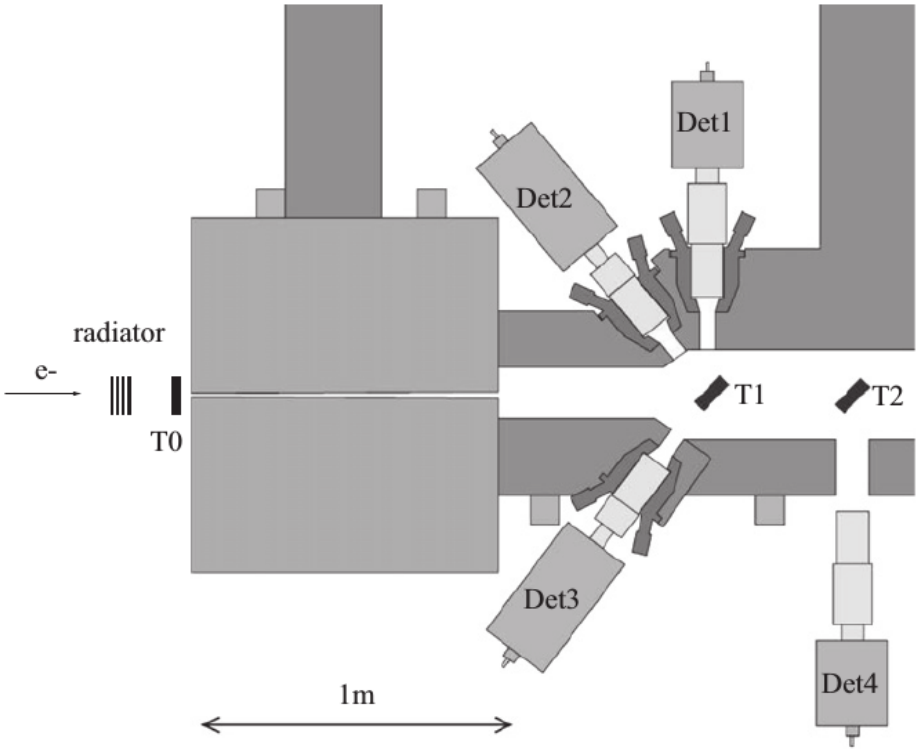

Figure 3.2: Schematic layout of DHIPS. The electron beam impinges on the radiator where continuous-energy bremsstrahlung is produced. At position T0 activation experiments can be performed. After the radiation has passed the copper collimator, the beam can be used for NRF experiments at two positions T1 and T2, respectively. Three HPGe detectors with BGO shielding surround the target position T1 to measure photons originating from reactions within the target. At position T2 parity assignments can be made using a segmented HPGe Clover detector.
Source: Reprinted from [132], Copyright 2011, with permission from Elsevier.

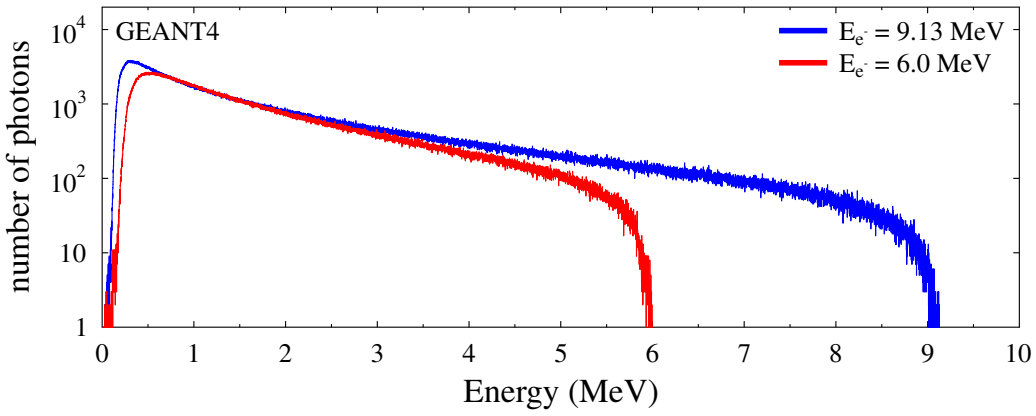

Figure 3.3: GEANT4 simulations for the spectral distribution of bremsstrahlung at DHIPS for electron beam energies of $E_{e^-} = 6.0$ MeV (red) and $E_{e^-} = 9.13$ MeV (blue).

3.2 HIγS

The major part of this doctoral thesis is dealing with NRF experiments performed at the High Intensity γ-ray Source (HIγS) [125] which is a joint project between Triangle Universities Nuclear Laboratory (TUNL) and the Duke Free Electron Laser Laboratory (DFELL). The HIγS facility is shown schematically in Fig. 3.4. An electron beam is generated in a photo-cathode microwave electron gun, bunched and pre-accelerated (E_{e^-} = 0.18 - 0.28 GeV) in an electron linear accelerator. The subsequent booster synchrotron is able to ramp up the energy up to 1.2 GeV before the electron bunches are injected into the Duke electron storage ring. Within the storage ring a free electron laser (FEL) is powered by the electron beam.

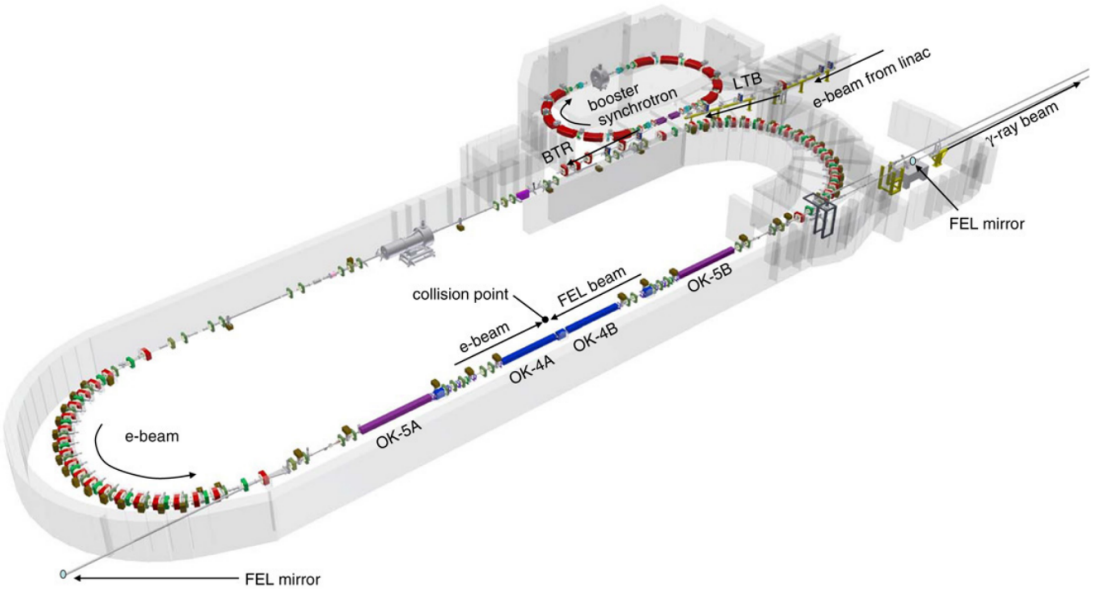

Figure 3.4: Scheme of the HIγS facility. Behind the electron linac and the booster synchrotron, electron bunches with energies up to 1.2 GeV are injected into the Duke electron storage ring. Within this ring high-energy photons can be produced by intra-cavity laser Compton backscattering. They are used for nuclear physics experiments 60 m downstream of the collision point. *Source*: Reprinted from [125], Copyright 2009, with permission from Elsevier.

Figure 3.5 shows a simplified scheme of the storage ring and the photon production method. In the optical klystron OK-4, the ring electrons are deflected by several wiggler magnets and, hence, emit horizontally polarized photons of a few electron volts. These photons are reflected by the FEL mirrors and collide with another electron bunch at the collision point. In the Compton backscattering process, the photon energy can be boosted up to 100 MeV with a total flux on target in the order of $\sim 10^8\ \gamma/s$ depending on the scattering angle. The γ-ray energy can be tuned by adjusting the electron energy as well as the FEL energy. Due to the polarization conservation of the Compton backscattering process a linearly polarized γ-ray beam is produced. The high-intensity photon beam passes the FEL mirror and is collimated by the precollimator and the primary collimator about 30 m and 60 m downstream of the collision point, respectively. Figure 3.6 shows the measured spectral distribution of the photon beam with a mean energy of E_γ = 8.0 MeV at the target position. Depending on the spacial distribution of the backscattered photons and the collimator size, the typical full width at half maximum (FWHM) of the beam energy profile is around 3 % of the peak energy.

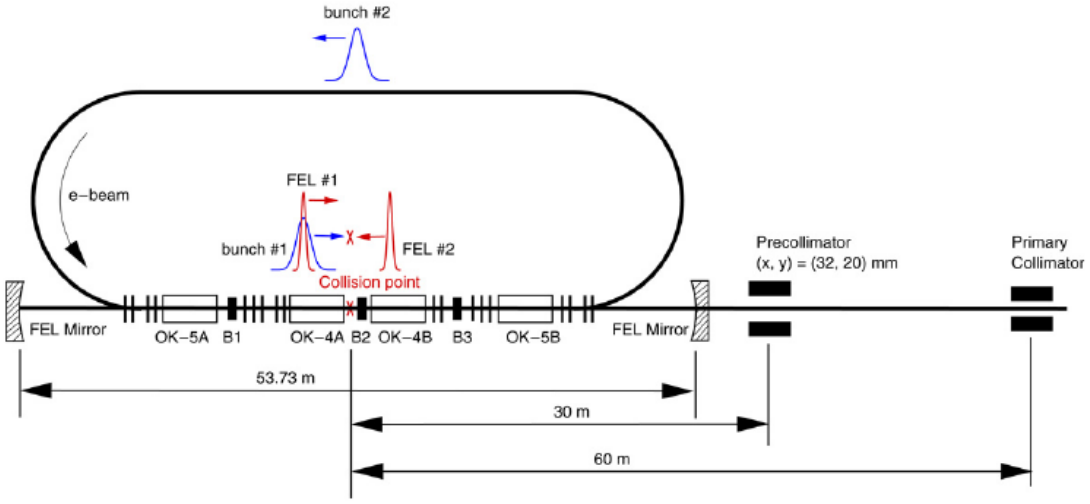

Figure 3.5: Simple scheme of the Duke electron storage ring focusing on the γ-ray production. A first electron bunch generates horizontally polarized laser photons. Afterwards they pass the wiggler system within the OK-4 and are reflected by the FEL mirror. At the collision point the photons are Compton backscattered by a second electron bunch and are boosted from a few eV to several MeV γ-ray energy.
Source: Reprinted from [125], Copyright 2009, with permission from Elsevier.

Two experimental halls are located behind the primary collimator, namely the Upstream Target Room (UTR) and the Gamma Vault, that use the high-energy γ-ray beam to perform nuclear physics experiments. The photon-scattering experiments were performed at the γ-γ coincidence setup γ^3 [126] located in the UTR.

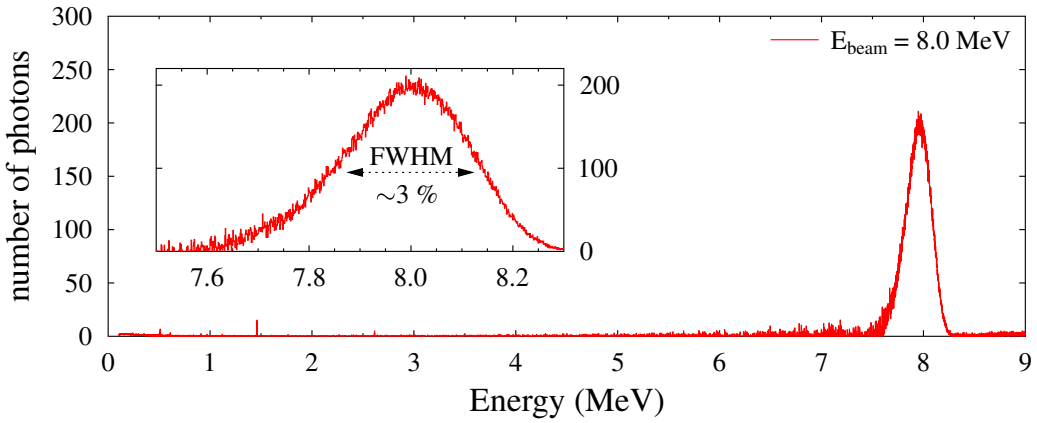

Figure 3.6: Spectral distribution a the γ-ray beam produced at HIγS for $E_{beam} = 8.0$ MeV. Inset: The full width at half maximum (FWHM) is about 3 % of the centroid beam energy.

3.2.1 The γ^3-setup

The γ^3-setup is located approximately 60 m from the collision point of the FEL. Figure 3.7 shows a technical drawing of the location. The γ-ray beam is collimated in the collimator room to match the beam-size condition for particular experimental requirements. For the measurements in 2013 a collimator diameter of 0.75" was used. Right after the collimator room three lead walls of different thicknesses (20 cm, 10 cm and 10 cm) were build to reduce the beam related background radiation, which mainly stems from small-angle scattering in the collimator. The γ^3-setup consists of two types of detectors: four HPGe detectors (3"×3") with an intrinsic efficiency of 60% relative to the 3"×3" NaI standard and four $LaBr_3$:Ce scintillators (3"×3"). They can be mounted on an aluminum wheel at different polar ($\vartheta = 90^\circ$ and $\vartheta = 135^\circ$) and azimuthal angles in $\Delta\varphi = 45^\circ$ steps. Furthermore, the mounting wheel can be rotated by a maximum angle of $\Delta\varphi = 45^\circ$ around the beam axis. The mounting structure is designed in a way that both types of detectors can be mounted at all possible positions.

For the experimental campaign in 2013 the detector setup is shown in Fig. 3.8. Two $LaBr_3$:Ce and two HPGe detectors each were placed at $\vartheta = 90^\circ$ and $\vartheta = 135^\circ$, respectively. The polar and azimuthal angles for every single detector are summarized in Table 3.1.

All detectors were wrapped in 2 mm of lead to reduce cross talk effects from scattering of photons from one detector to the other. Moreover, each detector face was shielded by different combinations of Cu and Pb discs to reduce the low-energy background originating primarly from non-resonant scattering of the monochromatic beam off the target material. Further reduction of the non-resonant background is realized by the vacuum-evacuated beam pipe. A medium vacuum of about 1 mbar to 10 mbar is created, which increases the mean free path length of photons within the tube and therefore strongly reduces the probability for atomic scattering. The beam-correlated background is reduced by one order of magnitude resulting in reduced count rates and dead time of the individual detectors as well as in an increase of the peak-to-background ratio in the measured spectra. A detailed description of the commissioning and

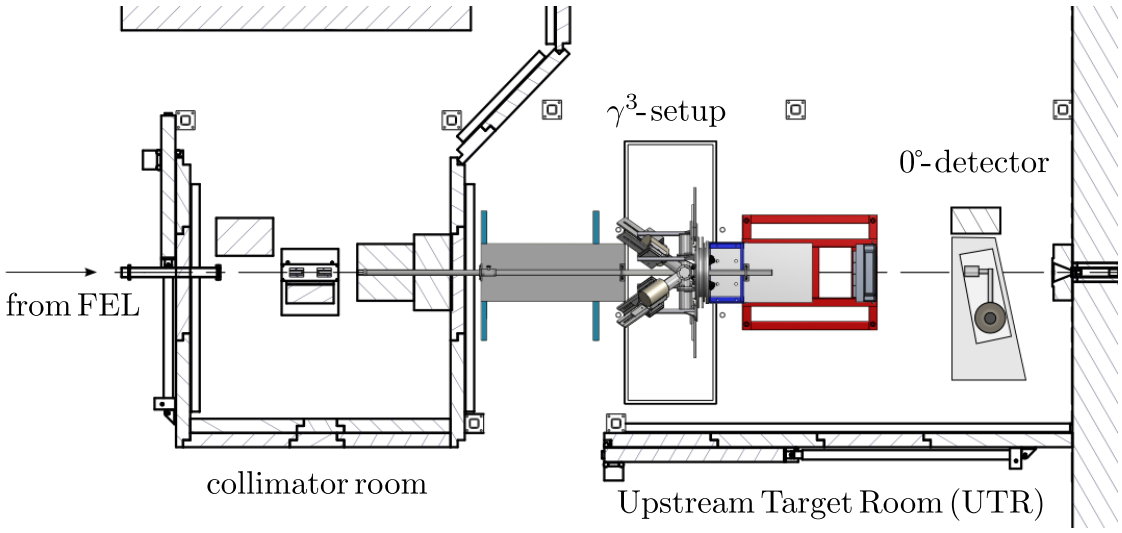

Figure 3.7: Technical drawing of the experimental site at HIγS. The impinging photon beam from the FEL is collimated by a 0.75" copper collimator. The γ^3-setup is located in the Upstream Target Room (UTR) behind the collimator. At the end of the UTR, the 0°-detector is used to monitor the spectral distribution of the photon beam (see Section 4.4.2).

	LaBr-1	LaBr-2	LaBr-3	LaBr-4
(ϑ, φ)	$(135^\circ, 135^\circ)$	$(135^\circ, 45^\circ)$	$(90^\circ, 0^\circ)$	$(90^\circ, 90^\circ)$
d (cm)	9.0(2)	8.9(2)	4.1(2)	4.1(2)

	HPGe-1	HPGe-2	HPGe-3	HPGe-4
(ϑ, φ)	$(90^\circ, 180^\circ)$	$(90^\circ, 270^\circ)$	$(135^\circ, 225^\circ)$	$(135^\circ, 315^\circ)$
d (cm)	6.2(2)	5.3(2)	9.3(2)	8.9(2)

Table 3.1: Detector positions for the experimental campaign in 2013. They were placed at different polar angles ϑ and azimuthal angles φ. The distance between the detector surface and the target position is given by d.

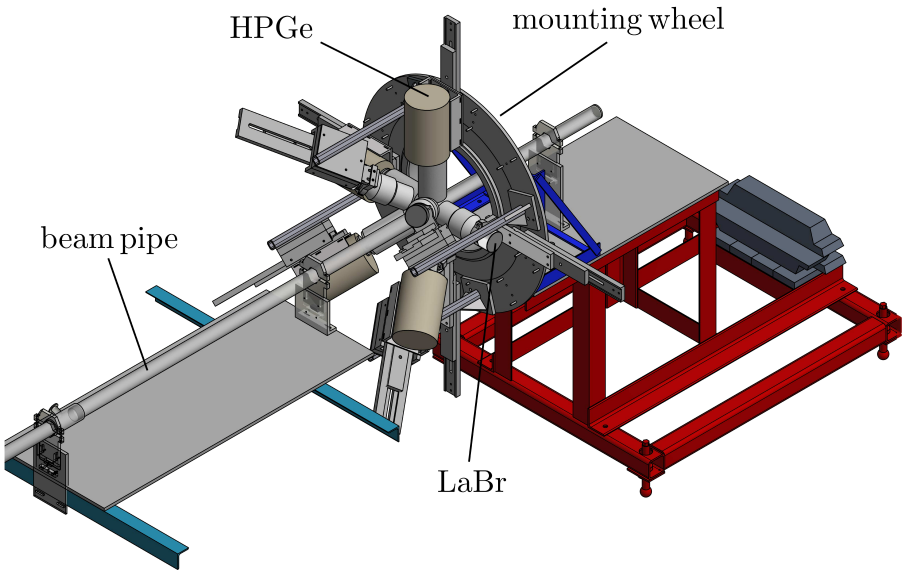

Figure 3.8: Technical drawing of the γ^3-setup during the experimental campaign in 2013. Four LaBr and four HPGe detectors are mounted on a rotatable wheel. For the exact detector positions see Table 3.1.

characteristics of the γ^3-setup can be found in Ref. [126].

3.2.2 Data acquisition

During the experiments in 2013, two independent data acquisition (DAQ) systems were used: the Canberra GENIE 2000 system and the Multi Branch System (MBS) [172] from GSI Helmholtzzentrum für Schwerionenforschung. The GENIE DAQ records spectra from single γ-ray spectroscopy with the HPGe detectors, i.e., without any coincidence conditions between several detectors. It has the advantage of shorter readout induced dead time. The dominant part of the detected photons during NRF experiments usually stem from non-resonant scattering of the beam photons off the target material usually leading to high event rates. The spectral distribution of this background radiation is exponentially increasing towards low energy. One way

to decrease the overall count rate and the dead time, respectively, is to apply energy thresholds in the trigger hardware to suppress the detection of γ-rays below these thresholds and cut off a substantial part of the non-resonant background radiation. Since the dead time in the GENIE DAQ is by default comparatively short, it allows to measure γ-ray spectra with very low energy thresholds. Hence, it is used for the single γ-ray spectroscopy of individual excited states in ^{128}Te using the HPGe detectors of the γ^3-setup. Furthermore, the resulting data file format can be easily converted to `ASCII` format using the free `xylib` tool [173].

The MBS is an event-based system that records data such as energy and time information for each event and detector in binary list mode data (LMD) files. An important component of this system is the flexible trigger logic TrLoII [174] implemented on the generic VME logic module VULOM4 from GSI. This module has 16 inputs for trigger signals and an output for a main trigger. The triggers in the MBS DAQ fall into to two classes: low-level triggers and high-level triggers. Low-level triggers are generated hardware wise in logical NIM modules using timing signals of the individual detectors. The TrLoII combines low-level triggers in a flexible manner by logical operations to create high-level triggers. Furthermore, a reduction factor can be applied to each high-level trigger within the TrLoII to reduce the total trigger rate in the DAQ, if necessary. The trigger generation matrix is illustrated in Table 3.2. For each detector type of the γ^3-setup, LaBr and HPGe, four low-level triggers are generated. One group is created by a logical OR operation of the individual detector triggers. Hence, an output is generated if at least one of the LaBr or HPGe detectors provided a good timing signal. The other group requires a

High-level triggers \ Low-level triggers	1 LaBr OR Low	2 LaBr OR High	3 HPGe OR Low	4 HPGe OR High	5 LaBr M2 Low	6 LaBr M2 High	7 HPGe M2 Low	8 HPGe M2 High	9 ———	10 HPGe 0°	11 RF / BPU	12 Pulser
1 Singles LaBr		✓										
2 Singles HPGe				✓								
3 Coincidence Low-Low	✓		✓									
4 Coincidence Low-High	✓			✓								
5 LaBr M2 High		✓			✓							
6 HPGe M2 High				✓			✓					
7 0°										✓		
8 Pulser												✓
9 Singles LaBr Low	✓											
10 Singles HPGe Low			✓									
11 Coincidence High-Low		✓	✓									

Table 3.2: Trigger generation matrix of the MBS DAQ in the experimental campaign at the γ^3-setup in 2013.

minimum multiplicity of two (M2), i.e. at least two detectors need to have triggered at the same time. Furthermore, the low-level triggers 1 to 8 are labeled with "Low" and "High". These labels correspond to the timing signal of each detector that is split into a low-energy threshold branch ("Low") and a high-energy threshold branch ("High"). A trigger for a single detector is generated only if the associated γ-ray energy exceeds a given threshold. The low-energy threshold is usually set as high as feasible to cut off a large part of the non-resonant background radiation and the pronounced electron-positron annihilation peak at 511 keV, but low enough to allow the detection of the minimum γ-ray energy of interest. In the case of ^{128}Te, the low-energy threshold was set to $\sim$ 600 keV to be able to measure coincidences to the ground-state decay of the first excited 2^+ state at 743 keV. The high-energy threshold was chosen to be around 1600 keV suppressing, in addition, the γ-rays from the intrinsic radioactivity of the LaBr detector material at 1435 keV and the natural background line from ^{40}K at 1460 keV. Figure 3.9 shows spectra from the measurement of the natural background radiation for HPGe

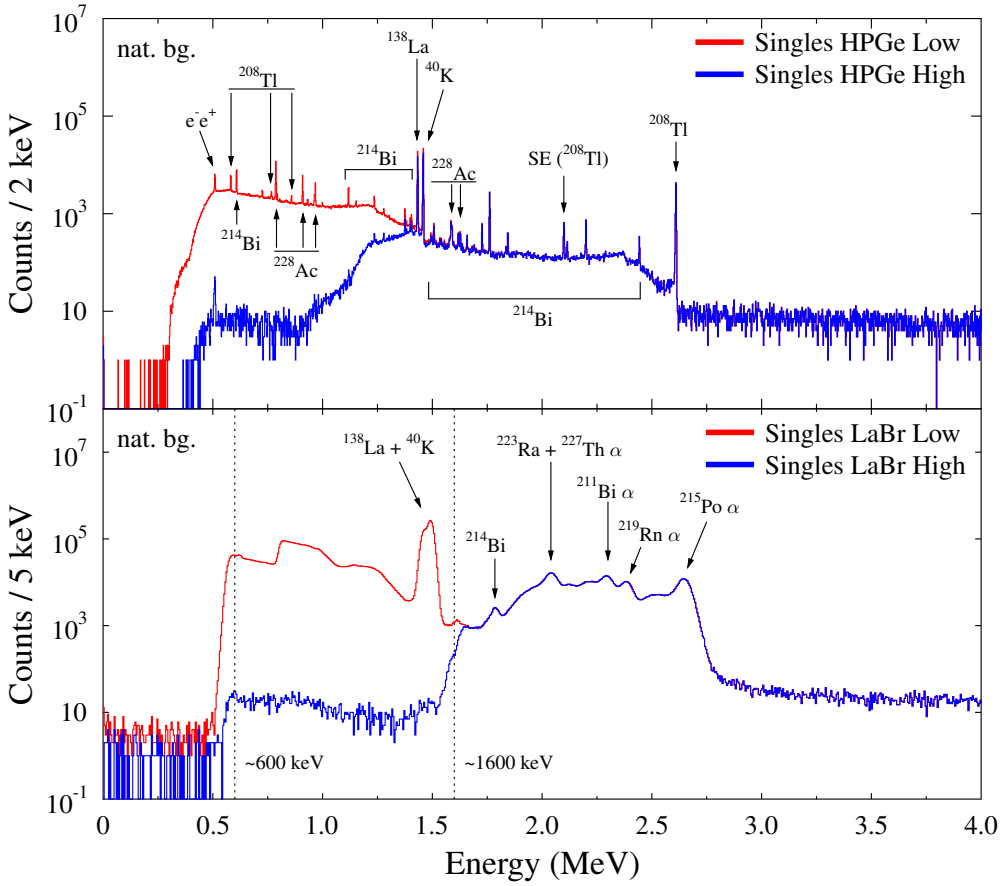

Figure 3.9: Spectra from single γ-ray spectroscopy measurements of the natural background radiation. Upper panel: HPGe spectrum with low (red) and high (blue) energy threshold. Isolated peaks stemming from natural background radiation are marked. Lower panel: LaBr spectrum with low (red) and high (blue) energy threshold. The vertical dotted lines indicate the two thresholds at $\sim$600 keV and $\sim$1600 keV. In addition to photons, LaBr scintillators are sensitive to charged particles such as α particles produced by the intrinsic radioactivity of the LaBr detectors. Hence, the spectrum is dominated by natural background radiation from the α decay of the Thorium chain.

(upper panel) and LaBr (lower panel) detectors. In each panel, the γ-ray spectra obtained for the low-energy threshold (red) and the high-energy threshold (blue) are shown. The reason for the different thresholds is that for the γ-γ coincidence measurements the photons involved have significantly different γ-ray energies. For instance, for the transition to the first excited 2^+ state and its subsequent ground-state decay γ-ray energies of 743 keV and $(E_{beam} - 743)$ keV have to be measured in coincidence. Since most of the beam energies used in the experiments with ^{128}Te are $E_{beam} > 4$ MeV, the energy of the primary transition is above 3 MeV. It follows that, e.g., for the coincidence between two LaBr detectors (high-level trigger `LaBr M2 High`) it is sufficient to require coincident low-level triggers from `LaBr M2 Low` and `LaBr OR High`. This means that at least two LaBr's have to have registered γ-rays exceeding the low-energy threshold, while at least one of them also exceeded the high-energy threshold. While, in general, the low-level trigger `LaBr M2 Low` incorporates all coincident events, the coincidence condition to `LaBr OR High` reduces the trigger rate for the high-level trigger `LaBr M2 High` by a factor of four. Based on these considerations, "good" events are filtered already online from the huge amount of incoming triggers and data, respectively, resulting in a reduction of the overall DAQ related dead time.

The great advantage of the TrLoII and the trigger generation matrix is the flexibility during the experiment. The high-level trigger conditions and definitions can be changed easily in software avoiding "hardware" re-wiring of the electronics to match changing experimental requirements.

4 Data analysis

This chapter is dedicated to the data analysis of the NRF experiments performed with ^{128}Te at DHIPS and HIγS. The experimental parameters, such as target masses and beam energies are summarized in Appendix A.1. The energy, intensity and angular distribution of the emitted photons are important observables that carry information about intrinsic properties of individual excited states and average quantities of the nucleus for different excitation energy regions. In the following, the deconvolution method to correct γ-ray spectra for their detector response is introduced, since it is used in various analysis steps throughout this chapter. Subsequently, the analysis of the data obtained from single γ-ray spectroscopy is presented. In the end a discussion of the γ-γ coincidence method is given.

4.1 Detector response deconvolution

A typical γ-ray spectrum measured with a "real" detector exhibits a certain structure following the electromagnetic interaction of γ-rays with the detector material. The three dominant processes are the photoelectric absorption, Compton scattering, and pair production [175, 176]. To illustrate these effects, Monte-Carlo simulations using the simulation toolkit `GEANT4` [169] are performed for two different photon energies of 2 MeV and 8 MeV and are shown in Fig. 4.1. A deposition of the complete γ-ray energy in the detector material results in the so-called full-energy peak (FEP) at the highest energy in the spectrum. This is achieved either by the photoelectric absorption of the photon, where its complete energy is transfered to a bound electron in an atomic shell or after multiple processes, such as Compton scattering with subsequent photoelectric absorption. Photons that are Compton scattered off electrons within the detector material deposit only a fraction of their energy, which leads to the broad distribution of the Compton continuum observed below the FEP. Pair production is possible, once the photon energy exceeds 1022 keV. Here, the photon is converted into an electron-positron pair, that shares the remaining photon energy equally. Usually, the positron annihilates with another electron in the detector resulting in two photons with an energy equivalent to their rest mass of 511 keV each. If one or both of these photons leave the detector and, hence, are not detected, the maximum deposited energy is reduced by 511 keV and 1022 keV, respectively. Due to the escape of these photons, single-escape (SE) and double-escape (DE) peaks emerge in the spectrum.

The spectra shown in Fig. 4.1 reflect the response of an HPGe detector to the impinging photons and is in general energy dependent. Furthermore, the detector response depends on the

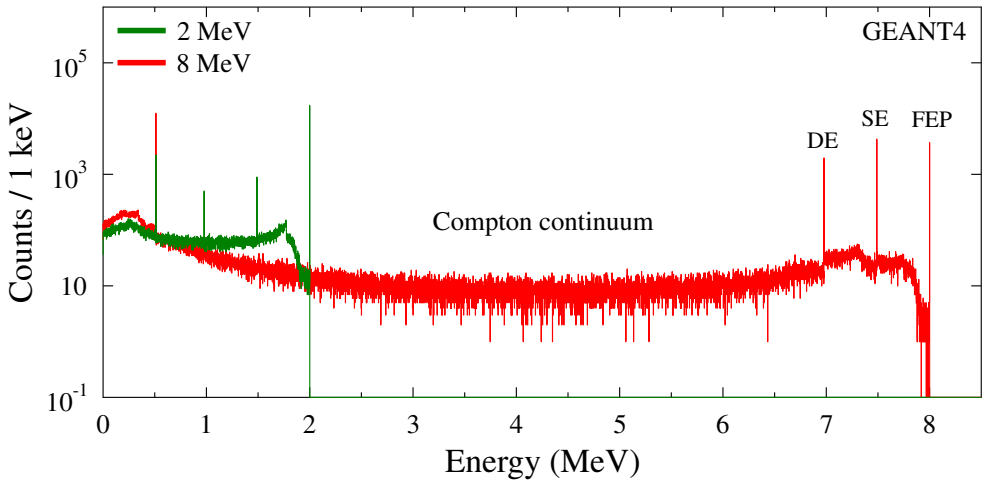

Figure 4.1: Simulation of the detector response of an HPGe detector with photon energies of 2 MeV (green) and 8 MeV (red). A deposition of the full photon energy results in a full-energy peak (FEP) in the spectrum. The single-escape (SE) and double-escape (DE) peaks emerge, if after the annihilation of an electron-positron pair one or both of the 511 keV γ-rays leave the detector. The distribution below the FEP is produced by Compton scattering of photons which deposit only a fraction of their energy.

detector material, size and geometry. Usually, this effect can be expressed as a linear transformation

$$m = \mathbf{R}n + \varepsilon \,. \tag{4.1}$$

The measured spectrum m is generated by a convolution[4] of the "true" spectrum n of the incoming photons with the detector response $\mathbf{R}$. In this representation, m and n are vectors with components m_i and n_i, respectively, which correspond to the number of counts in a given energy bin i. The square matrix $\mathbf{R}$ is composed of the individual detector response functions for each γ-ray energy. Due to statistical fluctuations, a small perturbation ε is usually present.

Different methods exist to extract n. In the data analysis used for this thesis a χ^2 minimization procedure is used to determine n from the measured spectrum m assuming that $\mathbf{R}$ is known. All components n_i are free parameters that are fitted to the experimental spectrum m using the `minuit` package of `ROOT`. One useful feature is that it is possible to set constraints on the fit parameters. Since a negative number of counts is unphysical, the condition $n_i \geq 0$ for all i is required. Examples for the detector response are given for two photon energies in Fig. 4.1. To obtain the full detector response matrix Monte-Carlo simulations are performed with `GEANT4` for energies up to 10 MeV in 1 keV steps.

As a simple test case, a spectrum of ^{32}S (black) measured with a LaBr detector is used (see Fig. 4.2). A strongly-excited 1^+ state is located at 8125 keV, which has a significantly large branching ratio to the first excited 2^+ state at 2230 keV. The peak from this branching transition is apparent at 5900 keV. To separate the full-energy peaks from the rest of the spectrum, the detector response is deconvoluted applying the introduced fitting procedure. The deconvoluted spectrum (red) contains full-energy events, only. The grey error band represents an estimation of the influence of statistical fluctuations to the deconvolution procedure. For this estimation, the procedure is repeated 50 times varying the input spectrum within its statistical uncertainties

[4] In the literature, the term "folding" is sometimes used synonymously for convolution.

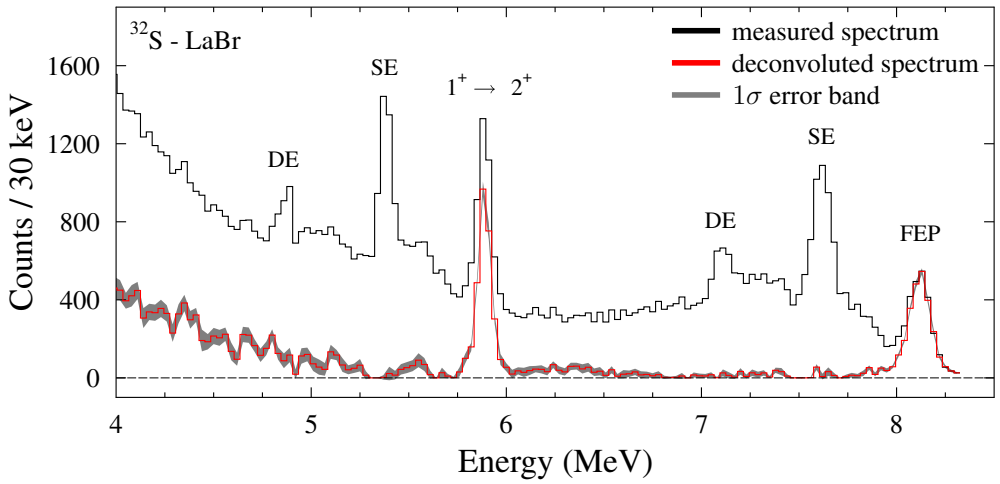

Figure 4.2: Measured LaBr spectrum of ^{32}S (black). The FEP at 8125 keV corresponds to the ground-state decay of a strongly-excited 1^+ state, while its transition to the first excited 2^+ state results in a peak at ∼5900 keV. The red spectrum is generated by the detector response deconvolution of the measured spectrum. The grey error band is the standard deviation of the deconvolution procedure taking into account statistical fluctuations of the input spectrum. For details see text.

for each iteration. The mean value and the corresponding standard deviation is computed for each energy bin from the 50 deconvoluted spectra.

This benchmark test confirms the applicability and reliability of this deconvolution method. This is important for the data analysis presented in later sections, since the experimental spectra obtained from measurements with ^{128}Te are more sophisticated due to the increasing number of peaks.

4.2 Level and γ-ray energy

Transition energies between excited states and their corresponding level energies can be extracted from energy-calibrated γ-ray spectra. The calibration is usually done with known γ-ray energies from radioactive sources, natural background radiation or with calibration standards that are measured simultaneously with the target of interest. In the following, an excited state with level energy E_x is excited by absorption of an incident photon. The emitted photon in the course of the subsequent ground-state decay has an energy E_γ that is less than E_x due to the recoil energy transfered to the nucleus during the emission process. The relation between the level energy and the measured photon energy is given by

$$E_x = E_\gamma \cdot \left(1 + \frac{E_\gamma}{2Mc^2} \cdot (1 - 2\cos\vartheta)\right) . \tag{4.2}$$

The expression depends on the nuclear mass M and the polar angle ϑ of the emitted photon with respect to the direction of the incident photon. Similarly, the expected γ-ray energy emitted from an excited state can be calculated by rearranging Eq. (4.2):

$$E_\gamma = \frac{Mc^2}{1-2\cos\vartheta} \cdot \left(\sqrt{1 + \frac{2E_x}{Mc^2} \cdot (1-2\cos\vartheta)} - 1 \right) . \tag{4.3}$$

4.3 Reaction rate and peak area

One of the objectives of NRF measurements is to determine cross sections for the excitation of individual states as well as cross sections averaged over an ensemble of states in a certain energy range. If a signal above background is observed in a γ-ray spectrum, its peak area is directly related to the excitation cross section for this particular reaction. The number of counts measured in a peak depends on the reaction rate and the detection probability of the reaction products. The number of reactions can be determined combinatorically accounting for the total number of target nuclei N_T, the absolute photon flux $N_\gamma(E_\gamma)$ at a certain γ-ray energy E_γ and the partial cross section $\sigma^0_{x,i}(E_\gamma)$ (see Eq. (2.14)) for a particular reaction. For now, the excitation from the ground state to the excited state x followed by the transition to the state i is considered. The total number of reactions R is then determined by

$$R = N_T \cdot \int N_\gamma(E) \cdot \sigma^0_{x,i}(E)\,\mathrm{d}E \tag{4.4}$$

where the integral runs over all possible energies. The typical width of a nuclear resonance is in the eV region or even below. Thus, one can assume that the photon flux N_γ is nearly constant in the regime where $\sigma^0_{x,i}$ is not zero and simplify Eq. (4.4):

$$\begin{aligned} R &= N_T \cdot N_\gamma(E_x) \cdot \int \sigma^0_{x,i}(E)\,\mathrm{d}E \\ &= N_T \cdot N_\gamma(E_x) \cdot I_{0\to x\to i} \,, \end{aligned} \tag{4.5}$$

with $I_{0\to x\to i}$ being the integrated cross section defined in Eq. (2.20).

Furthermore, it is important to know how many of the reactions R are actually registered by the present detection system. The two crucial parameters are the detection efficiency ε and the angular distribution $W_{0\to x\to i}$ of the emitted photons, which was discussed in Section 2.2.3. The experimentally measured peak area $A_{0\to x\to i}$ of an NRF reaction is then given by:

$$\begin{aligned} A_{0\to x\to i} &= R \cdot \int\limits_{\Delta\Omega} \varepsilon(E_x - E_i, \Omega) \cdot W_{0\to x\to i}(\Omega)\,\mathrm{d}\Omega \\ &= N_T \cdot N_\gamma(E_x) \cdot I_{0\to x\to i} \cdot \int\limits_{\Delta\Omega} \varepsilon(E_x - E_i, \Omega) \cdot W_{0\to x\to i}(\Omega)\,\mathrm{d}\Omega \,, \end{aligned} \tag{4.6}$$

where $\Delta\Omega$ is the opening angle of the detector. In general, γ-ray detectors have a finite size and are placed at a finite distance to the reaction point. In addition, the efficiency $\varepsilon(E_x - E_i, \Omega)$ may vary depending on the position and angle of the emitted photon relative to the detector surface. The integration over the solid angle $\Delta\Omega$ of the detector takes the finite dimensions into account. However, at large distances to the target the detector is usually assumed to be nearly point like. In that case, Eq. (4.6) can be simplified to

$$A_{0\to x\to i} = N_T \cdot N_\gamma(E_x) \cdot I_{0\to x\to i} \cdot \varepsilon(E_x - E_i) \cdot W_{0\to x\to i}(\Omega) \; . \tag{4.7}$$

This is approximately true for the detector setup at DHIPS. For the γ^3-setup, however, a close setup geometry was chosen for the experiments with ^{128}Te (see Chapter 3.2.1). Therefore, mainly Eq. (4.6) will be used throughout the analysis of the corresponding NRF experiments.

In the following, the ground-state transition $0 \to x \to 0$ is considered to illustrate the idea of corrections that have to be applied to extract $A_{0\to x\to 0}$ during the analysis. Note that the measured peak area A_{meas} at E_x in the experimental spectrum might not exactly correspond to the intensity of the transition of interest, but can be composed of different contributions:

$$A_{meas} = A_{0\to x\to 0} + A_{0\to y\to x\to 0} + A_{0\to y\to 0} \cdot \frac{I_{SE}}{I_{FEP}} \; . \tag{4.8}$$

The different parts that may contribute to A_{meas} are illustrated in Fig. 4.3.

Feeding transitions

For the extraction of $A_{0\to x\to 0}$ (blue area) the total peak area has to be corrected for so-called feeding transitions from higher-lying states (red area):

$$A_{0\to y\to x\to 0} = A_{0\to y\to 0} \cdot \frac{\Gamma_{y\to x}}{\Gamma_{y\to 0}} \cdot \frac{\int \varepsilon(E_x) \cdot W_{0\to y\to x\to 0}(\Omega)\, \mathrm{d}\Omega}{\int \varepsilon(E_y) \cdot W_{0\to y\to 0}(\Omega)\, \mathrm{d}\Omega} \; , \tag{4.9}$$

with $\Gamma_{y\to x}$ being the partial transition width from y to x and $\Gamma_{y\to 0}$ being the ground-state transition width of state y. Furthermore, the peak area $A_{0\to y\to 0}$ attributed to the ground-state decay of the feeding state at E_y has to be known. An indicator for feeding transitions is provided by the Ritz variation principle. It is based on the assumption that three or more peaks are observed

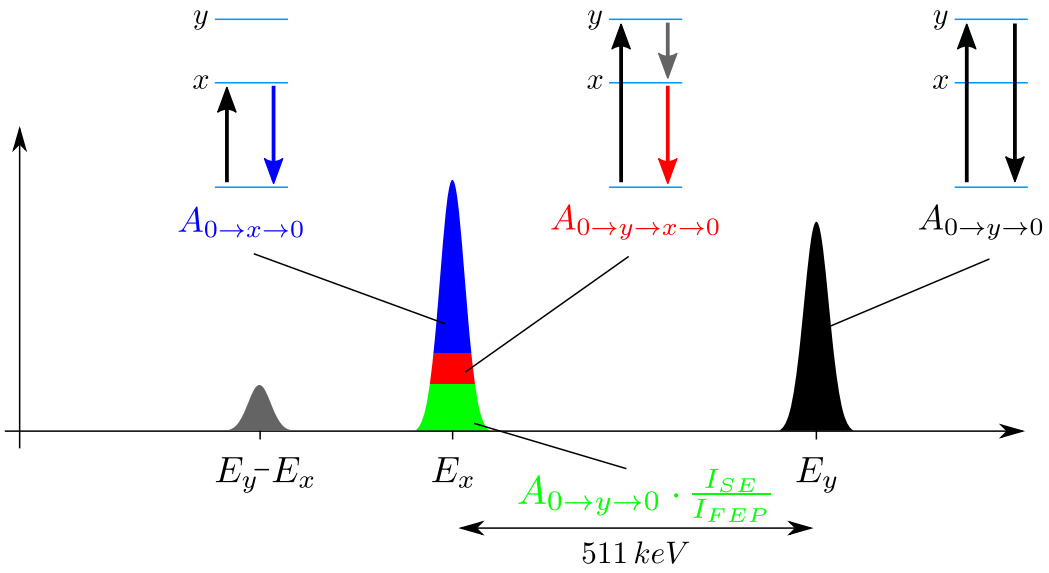

Figure 4.3: Scheme of different sources of intensity observed in γ-ray spectra recorded in photon-scattering experiments. For details see text.

in the γ-ray spectrum at energies E_w, E_x and E_y with $E_w < E_y$ as well as $E_x < E_y$. If the condition $E_w = E_y - E_x$ is fulfilled, the state at E_x might be fed by the higher-lying state at E_y (see Fig. 4.3), whereas a peak is observed at E_w corresponding to the energy of the emitted photons of the feeding transition (grey peak). The same applies for the interchange of E_x and E_w.

Single-escape correction

Another contamination source is given by the detector response. Aside from the Compton continuum, peaks from SE and DE processes are usually apparent in γ-ray spectra. If two peaks at E_x and E_y are separated by 511 keV, the energetically lower-lying peak has to be corrected for SE contributions (green area in Fig. 4.3). Therefore, the ratio between the SE intensity I_{SE} and the associated full-energy intensity I_{FEP} have to be determined. This can be done either with help of isolated peaks in the experimental spectrum or by Monte-Carlo simulations computing I_{SE}/I_{FEP} as a function of the γ-ray energy. Hence, the SE contribution from $A_{0\to y\to 0}$ to A_{meas} is calculated by $A_{0\to y\to 0} \cdot I_{SE}/I_{FEP}$. An analogous procedure is applied for DE corrections.

4.4 Photon-flux calibration

One quantity that needs to be determined to compute $I_{0\to x\to 0}$ is the photon flux $N_\gamma(E_x)$ at target position. It is usually simulated with `GEANT4` and then scaled to known cross sections from calibration standards.

4.4.1 DHIPS

During the measurements at DHIPS a small amount of enriched ^{11}B was attached to the ^{128}Te target. It is often used as calibration standard [132] since it exhibits a few strong transitions spread over a wide energy range from 2 MeV to 9 MeV. Furthermore, this approach minimizes systematic errors induced by varying experimental conditions during the measurements. Since disruptive factors that may occur during the experiment, such as fluctuating photon-flux intensities and dead time determination, are basically accounted for in the observables of the simultaneously measured calibration standard. The information about ^{11}B is summarized in Table 4.1.

Two NRF measurements were performed with ^{128}Te at DHIPS: one with an endpoint energy of $E_{e^-} = 6.00$ MeV and another one with $E_{e^-} = 9.13$ MeV. The HPGe spectra from both measurements are shown in Fig. 4.4 (black spectra). Usually, the product $N_\gamma\varepsilon$ is simulated as a function of the energy (red) and scaled to the well-known integrated cross sections of the observed ^{11}B transitions (black dots). The calibration points are determined by rearranging Eq. (4.7):

$$N_\gamma\varepsilon(E_x) = \frac{A^{^{11}B}}{N_T^{^{11}B} \cdot I^{^{11}B} \cdot W^{^{11}B}} \,. \tag{4.10}$$

Due to the extraction of $N_\gamma\varepsilon$ it is not necessary to know the absolute detection efficiency $\varepsilon(E_x)$ separately, e.g. from measurements with radioactive sources. Thus, additional uncertainties are avoided.

E_x (keV)	E_f (keV)	Γ (eV)	Γ_f/Γ (%)	I (keVfm^2)	$W(90^\circ)$	$W(130^\circ)$
2124.69	0	0.117(4)	100.0	4.98(17)	1.000	1.000
4444.98	0	0.55(5)	100.0	16.0(15)	0.93	1.017
5020.30	0	1.97(7)	85.8(4)	22.11(79)	0.92	1.019
	2124.69		14.2(4)		1.178	0.957
7285.51	0	1.14(8)	88.4(3)	9.68(68)	0.93	1.017
	4444.98		5.3(4)		1.064	0.985
	5020.30		6.3(4)		0.94	1.014
8920.47	0	4.37(3)	97.3(1)	29.97(21)	0.93	1.017
	4444.98		2.7(1)		1.068	0.984

Table 4.1: Summary of the information about ^{11}B. Given are the level energy E_x, the total level width Γ and the branching ratio Γ_f/Γ to the final level E_f. Furthermore, the corresponding integrated cross sections I and angular distributions W for the relevant polar angles of $\vartheta = 90^\circ$ and $\vartheta = 130^\circ$ are tabulated.

It should be noted, that due to the continuous-energy bremsstrahlung the ^{11}B levels at 2124 keV, 4444 keV and 5020 keV are not exclusively excited from the ground state, but are also fed by energetically higher-lying states. Hence, their peak areas have to be corrected for the associated feeding contributions as discussed in the previous section. An excellent agreement between the energy dependence of the simulations and the ^{11}B data points is found. Even the decrease of $N_\gamma\varepsilon$ in the vicinity of the endpoint energy is well described in the 9.13 MeV measurement.

4.4.2 HIγS

The spectral distribution of the incoming photon beam provided at the HIγS facility is measured with a 123 % HPGe detector (zero-degree detector) placed in the beam behind the target. The beam intensity is strongly reduced during this measurement to avoid high count rates. The measured spectrum as well as the deconvoluted spectrum are shown in Fig. 4.5. The energy distribution of the incoming beam corresponds approximately to a Gaussian shape.

Due to the quasi-monochromatic character of the beam, the idea of using ^{11}B as calibration standard is not feasible. In most cases, the corresponding level energies in ^{11}B do not coincide with the photon beam energies chosen for the measurement with ^{128}Te and, hence, are not excited. However, previously known integrated cross sections for transitions from the target itself can be used to determine the absolute photon flux for the associated energy settings. At least one known cross section per beam energy is necessary to calibrate the photon flux. This approach is illustrated in Fig. 4.6 for three measurements. In each case, the transitions in ^{128}Te (red dots) known from the DHIPS data are displayed. Their integrated cross sections are determined from the DHIPS experiments as described before. Note, that the data points describe the energy dependence of the beam profile (black) very well.

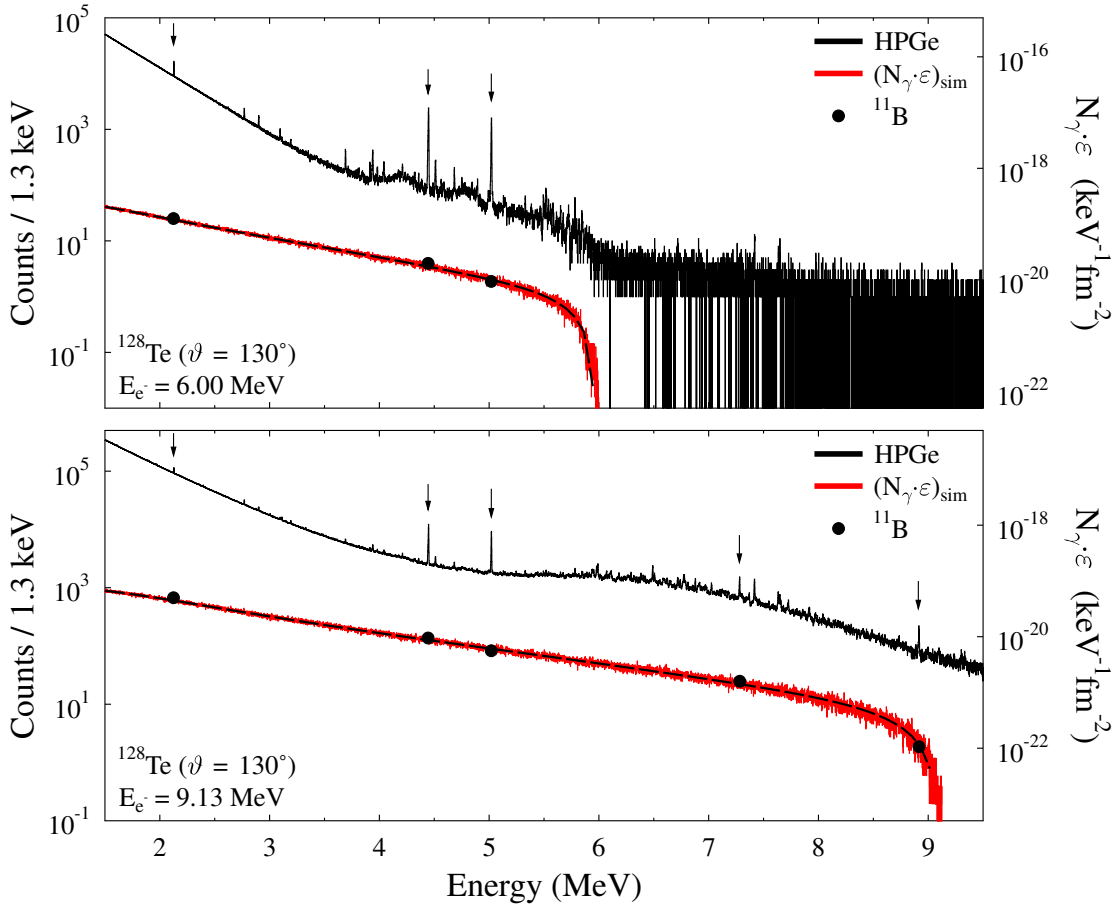

Figure 4.4: Upper panel: Spectrum of ^{128}Te recorded in single γ-ray spectroscopy at DHIPS with an endpoint energy of 6.0 MeV (black). The simulated energy-dependent product $N_\gamma\varepsilon$ is scaled to experimental values (black dots) determined from known integrated cross sections of excited states in ^{11}B. Lower panel: Same quantities as in the upper panel for the measurement with E_{e^-} = 9.13 MeV.

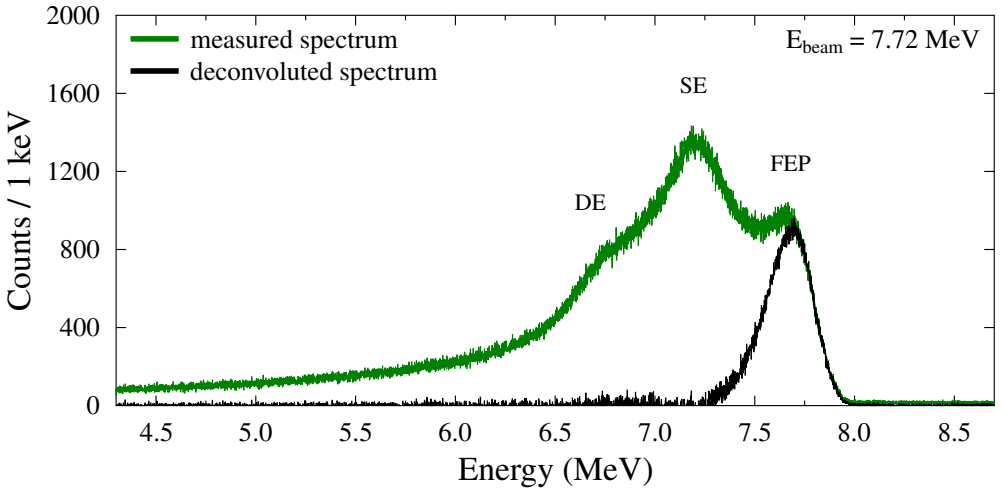

Figure 4.5: Beam profile measurement with the zero-degree detector for $E_{beam} = 7.72$ MeV. The measured spectrum is shown in green. The spectral distribution of the photon beam impinging on the target (black) is obtained after deconvolution of the detector response.

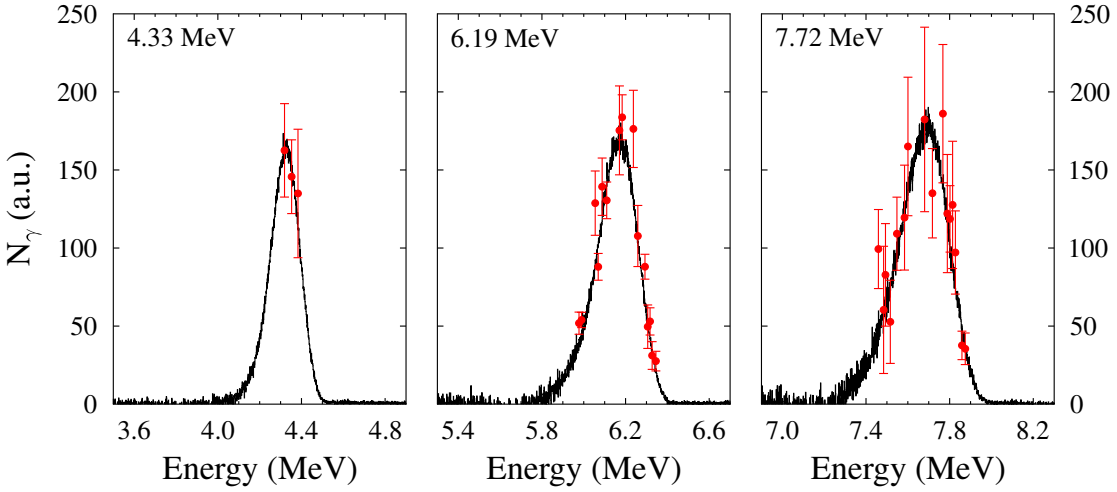

Figure 4.6: Photon beam distribution for three different beam energies (black). The absolute photon flux N_γ is determined by scaling each beam shape to the integrated cross sections of excited states in ^{128}Te (red dots), that are determined in the DHIPS experiment.

4.5 State-to-state analysis

The following Section focuses on the study of properties of individual excited states using γ-ray spectra obtained with HPGe detectors. Figure 4.7 shows a comparison of the HPGe spectrum recorded in the DHIPS measurement with $E_{e^-} = 6.0$ MeV at a polar angle of $\vartheta = 130^\circ$ (see Fig. 4.7.a)) and the spectra from the γ^3-setup at HIγS with $E_{beam} = 4.33$ MeV (see Fig. 4.7.b)-d)). The labels "vertical", "horizontal" and "backward" correspond to the position angles (ϑ,φ) of the detectors of (90°, 270°), (90°, 90°) and (135°, 225° / 315°), respectively.

One of the main differences between both measurements is the superior peak-to-background ratio in the HIγS experiment compared to the DHIPS experiment. This is mainly due to the non-resonant background radiation induced by the photon beams, which is much more pronounced in measurements with bremsstrahlung than with quasi-monochromatic photon beams. Furthermore, peaks stemming from strong transitions of ^{11}B (see Fig. 4.7.a)), that are used for the photon-flux calibration (see Section 4.4), additionally complicate the γ-ray spectrum. The photon-flux calibration, however, is crucial for the determination of integrated cross sections of single excited states in ^{128}Te. The linear polarization of the HIγS photon beam allows for the determination of spin-parity quantum numbers of isolated states.

4.5.1 Integrated cross section

The integrated cross section for individual transitions is determined from a state-to-state analysis, i.e. extracting the intensities of isolated peaks in the HPGe spectra. Usually, the DHIPS experiment with continuous-energy bremsstrahlung is used to determine integrated cross sections relative to the calibration standard ^{11}B (see, e.g. Ref. [132]). Due to the wide excitation energy range covered by the bremsstrahlung beam from a few hundreds of keV up to the endpoint energy of 6.0 MeV and 9.13 MeV (see Section 3.1.1), a large number of excited states in ^{128}Te can be investigated simultaneously. The integrated cross section for the transition sequence $0 \to x \to i$ is determined via

$$I_{0\to x\to i} = \frac{A_{0\to x\to i}}{N_T \cdot N_\gamma(E_x) \cdot \int\limits_{\Delta\Omega} \varepsilon(E_x - E_i, \Omega) \cdot W_{0\to x\to i}(\Omega)\, \mathrm{d}\Omega} \,. \tag{4.11}$$

The number of target nuclei N_T can be computed from the target mass m_T of the enriched isotope X and the corresponding molar mass M:

$$N_T = N_A \cdot \frac{m_T(X)}{M(X)} \,, \tag{4.12}$$

where the Avogadro constant is given by N_A. Usually, at least two NRF experiments at two different endpoint energies are performed at DHIPS. A comparison of the integrated cross sections determined at $E_{e^-} = 9.13$ MeV and $E_{e^-} = 6.0$ MeV allows to identify excited states that may be fed by energetically higher-lying levels (see Section 4.3). It should be noted, that the NRF measurements with the γ^3-setup also allow to extract integrated cross section of individual excited states via Eq. 4.11.

4.5.2 Spin-parity quantum number

Comparing the three spectra Fig. 4.7.b)-d) recorded in the HPGe detectors of the γ^3-setup it is possible to extract spin and parity quantum numbers of photo-excited states in ^{128}Te. Due

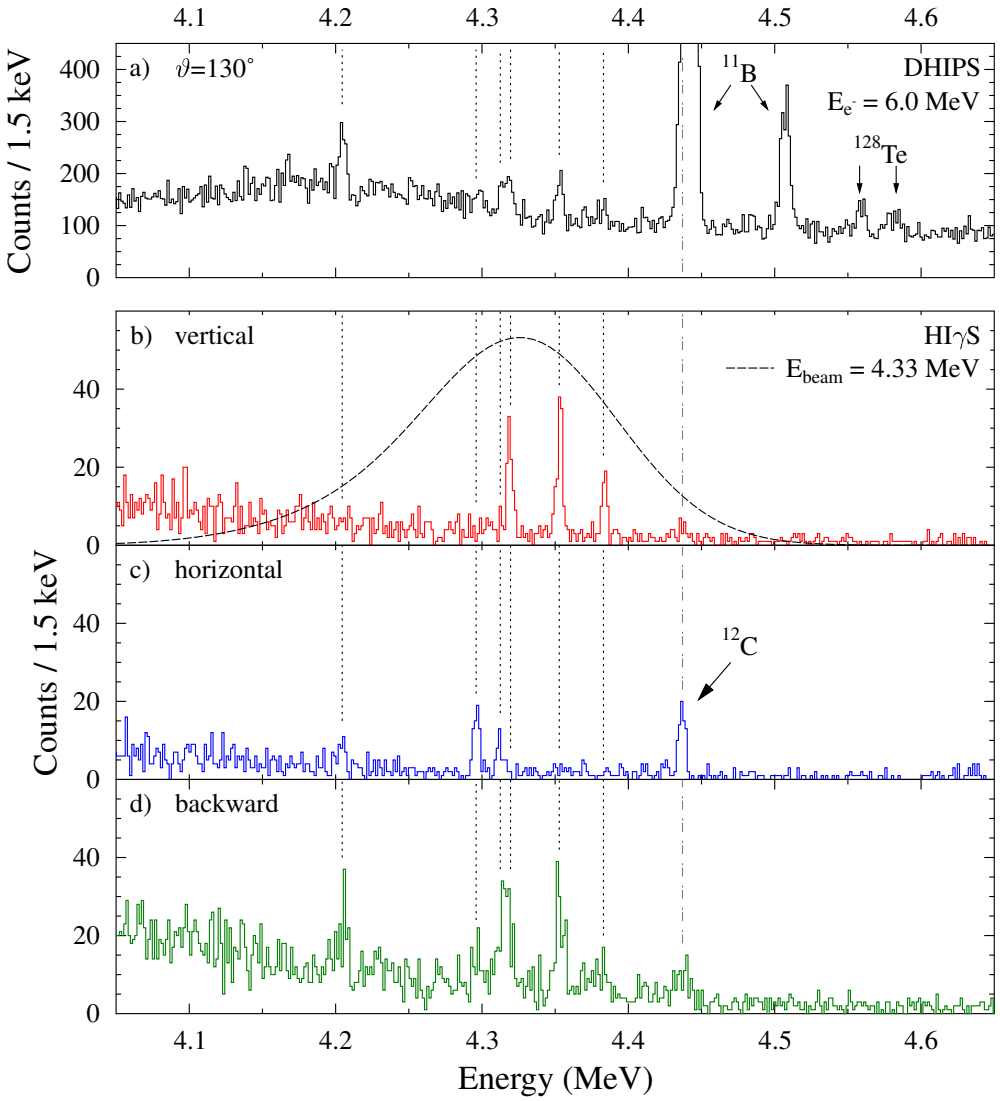

Figure 4.7: HPGe spectra of ^{128}Te in the energy range between 4.1 MeV and 4.6 MeV. a) Spectrum from the NRF experiment at DHIPS with an endpoint energy of 6.0 MeV and polar angle $\vartheta = 130°$. Spectrum measured perpendicular b) and parallel c) to the polarization plane of the photon beam at HIγS with E_γ = 6.4 MeV. The beam profile is shown in dashed lines. d) Spectrum from the backward HPGe detectors of the γ^3-setup. Vertical dotted lines indicate ground-state transitions of excited states in ^{128}Te that are observed in both experiments, while the dashed-dotted vertical line corresponds to the $0^+ \rightarrow 2^+ \rightarrow 0^+$ transition in ^{12}C at 4438 keV. The ^{128}Te transitions between 4.5 MeV and 4.6 MeV in a) are not excited in the shown HIγS experiment due to the narrow spectral distribution of the photon beam. The experiment with bremsstrahlung at DHIPS allows to deduced integrated cross sections of individual photo-excited states in ^{128}Te. Complementary, the comparison of the three spectra of the γ^3-setup provide information on the spin and parity quantum number of excited states. For more details see text in the upcoming Sections.

to the excitation via a linearly polarized photon beam the angular distribution of the emitted photons depends on the specific quantum numbers of the associated nuclear levels (see Section 2.2.3). Two asymmetries Σ_v and Σ_h are extracted to assign spin-parity quantum numbers

J^π to individual excited states

$$\Sigma_v = \frac{A_v - A_b}{A_v + A_b} \,, \tag{4.13}$$

$$\Sigma_h = \frac{A_h - A_b}{A_h + A_b} \,, \tag{4.14}$$

where A_v, A_h and A_b are the peak areas observed in the vertical, horizontal and backward detectors. Figure 4.8.a) and b) show experimental results from measurements between 4.0 MeV and 4.4 MeV for both asymmetries. The dashed lines indicate the expectation values for spin-parity quantum numbers of 1^- (red), 1^+ (green) and 2^+ (blue) of the excited state. The information of both quantities are combined in the correlation plot shown in Fig. 4.8.c). The circled crosses indicate the expectation values for the different spin-parity quantum numbers. A clear separation between $J^\pi = 1^-$ (red dots) states to $J^\pi = 1^+, 2^+$ (green triangles, blue squares) is achieved. Even though the expectation values for $J^\pi = 1^+$ and $J^\pi = 2^+$ are located closer to each other than to $J^\pi = 1^-$ it is still possible to distinguish between both spin-parity quantum numbers. In the given example, one excited state cannot be assigned a definite spin-parity quantum number (black star). In addition, the ground-state transition from the first excited 2^+_1 state at 4438 keV in ^{12}C is observed (yellow diamond) and serves as a test case for this method. This transition is present due to the target container that is made of polyethylen.

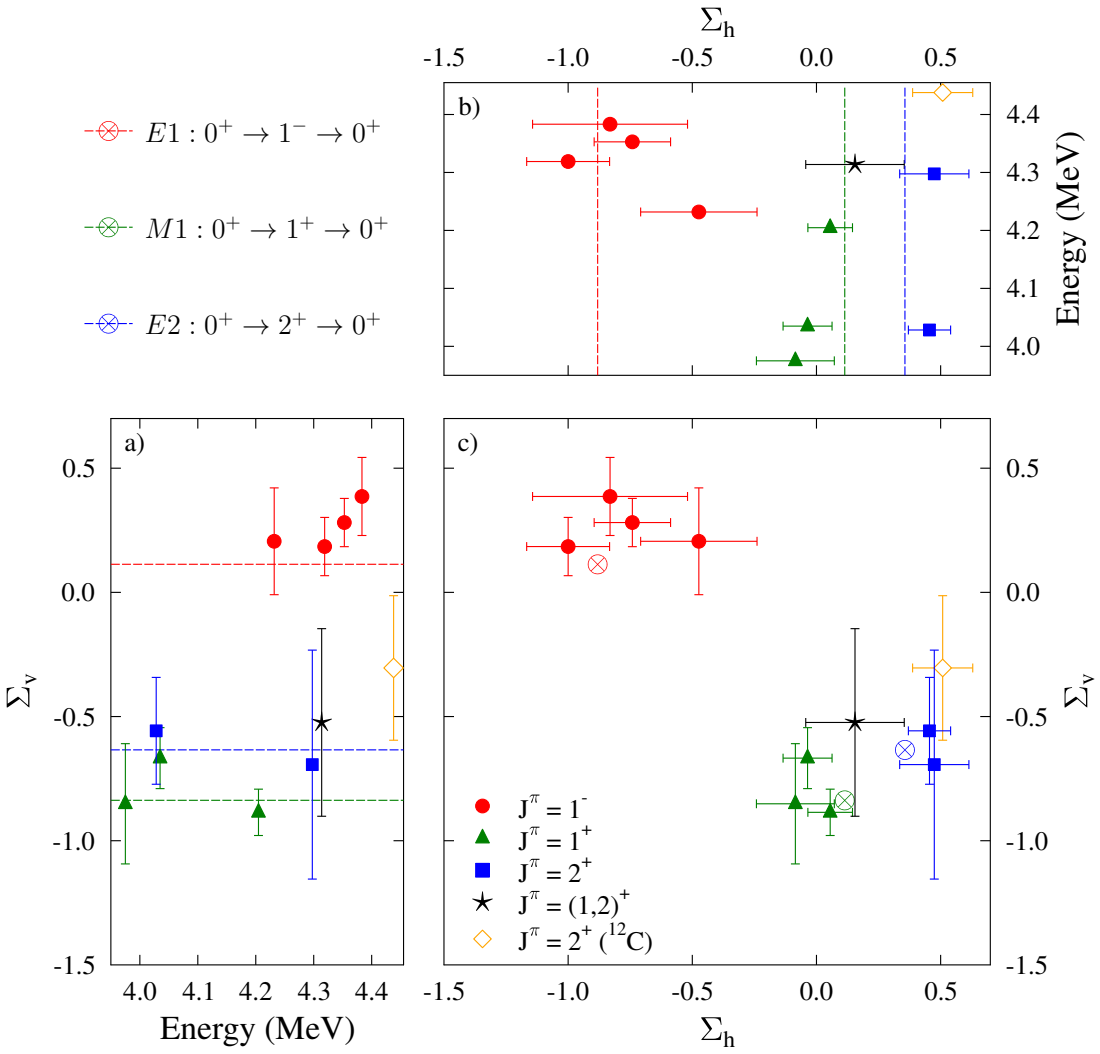

Figure 4.8: Asymmetries Σ_v (a) and Σ_h (b) determined in the HIγS measurements for excited states in the energy range from 4.0 MeV to 4.4 MeV. The correlation of both asymmetries (c) allows for spin-parity assignments. For details see text.

4.6 Average quantities

4.6.1 Photoabsorption cross section

In the end of Section 1.2, a method to study photoabsorption cross sections ($\sigma_\gamma = \sigma_{\gamma\gamma} + \sigma_{\gamma\gamma'}$) with quasi-monochromatic photon beams was introduced. A schematic illustration of the idea to determine also the inelastic contribution $\sigma_{\gamma\gamma'}$, firstly proposed in Ref. [71], is shown in Fig. 4.9. Nuclear levels in a narrow energy window are excited by the photon beam at HIγS (grey-filled gaussian). The full intensity measured for ground-state transitions of the excited states can be related to the elastic cross section (see Fig. 4.9.a)). Direct transitions to intermediate levels (dashed arrows in Fig. 4.9.b)) are usually too weak to be observed in single γ-ray spectroscopy measurements. However, it is generally assumed that most of the cascading transitions decay via the first excited 2^+ states. The intensity measured in these states (solid arrow in Fig. 4.9.b)), therefore, enables an approximation of the inelastic cross section.

Elastic cross section

Instead of analyzing isolated peaks, it is possible to extract average cross sections for the energy range covered by the quasi-monochromatic photon beam at HIγS. Figure 4.10 shows spectra of ^{128}Te recorded with an HPGe detector (upper panel) and a LaBr scintillator (lower panel) with $E_{beam} = 6.4$ MeV. The spectral distribution of the beam is indicated by the dotted line. Both panels show the measured spectrum (black) and the deconvoluted spectrum (red) with its 1σ error band (grey). After the deconvolution only full-energy events are present in the spectra. The

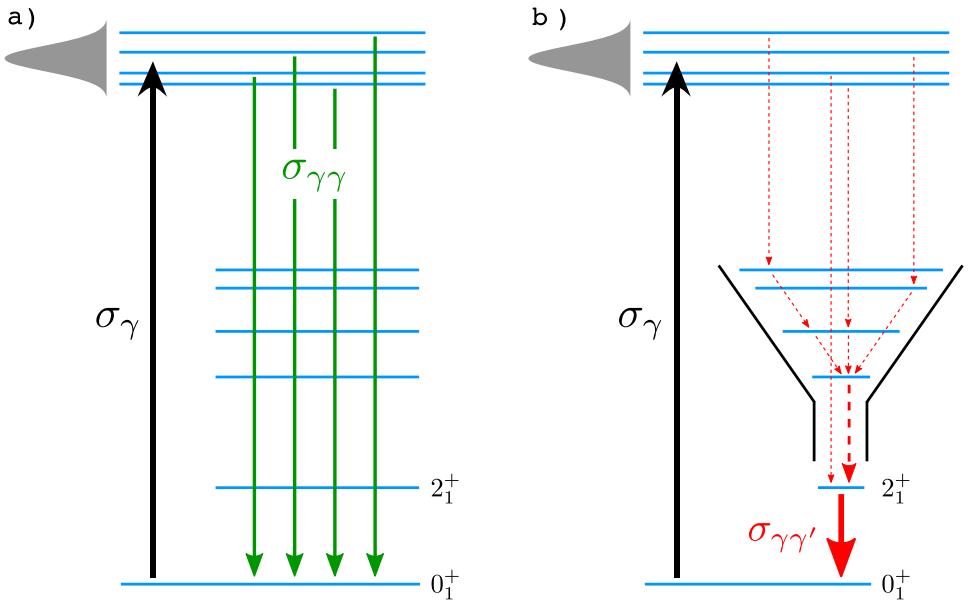

Figure 4.9: Extraction of photoabsorption cross sections using quasi-monochromatic photon beams. a) The ground-state transition intensity observed for a given excitation energy region is connected to the elastic cross section $\sigma_{\gamma\gamma}$. b) The intensity from cascading events are assumed to be collected in the first excited 2^+ states and, hence, can be used to estimate the inelastic cross section $\sigma_{\gamma\gamma'}$ for a given energy region. The photoabsorption cross section σ_γ is defined as the sum of both contributions.

upper panel illustrates, that the observed intensity in the energy region of the beam is located in resolved peaks as well as in the continuum below those peaks. This continuum, often referred to as "unresolved" strength, is the accumulated dipole strength from hundreds to thousands of weakly-excited states, while only a few strong dipole transitions are observed as isolated peaks. Since the nuclear level density increases exponentially with the excitation energy (see, e.g. Section 2.1.19 the amount of strength that is "hidden" in the continuum strongly increases compared to the strength located in peaks. Hence, average cross sections are determined to account for the total dipole strength in a given energy region. Following the definition from Eq. (2.27) and Eq. (4.11), the elastic cross section can be expressed as

$$\sigma_{\gamma\gamma} = \frac{\sum_x I_{0\to x\to 0}}{\Delta E} = \frac{1}{N_T N_\gamma^{tot}} \cdot \sum_x \frac{A_{0\to x\to 0}}{\int\limits_{\Delta\Omega} \varepsilon(E_x) W_{0\to x\to 0}\, \mathrm{d}\Omega} \,, \tag{4.15}$$

with $N_\gamma^{tot} = \int\limits_0^\infty N_\gamma(E)\,\mathrm{d}E$ being the integrated total photon flux. Here, the sum runs over all excited states x in the covered energy region. This means, the full intensity within the excitation energy range is integrated whether it is located in the continuum or in peaks.

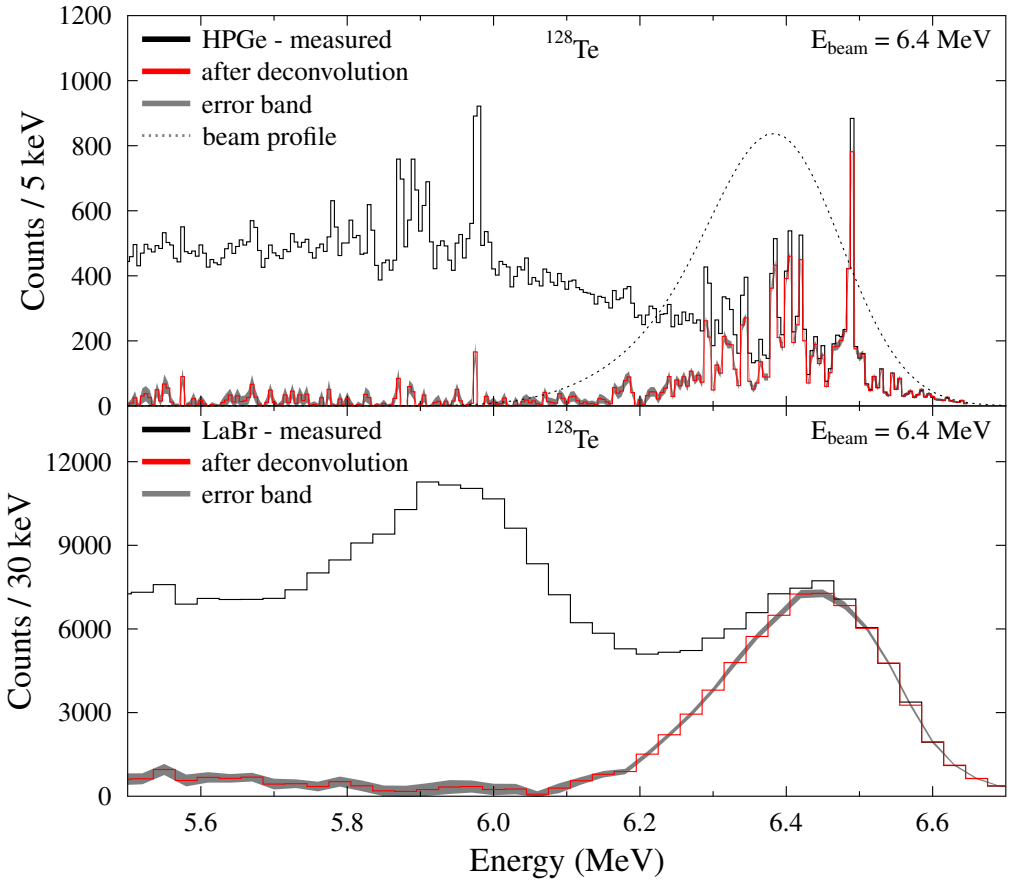

Figure 4.10: HPGe (upper panel) and LaBr (lower panel) spectra from single γ-ray spectroscopy with beam energy of $E_{beam} = 6.4$ MeV (black). Spectrum after deconvolution of detector response (red). Beam profile of impinging photon beam is shown in dotted lines.

Inelastic cross section

The probability for transitions to lower-lying levels rather than the ground state is described by the inelastic cross section defined in an analogous way as in Eq. (4.15)

$$\sigma_{\gamma\gamma'} = \frac{\sum_x \sum_{i\neq 0} I_{0\to x\to i}}{\Delta E} = \frac{1}{N_T N_\gamma^{tot}} \cdot \sum_x \sum_{i\neq 0} \frac{A_{0\to x\to i}}{\int\limits_{\Delta\Omega} \varepsilon(E_x - E_i) W_{0\to x\to i}\, \mathrm{d}\Omega} \,. \tag{4.16}$$

The investigation of the low-energy part of the HPGe spectra obtained at HIγS for the energy setting of $E_{beam} = 6.4$ MeV reveals transitions of the first excited states in ^{128}Te (see Fig. 4.11). The ground-state transition of the 2_1^+ state is clearly observed at 743 keV as well as the transitions $4_1^+ \to 2_1^+$ and $2_2^+ \to 2_1^+$. As illustrated in Fig. 4.9, their transition intensities can be used to determine the inelastic cross section

$$\sigma_{\gamma\gamma'} \approx \frac{1}{N_T N_\gamma^{tot}} \cdot \sum_j \frac{A_{2_j^+\to 0_1^+}}{\int\limits_{\Delta\Omega} \varepsilon(E_{2_j^+}) W_{2_j^+\to 0_1^+}\, \mathrm{d}\Omega} \,. \tag{4.17}$$

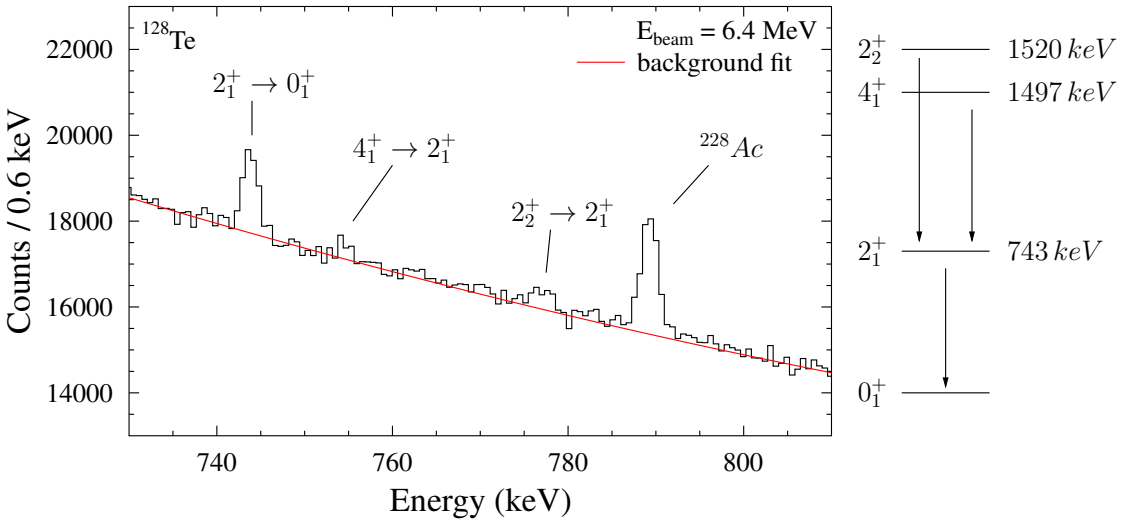

Figure 4.11: The low-energy part of the γ-ray spectrum recorded with HPGe detectors in the measurement on ^{128}Te with $E_{beam} = 6.4$ MeV. Decays of the first excited states in ^{128}Te are observed. These levels are populated in cascade transitions by states excited in the energy region of the incoming photon beam. The transition intensity of the 2_1^+ state is used as an approximation of the inelastic cross section $\sigma_{\gamma\gamma'}$.

4.6.2 Branching ratio

In the preceding Section, an experimental approach for the determination of the photoabsorption cross section (σ_γ) via the elastic ($\sigma_{\gamma\gamma}$) and the inelastic ($\sigma_{\gamma\gamma'}$) cross section was introduced.

An alternative expression of σ_γ can be achieved by substituting the integrated cross section in Eq. (2.27) by Eq. (2.20)

$$\sigma_\gamma = \frac{\sum_x I_{0\to x}}{\Delta E} = (\pi\hbar c)^2 \cdot \frac{g}{E_x^2} \cdot \frac{\sum_x \Gamma_{0,x}}{\Delta E} \,, \tag{4.18}$$

where the sum runs over all ground-state transition widths $\Gamma_{0,x}$ of excited states x in the energy bin ΔE. In a similar way the $\sigma_{\gamma\gamma}$ can be expressed as

$$\sigma_{\gamma\gamma} = \frac{\sum_x I_{0\to x}}{\Delta E} = (\pi\hbar c)^2 \cdot \frac{g}{E_x^2} \cdot \frac{\sum_x \Gamma_{0,x}^2/\Gamma_x}{\Delta E} \,, \tag{4.19}$$

with Γ_x being the total transition width of the state x. An average ground-state branching ratio can be computed from the ratio of Eqs. (4.18) and (4.19)

$$\langle b_0 \rangle = \frac{\sigma_{\gamma\gamma}}{\sigma_\gamma} = \frac{\sum_x \Gamma_{0,x}^2/\Gamma_x}{\sum_x \Gamma_{0,x}} = \frac{\sum_x \Gamma_{0,x} \cdot b_{0,x}}{\sum_x \Gamma_{0,x}} \,. \tag{4.20}$$

Note, that $\langle b_0 \rangle$ is defined as the strength-weighted average of the ground-state branching ratios $b_{0,x} = \Gamma_{0,x}/\Gamma_x$ of all individual excited states x in the energy bin ΔE.

In the same fashion, branching ratios to other excited states can be determined. In Section 5.3.1.3, branching ratios to the first excited 2_1^+ state in ^{128}Te will be extracted from the γ-γ coincidence measurements. Their definition differs slightly from Eq. (4.20) since the average transition intensity to the 2_1^+ state is measured relative to the ground-state transition intensity

$$\langle b_{2^+} \rangle = \frac{\sum_x \Gamma_{0,x} \cdot \Gamma_{2^+,x}/\Gamma_x}{\sum_x \Gamma_{0,x}^2/\Gamma_x} \,, \tag{4.21}$$

where $\Gamma_{2^+,x}$ corresponds to the transition width from the excited state x to the 2_1^+ state.

4.7 Population of low-lying 2^+ states

Figure 4.12 provides the sum spectrum of all HPGe detectors for ^{128}Te obtained from the measurement at a beam energy of $E_{beam} = 8.28$ MeV. Peaks originating from transitions of low-lying excited states in ^{128}Te are apparent. As discussed before, these states cannot be excited directly by the impinging photon beam due to the narrow energy width of its spectral distribution. In Section 4.6.1, a method was introduced to use the intensities collected in the first 2^+ states to estimate the inelastic cross section. In this part, the population of the individual excited 2^+ states is analyzed as a function of their level energy $E_x(2_i^+)$. Figure 4.13.a) illustrates exemplarily the population intensities of each observed 2_i^+ state relative to the total intensity in the 2_1^+ state for $E_{beam} = 8.28$ MeV. The data points follow an exponential function $C \cdot \exp[-\lambda \cdot E_x(2_i^+)]$. For each energy setting, the parameters of this function are determined. The experimental results and the associated exponential function for three measurements are shown in Fig. 4.13.b). In particular, the fit parameter λ provides additional information on the underlying photon strength function for ^{128}Te. This will be discussed in Section 5.2.4.

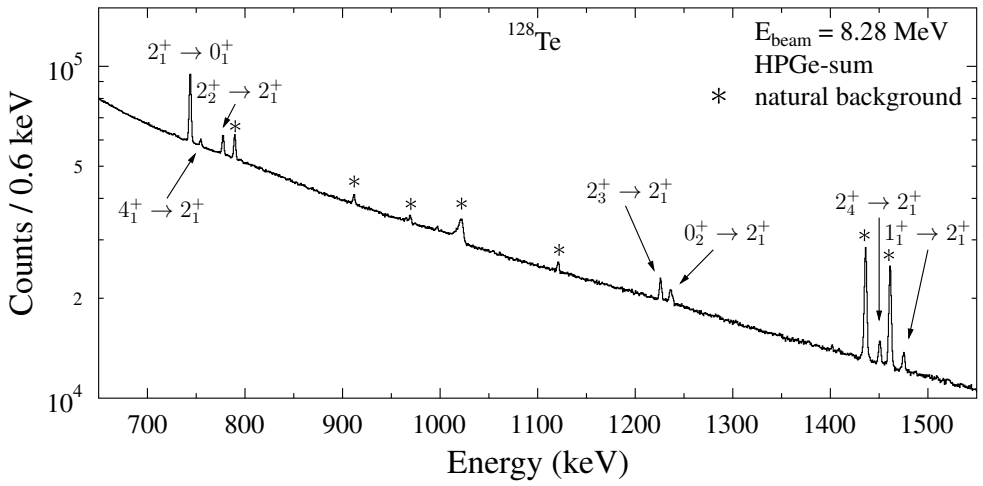

Figure 4.12: Sum spectrum of all HPGe detectors in the $E_{beam} = 8.28$ MeV measurement with ^{128}Te. Transitions of low-lying states, in particular 2^+ states are observed. Peaks stemming from natural background radiation or intrinsic radioactivity of the LaBr material are marked with asterisks. Detailed information on the various lines from background radiation can be found in Fig. 3.9.

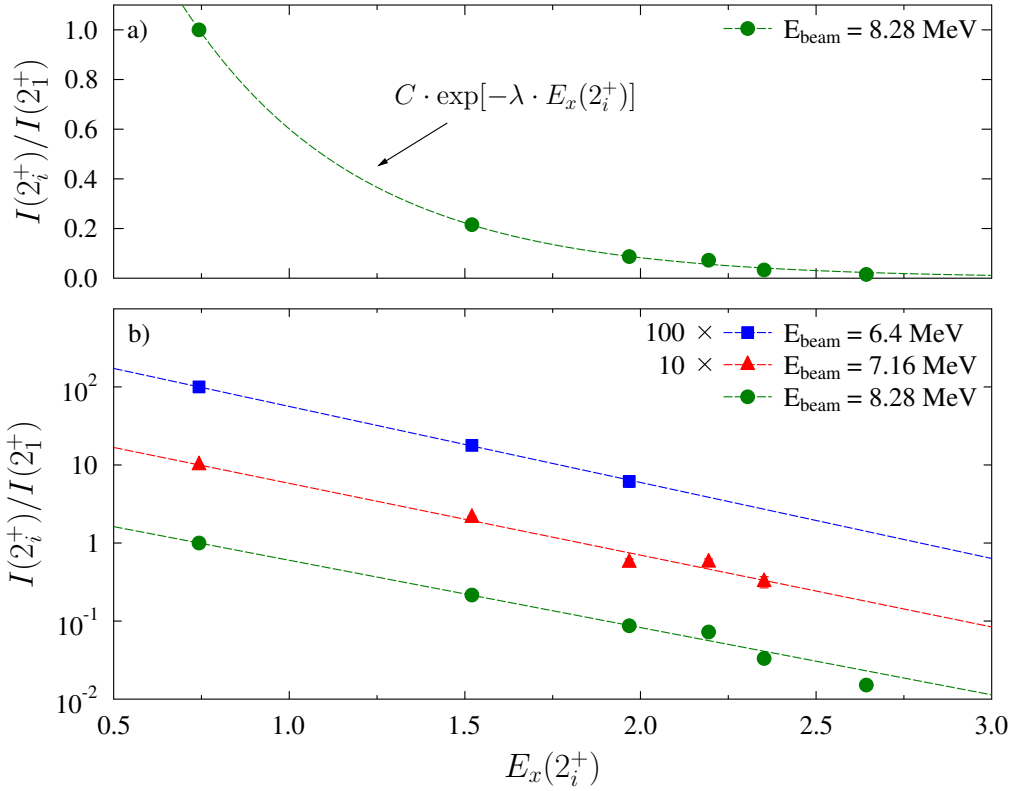

Figure 4.13: Relative population of low-lying 2^+ states. a) Linear scale of $I(2_i^+)/I(2_1^+)$ for a beam energy setting of $E_{beam} = 8.28$ MeV. The experimental data points follow an exponential as a function of the level energy $E_x(2_i^+)$. b) Comparison between different beam energies. For a better overview, the data points for $E_{beam} = 6.4$ MeV and $E_{beam} = 7.16$ MeV are scaled by 100 and 10, respectively.

4.8 γ-γ coincidence method

Until now, data from single γ-ray spectroscopy were discussed and analyzed. However, the main reason to use the γ^3-setup for NRF experiments at HIγS is its capibility of performing γ-γ coincidence measurements. In this Section, the different steps in the corresponding data analysis are presented.

4.8.1 Detector timing

The list mode data obtained from the MBS contains information on the energies, detector times and trigger conditions for each recorded event. For the decision if two photons were observed in coincidence one needs to analyze the relative time between the two signals generated in two detectors. Figure 4.14 shows time difference spectra of the recorded signals between two detectors in the measurement with E_{beam}= 8.0 MeV. The time-difference spectrum between two LaBr detectors, namely LaBr-3 and LaBr-4 are shown in Fig. 4.14.a). For the black spectrum no further conditions are applied, while an energy cut on the ground-state transition of the 2_1^+ state in LaBr-3 is performed for the red spectrum. A prominent peak is observed around Δt=0 ns and corresponds to coincident events registered in both detectors. The inset presents the time spectrum on a logarithmic scale. On the left-hand side as well as on the right-hand side additional peaks can be seen. The time difference between two succeeding peaks is about 180 ns. Every 180 ns a photon burst is generated in the FEL of the storage ring and impinges on the target within the γ^3-setup. These additional peaks originate from random coincidences of events generated by photon bursts before and after the actual photon beam bunch, respectively. Hence, proper coincidences are obtained by selecting the dominant peak in the region of dotted lines in Fig. 4.14.a). The cut on $E(2_1^+)$ prepares a narrow coincidence peak at Δt=0 ns, which includes all events measured in coincidence to it.

The time-difference spectrum for LaBr-3 and HPGe-2 is shown in Fig. 4.14.b). The coincidence peak is not as well-shaped as in the case for two LaBr detectors. The rise time of energy signals from HPGe detectors depend on the position in the crystal where the corresponding photon energy is deposited. In particular, for low γ-ray energies the signals show a comparatively large jitter. This leads to walk effects within the constant fraction discriminators (CFD), which are used to define the time of a given signal. Consequently, the time-difference spectrum between two HPGe detectors exhibits a much broader distribution, which is shown in Fig. 4.14.c) for HPGe-2 and HPGe-1. Note the difference in the total number of events for the three spectra, which is caused by the different detection efficiencies of both detector types.

4.8.2 Coincidence measurement

The summed LaBr-LaBr coincidence matrix from the measurement with $E_{beam} = 8.0$ MeV is shown in Fig. 4.15 with conditions set on the associated coincidence peak of the time-difference spectrum discussed in the previous Section. The energy thresholds of 600 keV and 1600 keV for the low and high threshold, respectively, are visible. Since the energy of the incoming photon beam is quasi-monochromatic, the summed energy measured in two detectors is limited to this value. Hence, a triangular shape is apparent in the coincidence matrix. Several prominent lines are observed that highlight an enhanced probability for coincident events with the corresponding γ-ray energy.

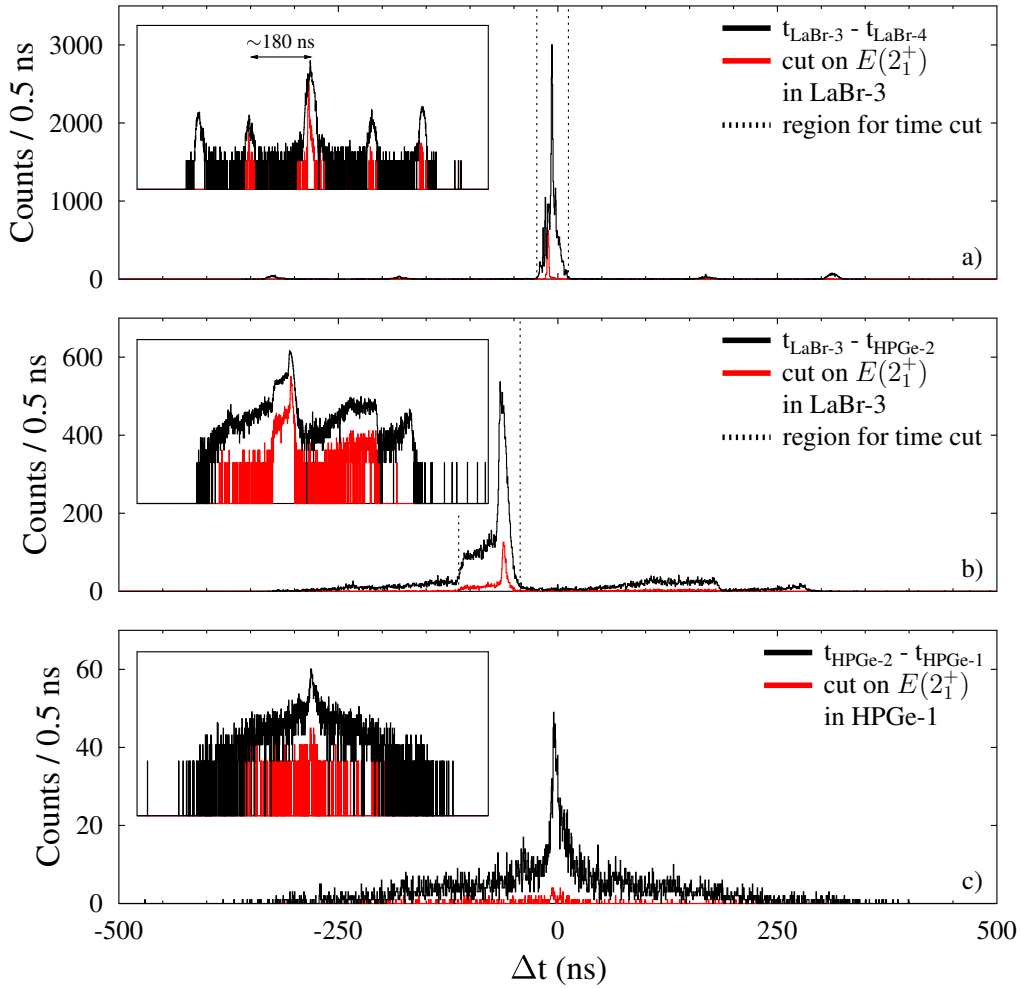

Figure 4.14: Time-difference spectra from the measurement with energy setting $E_{beam} = 8.0$ MeV. a) Between LaBr-3 and LaBr-4 without any condition (black) and with cut on the transition energy $E(2_1^+)$ of the first excited 2_1^+ state in LaBr-3 (red). The dominant peak around $\Delta t = 0$ corresponds to true coincident events between the two detectors. Inset: Logarithmic scale. The two peaks to each side of the dominant peak emerge from coincidences to preceding and subsequent beam pulses, respectively. b) Time difference between LaBr-3 and HPGe-2. c) Time-difference spectrum between HPGe-2 and HPGe-1.

A matrix for HPGe-LaBr coincidences is shown in Fig. 4.16. The coincidence lines are less pronounced due to the low detection efficiencies of the HPGe detectors. Furthermore, the energy resolution of the HPGe is reflected by the thickness of the associated lines.

4.8.3 Projected spectra

The projections of both matrices on their y-axis are shown for the energy region from 0.6 MeV to 1.6 MeV in Fig. 4.17.a) for the LaBr-LaBr matrix and in Fig. 4.17.b) for the HPGe-LaBr matrix. Transitions from low-lying excited states, in particular 2^+ states are present in both spectra. Requiring the condition that one of the LaBr detectors has to have observed a γ-ray with $E_{LaBr} > 2$ MeV (red) the peak-to-background ratio increases. The main difference is given

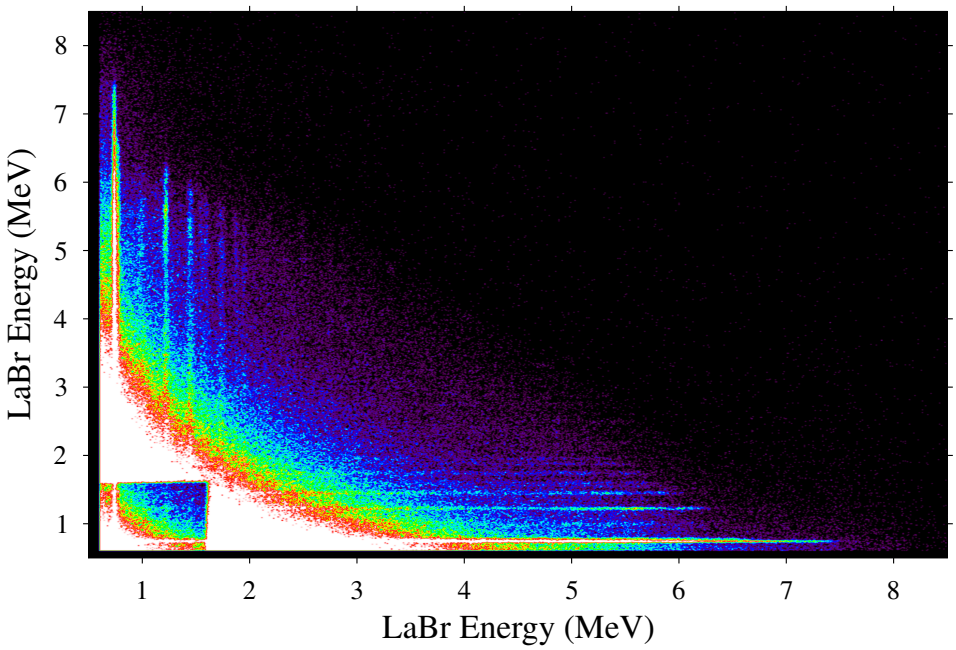

Figure 4.15: Coincidence matrix from the $E_{beam} = 8.0$ MeV measurement. Summed matrix for all combinations of coincidences between two LaBr detectors.

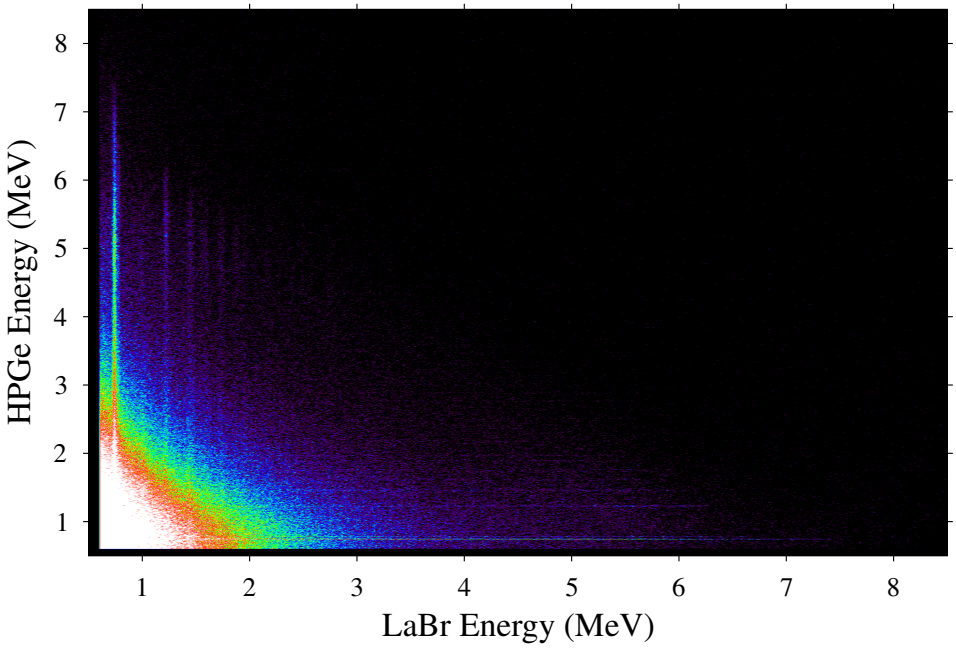

Figure 4.16: HPGe-LaBr coincidence matrix from the $E_{beam} = 8.0$ MeV measurement.

by the different energy resolution and photopeak-detection efficiency in both detector types. The γ-ray energies emitted in the transitions $2_2^+ \rightarrow 2_1^+$ and $2_1^+ \rightarrow 0_1^+$ can be separated in the HPGe spectrum, while they can hardly be resolved in the LaBr spectrum.

Figure 4.18 shows a comparison of the summed Singles LaBr spectrum (grey) with coincidence spectra extracted from setting cuts on different energy regions. After the energy cut on the ground-state transition of the 2_1^+ state the maximum of the resulting coincidence spectrum

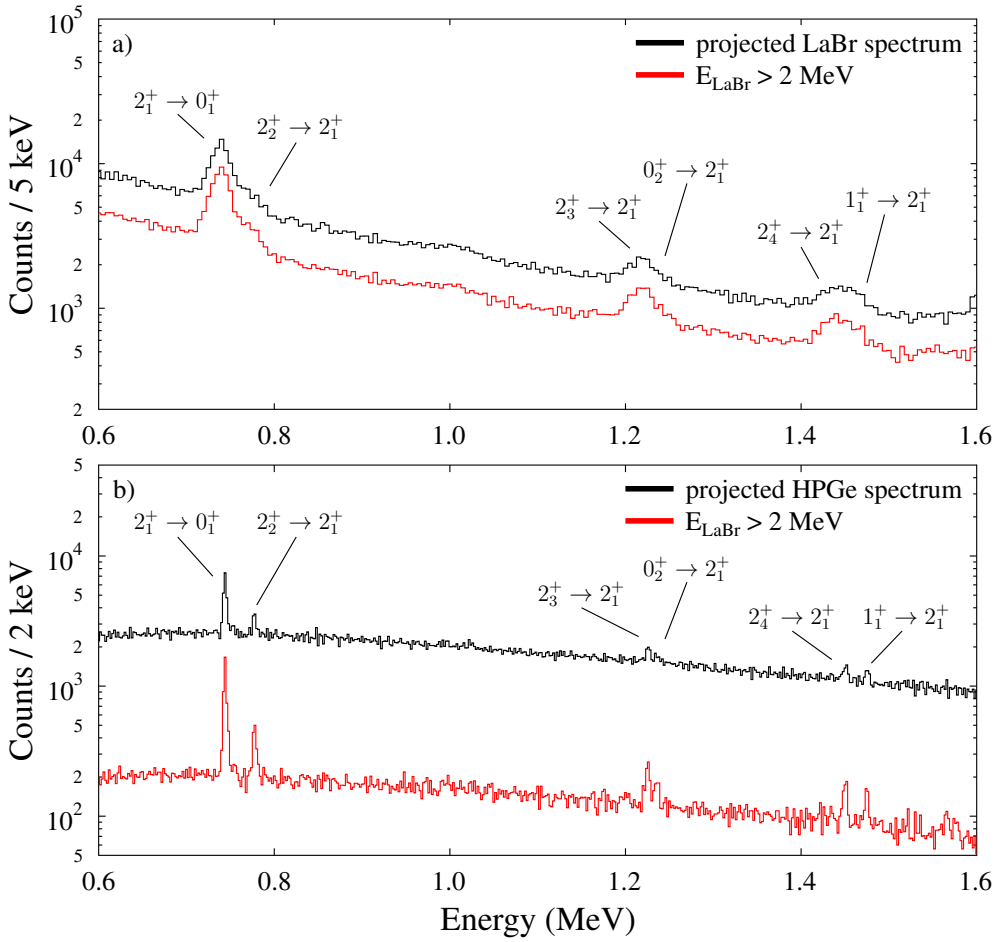

Figure 4.17: Projection of the coincidence matrices from Figs. 4.15 and 4.16. a) Low-energy region of the projection from LaBr-LaBr coincidences (black). The peak-to-background ratio clearly improves requiring one of the LaBr to have measured a photon with $E_{LaBr} > 2$ MeV. b) Projection on the HPGe axis from the HPGe-LaBr coincidence matrix. Transitions from several low-lying excited states are observed.

(red) is around E_{beam}-$E(2_1^+)$. Due to the quasi-monochromacy of the impinging photon beam the total energy measured in all detectors is limited to E_{beam}. This spectrum contains all events that were observed in coincidence to the energy cut (red shaded area in the inset), i.e. "true" coincidences to the decay of the 2_1^+ and random coincidences to the background radiation at this energy. Due to the energy resolution of the LaBr detectors it is not possible to set separate energy cuts on the decays of the 2_3^+ and 0_2^+ state (green shaded area). The same applies for the 2_4^+ and 1_1^+ states (blue shaded area). Cuts on the summed peaks generate the corresponding summed coincidence spectra (green and blue). Similar to the previous case, the maximum measured γ-ray energies are around E_{beam}-$E(2_3^+)$ and E_{beam}-$E(2_4^+)$, respectively. The events located in this energy region correspond to direct transitions from excited states at E_{beam} to the associated lower-lying excited states. In analogy to the Singles LaBr spectrum the complete detector response of the emitted photons are apparent in the coincidence spectra. To extract the full-energy events a detector response deconvolution has to be performed (see Section 4.1). For the estimation of the background originating from random coincidences a cut is applied slightly above the region of, e.g., the decay of the 2_1^+ state (see Fig. 4.19). The corresponding spectrum

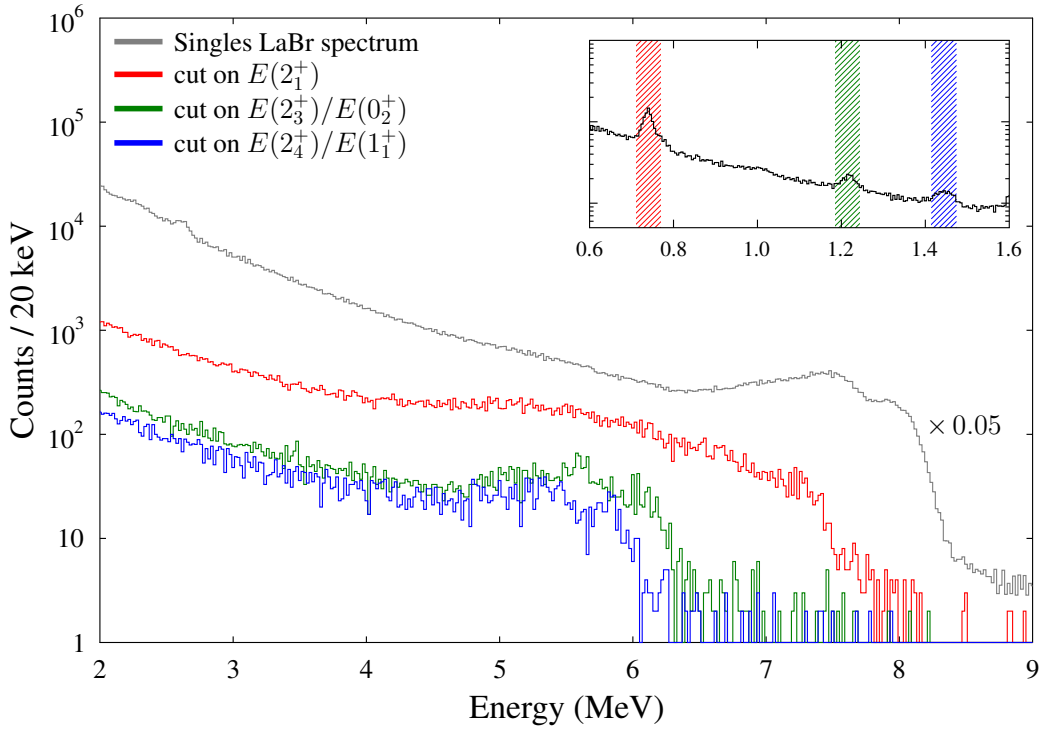

Figure 4.18: Projection on the LaBr energy of the LaBr-LaBr coincidence matrix in Fig. 4.15. The summed singles LaBr spectrum (grey) is scaled by a factor of 0.05 for comparison. The inset provides the regions for the different energy cuts resulting in the spectra with the same color code. For details see text.

(orange) shows a smooth energy behavior. At excitation energies around 5 MeV to 8 MeV, the amount of events from random coincidences are about an order of magnitude lower than the events from the "true" coincidences. For a proper analysis the coincidence spectrum has to be corrected for these events.

Two examples for the cut on $E(2_1^+)$ are shown in Fig. 4.20, namely for the energy settings $E_{beam} = 6.19$ MeV (upper panel) and $E_{beam} = 8.0$ MeV (lower panel). About 743 keV below the beam profile (dashed grey line) the full-energy peak from direct transitions to the 2_1^+ state is present. In addition, the single-escape and double-escape peak, respectively, are observed as well. After the deconvolution procedure, the full-energy events (red) are extracted from the spectra. The relative errors after deconvolution (grey band) range from $\sim$ 10 % in the full-energy region up to $>$ 20 % in the region below. For $E_{beam} = 6.19$ MeV, the spectrum below these events is composed of the atomic background induced by the photon beam. This is different for the $E_{beam} = 8.0$ MeV measurement. In addition to the atomic background, it contains photons from transitions to low-lying states other than the 2_1^+, such as the 2_2^+ and 2_3^+ states. The direct population of these levels is observed as well since they decay predominantly via the 2_1^+ state and, hence, are measured in coincidence to its ground-state transition. The beam profile is shifted by the corresponding level energies (blue dashed line) to indicate their expected position in the spectrum.

The cross section for the direct population of a low-lying excited state i extracted from a coincidence measurement is defined in a similar fashion to Eq. (4.15)

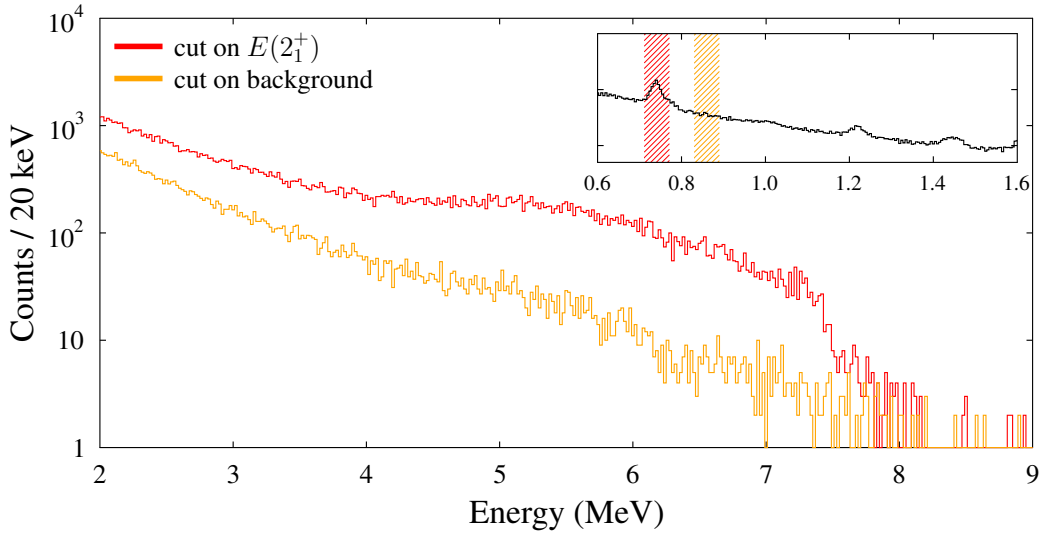

Figure 4.19: Determination of random coincidences. For the case of the decay of the 2_1^+ state an energy cut directly above this energy is used to estimate background from random coincidences (orange).

$$\sigma_{0\to x\to i} = \frac{1}{N_T N_\gamma^{tot}} \cdot \sum_x \frac{A_{0\to x\to i}^{coinc}}{\int\limits_{\Delta\Omega_1\Delta\Omega_2} \varepsilon_1(E_x - E_i)\cdot\varepsilon_2(E_i - E_j)\cdot W_{corr}\,\mathrm{d}\Omega_1\mathrm{d}\Omega_2}$$
$$= \frac{1}{N_T N_\gamma^{tot}} \cdot \frac{A_{sum}^{coinc}}{\int\limits_{\Delta\Omega_1\Delta\Omega_2} \varepsilon_1(E_{\gamma_1})\cdot\varepsilon_2(E_{\gamma_2})\cdot W_{corr}\,\mathrm{d}\Omega_1\mathrm{d}\Omega_2}\,, \tag{4.22}$$

where N_T and N_γ^{tot} are the total number of target nuclei and the integrated photon flux, respectively. The full-energy peak area $A_{0\to x\to i}^{coinc}$ and A_{sum}^{coinc}, respectively, are extracted from the projected coincidence spectrum after detector response deconvolution. Furthermore, the quantities $\varepsilon_1(E_x - E_i)$ and $\varepsilon_2(E_i - E_j)$ are the efficiencies for detecting the γ-rays emitted in the transitions $x \to i$ and $i \to j$, respectively. The angular correlation function W_{corr} between the two successively emitted photons is given by Eq. (2.41).

4.8.4 Distinction between $E1$, $M1$ and $E2$ transitions

Excitations via real photons induce dipole and quadrupole transitions populating $J^\pi = 1^-, 1^+$ and 2^+ states in even-even nuclei, such as ^{128}Te. In the analysis of the LaBr-LaBr coincidences in the preceding Section it is not specified which set of excited states contribute to the total population intensity of, e.g., the first excited 2_1^+ level. A separation of their relative contribution, however, is crucial to study the decay behavior of 1^- states in the PDR region in greater detail.

For ground-state transitions, a method to assign spin-parity quantum numbers for isolated excited states in single γ-ray spectroscopy was introduced in Section 4.5.2. For primary transitions to lower-lying states determined from the analysis of γ-γ coincidence data an equivalent approach is applied, which will be introduced in the following.

As discussed in Section 2.2.3 for the correlation between two successively emitted photons γ_1 and γ_2, the directional distribution function of γ_1 depends on the observation direction of

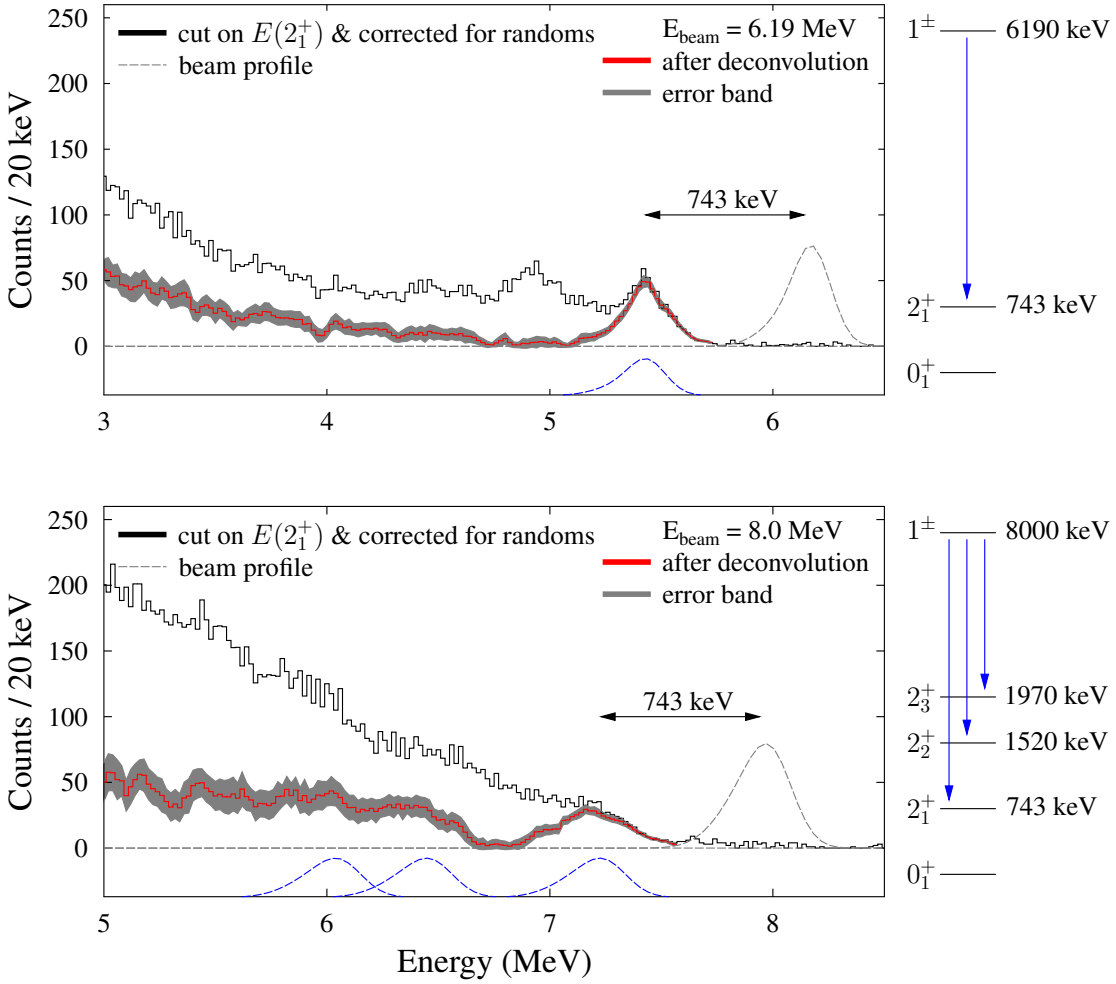

Figure 4.20: Upper panel: Spectrum from LaBr-LaBr coincidences corrected for random coincidences from the measurement with $E_{beam} = 6.19$ MeV (black). The beam profile is indicated by the dashed grey line. A deconvolution of the detector response reveals the intensity at around 5.5 MeV from primary transitions to the 2_1^+ after photo-excitation (red). The beam profile is shifted by the energy of the 2_1^+ state (blue dashed curve) to illustrate the expected position of the full-energy events. The grey band corresponds to the uncertainty within the 1σ region of the deconvolution procedure. Lower panel: Measurement with $E_{beam} = 8.0$ MeV. After the detector response deconvolution intensity is observed at E_{beam}-$E(2_1^+)$ corresponding to the direct decay to the 2_1^+ state. Furthermore, the direct population of the additional low-lying levels, such as the 2_2^+ and 2_3^+ state can be identified. The corresponding transition energy are indicated by energy-shifted beam profiles (blue dashed curve).

γ_2 (see Figs. 2.6 and 2.7). The general formalism of angular correlation functions in Eq. (2.41) was implemented into the technical computing program `Mathematica` [177]. In that way, analytical expressions for distinct cases mandatory for the analysis of the current coincidence measurements were derived. However, in these angular distributions the finite size of the target

I	II	III	IV	V	VI	VII
L3-L1	L1-L2	L4-L1	L1-L4	L3-L4	L4-L3	L1-L3
L3-L2	L2-L1	L4-L2	L2-L4	—	—	L2-L3

Table 4.2: Twelve LaBr-LaBr combinations are grouped into seven detector groups labeled by roman numbers according to their angular correlation functions.

and the detectors in real experiments are not taken into account. Hence, the directional distribution functions for the spin sequences given above were implemented into GEANT4 simulations of the γ^3-setup. In the following, γ-γ coincidences measured with the LaBr detectors will be exploited. The four LaBr scintillators are placed at different polar and azimuthal angles (ϑ, φ):

- LaBr1: $(135^\circ, 135^\circ)$,
- LaBr2: $(135^\circ, 45^\circ)$,
- LaBr3: $(90^\circ, 0^\circ)$,
- LaBr4: $(90^\circ, 90^\circ)$.

Using all LaBr scintillators, in total, twelve combinations LaBrX-LaBrY for coincidence measurements can be produced. Here, the photons γ_1 and γ_2 are observed in LaBrX and LaBrY, respectively. Some of the combinations can be grouped together, since the resulting angular correlations for the given setup geometry are the same. In total, seven detector groups can be defined and are tabulated in Table 4.2. The γ-cascades considered in the following part of the data analysis are

- $0^+ \xrightarrow{\vec{\gamma}_0} 1^- \xrightarrow{\gamma_1} 2^+ \xrightarrow{\gamma_2} 0^+$,
- $0^+ \xrightarrow{\vec{\gamma}_0} 1^+ \xrightarrow{\gamma_1} 2^+ \xrightarrow{\gamma_2} 0^+$,
- $0^+ \xrightarrow{\vec{\gamma}_0} 2^+ \xrightarrow{\gamma_1} 2^+ \xrightarrow{\gamma_2} 0^+$.

For each group, GEANT4 simulations were conducted. The close setup geometry and the rather pronounced angular distributions for the transition sequences have an impact on the effectively measured angular correlation W_{corr} as well as on the attributed photopeak efficiency ε. Thus, the product $\varepsilon \cdot W_{corr}$ integrated over the solid angle $\Delta\Omega$ of each detector is a suited quantity to compare with experimental values:

$$\langle \varepsilon \cdot W_{corr} \rangle = \int_{\Delta\Omega} \varepsilon(\Omega, E_\gamma) \cdot W_{corr}(\Omega)\, \mathrm{d}\Omega \,. \tag{4.23}$$

Figure 4.21 shows the simulated $\langle \varepsilon \cdot W_{corr} \rangle$ values for all detector groups and the spin sequences of interest. The lines connecting the data points are shown to guide the eye. The values for each spin sequence exhibit a different behavior as a function of the detector group. Hence, a comparison of the experimental results for all detector groups to the simulated expectation values allows for a distinction between the three relevant spin sequences.

As a benchmark, a measurement with ^{32}S was used to test the simulated angular correlations for successively emitted photons. In ^{32}S, an isolated 1^+ state is located at 8125 keV, which has

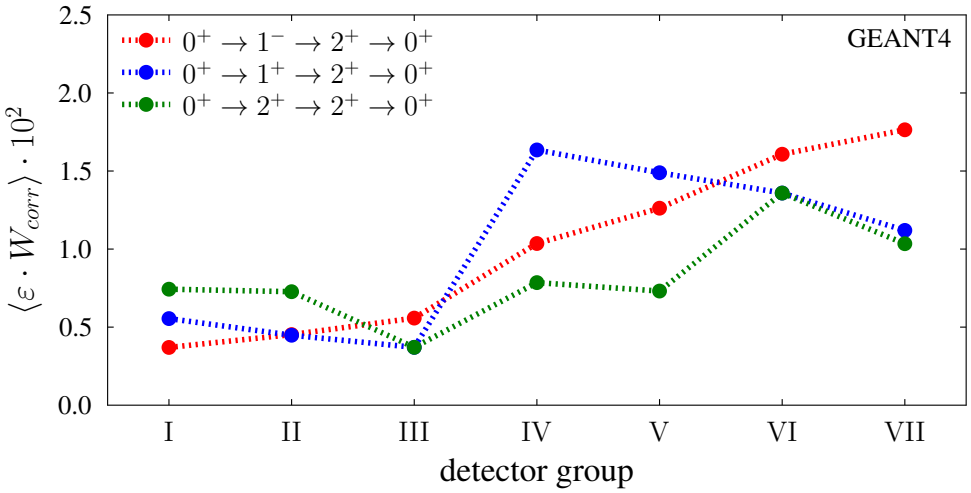

Figure 4.21: Simulated angular correlations $\langle \varepsilon \cdot W_{corr} \rangle$ for coincidence measurements as a function of the defined detector groups. The overall behavior changes for different spin sequences.

a branching ratio of about 14 % to the first excited 2_1^+ state with a mixing ratio of $\delta \approx 0$, i.e. pure M1 transition. The analysis presented in Section 4.8.3 was performed separately for each detector group to extract

$$\langle \varepsilon_1 \cdot W_{corr} \rangle \cdot \sigma_{0 \rightarrow x \rightarrow i} = \frac{1}{N_T N_\gamma^{tot}} \cdot \frac{A_{sum}^{coinc}}{\int\limits_{\Delta\Omega_2} \varepsilon_2(E_{\gamma_2})\, \mathrm{d}\Omega_2} \,, \tag{4.24}$$

where the integral term in Eq. (4.22) is factorized into

$$\int\limits_{\Delta\Omega_1 \Delta\Omega_2} \varepsilon_1(E_{\gamma_1}) \cdot \varepsilon_2(E_{\gamma_2}) \cdot W_{corr}\, \mathrm{d}\Omega_1 \mathrm{d}\Omega_2 = \langle \varepsilon_1 \cdot W_{corr} \rangle \cdot \int\limits_{\Delta\Omega_2} \varepsilon_2(E_{\gamma_2})\, \mathrm{d}\Omega_2 \,. \tag{4.25}$$

The `minuit` package of `ROOT` was used for a χ^2 minimization procedure to determine $\sigma_{0 \rightarrow x \rightarrow i}$ as a scaling factor between experiment and simulation. This was performed for the different transition sequences. Figure 4.22.a) shows the minimal χ^2_{red} and the corresponding results for the example of $1^- \rightarrow 2^+$. The simulated angular correlations (red dots) are not in good agreement to the experimental data points (black squares). The same applies for $2^+ \rightarrow 2^+$ in Fig. 4.22.c). The best agreement is found in Fig. 4.22.b) for the true spin sequence $1^+ \rightarrow 2^+$ with $\chi^2_{red} = 3.0$. Consequently, this example serves as a proof of principle that this approach is sensitive to the spin-parity quantum number of excited states populating a lower-lying 2^+ state and that the performed simulations are accurate to describe the observed angular distributions.

In the test with ^{32}S, an isolated excited state was investigated. In general, different sets of states, i.e. 1^-, 1^+ and 2^+ states, may contribute to the total intensity measured in the direct population of the 2^+ level

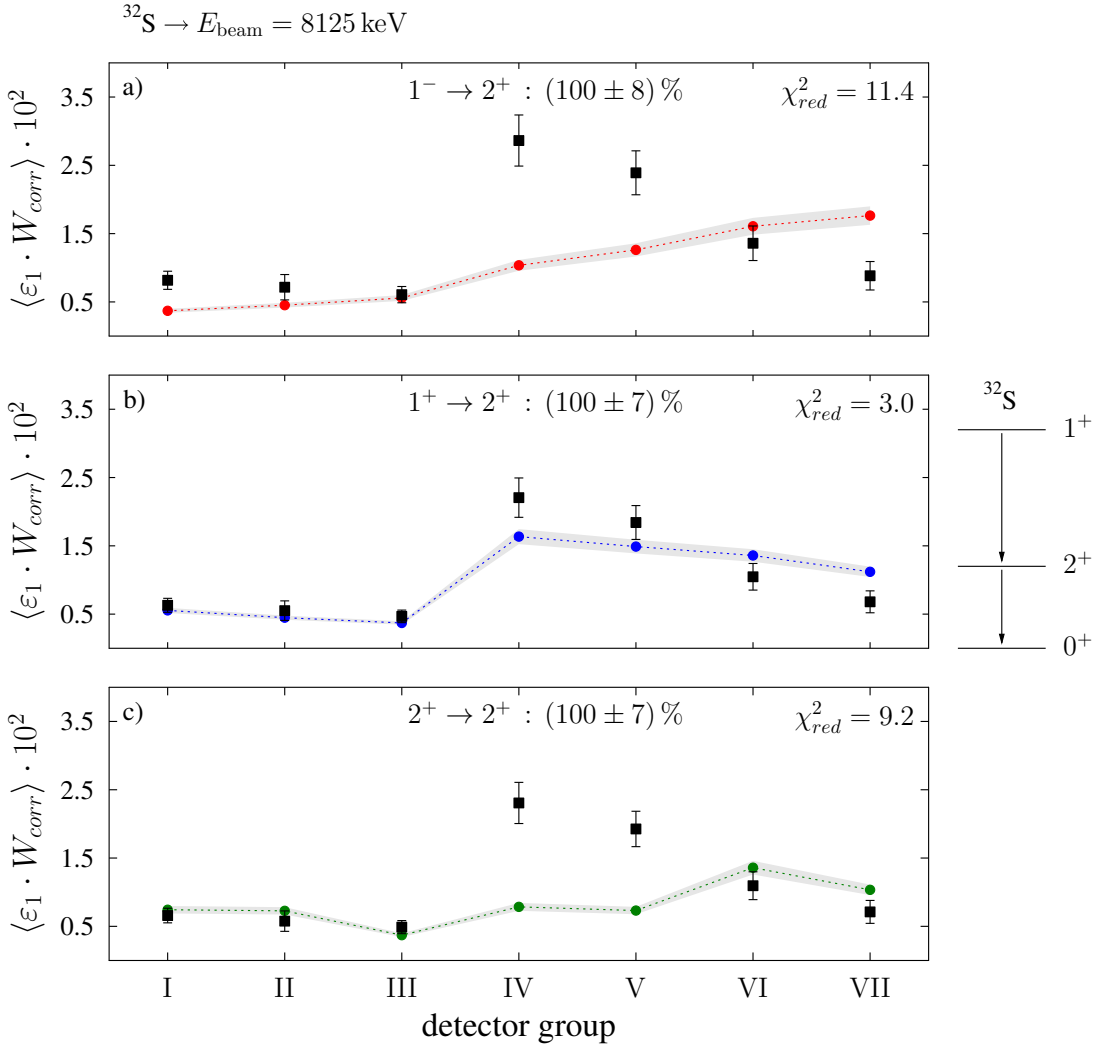

Figure 4.22: Experimental angular correlations (black squares) from measurements with ^{32}S at $E_{beam} = 8125$ keV. The primary transition $1^+ \rightarrow 2^+_1$ is measured in coincidence to the ground-state transition of the 2^+_1 state. The experimental data points are scaled to the simulated values shown in Fig. 4.21 via a χ^2 minimization procedure. The fit to the hypothetical $1^- \rightarrow 2^+$ primary transition is shown in a), to the $1^+ \rightarrow 2^+$ transition in b) and the $2^+ \rightarrow 2^+$ transition in c). The best fit is achieved for b), which strongly indicates that the applied method is useful to determine the spin-parity quantum numbers of the states directly populating the 2^+_1 state.

$$A^{coinc}_{sum} = \sum A^{coinc}_{0^+\rightarrow 1^-\rightarrow 2^+} + \sum A^{coinc}_{0^+\rightarrow 1^+\rightarrow 2^+} + \sum A^{coinc}_{0^+\rightarrow 2^+\rightarrow 2^+}$$

$$\propto \sum_{J^\pi = 1^-, 1^+, 2^+} \langle \varepsilon_1 \cdot W_{corr} \rangle_{J^\pi} \cdot \sigma_{0^+\rightarrow J^\pi \rightarrow 2^+} \, . \tag{4.26}$$

Therefore, a detailed analysis of the different possible contributions is shown in Fig. 4.23 for the measurement with ^{128}Te at $E_{beam} = 8560$ keV. The experimental data points (black squares) are fitted to the angular correlation values for $1^- \rightarrow 2^+$, $1^+ \rightarrow 2^+$ and $2^+ \rightarrow 2^+$ transitions in

Fig. 4.23. a), b) and d), respectively. Furthermore, angular correlations with mixing ratios of $\delta = 100$ are tested in Fig. 4.23. c) and e). In Fig. 4.23. f), a superposition of the correlation functions from Fig. 4.21 are used.

Comparing the χ^2_{red} values from the different cases, the analysis clearly favors, that the dominant part of the direct population of the 2^+_1 state originates from 1^- states. Even though, the simultaneous fit in Fig. 4.23. f) suggests a 9 % contribution of $2^+ \xrightarrow{\delta=0} 2^+$ transitions, its relative uncertainty is larger than 100 %. Thus, the total population intensity is assumed to come from $1^- \rightarrow 2^+$ transitions for the analyzed case. This procedure is applied to all coincidence measurements with ^{128}Te.

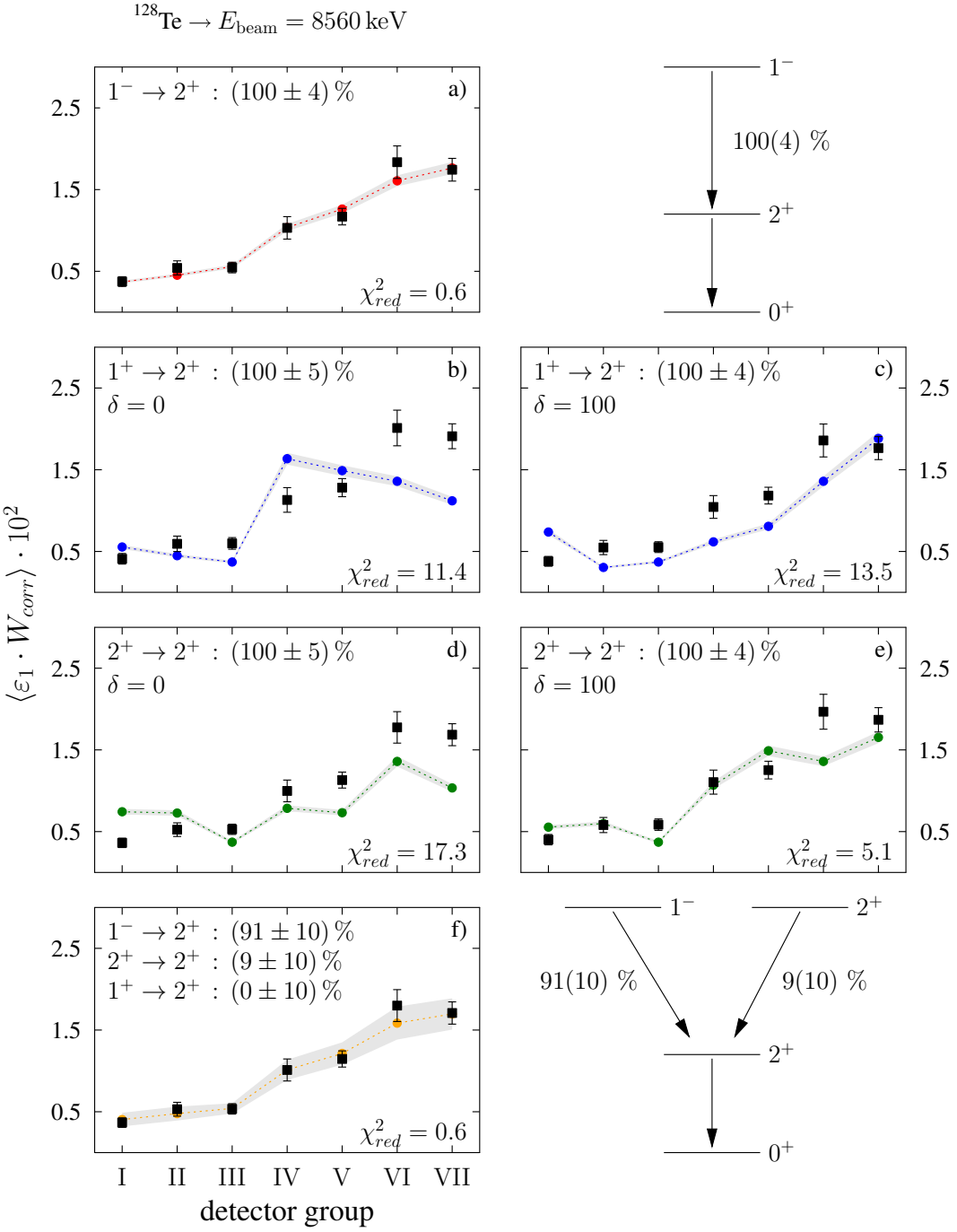

Figure 4.23: Experimental angular correlations from measurements with ^{128}Te at E_{beam} = 8560 keV (black squares). Theoretical angular correlation values from primary transitions to the first excited 2^+_1 state with different initial spin-parity quantum numbers are tested. Panels a),b) and d) show the $\langle \varepsilon_1 \cdot W_{corr} \rangle$ discussed in Fig. 4.21 and Fig. 4.22. In panel c) and e), a mixing ratio of $\delta = 100$ is introduced in the corresponding transition. Panel f) provides a fit of the linear combination of the angular correlations for $1^- \rightarrow 2^+$, $1^+ \xrightarrow{\delta=0} 2^+$ and $2^+ \xrightarrow{\delta=0} 2^+$.

5 Results & Discussion

5.1 State-to-state analysis

In this Section, the results for the analysis of isolated photo-excited states in ^{128}Te observed at DHIPS and HIγS are presented and discussed.

5.1.1 Spin-parity quantum numbers in ^{128}Te

In total, 301 photo-excited states from 0.7 MeV up to the neutron separation energy $S_n = 8.8$ MeV are observed. Above $\sim$3.3 MeV, 292 states have been investigated for the first time in NRF measurements. In Section 4.5.2, the different angular distributions of the γ-rays emitted in the de-excitation of an excited state are exploited to determine spin-parity quantum numbers J^π of these states. Figure 5.1 shows the asymmetries Σ_v (a) and Σ_h (b) and their correlation (c) for all nuclear levels in ^{128}Te observed in the experiment at HIγS. The correlation plot illustrates the sensitivity for the distinction between 1^- states on one hand and 1^+ and 2^+ states, respectively, on the other hand. For instance, the nuclear level at 3136 keV (green square with $\Sigma_v = 0.44(55)$ in Fig. 5.1.a)) would indicate $J^\pi = 1^-$. However, taking the information of Σ_h into account, this state is clearly assigned to be a 2^+ state, which is in agreement with Ref. [178]. The comparison of the statistical uncertainties for the same data points in both asymmetries shows that Σ_v is more sensitive to 1^- states, while Σ_h exhibits an increased sensitivity for 1^+ and 2^+ states, respectively. Thus, even in cases with low statistics, the combination of Σ_v and Σ_h allows for an unambiguous separation of states with negative and positive parity quantum numbers, respectively. The energy region above 4 MeV is clearly dominated by 289 states with $J^\pi = 1^-$ (red dots). Between 2.7 MeV and 5.5 MeV six states are assigned $J^\pi = 1^+$ (blue triangles), three states have $J^\pi = 2^+$ (green squares) and for three levels only positive parity quantum numbers can be assigned, hence labeled as $J^\pi = (1,2)^+$ (black stars).

Low-lying collective dipole excitations

The region below 3.3 MeV was previously studied in γ-ray spectroscopy following inelastic scattering of accelerator-produced neutrons investigating collective excitations in ^{128}Te [179]. Of particular interest is the $J = 1$ level at 2763 keV, which is the best candidate for the lowest-lying mixed symmetry 1^+_1 state (see for a recent review Ref. [180]) in ^{128}Te according to calculations within the quasiparticle-phonon model (QPM) [57]. However, the parity quantum number of this state is unknown. Thus, in the analysis of Ref. [179] it was assumed that this state has positive parity. Furthermore, a candidate for the two-phonon $1^-_{[2^+_1 \otimes 3^-_1]}$ state (see, e.g. Refs. [20, 40, 43]) is presumed to be at 3185 keV. Unfortunately, also in this case no information on the associated parity quantum number was available. The correlation plot in Fig. 5.1.c) confirms the assumptions made by the authors of Ref. [179] leading to the assignments $J^\pi = 1^+$ and $J^\pi = 1^-$ for the 2763 keV and 3185 keV level, respectively. In addition, $J^\pi = 1^+$ is assigned for the excited state at 3105 keV.

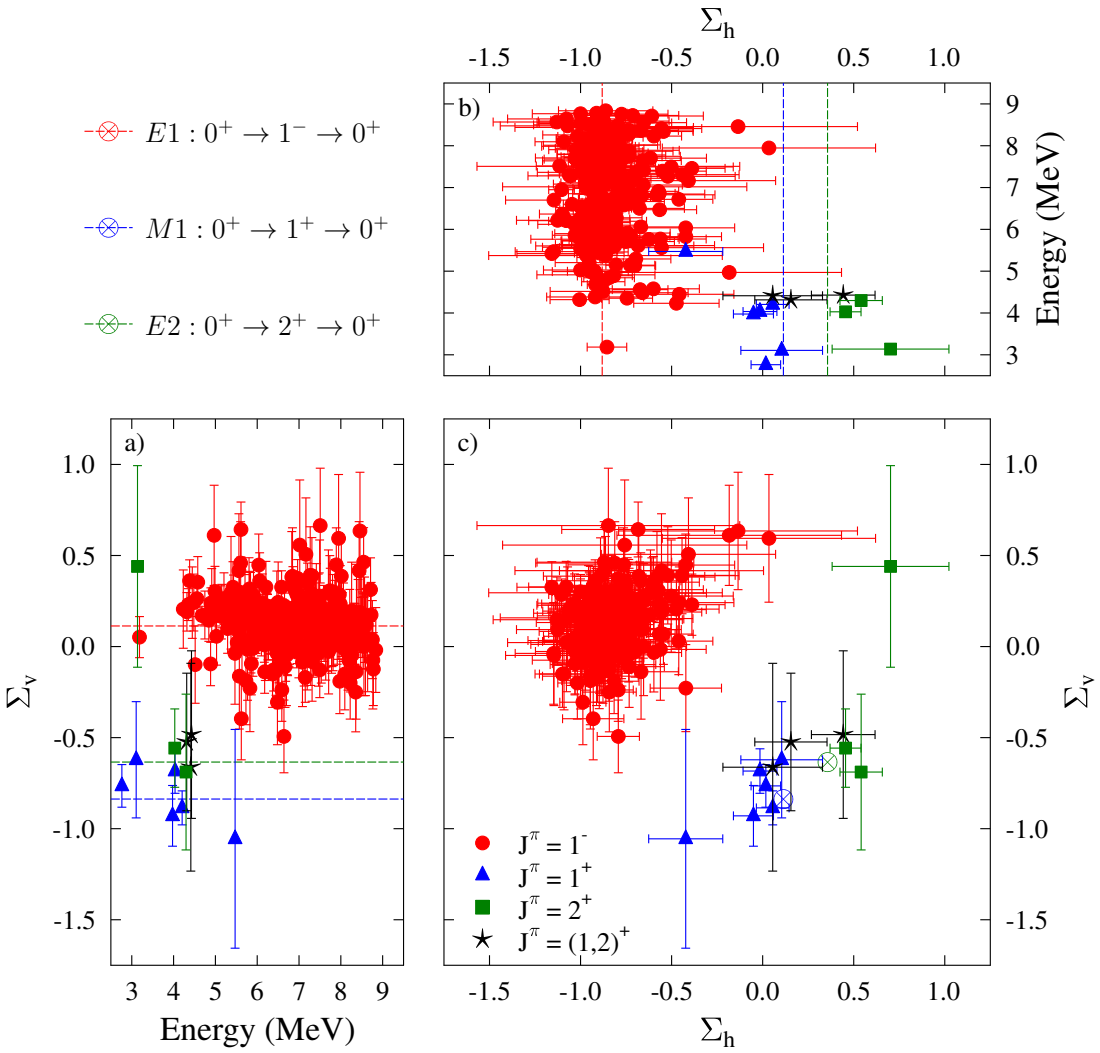

Figure 5.1: Asymmetries Σ_v (a) and Σ_h (b) determined at HIγS for excited states in the energy range from 2.7 MeV to 9.0 MeV. The correlation of both asymmetries (c) allows for spin-parity assignments. An assignment is performed, if the experimental results for Σ_v and Σ_h agree within their 2σ-region to one of the expectation values for different transition characters $E1$, $M1$ and $E2$. In total, 289 photo-excited states in ^{128}Te are assigned to have $J^\pi = 1^-$, 6 states have $J^\pi = 1^+$, while 3 excited states are determined to have $J^\pi = 2^+$. For 3 levels only positive parity is assigned, i.e. $J^\pi = (1,2)^+$.

5.1.2 Dipole-strength distribution in ^{128}Te

5.1.2.1 Integrated cross sections from DHIPS

Integrated cross sections $I_{0\to x\to 0}$ for individual ground-state transitions in ^{128}Te are determined using Eq. (4.11). The experimental results extracted from the DHIPS measurements at $E_{e^-} = 6.00$ MeV and $E_{e^-} = 9.13$ MeV are shown in Fig. 5.2.a) and Fig. 5.2.b), respectively. Different class of states are shown, i.e. 1^- (red), 1^+ (blue), 2^+ (green) and $(1,2)^+$ (black) states. Furthermore, the experimental sensitivity is indicated by dashed lines. The integrated cross sections for E1 excitations exhibit a flat behavior at low energies, while above ~ 5 MeV up to the neutron separation threshold $S_n = 8.8$ MeV a concentration of increased E1 strength is observed. At energies below 5 MeV, ground-state decays of low-lying 2^+ states are found, in particular in the $E_{e^-} = 9.13$ MeV measurement. This is an indication, that these states have been populated by nuclear levels at higher excitation energies rather than being excited from the ground state. A comparison of the cross sections extracted from both measurements is given in Fig. 5.2.c). A ratio of $I_{9.13}/I_{6.00} \approx 1$ shows that the attributed excited levels are not or only weakly fed in the 9.13 MeV experiment relative to the experiment at 6.00 MeV. This is the case for the levels observed between 4 MeV and 6 MeV. For excited states at lower energies, the ratio exhibits $\mathrm{I}_{9.13}/\mathrm{I}_{6.00} > 1$ indicating an increased contribution from feeding transitions. The sensitivity of NRF experiments using continuous-energy bremsstrahlung is usually not high enough to determine the origin of the feeding contributions. Thus, for the cases with $I_{9.13}/I_{6.00} > 1$ the integrated cross sections determined from the $E_{e^-} = 6.00$ MeV experiment are used. Otherwise, if feasible weighted averages of both measurements are computed for the individual cross sections.

5.1.2.2 Reduced transition probability for $E1$ transitions

The integrated cross sections obtained from the DHIPS measurements are used to calibrate the photon flux of the quasi-monochromatic photon beam at HIγS (see Section 4.4.2). As illustrated in Fig. 4.7, the spectra obtained with the γ^3-setup at HIγS exhibit a superior peak-to-background ratio in the excitation energy region compared to the DHIPS spectra. Hence, additional weakly-excited states can be observed, that are below the experimental sensitivity limit at DHIPS. About 183 photo-excited states are extracted from the γ-ray spectra recorded with the HPGe detectors at DHIPS, while 301 excited states are obtained from the analysis of the HPGe spectra at HIγS. The following part focuses on the discussion of the $B(E1)\uparrow$ strength distribution measured in ^{128}Te. Combining Eqs. (2.20) and (2.23), the reduced $E1$ transition probability can be directly calculated from the integrated cross section

$$\frac{B(E1)\uparrow}{\mathrm{e^2fm^2}} = 2.486\cdot 10^{-3}\cdot\frac{\Gamma}{\Gamma_0}\cdot\frac{I_{0\to x\to 0}}{\mathrm{keVfm^2}}\cdot\frac{\mathrm{MeV}}{E_x}\,, \tag{5.1}$$

where Γ_0/Γ is the ground-state branching ratio. This term arises from the fact, that in classical NRF experiments the measured integrated cross section for ground-state transitions is proportional to Γ_0^2/Γ. An alternative approach, that is not covered in this thesis, is the method of self absorption [19, 181]. It is sensitive to Γ_0 and therefore suited to extract reduced transition strengths in a direct way. In this work, however, $\Gamma_0/\Gamma = 1$ is assumed, if no branching from the excited state to lower-lying states is observed. Nevertheless, it cannot be excluded that many

very weak transitions, which are not observed in the experiment, contribute substantially to the total transition width Γ resulting in $\Gamma_0/\Gamma < 1$:

$$\frac{\Gamma_0}{\Gamma} = \frac{\Gamma_0}{\Gamma_0 + \Gamma_1 + \Gamma_2 + ...} < 1 \,, \tag{5.2}$$

where Γ_1, Γ_2, and so on represent the individual transition widths to states other than the ground state. Without additional information on the complete decay behavior, the accurate description of the transition strengths, the product $\Gamma_0/\Gamma \cdot B(E1) \uparrow$ is considered. A comparison of the

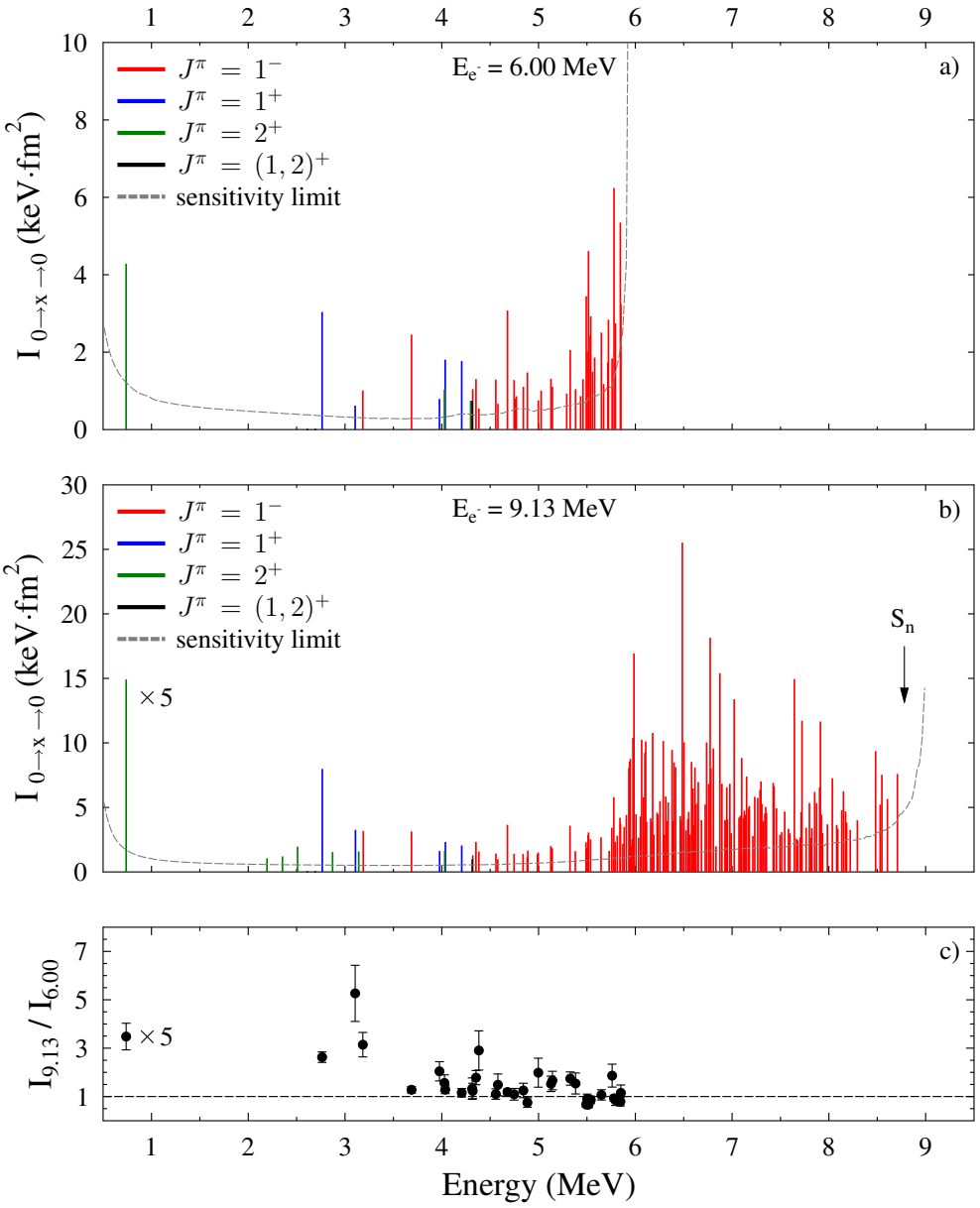

Figure 5.2: Integrated cross sections determined for excited states in ^{128}Te at DHIPS with bremsstrahlung endpoint energies of 6.0 MeV (a) and 9.13 MeV (b). The corresponding experimental sensitivity limits are illustrated by dashed lines. Panel c) shows the ratio $I_{9.13}/I_{6.00}$. Values $I_{9.13}/I_{6.00} > 1$ indicate an increased feeding of the associated states from excited states above 6.0 MeV in the measurement with $E_{e^-} = 9.13$ MeV.

$\Gamma_0/\Gamma \cdot B(E1)\uparrow$ strength determined at both experimental sites is shown in Fig. 5.3. The dashed line illustrates the accumulated strength as a function of the energy in 200 keV bins. In particular, above ~7 MeV additional $E1$ transitions are observed at HIγS. Therefore, the cumulative sum of the strength increases more above this energy compared to the DHIPS results. The $\Gamma_0/\Gamma \cdot B(E1)\uparrow$ strength summed between 3 MeV and 8.8 MeV is about 303(38) $10^{-3}e^2fm^2$ for DHIPS and 442(55) $10^{-3}e^2fm^2$ for HIγS. This is a difference of about 46 %, which is caused by 129 additional weakly-excited 1^- states observed only at HIγS.

5.1.2.3 Comparison to QPM calculations

In a previous work, the dipole-strength distribution in the isotope ^{130}Te was investigated in NRF measurements at DHIPS and HIγS [182]. The experimental $B(E1)\uparrow$ values for ^{128}Te and ^{130}Te are shown in Fig. 5.4.a) and Fig. 5.4.b), respectively, assuming $\Gamma_0/\Gamma = 1$ for comparison reasons. In both nuclei, a resonance-like concentration of $B(E1)\uparrow$ strength is observed around ~6.5 MeV. Furthermore, their summed strength is comparable being $\sum B(E1)\uparrow =$ 0.442(55) $10^{-3}e^2fm^2$ for ^{128}Te and $\sum B(E1)\uparrow =$ 0.476(35) $10^{-3}e^2fm^2$ for ^{130}Te.

The experimental results are compared to calculations within the quasi-particle phonon model (QPM) [57]. In this model, excited states in even-even nuclei are treated in terms of phonons. For the current calculations, the so-called $1p1h$ doorway 1^- states are coupled to complex $2p2h$ and $3p3h$ configurations. The calculated $B(E1)\uparrow$ strength distributions for ^{128}Te [183] and ^{130}Te [184] are shown in Fig. 5.4.c) and d). A similar accumulation of strength in the region around 6 MeV is apparent in the QPM calculations. Furthermore, the absolute scale of strongly-excited states predicted by the QPM are in good agreement with the experimental findings for both tellurium isotopes. The cumulative sums (dashed blue lines) show a similar

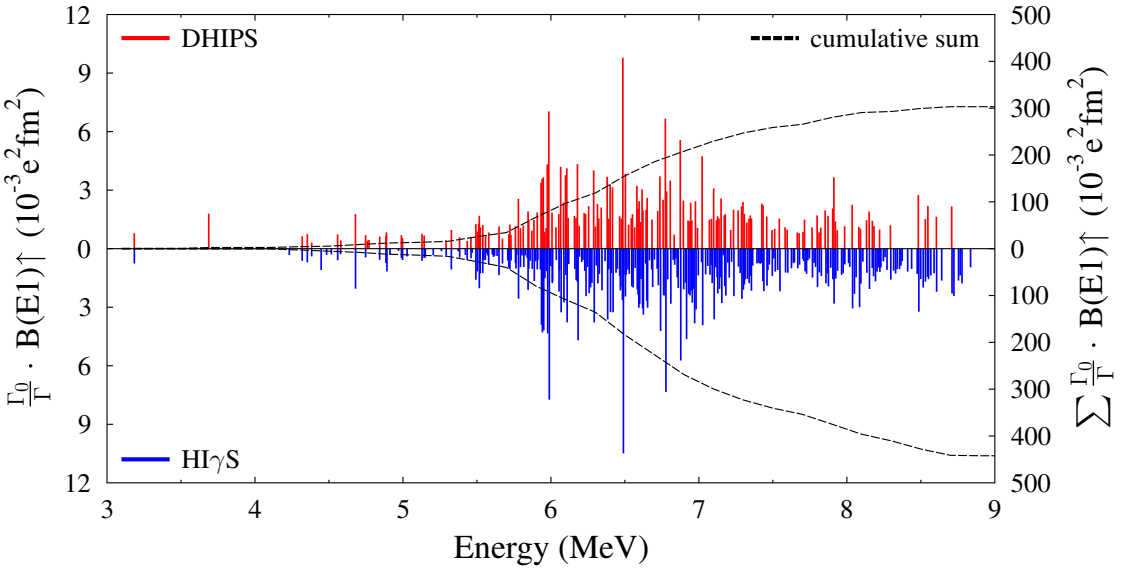

Figure 5.3: Upper panel: Reduced transition strengths $\frac{\Gamma_0}{\Gamma} \cdot B(E1)\uparrow$ for excited states in ^{128}Te observed at DHIPS. The accumulated strength as a function of the energy is shown as dashed line, that saturates at about 303(38) $10^{-3}e^2fm^2$. Lower panel: $\frac{\Gamma_0}{\Gamma} \cdot B(E1)\uparrow$ values determined in the HIγS experiments. Due to the superior peak-to-background ratio at HIγS, additional weakly excited states are observed in comparison to DHIPS. This leads to an increase of the cumulative strength of about 46 % to 442(55) $10^{-3}e^2fm^2$.

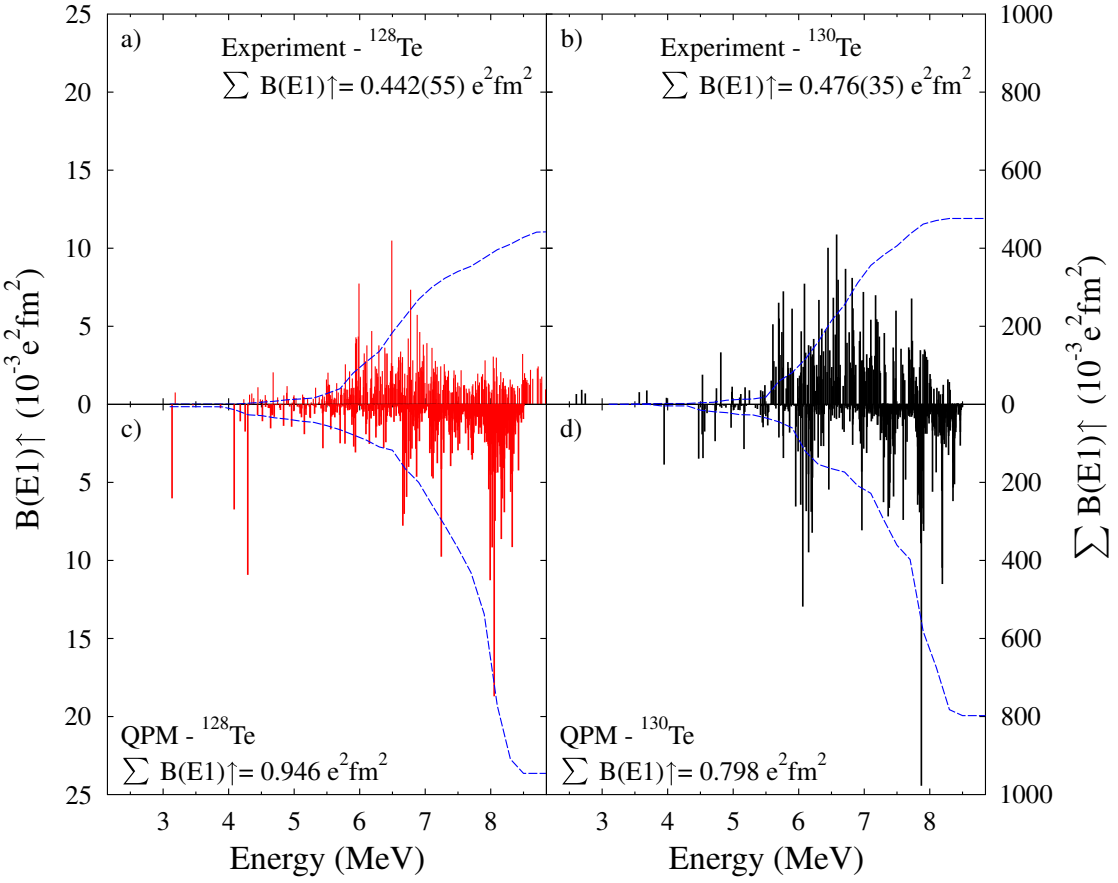

Figure 5.4: Experimental $B(E1)\uparrow$ strength distribution for ^{128}Te (a) and ^{130}Te (b). Predictions from QPM calculations are shown for ^{128}Te (c) and for ^{130}Te (d). The corresponding cumulative sum is displayed as dashed blue line.

behavior as a function of the excitation energy for the experimental data and the QPM calculations up to about 7 MeV. Above that energy, a substantial discrepancy between experiment and theory is apparent, which results in a factor of $\sim$2 larger total $B(E1)\uparrow$ strength in the theoretical calculations. One reason for the systematic discrepancy may be due to the lack of knowledge of the ground-state branching ratio Γ_0/Γ for each excited state in the experiment. Since $\Gamma_0/\Gamma = 1$ is assumed, the experimentally extracted $B(E1)\uparrow$ values represent a lower limit for their true strength.

Another explanation is that the total strength in a given energy region is distributed over many excited states each too weakly excited to be observed in the experiment. Up to now, the $B(E1)\uparrow$ strength distribution was discussed as a function of the excitation energy. In Fig. 5.5, the total strength is shown as a function of the $B(E1)\uparrow$ of the individual states. For this, the individual $B(E1)\uparrow$ values are grouped according to their strength and are summed. This means, e.g., that the strengths of all excited states fulfilling the condition $2{\cdot}10^{-3}$e^{2}fm^2 $\leq B(E1)\uparrow$ $<3{\cdot}10^{-3}$e^{2}fm^2 are added up to $\sum B(E1)\uparrow$ and displayed as the height of the associated bin. This way of illustration provides information about the fragmentation of the total strength, i.e. how the strength is distributed over the individual excited states. The upper panel of Fig. 5.5 shows the results for ^{128}Te. The fragmentation determined from the QPM calculations (shaded bars) and the experiment (red bars) show a similar distribution for $B(E1)\uparrow > 2{\cdot}10^{-3}$e^{2}fm^2.

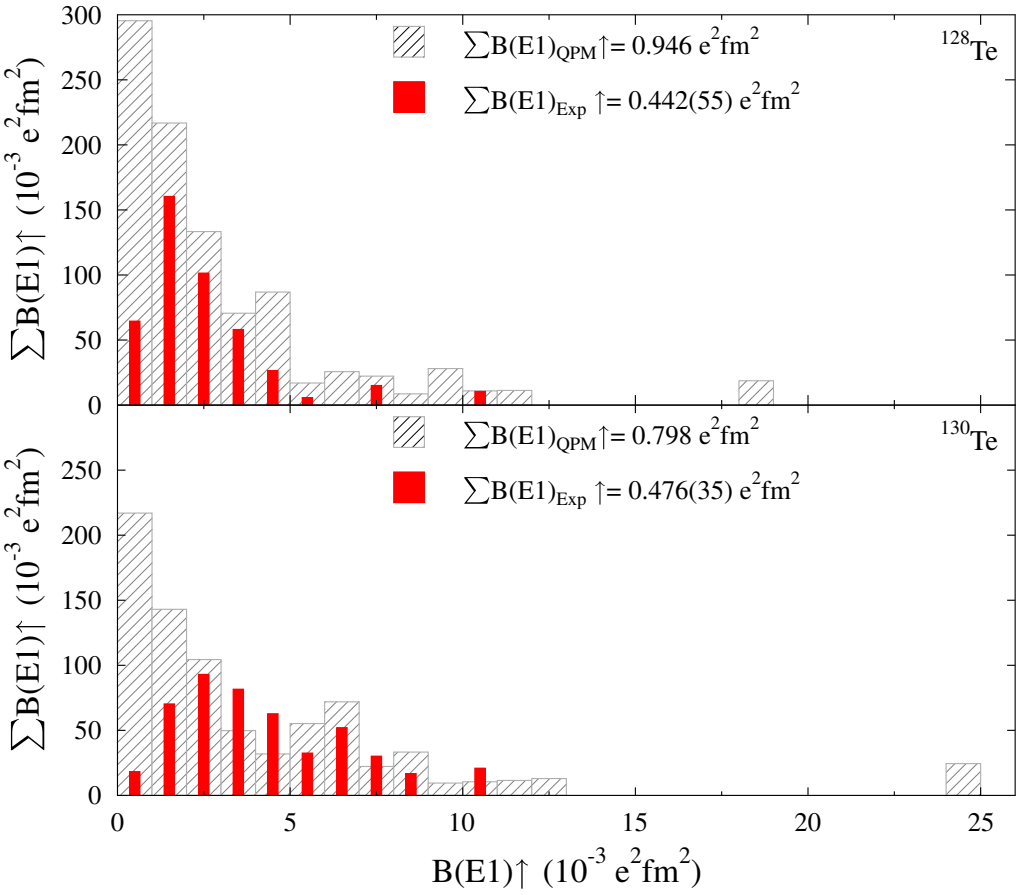

Figure 5.5: Experimental fragmentation of the $B(E1)\uparrow$ strength (red bars) in ^{128}Te (upper panel) and ^{130}Te (lower panel). The experimental results are compared to QPM calculations (shaded bars). For details see text.

The largest discrepancy in $\sum B(E1)\uparrow$ is found for transition strengths below $2{\cdot}10^{-3}$e^{2}fm^2. The missing strength in this region is about $288{\cdot}10^{-3}$e^{2}fm^2. A similar observation is made for ^{130}Te (lower panel). While the experimentally determined fragmentation is in good agreement to the QPM predictions above $2{\cdot}10^{-3}$e^{2}fm^2, a discrepancy of $271{\cdot}10^{-3}$e^{2}fm^2 is apparent in total for individual states with $B(E1)\uparrow < 2{\cdot}10^{-3}$e^{2}fm^2 values. It follows that about one third of the $B(E1)\uparrow$ strength in the QPM predictions is located in many weakly-excited states, that are not observed in the experiment which is an indication for the limited experimental sensitivity.

The good agreement to the experimental results of the fragmentation in both tellurium isotopes for excited states with $B(E1)\uparrow > 2{\cdot}10^{-3}$e^{2}fm^2 indicates that the damping mechanism of the PDR is well described by the QPM by the coupling of the PDR doorway states to complex configurations. Moreover, the results and discussions in the upcoming Section will provide additional evidence for the outlined interpretation of the missing strength, which is "hidden" in the so-called continuum below isolated and resolved transitions.

5.2 Average quantities

5.2.1 Photoabsorption cross sections for ^{128}Te and ^{130}Te

In Section 4.6.1, a method is outlined to extract average cross sections from the NRF measurements at HIγS. The effect of the detector response deconvolution of the γ-ray spectra obtained with HPGe and LaBr detectors is illustrated in Fig. 4.10 for $E_{beam} = 6.4$ MeV. The remaining intensity in the spectrum in the vicinity of the photon beam corresponds to ground-state transitions of excited states in ^{128}Te, only. Using Eq. 4.15, the elastic cross section is extracted for all energy settings ranging from 2.7 MeV to 8.9 MeV. The upper left panel of Fig. 5.6 shows two types of elastic cross sections. One is determined from the sum of isolated peaks in the HPGe spectra ($\sigma^{p}_{\gamma\gamma}$, red triangles). The other one takes the complete spectrum after deconvolution, i.e. the continuum into account. This is performed for the HPGe ($\sigma_{\gamma\gamma,HPGe}$, blue triangles) as well as for the LaBr detectors ($\sigma_{\gamma\gamma,LaBr}$, orange dots). The results for $\sigma_{\gamma\gamma,HPGe}$ and $\sigma_{\gamma\gamma,LaBr}$ are in very good agreement, thus, the weighted average of both cross sections are used for the upcoming discussions and will be denoted simply as $\sigma_{\gamma\gamma}$. The dipole strength below 4.5 MeV is mainly apparent as resolved peaks in the HPGe spectra, while at higher energies the unresolved strength from weakly-excited states hidden in the continuum cannot be neglected. This is also expressed in the normalized difference (lower left panel)

$$D = \frac{\sigma_{\gamma\gamma} - \sigma^{p}_{\gamma\gamma}}{\sigma_{\gamma\gamma}} \,, \tag{5.3}$$

which illustrates the relative amount of the complete elastic cross section that is missed in the analysis of isolated peaks, only. Above 6 MeV, it is increasing monotonously with the excitation energy up to 70 %, whereas around 5 MeV a local maximum is found, indicating that about 50 % of the strength is located in the continuum. This finding is consistent with the discussion of the fragmentation of the $B(E1)\uparrow$ strength in Section 5.1.2.3, where a large fraction of the ground-state transition strength is not observed in isolated peaks, but is carried by many weakly-excited states that are missed due to the limited experimental sensitivity (see Fig. 5.5).

The same analysis steps are performed for ^{130}Te between 5.5 MeV and 8.5 MeV. The right part of Fig. 5.6 compares the elastic cross sections measured in resolved peaks and extracted from the deconvoluted spectra. The normalized difference D indicates that less than 40 % of the complete ground-state transition strength is missed even above 7 MeV, if only peaks are analyzed. In conclusion, a larger fraction of the elastic cross section is found in isolated peaks compared to ^{128}Te.

Comparison to QPM calculations

The elastic ($\sigma_{\gamma\gamma}$, green triangles), inelastic ($\sigma_{\gamma\gamma'}$, red dots) and the photoabsorption cross sections (σ_{γ}, black squares) are shown in Fig. 5.7. In both tellurium nuclei, $\sigma_{\gamma\gamma'}$ is steadily increasing with the excitation energy, while $\sigma_{\gamma\gamma}$ saturates and slightly decreases above $\sim$6.5 MeV. Between 7 MeV and 9 MeV, σ_{γ} in ^{128}Te is clearly dominated by the inelastic contribution, in contrast to ^{130}Te where this effect is observed to be weaker. The lower panels of Fig. 5.7 show the photoabsorption cross sections computed from the corresponding QPM calculations. For comparison reasons, the theoretical values are determined in the same fashion as the experimental results. Therefore, the calculated strength distribution from Fig. 5.4 is weighted with the

spectral shape of the photon flux for each beam energy setting

$$\sigma_{\gamma}^{QPM} = \frac{\sum_x I_{0\to x}^{QPM} \cdot N_{\gamma}(E_x)}{\int_0^{\infty} N_{\gamma}(E)\,\mathrm{d}E}\,, \tag{5.4}$$

with $I_{0\to x}^{QPM}$ being the integrated photoabsorption cross section for a nuclear level x at excitation energy E_x. The overall shape of σ_{γ}^{QPM} as a function of the beam energy is in good agreement to the experimental results. In ^{128}Te, the accumulated photoabsorption cross section between 5.5 MeV and 8.5 MeV is 164(9) mb for the experimental values and 95 mb for the QPM calculations. This is a difference of about 73 % between experiment and theory. It should be mentioned, that the QPM calculations were performed up to a cutoff energy of 8.5 MeV, only. Therefore, photoabsorption cross sections for the last two beam energy settings of 8.56 MeV and 8.92 MeV cannot be computed. However, the trend of the QPM calculations as a function of the excitation energy suggests a further increase of σ_{γ}^{QPM}. Taking the last theoretical value of 28 mb at 8.28 MeV as lower limit for the photoabsorption cross section at 8.56 MeV a total sum of 123 mb for the QPM calculations is found. The discrepancy is reduced to about 33 %. Furthermore, the experimental elastic cross sections are in general composed of contributions from $E1$, $M1$ and $E2$ transitions of excited states to the ground-state. As will be shown in the next Section for ^{128}Te, about 2 % to 10 % of the elastic cross section between 4.5 MeV and

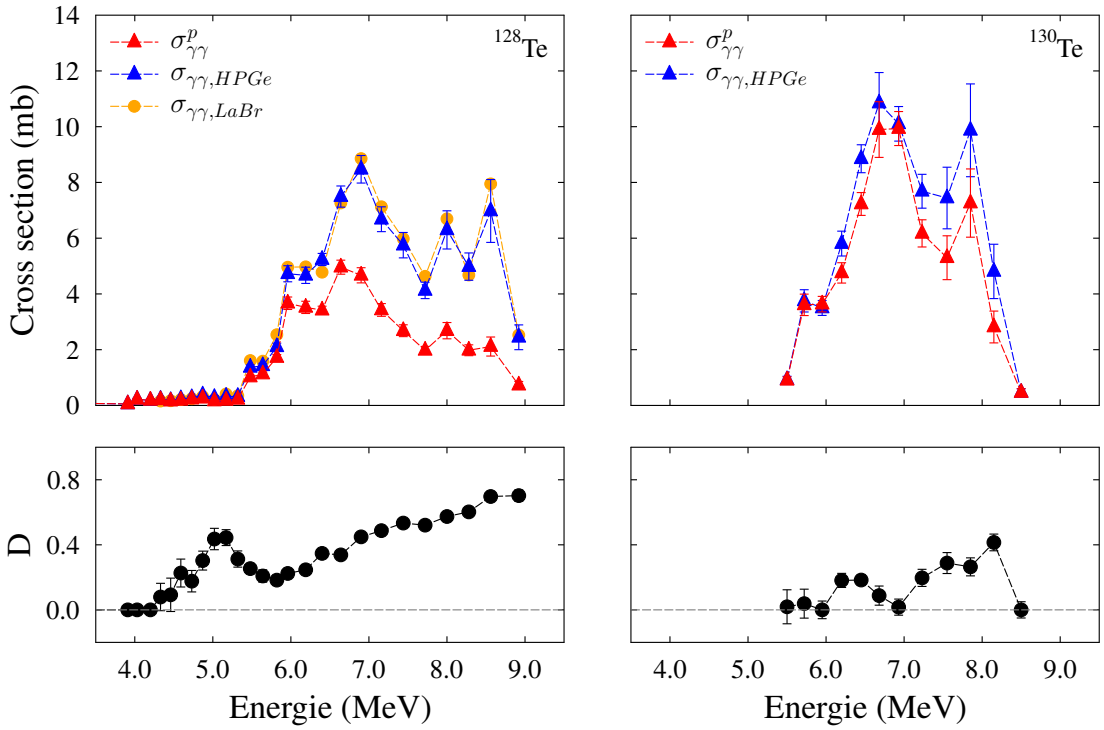

Figure 5.6: Upper left part: Comparison of the elastic cross section for ^{128}Te determined by analyzing isolated peaks ($\sigma^{p}_{\gamma\gamma}$, red triangles) in the γ-ray spectrum recorded in the HPGe detectors of the γ^3-setup. The complete strength taking the unresolved strength in the continuum after deconvolution into account $\sigma^{c}_{\gamma\gamma}$ is shown in blue triangles. Lower left part: The normalized difference D between both elastic cross section. Right part: Results from the same analysis performed on the data from the NRF measurements with ^{130}Te.

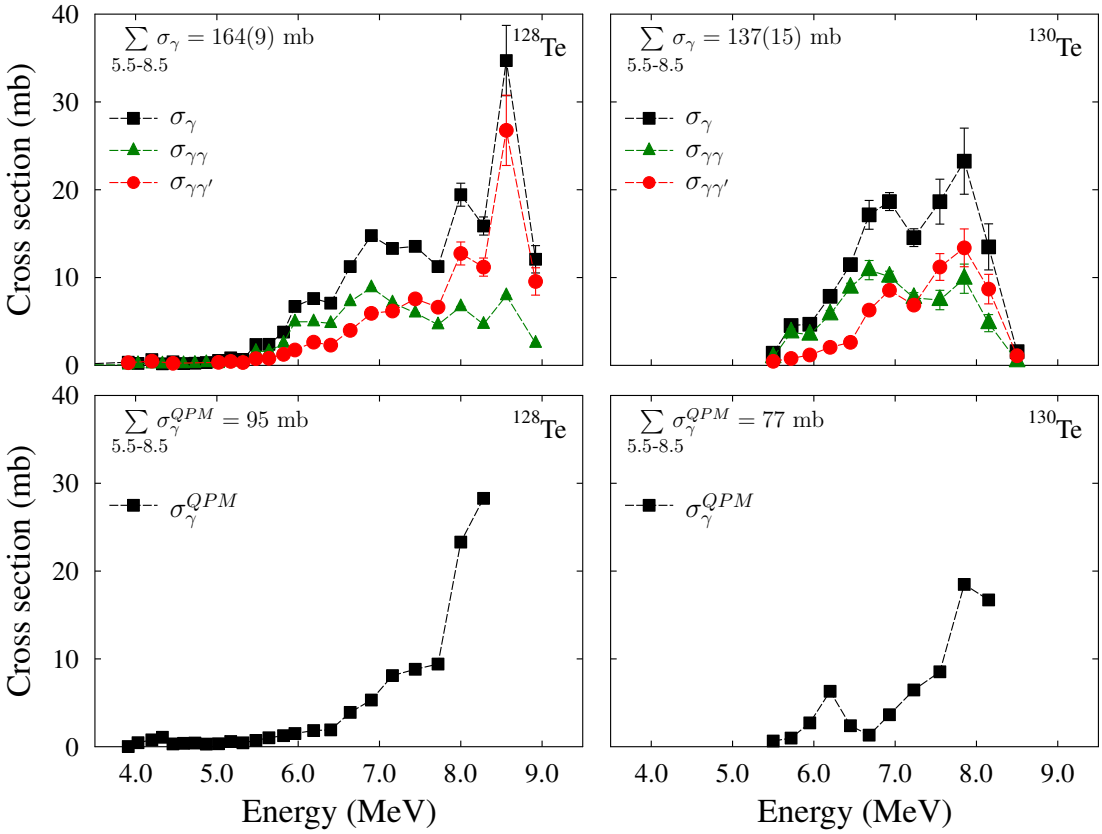

Figure 5.7: Upper left panel: Inelastic (red dots), elastic (green triangles) and photoabsorption cross sections (black squares) determined for ^{128}Te. Lower left panel: Photoabsorption cross sections computed from the QPM calculations. Right part: Results from same analysis performed with ^{130}Te.

8.9 MeV is attributed to $M1$ excitations. But the QPM calculations consider $E1$ strength, only, providing an additional reason for the difference between experiment and theory.

For ^{130}Te, the difference of the experimentally determined photoabsorption cross sections to the QPM calculations is about 77 % being in the same regime as for ^{128}Te. In general, the same effects as outlined in the discussion for ^{128}Te can influence the discrepancy to the QPM predictions.

Systematic investigations of the dipole strength distribution in the $N = 82$ isotones (see, e.g. Ref. [56]) indicated that the predicted distributions are usually shifted by about 500 keV to higher excitation energies in comparison to the experimental results. Hence, a non-negligible part of the accumulated photoabsorption cross section computed from the QPM calculations is located above the cutoff energy of 8.5 MeV. It is noted here, that an extension of the QPM calculations to higher excitation energies is in preparation for both tellurium isotopes to allow a better comparison of the photoabsorption cross sections above 8.5 MeV.

Comparison to (γ,xn) data

The photoabsorption cross sections for ^{128}Te (filled red circles) and ^{130}Te (filled blue squares) derived in this work are shown together with results from (γ,n) and $(\gamma,2n)$ reactions (open red circles and open blue squares) from Ref. [116] in Fig. 5.8. The dipole strength is clearly

dominated by the IVGDR with its maximum located around 15 MeV. In spherical nuclei, the shape of the IVGDR above the neutron separation threshold S_n is usually described by a standard lorentzian (SLO):

$$\sigma_\gamma^{SLO}(E_\gamma) = \sigma_0 \frac{\Gamma_0^2 E_\gamma^2}{(E_\gamma^2 - E_0^2)^2 + \Gamma_0^2 E_\gamma^2} \,. \tag{5.5}$$

The resonance is located at the resonance energy E_0, has a width of Γ_0 and a maximum of σ_0. As can be seen from the data points, the IVGDR in both tellurium isotopes does not differ very much above S_n. Therefore, the parameters for the SLO (dashed line) are taken from Ref. [116] for ^{128}Te. The photoabsorption cross sections extracted from the (γ,γ') experiments connect smoothly to the (γ,n)+$(\gamma,2n)$ values except for the last data point around S_n. In comparison to the SLO, an enhancement of the measured dipole strength is present in both nuclei between 6 MeV and 8 MeV. However, the extrapolation of the SLO to energies below 6 MeV overestimates the measured photoabsorption cross sections. Thus, it might be questionable to which extend it makes sense to apply a lorentzian function derived from photoabsorption data around the maximum of the IVGDR to excitation energies below the neutron separation threshold. The results below 6 MeV show a much stronger decrease as expected from the SLO extrapolation. Indeed, the cross sections seem to follow an exponential shape. This behavior towards lower energies was reported in other nuclei before, such as ^{138}Ba [71], ^{142}Nd [185] and in a recent letter in ^{130}Te [73].

The energy-weighted sum rule for the integrated electric-dipole strength in atomic nuclei is usually used to compare the amount of $E1$ strength measured for different excitation modes and is given by

$$\int_0^\infty \sigma(E)\mathrm{d}E = \frac{2\pi^2 e^2 \hbar}{mc}\frac{NZ}{A} = 60\frac{NZ}{A}\mathrm{MeVmb}\,, \tag{5.6}$$

which is derived from the Thomas-Reiche-Kuhn (TRK) sum rule [17, 18]. It can be expressed as a function of the neutron number N, proton number Z and the atomic mass A. The total $E1$ strength measured between 5.5 MeV and 8.5 MeV exhausts about 3.3(2) % for ^{128}Te and about 2.6(3) % for ^{130}Te of the TRK sum rule. Sometimes the additional strength on top of the SLO extrapolation of the IVGDR is compared, which is 0.35(13) % for ^{128}Te and 0.52(11) % for ^{130}Te. Within their uncertainties the total strength as well as the strength exceeding the IVGDR extrapolation are in good agreement for both nuclei.

5.2.2 $M1/E1$ ratio in ^{128}Te

In Section 5.1.1, spin-parity quantum numbers of individual excited states are determined. Complementary to that, the analysis of the LaBr spectra allow for the decomposition of the elastic cross section into $E1$, $M1$ and $E2$ contributions. For each beam energy setting an analogous procedure to the one outlined in Section 4.5.2 is performed. Instead of analyzing isolated peaks, the complete ground-state transition intensity measured in each of the four LaBr detectors are used to compute the asymmetries Σ_v and Σ_h defined in Eqs. (4.13) and (4.14). The values for ^{128}Te are shown in Fig. 5.9.a) and b). From the correlation plot in Fig. 5.9.c) it is clear that the dipole strength between 4.7 MeV and 8.9 MeV is dominated by $E1$ strength. As reference, the asymmetries for the measurement of ^{32}S at $E_{beam} = 8.125$ MeV is shown (black star), which proves that the applied method is valid.

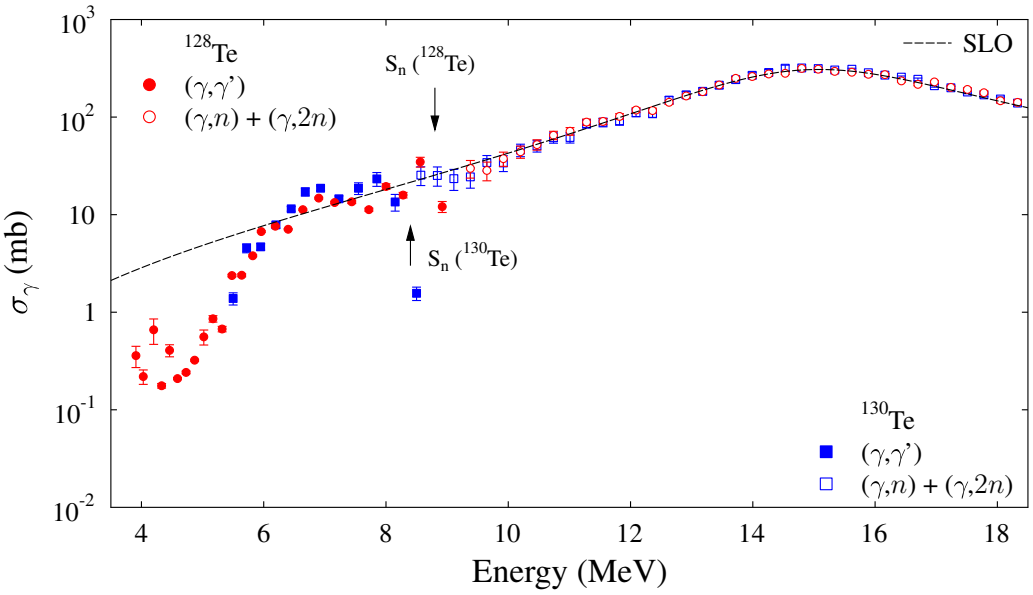

Figure 5.8: Photoabsorption cross sections for ^{128}Te (red) and ^{130}Te (blue). Data above the neutron separation threshold S_n are taken from (γ,n) and $(\gamma,2n)$ measurements in Ref. [116]. The (γ,γ') data for ^{130}Te were already published in Ref. [73], while the ^{128}Te values are from this work. A standard lorentzian (SLO) fit to the data points in the region of the maximum of the IVGDR is shown (dashed line).

In the following it is assumed that the intensity measured in one of the LaBr detectors is due to $E1$ and $M1$ ground-state transitions, only. Thus, the intensity A_v observed in the vertical LaBr detector after detector response deconvolution is proportional to the sum of both contributions

$$A_v \propto I_{E1} \cdot \langle \varepsilon W \rangle_v^{E1} + I_{M1} \cdot \langle \varepsilon W \rangle_v^{M1} \ , \tag{5.7}$$

where I_{E1} and I_{M1} are the cross sections for $E1$ and $M1$ ground-state transitions following photoabsorption, respectively. The terms $\langle \varepsilon W \rangle_v^{E1}$ and $\langle \varepsilon W \rangle_v^{M1}$ are defined in Eq. (4.23) for the associated angular distributions. Consequently, the intensities A_v and A_h give access to the ratio

$$\frac{I_{M1}}{I_{E1}} = \frac{(A_h/A_v) \cdot \langle \varepsilon W \rangle_v^{E1} - \langle \varepsilon W \rangle_h^{E1}}{\langle \varepsilon W \rangle_h^{M1} - (A_h/A_v) \cdot \langle \varepsilon W \rangle_v^{M1}} \ . \tag{5.8}$$

As a test, this ratio is computed for the measurement with ^{32}S which has a strongly-excited 1^+ state at 8125 keV that decays via $M1$ transition directly to the ground state. The result of $I_{M1}/I_{E1} = 54.3(44)$ shows that less than 2 % is assigned to $E1$ strength indicating the sensitivity limit and the validity of this approach.

The I_{M1}/I_{E1} ratios for the experiment with ^{128}Te are shown Fig. 5.10. The relative contribution from $M1$ strength to the total ground-state transition strength above 4.8 MeV does not exceed more than $\sim$10 %. Between 5.5 MeV and 6.5 MeV a "dip"-like structure is observed with a minimum of 1.3 % at 6.19 MeV. Therefore, especially in this region the elastic cross section is dominantly composed of $E1$ strength.

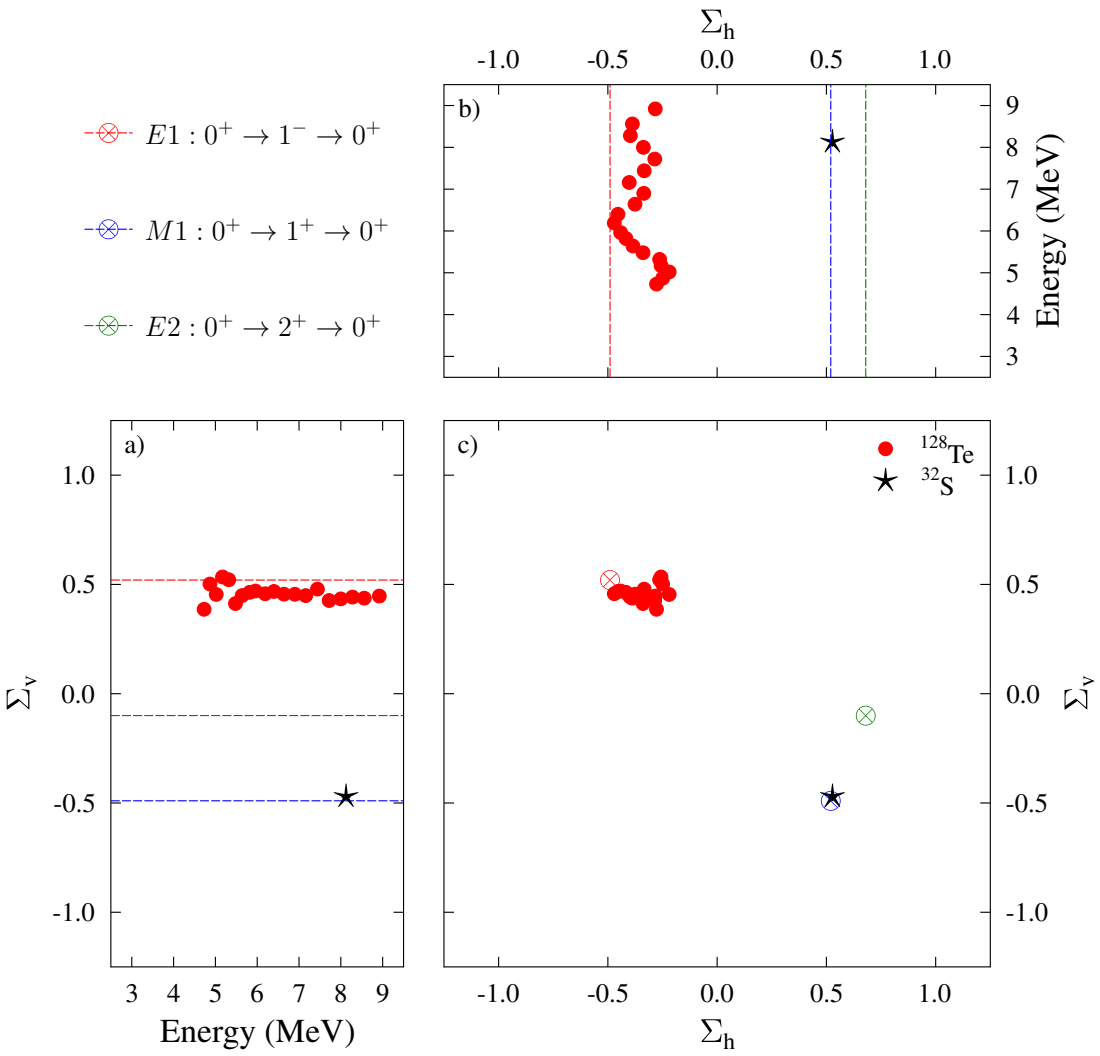

Figure 5.9: Asymmetries Σ_v (a) and Σ_h (b) determined for the ground-state transition intensities obtained with the LaBr detectors. The correlation of Σ_v and Σ_h in c) indicates that the dipole strength between 4.5 MeV and 8.9 MeV is dominantly $E1$ strength.

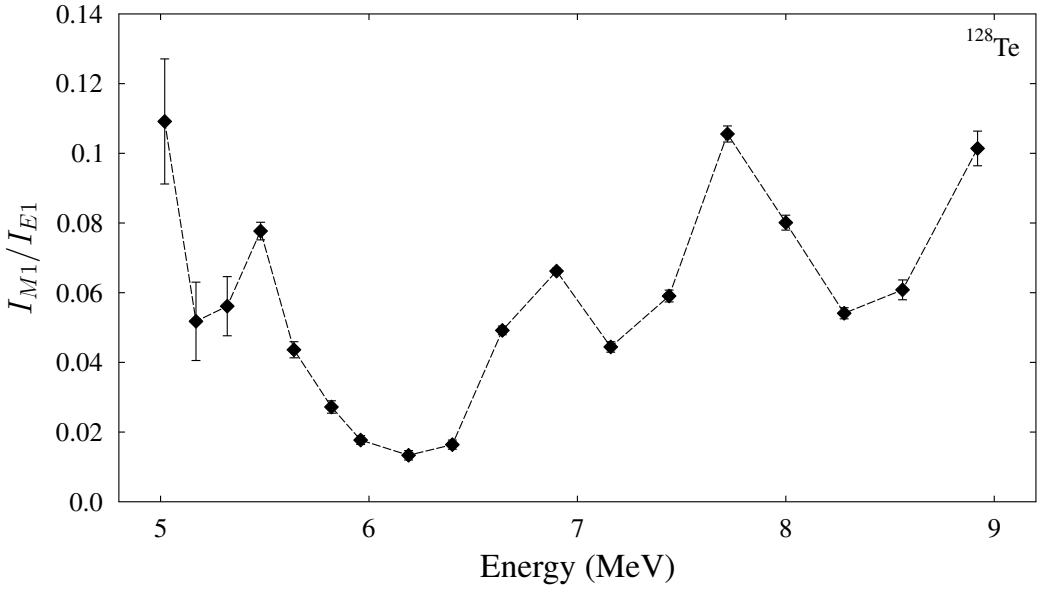

Figure 5.10: The $M1$ to $E1$ ratio for the strength observed for ground-state transitions in ^{128}Te. The relative contribution from $M1$ transitions is less than 10 % for the covered energy range.

5.2.3 Ground-state branching ratios in ^{128}Te and ^{130}Te

From the extracted cross sections the average ground-state branching ratios $\langle b_0 \rangle = \sigma_{\gamma\gamma}/\sigma_\gamma$ are determined for both tellurium isotopes. Figure 5.11 compares the corresponding results for ^{128}Te (red squares) and ^{130}Te (blue dots). The overall smooth decreasing of $\langle b_0 \rangle$ above 6.5 MeV is comparable for both nuclei. This trend can be understood with the concept of the photon strength function in the framework of the statistical model (see Section 2.1.2 and 2.1). Here, the decay probability is governed by the value of the PSF as a function of the γ-ray energy. The higher the excitation energy the smaller is the relative difference of the PSF at different γ-ray energies assuming a comparatevily smooth increase of the PSF with E_γ. Therefore, with increasing excitation energy the probability for the transition to the ground state becomes smaller compared to the total decay probability to other energy regions. For very low excitation energies nuclear structure properties usually play the leading role in describing the decay behavior of atomic nuclei. One interesting question that arises here is how to deal with the intermediate region, where nuclear structure models as well as statistical methods might be applicable. From the statistical model, one would expect a saturation of $\langle b_0 \rangle$ towards low excitation energies, if the involved PSF shows a smooth and continuously falling course. A saturation might be apparent between 5.5 MeV and 6.5 MeV at $\langle b_0 \rangle \approx 66$ % for ^{128}Te and $\langle b_0 \rangle \approx 75$ % for ^{130}Te. However, below that energy region the $\langle b_0 \rangle$ drops down to about 40 % in ^{128}Te and starts to fluctuate between very low values and $\langle b_0 \rangle = 1$. A branching ratio of $\langle b_0 \rangle = 1$ is assigned if no decay of the first excited 2_1^+ state is observed in the HPGe spectra which results in an inelastic cross section of $\sigma_{\gamma\gamma'} = 0$ (see Section 4.6.1).

Certainly, the decay behavior below 5 MeV is determined by the properties of individual excited states. In particular, the three data points between 3.9 MeV and 4.5 MeV indicate ground-state branching ratios of 0.15(3), 0.27(4) and 0.42(5). In the state-to-state analysis of ^{128}Te in Section 5.1.1, a group of 1^+, 2^+ and $(1,2)^+$ levels are observed in this energy region. From the perspective of nuclear structure, some low-lying excited states are understood to arise from the coupling of low-lying phonons. These two- or multi-phonon states usually exhibit enhanced transition rates to low-lying excited states rather than the ground state. However, further data are needed to make a reliable statement about the structure of these states.

The analysis of the average ground-state branching ratios in ^{128}Te and ^{130}Te show that the concept of describing the decay properties of the nucleus by average quantities is applicable only at energy regions with a sufficient amount of nuclear levels. In both nuclei, the smooth behavior of $\langle b_0 \rangle$ above $\sim$5 MeV indicates such energy regime. Below that region, large fluctuations are observed since the average decay properties are governed by a few individual excited states. Therefore, the experimental results above 5 MeV, only, will used in the following discussions and in the comparison to statistical model calculations in Section 5.4.

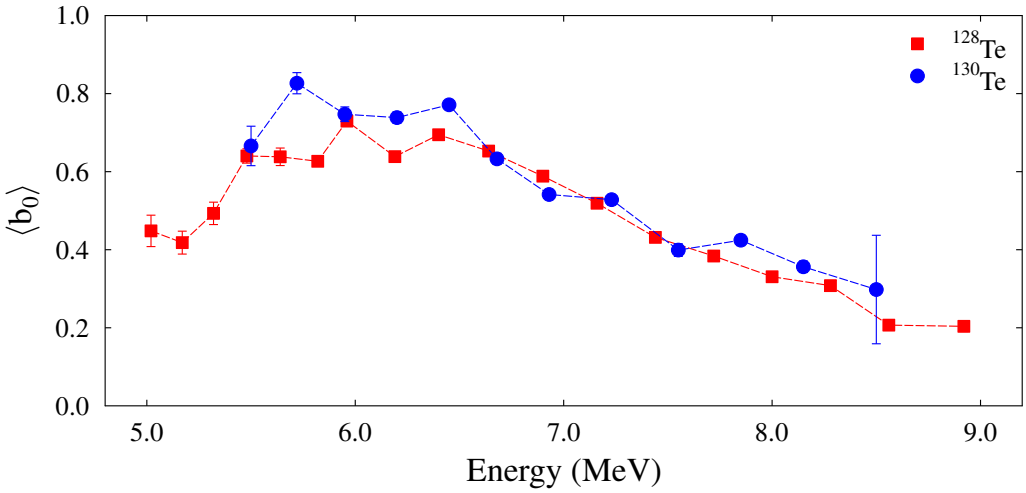

Figure 5.11: Average ground-state branching ratios for ^{128}Te (red squares) and ^{130}Te (blue dots).

5.2.4 Population of low-lying 2^+ levels in ^{128}Te and ^{130}Te

In the determination of the inelastic cross section in Section 4.6.1, the intensity observed in the first excited 2^+ states is investigated. As discussed in Fig. 4.13, the relative population intensities of these levels as a function of their level energy follow an exponential behavior. For a quantitative analysis, for each beam energy setting where at least two low-lying levels are observed the parameter λ is determined for the function $C \cdot \exp[-\lambda \cdot E_x(2_i^+)]$. In Fig. 5.12, the results are shown as a function of the beam energy for ^{128}Te (red squares) and for ^{130}Te (blue triangles). For both isotopes, the λ parameter is approximately constant. The average over all data points of both isotopes is determined to be $\lambda = 2.08(3)$ MeV^{-1} for the covered energy range.

The λ parameters exhibit a particular sensitivity on the underlying photon strength functions for the population of lower-lying excited states. This will be discussed in more detail in Section 5.4.

5.3 γ-γ coincidence measurements with ^{128}Te

5.3.1 Direct population of the 2_1^+ state

The analysis of data from γ-γ coincidence measurements is introduced in Section 4.8. In this Section, the results for the direct population of the first excited 2_1^+ state in ^{128}Te at 743 keV are presented.

5.3.1.1 Average cross section

The procedure to extract transition probabilities for direct transitions to low-lying excited states is explained in Section 4.8.3. The cross sections $\sigma^{sum}_{0_1^+ \to J^\pi \to 2_1^+} = \sigma^{sum}_{J^\pi \to 2_1^+}$ are determined from the analysis of all LaBr-LaBr coincidences and are shown as a function of the beam energy in

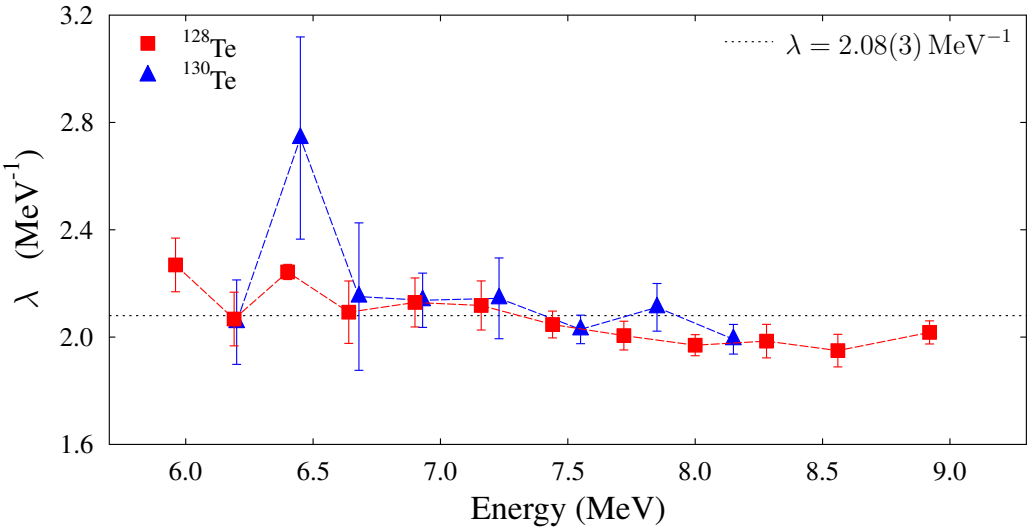

Figure 5.12: The experimental λ parameter determined for ^{128}Te (red squares) and ^{130}Te (blue triangles) as a function of the excitation energy.

Fig. 5.13. It is about $\sigma^{sum}_{J^\pi \to 2^+_1}$ <0.25 mb below 5.5 MeV, while above this energy it increases up to $\sigma^{sum}_{J^\pi \to 2^+_1} = 2.4$ mb.

5.3.1.2 Multipole decomposition of $\sigma^{sum}_{J^\pi \to 2^+_1}$

The cross section $\sigma^{sum}_{J^\pi \to 2^+_1}$ is determined from the analysis of the summed spectra for LaBr-LaBr coincidences. Hence, the total cross section for the transition from the excitation energy region to the 2^+_1 state is extracted. The directional correlation of the emitted photons measured in coincidence in two LaBr detectors can be used to distinguish between different types of transitions, such as $E1$, $M1$ and $E2$ transitions. The corresponding analysis was introduced in Section 4.8.4. Indeed, the product $\langle \varepsilon_1 \cdot W_{corr} \rangle_{J^\pi} \cdot \sigma_{J^\pi \to 2^+_1}$ (see Eq. (4.24)) is determined for each detector combination and compared to simulated directional correlations, where $\sigma_{J^\pi \to 2^+_1}$ are used as fit parameters (see Eq. 4.26).

In total, twelve measurements with beam energy settings from 5.82 MeV to 8.56 MeV have sufficient statistics in the coincidence spectra of two LaBr detectors to perform this kind of analysis for ^{128}Te. The experimental results are fitted to different sets of simulated directional correlation functions. The χ^2_{red} for each fit are shown for the different spin sequences in Fig. 5.14. The supplement ($\delta = 100$) specifies that a mixing ratio for the $1^+ \to 2^+_1$ and $2^+ \to 2^+_1$ transitions is used. For all shown measurements, the lowest χ^2_{red} values are found for pure $1^- \to 2^+_1$ transitions and for the superposition of $1^- \to 2^+_1$ with directional correlations from other spin sequences. The other cases, such as $1^+ \to 2^+_1$ and $2^+ \to 2^+_1$ are omitted in the following. The six combinations that are favored by their low χ^2_{red} value are studied in more detail in Fig. 5.15. The cross section determined from the analysis of the summed LaBr-LaBr coincidences $\sigma^{sum}_{J^\pi \to 2^+_1}$ (black squares) is compared to the fitted cross section $\sigma_{1^- \to 2^+_1}$ (red triangles) assuming purely $1^- \to 2^+_1$ transitions in Fig.5.15.a). A very good agreement is observed, which indicates that the data is consistent with the assumption of a pure $E1$ component in the cross section.

However, in principle additional contributions from other primary excited states may be possible. Figures 5.15.b) and c) show the fit results for including contributions from 1^+ states. Their contribution to the summed cross section is less than 10 % for most of the covered energy

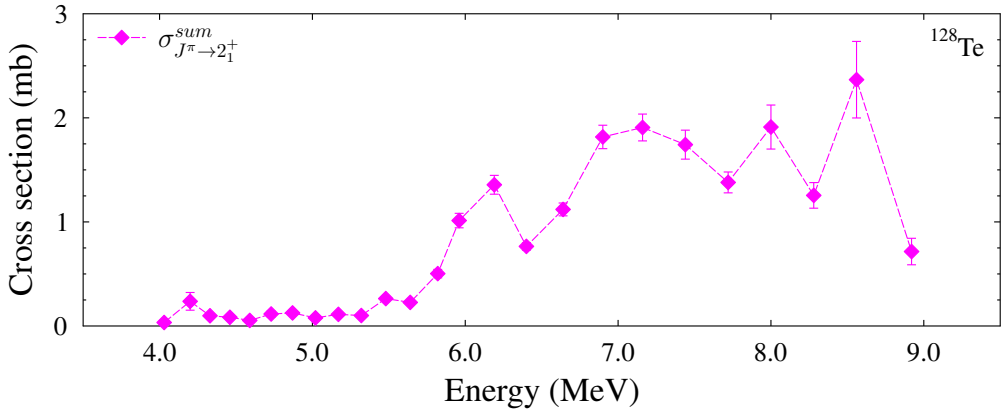

Figure 5.13: Average cross section determined for the direct transition to the first excited 2^+_1 state in ^{128}Te after photo-excitation. The $\sigma^{sum}_{J^\pi \to 2^+_1}$ values (purple diamonds) are shown as a function of the excitation energy.

region except for the data points at 7.44 MeV and 7.72 MeV in b) and 6.9 MeV in c).

The same analysis is performed for a combination of 1^- and 2^+ states that populate the first excited 2^+_1 state in Figs. 5.15.d) and e). The results in d) show that about 10 % to 30 % of $\sigma^{sum}_{J^\pi \to 2^+_1}$ may be attributed to $2^+ \to 2^+_1$ transitions, while an enhanced cross section is observed at 6.9 MeV. Considering pure $E2$ transitions in e), a fraction of ∼50 % and ∼30 % is determined for 7.44 MeV and 7.72 MeV, while the contribution in the remaining energy region is small.

A comparison of the results from b) to e) reveals that the main contributions from 1^+ and 2^+ states are observed at 6.9 MeV and 7.44 MeV. Therefore, it is difficult to unambiguously distinguish between both contributions. Therefore, a simultaneous fit of the cross sections $\sigma_{1^-\to 2^+_1}$, $\sigma_{1^+\to 2^+_1}$ and $\sigma_{2^+\to 2^+_1}$ is performed and shown in Fig. 5.15.f). The cross section $\sigma_{1^-\to 2^+_1}$ determined for this combination exhibits between 52 % and 90 % of the total cross section $\sigma^{sum}_{J^\pi \to 2^+_1}$ for the direct transitions to the 2^+_1 level indicating that a dominant part stems from 1^- states in

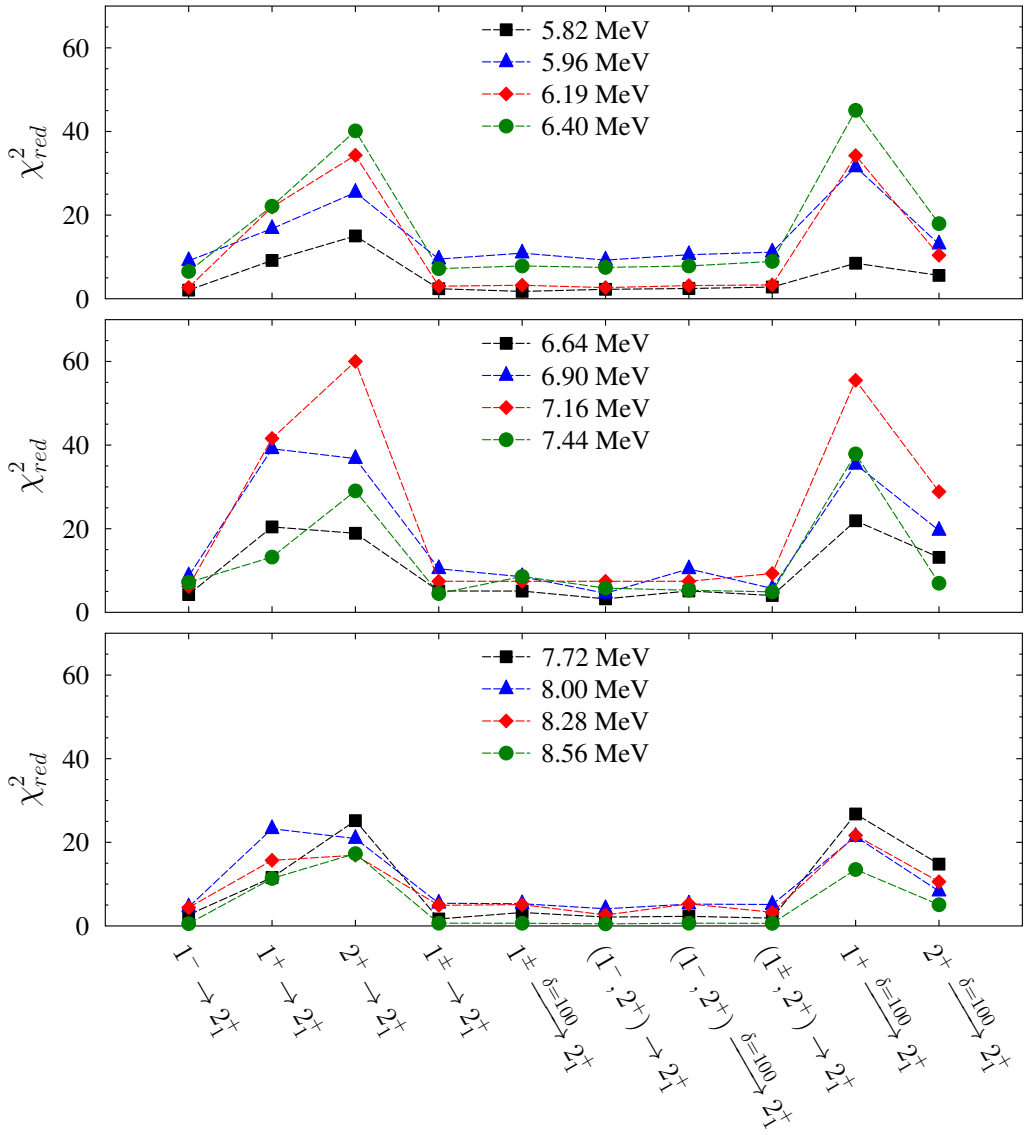

Figure 5.14: Reduced χ^2 values from the multipole decomposition procedure. For each beam energy setting different combinations of transitions are used. For details see text.

the covered energy region.

The presented multipole decomposition analysis shows that it is possible to extract the fraction of $\sigma^{sum}_{J^\pi \to 2^+_1}$ stemming from $E1$ transitions, while an unambiguous separation between contributions from $M1$ and $E2$ transitions is difficult.

5.3.1.3 Average branching ratios

The average ground-state branching ratio $\langle b_0 \rangle$ for ^{128}Te and ^{130}Te (see Section 5.2.3) was extracted from transitions observed in the spectra from the single γ-ray spectroscopy measurements. In particular, the $2^+_1 \to 0^+_1$ transition provided an estimation for the total inelastic cross

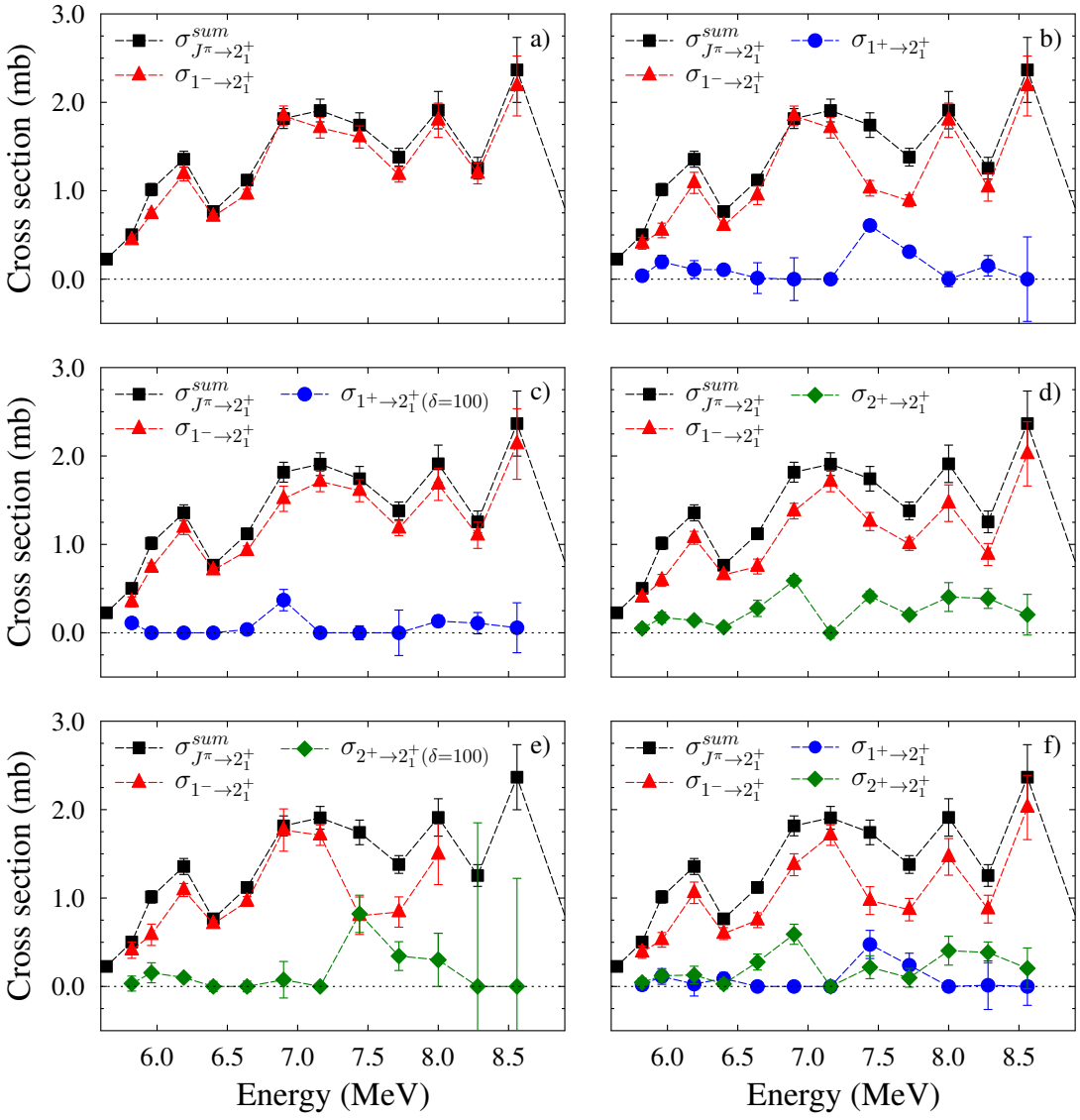

Figure 5.15: Cross section for the direct transition from excited states to the first excited 2^+_1 level extracted from γ-γ coincidences. The cross section $\sigma^{sum}_{J^\pi \to 2^+_1}$ (black squares) extracted from the summed LaBr-LaBr coincidences is compared to fit results taking the directional correlation of $1^- \to 2^+_1$ (red triangles), $1^+ \to 2^+_1$ (blue dots) and $2^+ \to 2^+_1$ (green diamonds) transitions into account. For details see text.

section. However, information about the detailed decay path populating the 2_1^+ state is not easily accessible. With the cross sections $\sigma^{sum}_{J^\pi \to 2_1^+}$ determined in the previous Section it is possible to study its relation to the elastic and inelastic cross section.

One quantity that was studied in ^{140}Ce in Refs. [128, 186] exploiting the γ-γ coincidence method of the γ^3-setup is the ratio of the direct population of the 2_1^+ state to the ground-state transition intensity (see Eq. (4.21))

$$\langle b_{2_1^+} \rangle = \frac{\sum_x \Gamma_{0,x} \cdot \Gamma_{2_1^+,x}/\Gamma_x}{\sum_x \Gamma^2_{0,x}/\Gamma_x} = \frac{\sigma_{J^\pi \to 2_1^+}}{\sigma_{\gamma\gamma}} \,. \tag{5.9}$$

The transition width from the excited state x to 2_1^+ is given by $\Gamma_{2_1^+,x}$, the ground-state transition width is $\Gamma_{0,x}$, and the corresponding total width is expressed by Γ_x. The experimental results for $\langle b_{2_1^+} \rangle$ (black squares) are shown as a function of the excitation energy in the upper panel of Fig. 5.16. In the range from 5 MeV to 9 MeV $\langle b_{2_1^+} \rangle$ is approximately constant.

The total inelastic cross section $\sigma_{\gamma\gamma'}$ is the sum of all events that do not decay directly to the ground state, but decay via cascade transitions. The fraction of $\sigma_{\gamma\gamma'}$ that is attributed to the direct decay to the 2_1^+ state is expressed by $\langle b_{in} \rangle = \sigma_{J^\pm \to 2_1^+} / \sigma_{\gamma\gamma'}$ and shown in the lower panel of Fig. 5.16. Between 5.64 MeV and 6.64 MeV a "bump"-like structure is observed for $\langle b_{in} \rangle$ compared to the smooth behavior before and after this energy range. This indicates that the

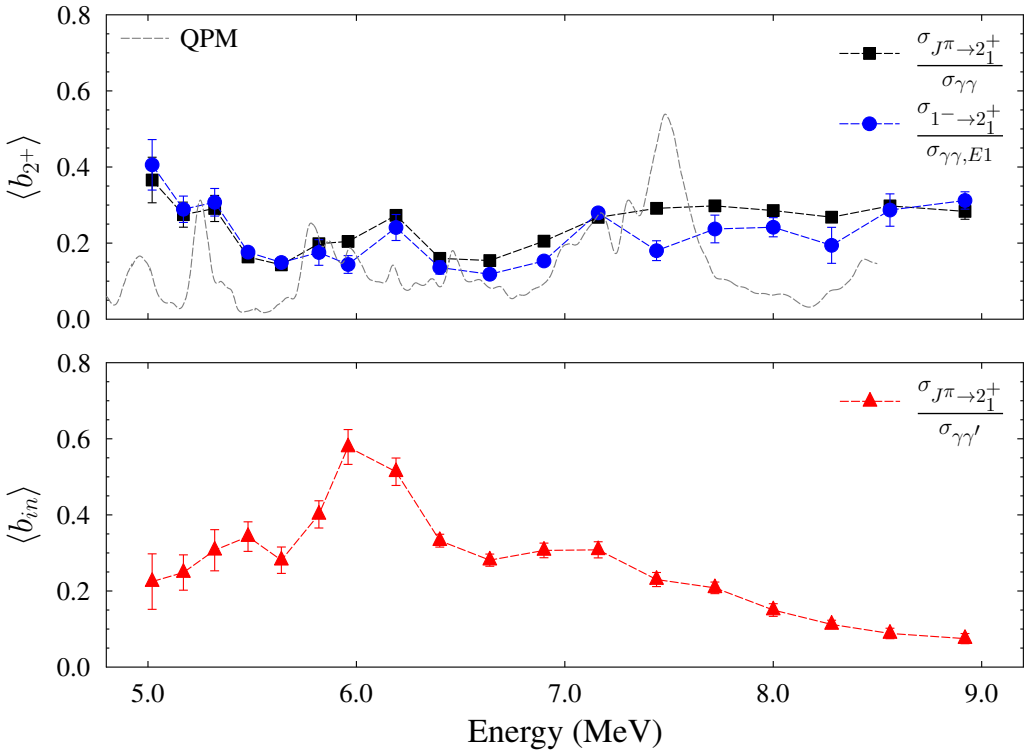

Figure 5.16: Upper panel: The black squares show the $\langle b_{2_1^+} \rangle$ defined in Eq. (5.9). The grey dashed line illustrates predictions from QPM calculations, which include purely $E1$ transitions for the ground state and the first excited 2_1^+. For comparison to the QPM, $\langle b_{2_1^+} \rangle$ is computed taking only the $E1$ part of the cross sections $\sigma_{J^\pi \to 2_1^+}$ and $\sigma_{\gamma\gamma}$ into account (blue dots). Lower panel: Ratio $\langle b_{in} \rangle$ (red triangles) as a function of the excitation energy for ^{128}Te.

excited states in this energy region exhibit an increased probability for the direct population of the 2_1^+ instead of cascading via intermediate levels and make up about 50 % of the total inelastic cross section at in this regime.

5.3.1.4 Comparison to QPM calculations

The average branching ratio $\langle b_{2_1^+} \rangle$ is also determined from QPM calculations on ^{128}Te up to an cutoff energy of 8.5 MeV. The calculated $B(E1)\uparrow$ strength distribution for ground-state excitations was shown in Fig. 5.4 and discussed in Section 5.1.2.3. In addition, the transition width $\Gamma_{2_1^+,x}$ to the first excited 2_1^+ state were computed for each 1^- state. To extract $\langle b_{2_1^+} \rangle$ as defined in Eq. (5.9), total transition width is approximated by $\Gamma_x \approx \Gamma_{0,x} + \Gamma_{2_1^+,x}$. The branching ratios obtained for each excited state are averaged using a Lorentz-shape distribution with a width of 500 keV to account for the spectral photon beam distribution at HIγS. Note, that the calculated $\langle b_{2_1^+} \rangle$ values within the QPM take only 1^- states into account. Hence, for the experiment only the contributions stemming from $E1$ excitations are extracted from the cross sections $\sigma_{J^\pi \to 2_1^+}$ and $\sigma_{\gamma\gamma}$ from the multipole decomposition and the I_{M1}/I_{E1} ratio, respectively. The resulting branching ratios are shown in the upper panel of Fig. 5.16 (blue dots). The QPM predictions are displayed as dashed grey curve. The QPM calculations are in very good agreement to the experimental results over the covered energy range. So far, the fragmentation of the $B(E1)\uparrow$ strength is usually well described by the coupling of the PDR doorway 1^- states to complex configurations (see Section 5.1.2.3 and Refs. [55, 56]). The present agreement in $\langle b_{2_1^+} \rangle$ indicates that the QPM is also appropriate in describing the coupling of the PDR to the first excited 2_1^+ state in ^{128}Te. The same observation was made for ^{140}Ce recently published in Ref. [128].

5.3.2 Photoabsorption cross section build on the 2_1^+ state

In the laboratory, photoabsorption experiments are usually performed with the nucleus being in the ground state. Photoabsorption from an excited state is a challenging if not impossible task, up to now. For the case of the first excited 2_1^+ state, one would need to measure the average transition widths $\Gamma_{2_1^+,x}$ from the 2_1^+ level to an excited state x. Then it would be possible to determine the photoabsorption cross section build on the 2_1^+ state in the same fashion as for the ground state. The corresponding relation is adapted from Eq. (4.18)

$$\sigma_\gamma^{2_1^+} = (\pi\hbar c)^2 \cdot \frac{g_{2_1^+}}{(E_x - E_{2_1^+})^2} \cdot \frac{\sum_x \Gamma_{2_1^+,x}}{\Delta E} \,, \tag{5.10}$$

with $g_{2_1^+} = (2J_x + 1)/(2J_{2_1^+} + 1)$ and $E_{2_1^+}$ being the level energy of the 2_1^+ state. However, it is not possible to extract $\sum_x \Gamma_{2_1^+,x}$ directly from NRF measurements. The quantity that can be determined from the analysis of the γ-γ coincidence data at the γ^3-setup is the average cross section $\sigma^{sum}_{J^\pi \to 2_1^+}$ for the direct population of the first excited 2_1^+ state following photo-excitation. This can be expressed as

$$\sigma^{sum}_{J^\pi \to 2_1^+} = (\pi\hbar c)^2 \cdot \frac{g_0}{E_x^2} \cdot \frac{\sum_x \Gamma_{2_1^+,x} \cdot \Gamma_{0,x}/\Gamma_x}{\Delta E} \,, \tag{5.11}$$

where $\Gamma_{0,x}$ is the ground-state transition width and Γ_x the total width of the state x. The spin factor is given by $g_0 = (2J_x+1)/(2J_0+1)$. Note, that the experimental observable is proportional to $\sum_x \Gamma_{2_1^+,x} \cdot \Gamma_{0,x}/\Gamma_x$ including the ground-state branching ratio $\Gamma_{0,x}/\Gamma_x$ for each excited state x. The whole analysis procedure considers average quantities, only. Therefore, it can be corrected by the average ground-state branching ratio $\langle b_0 \rangle$ determined in Section 5.2.3 to extract

$$\sum_x \Gamma_{2_1^+,x} = \frac{\sum_x \Gamma_{2_1^+,x} \cdot \Gamma_{0,x}/\Gamma_x}{\langle b_0 \rangle} \,. \tag{5.12}$$

Implementing this relation into Eq. (5.11), it can be written as

$$\sum_x \Gamma_{2_1^+,x} = \frac{\sigma^{sum}_{J^\pi \to 2_1^+}}{\langle b_0 \rangle} \cdot \frac{E_x^2}{g_0} \cdot \frac{\Delta E}{(\pi\hbar c)^2} \,. \tag{5.13}$$

Finally, the combination of Eqs. (5.10) and (5.13) leads to the simple relation that enables an experimental extraction of the average photoabsorption cross section build on the 2_1^+ state

$$\sigma_\gamma^{2_1^+} = \frac{g_{2_1^+}}{g_0} \cdot \left(\frac{E_x}{E_x - E_{2_1^+}} \right)^2 \cdot \frac{\sigma^{sum}_{J^\pi \to 2_1^+}}{\langle b_0 \rangle} \,. \tag{5.14}$$

It should be emphasized, that all terms in this equation are known either from experiment or theoretical considerations of the excitation mechanism. Since real-photon scattering experiments are particularly selective to dipole excitations the spin factors $g_{2_1^+}$ and g_0 are known. For an even-even nucleus, such as ^{128}Te, predominantly $J_x = 1$ states are excited from the $J_0 = 0^+$ ground state. The excitation energy E_x is known from the photon beam, which is quasi-monochromatic on the scale of 200 keV to 300 keV. The other two quantities, $\sigma^{sum}_{J^\pi \to 2_1^+}$ and $\langle b_0 \rangle$ were determined in previous Sections.

The results for $\sigma_\gamma^{2_1^+}$ (red dots) are displayed together with σ_γ (black squares) in the upper panel of Fig. 5.17. It is noted, that they are shown as a function of the γ-ray energy E_γ. For the photoabsorption cross section from the ground state $E_\gamma = E_{beam}$, while for the absorption from the 2_1^+ state $E_\gamma = E_{beam} - E_{2_1^+}$. Hence, both data sets are shifted by 743 keV. The absolute values for $\sigma_\gamma^{2_1^+}$ are about an order of magnitude smaller than σ_γ for most of the covered energy region. Note, that the shown experimental values are the total photoabsorption cross sections, i.e. in general they include contributions from $E1$, $M1$ and $E2$ transitions.

One of the key points of this thesis is the determination of the photon strength function for $E1$ transitions. It is directly linked to the corresponding photoabsorption cross section (see also Eq. (2.9))

$$f_{E1}(E_\gamma) = \frac{1}{(\pi\hbar c)^2} \cdot \frac{\sigma_{\gamma,E1}}{g \cdot E_\gamma} \,. \tag{5.15}$$

Here $\sigma_{\gamma,E1}$ is the fraction of the photoabsorption cross section attributed to $E1$ excitations. It is assumed that the I_{M1}/I_{E1} ratio determined for the elastic cross section in Section 5.2.2 is a good estimation for the fraction of $E1$ induced transitions in the photoabsorption cross section from the ground state. Thus, it is used to determine

$$\sigma_{\gamma,E1} = \sigma_\gamma \cdot \frac{I_E}{I_{E1} + I_{M1}} = \frac{\sigma_\gamma}{1 + I_{M1}/I_{E1}} \,. \tag{5.16}$$

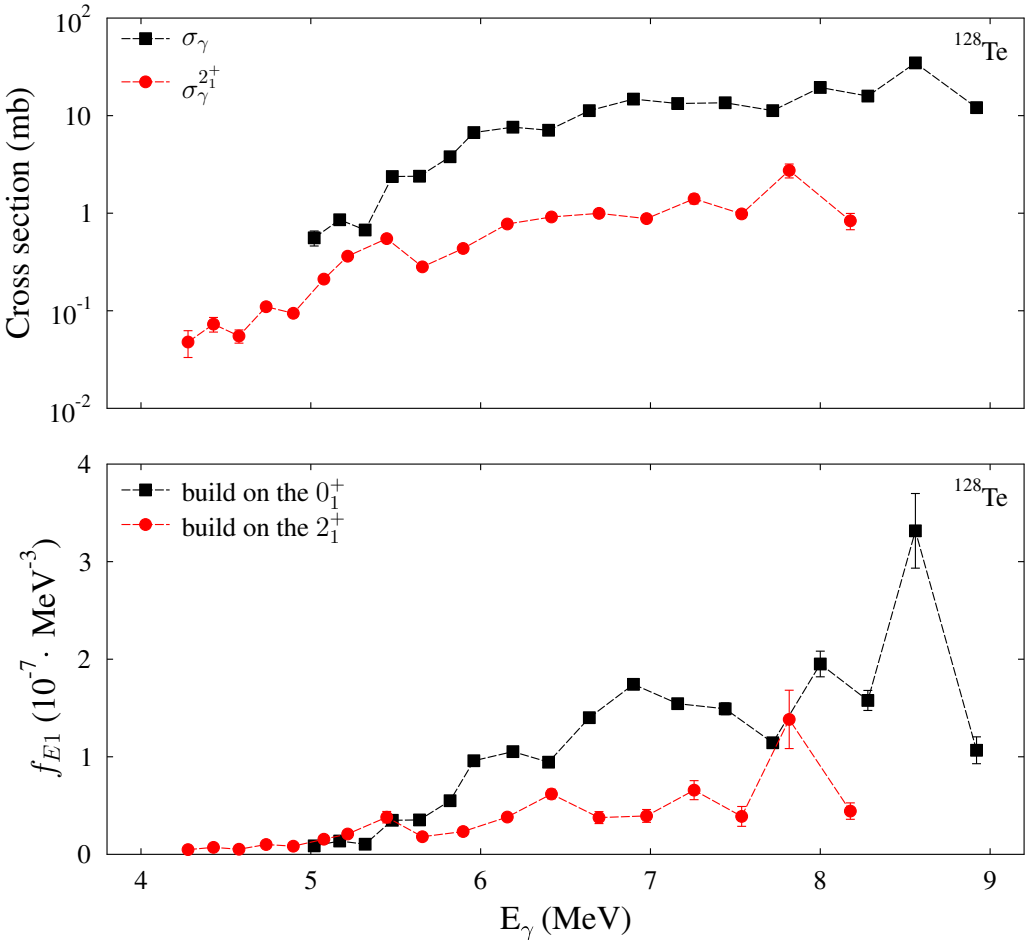

Figure 5.17: Upper panel: Photoabsorption cross section from the ground state (σ_γ, black squares) and from the first excited 2_1^+ state ($\sigma_\gamma^{2_1^+}$, red dots). Lower panel: Photon strength functions for $E1$ transitions build on the ground state (black squares) and on the 2_1^+ state (red dots).

The $E1$ fraction of $\sigma_\gamma^{2_1^+}$ was determined by the multipole decomposition performed in the previous Section. The f_{E1} build on the ground state and the one build on top of the first excited 2_1^+ state are shown in the lower panel of Fig. 5.17. According to the Brink-Axel hypothesis [113, 114] the photon strength function is independent of the excitation energy. Thus, both f_{E1} as a function of E_γ are expected to be equivalent to each other. However, a discrepancy of the absolute scale of a factor of three to four is observed been both data sets, in particular above 5.5 MeV. Below that energy, both functions seem to follow a comparable smooth trend.

Based on the available data one can conclude that the Brink-Axel hypothesis is not valid below the neutron separation threshold in ^{128}Te especially for the energy range between 5.5 MeV and 8 MeV. An enhancement of the photon strength function build on the ground state is observed in comparison to the one build on the 2_1^+ state. Furthermore, it is emphasized that this is the first model-independent determination of the $E1$ photon strength function build on an excited state. The NRF reaction guarantes that predominantly 1^- states are populated from the 0^+ ground state in ^{128}Te. Alternative approaches, that were discussed in Section 1.2 are usually dependent on nuclear reaction models and statistical model calculations.

5.4 Comparison to statistical model calculations

This Section is dedicated to the question if the extracted experimental results for the average decay behavior in ^{128}Te and ^{130}Te can be described within the statistical approach. It is important to tackle this problem, since calculations within the statistical model are often used to extract full photoabsorption cross sections from photon scattering experiments below particle-emission thresholds (see, e.g. [66, 72]). However, it is not clear down to which energy region this approach is applicable. Another task that is interesting to study is the influence of the low-energy part of photon strength functions and in particular the one for $E1$ transitions on the decay behavior of both tellurium isotopes. Below a certain excitation energy, that is usually not well defined, the photon strength function cannot be determined by measuring the photoabsorption cross section, because the number of nuclear levels is not sufficient for a reliable extraction of average decay properties.

The `DICEBOX` code

In the following, the experimental results are compared to simulations within the statistical model. For this purpose a modified version of the Monte Carlo based `DICEBOX` code [187] is used which was adapted to simulate γ cascades from (γ,γ') reactions. The two main input quantities are the nuclear level density (NLD) and photon strength functions (PSF) for $E1$, $M1$ and $E2$ transitions. As a first step, the code generates an artificial nucleus (called nuclear realization) with a random level scheme according to the properties given by the NLD and the PSF's. For each level the partial radiation width to the ground state and a total radiation width is assigned taking Porter-Thomas fluctuations into account [188]. Below a critical energy E_c the level scheme as well as the decay properties of the nucleus are assumed to be fully known and are taken from experimental data. Hence, for each nuclear realization the low-energy part is identical, whereas the spectrum above E_c varies. In the simulations for ^{128}Te and ^{130}Te the critical energy is set to $E_c = 2.6$ MeV, because their level scheme and the corresponding spectroscopic properties are presumably completely known (see [178, 189]). After the generation of a nuclear realization, the levels are randomly "excited" via photoabsorption according to a predefined photon flux distribution and their ground-state transition width. The photon flux distribution is taken from the experiment. The randomly populated level decays back to the ground state via γ cascades. In this way, the real NRF experiment is simulated within the statistical model repeating the excitation process 10^5 times per beam energy. To estimate the influence of Porter-Thomas fluctuations on the average decay properties the simulation is performed for 30 different randomly "diced" nuclear realizations. For each realization, the decay properties are extracted and averaged. Finally, a mean value with its standard deviation is determined from 30 nuclear realizations.

Nuclear level density for ^{128}Te and ^{130}Te

As outlined in Section 2.1.1 the NLD below the neutron separation threshold is usually not known experimentally. Thus, the NLD is parametrized by the BSFG model (see Section 2.1.1). For ^{128}Te, the parameters $a = 13.36$ MeV^{-1} and $E_1 = 1.04$ MeV are used, while for ^{130}Te the values are $a = 12.36$ MeV^{-1} and $E_1 = 1.16$ MeV. These parameters are determined from Ref. [143]. A comparison of the resulting level densities as a function of the excitation energy is given in Fig. 5.18. The level density for ^{128}Te (black solid line) is between a factor of two at

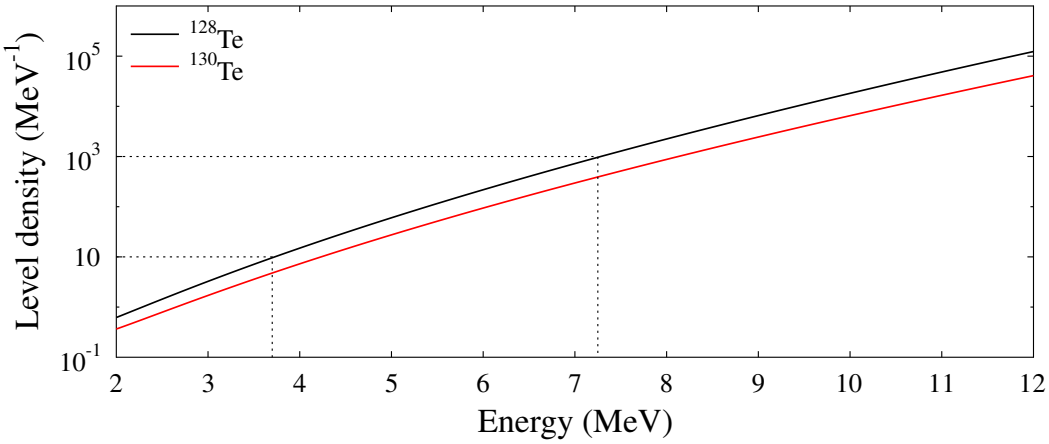

Figure 5.18: Level density functions for ^{128}Te (black solid line) and ^{130}Te (red solid line). The dotted lines indicate the region where the level density increases from 10 levels per MeV to 1000 levels per MeV.

3.5 MeV and a factor of three at 12 MeV larger than for ^{130}Te (red solid line). The dotted lines are meant to lead the eye.

Photon strength functions for ^{128}Te and ^{130}Te

For the comparison between the experimental data and the DICEBOX simulations different sets of $E1$-PSF's are used and are illustrated in Fig. 5.19. One commonly applied model is the SLO (dotted magenta line) that is motivated by the shape of the photoabsorption cross section around the maximum of the IVGDR. The other models use experimental results. The photon strength function for $E1$ excitations in ^{128}Te is determined in Section 5.3.1 (see Fig. 5.17). In the case of ^{130}Te it will be assumed that the PSF determined from the photoabsorption cross sections is dominantly attributed to $E1$ transitions. As previously discussed, the PSF's at energies below $\sim$5 MeV are not known. Thus, three different extrapolations to low γ-ray energies are used. The first one is the parametrization from the generalized lorentzian (see, e.g. [150]) that is shown in Fig. 5.19 (GLOexp, dashed-dotted green line), which is similar to the SLO, but has an energy-dependent damping width and a non-zero limit for γ-ray energies approaching zero. The other two extrapolations are motivated by the exponential decrease of the photoabsorption cross section towards low excitation energies (see, e.g. Fig. 5.8). This low-energy trend was observed in several nuclei so far [71, 73, 185]. Hence, the cross section below 5 MeV is extrapolated by

$$\sigma_\gamma(E_\gamma < 5\ \text{MeV}) = A \cdot \exp(B \cdot E_\gamma)\ . \tag{5.17}$$

For ^{128}Te, the function for EXPflat (solid red line) is fitted to the experimental σ_γ between 3 MeV and 4.7 MeV. The parameters for EXPsteep (dashed blue line) are determined in the range from 4.8 MeV and 5.8 MeV. In a similar fashion, the parameters for ^{130}Te are determined. All parameters are summarized in Table 5.1. Models for the $M1$-PSF and $E2$-PSF, such as the single-particle and the SLO parametrization, respectively, are taken from Ref. [190]. The latter two PSF's are usually about one to two orders of magnitued smaller than the $E1$-PSF which is in accordance to the relative probabilities for $E1$, $M1$ and $E2$ transitions discussed for NRF experiments (see Section 2.2).

	A_{flat} (10^{-3} mb)	B_{flat} (MeV^{-1})	A_{steep} (10^{-7} mb)	B_{steep} (MeV^{-1})
^{128}Te	6.75	0.75	6.16	2.7
^{130}Te	2.5	0.75	5.3	2.3

Table 5.1: Parameters for the exponential parametrization of the photoabsorption cross section below 5 MeV.

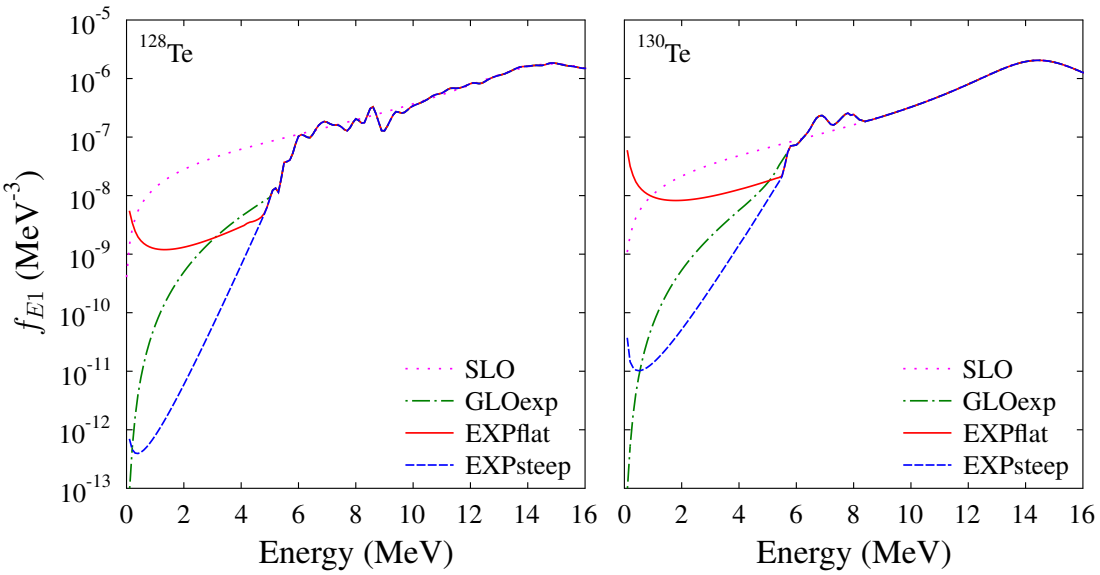

Figure 5.19: Models for the $E1$-PSF used in the statistical model simulations with DICEBOX. The $E1$-PSF models used in the simulations for ^{128}Te are illustrated in the left panel, while the right panel shows the models for ^{130}Te. For details see text.

5.4.1 Comparison to $\langle b_0 \rangle$ and λ for ^{128}Te and ^{130}Te

The experimental results for $\langle b_0 \rangle$ and λ are compared to the values from the DICEBOX simulations for ^{128}Te and ^{130}Te. In these simulations the different $E1$-PSF models from Fig. 5.19 are tested.

General discussion

For a better understanding of the upcoming discussion, it is important to understand how the PFS's influence the decay behavior of the nucleus. Due to the $J_0^\pi = 0^+$ ground state of even-even nuclei, such as ^{128}Te and ^{130}Te, $J^\pi = 1^-$ states are predominantly populated from the ground state via $E1$ excitations. Their subsequent decay is in general governed by the absolute scale and the γ-ray energy dependence of all PSF's. For instance, the direct decay back to the ground state is solely described by the value of $f_{E1}(E_\gamma)$ at $E_\gamma = E_x$. For transitions to lower-lying states other than the ground state the PSF values at $E_\gamma < E_x$ are important. Assuming that the $E1$-PSF is kept fixed then the probability for ground-state transitions of 1^- states is also kept fixed. Now, a variation of the absolute scale of the $M1$-PSF will translate into a shift of $\langle b_0 \rangle$. An increase of the $M1$-PSF enhances the $M1$ transition probability for all E_γ relative to the probability for $E1$

transitions. This results in a reduction of $\langle b_0 \rangle$, because the ground state can only be reached by $E1$ transitions. The opposite effect is achieved for a decrease of the overall $M1$-PSF.

Another way to influence the simulated $\langle b_0 \rangle$ is to change the low-energy behavior of the $E1$-PSF. If the $E1$-PSF is suppressed at $E_\gamma < E_x$ relative to the value at E_x then deexcitations involving low γ-ray energies are also suppressed. Hence, the average ground-state branching ratio is increased. In contrast to this, an enhancement of the low-energy part of the $E1$-PSF will result into an increased transition probability with $E_\gamma < E_x$ and, thus, into a decrease of $\langle b_0 \rangle$.

A similar impact is found for the parameter λ which describes the relative population intensity of low-lying 2^+ states (see Section 5.2.4). Consequently, the population of these states is connected to the probability for γ cascades via intermediate levels, i.e. the behavior of the PSF's at low γ-ray energies play an important role.

A detailed introduction into the concept of photon strength functions and their impact on the decay behavior of the nucleus is found in Section 2.1.2.

The following systematic analysis aims for the identification of the type of $E1$-PSF that describes the experimental data the best. However, the absolute scale of the $M1$-PSF is not known and, hence, is used as a free parameter. For the sake of comparability between the results from different $E1$-PSF's, the $M1$-PSF is adjusted to reproduce the experimental $\langle b_0 \rangle$ values at excitation energies above 7 MeV, where the statistical model is assumed to be appropriate in the description of the decay behavior.

^{130}Te

The simulated $\langle b_0 \rangle$ results for ^{130}Te are given in Fig. 5.20.a) and b) together with the experimental values. One can see, that the simulation with the SLO clearly underestimates the experimental data points even though the $M1$-PSF is set close to zero. This indicates that the $E1$-PSF at $E_\gamma < E_x$ is too high. Therefore, the other $E1$-PSF models exhibit a suppression at low γ-ray energies. Consequently, their $\langle b_0 \rangle$ values show a much better agreement with the experimental results above 6.5 MeV. Nevertheless, all models fail in the description of $\langle b_0 \rangle$ for the energy region below 6.5 MeV.

The GLOexp and the EXPsteep overestimate the values for λ shown in Fig. 5.20.c) and d). In general, an increase of λ corresponds to a steeper decreasing exponential function describing the relative population of the low-lying 2^+ states (compare Section 4.7). This means, that the energetically lowest lying 2^+ states are much stronger populated than the other ones. Hence, the associated $E1$-PSF is too strongly suppressed at low γ-ray energies ($\leq$3 MeV), which are needed for the population of the higher-lying 2^+ states via multi-step cascades. Therefore, models which do not exhibit a too strong decrease towards low E_γ show the best agreement, such as the SLO and the EXPflat. This clearly shows that the parameter λ is well suited to put a complementary contrain on the low-energy behavior of the $E1$-PSF compared to the discussion of $\langle b_0 \rangle$.

The combination of the information determined from the analysis of $\langle b_0 \rangle$ and λ leads to the conclusion that the model that describes both quantities simultaneously for excitation energies above 6.5 MeV is the EXPflat. However, none of the models is able to reproduce the $\langle b_0 \rangle$ for energies below 6.5 MeV. Hence, it is concluded that the statistical model is not an appropriate tool to describe the decay behavior of ^{130}Te in that energy region. This analysis together with a brief discussion were published as a letter in Ref. [73].

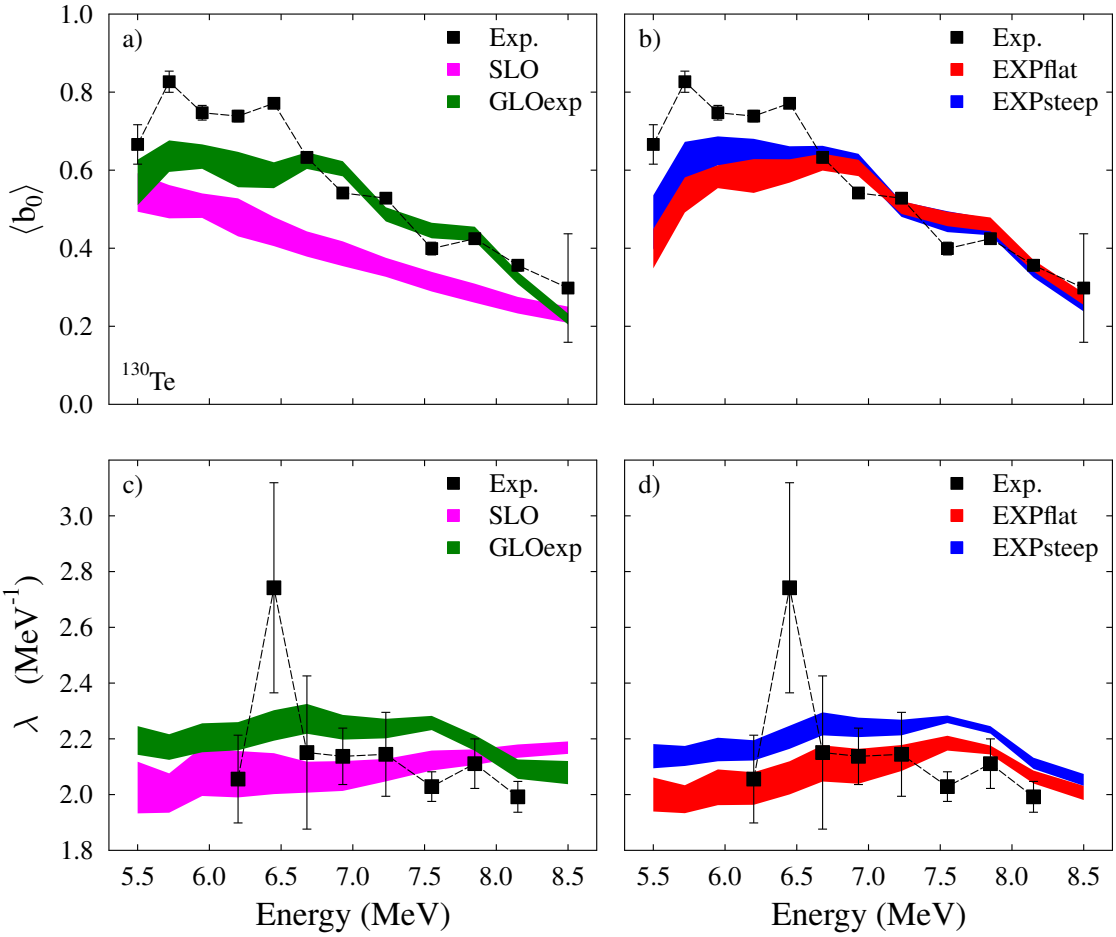

Figure 5.20: The average ground-state branching ratio $\langle b_0 \rangle$ and the parameter λ in ^{130}Te are compared as a function of the excitation energy to stastistical models calculations.

^{128}Te

Figure 5.21 shows the comparison of the experimental data to the DICEBOX simulations for ^{128}Te. A similar behavior of the different $E1$-PSF's is observed as for the case of ^{130}Te. The SLO completely fails in the description of $\langle b_0 \rangle$, while the other models show a good agreement. Even below 6.5 MeV they reproduce the average ground-state branching ratios fairly well. For the parameter λ the simulated results show the same effect as a function of the $E1$-PSF as for ^{130}Te. The best agreement is also found for the EXPflat model. The GLOexp and EXPsteep overestimate λ at all excitation energies.

Contrary to ^{130}Te, the statistical approach seems to be able to describe $\langle b_0 \rangle$ and λ in ^{128}Te for the given energy range.

5.4.2 Comparison to $\langle b_{2_1^+} \rangle$ and $\langle b_{in} \rangle$ for ^{128}Te

In the analysis of the γ-γ coincidence data it was possible to investigate the direct decay from primary excited states to the first excited 2_1^+ level in ^{128}Te (see Section 5.3.1). The extracted cross section $\sigma^{sum}_{J^\pi \to 2_1^+}$ is compared to the elastic and inelastic cross section, respectively, expressed in the branching ratio $\langle b_{2_1^+} \rangle$ and the quantity $\langle b_{in} \rangle$. In the following, the experimental

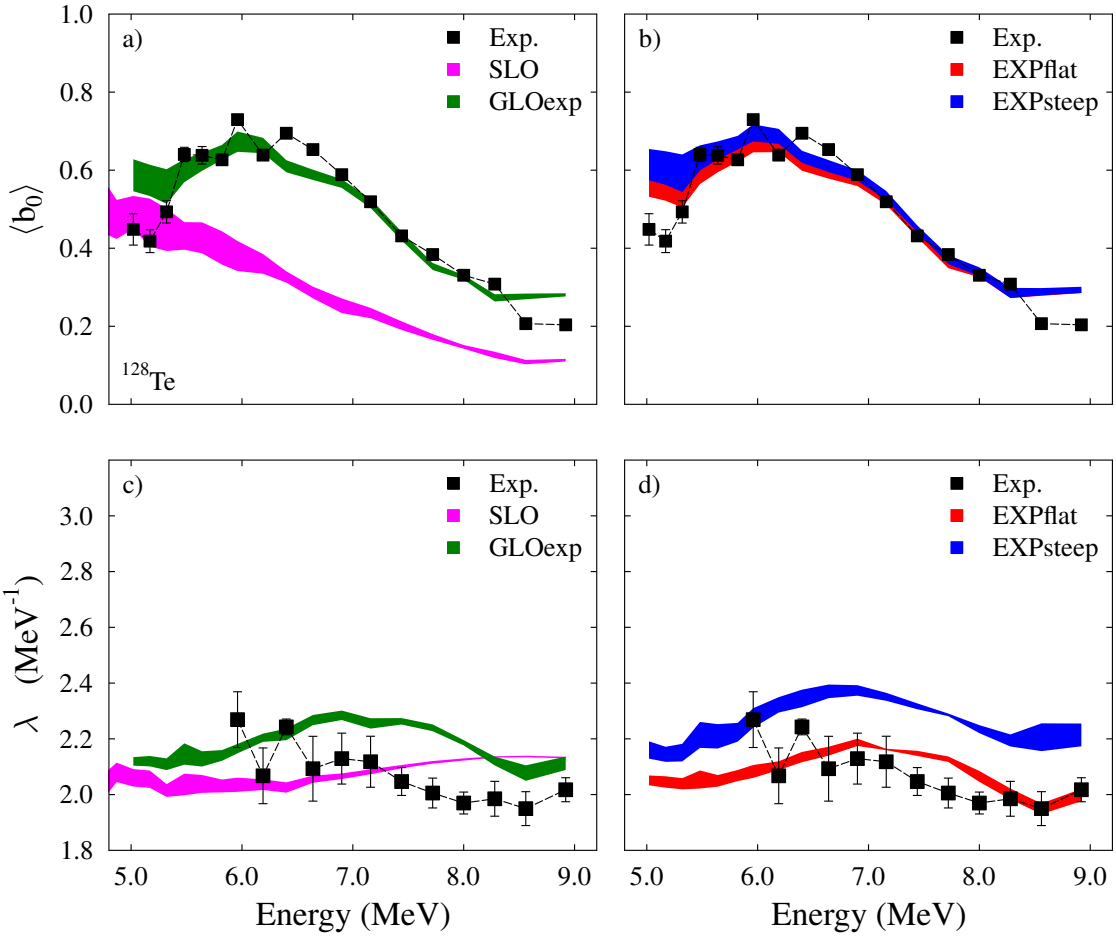

Figure 5.21: The average ground-state branching ratio $\langle b_0 \rangle$ and the parameter λ in ^{128}Te are compared as a function of the excitation energy to stastistical models calculations.

results are discussed together with the statistical model calculations illustrated in Fig. 5.22. The experimental data for $\langle b_{2_1^+} \rangle$ show a constant value of about $\langle b_{2_1^+} \rangle \approx 0.3$ above 7 MeV pointing out that the relative transition probability to the ground state and the first excited 2_1^+ state is independent of the excitation energy. Below that region fluctuations are apparent. The SLO model shows a constant trend as a function of the excitation energy as well, but underestimating the experimental values above 7 MeV. However, a good agreement within the Porter-Thomas fluctuations is achieved below 7 MeV.

The other models, that include experimental results for the $E1$-PSF above 5 MeV exhibit a different structure in $\langle b_{2_1^+} \rangle$ as a function of the energy compared to the SLO calculations. Still, none of these models is doing well in the comparison to the experiment. According to the Brink-Axel hypothesis the strength functions on the ground state are equivalent to ones build on top of excited states. This assumption is one the features in the DICEBOX code. The discrepancy between the experimental data points and the simulations provides additional evidence for the violation of the Brink-Axel hypothesis below the neutron-emission threshold in ^{128}Te; at least for the comparison of the PSF's build on the ground state and the first excited 2_1^+ state. This statement was already pointed out in Section 5.3.2.

In the two lower panels of Fig. 5.22 the ratio $\langle b_{in} \rangle$ is shown, which is the contribution of the direct population of the 2_1^+ state relative to the total inelastic cross section. In the DICEBOX

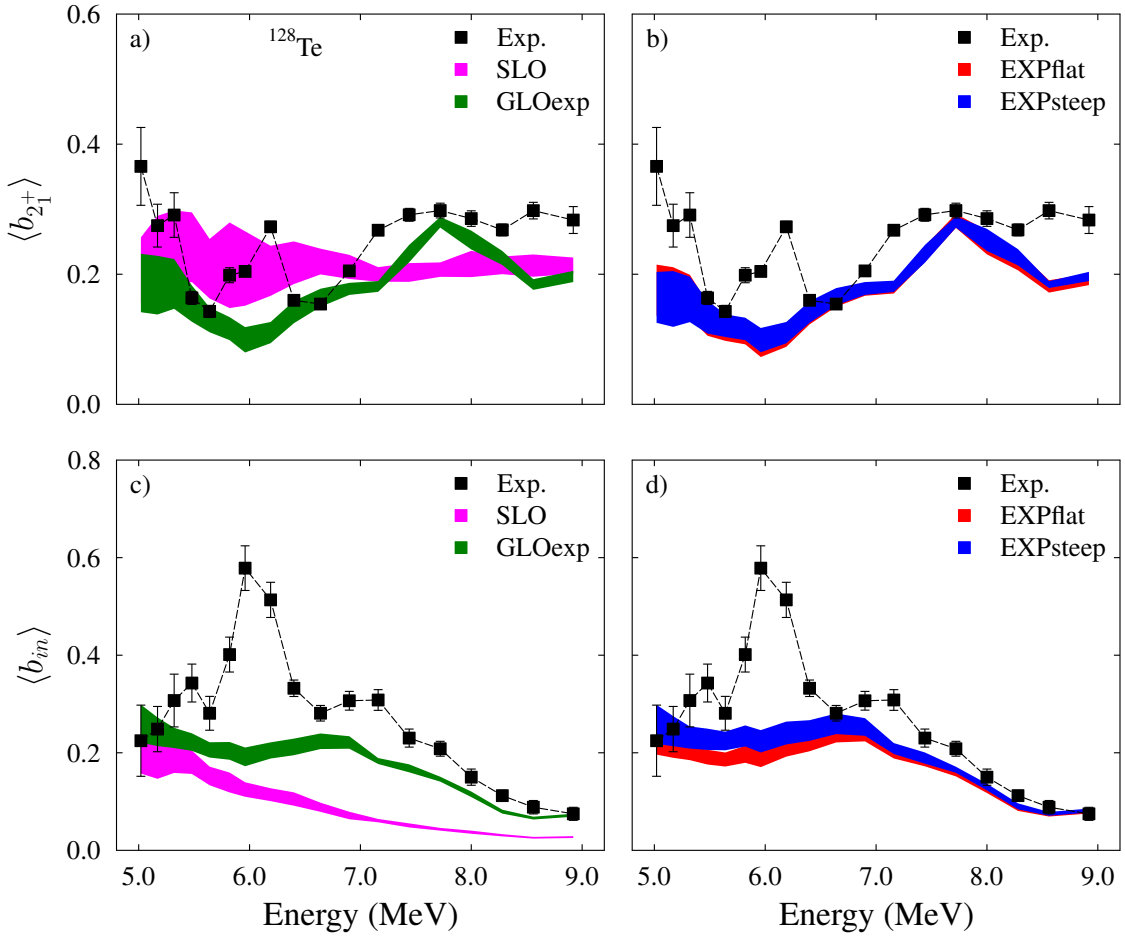

Figure 5.22: Comparison of $\langle b_{2_1^+} \rangle$ and $\langle b_{in} \rangle$ extracted from NRF data on ^{128}Te to the statistical model.

calculations, the de-excitation is ruled by stastistical decays. The simulations for GLOexp, EXPflat and EXPsteep reflect roughly the overall shape of $\langle b_{in} \rangle$ above 6.5 MeV even though they predict slightly lower absolute values. However, a strong enhancement of the probability for direct transitions to the 2_1^+ state is observed between 5.5 MeV and 6.5 MeV in the experiment. This feature cannot be described by any of the $E1$-PSF models. This indicates that other effects beside the statistical decay play particular role in that region. Interestingly enough, the I_{M1}/I_{E1} ratio (see Fig. 5.10) for the ground-state decay has a clear minimum in the same energy range, i.e. this region is dominated by the ground-state transition of 1^- states. In addition, the analysis of the multipole components of $\sigma_{J^\pi \to 2_1^+}$ (see Section 5.3.1) revealed that the cross section between 5.5 MeV and 6.5 MeV arises predominantly from $1^- \to 2_1^+$ transitions independent of the components used in the associated fitting procedure. These observations lead to the conclusion that this set of excited 1^- states exhibit a different structure and decay behavior compared to the other excited states.

5.4.3 Conclusion

This Section was dedicated to the comparison of the decay properties extracted from the photon-scattering experiments with ^{128}Te an ^{130}Te to statistical model calculations. Although, none of

the $E1$-PSF models that were tested reproduces all experimental results simultaneously for the covered excitation energy region. Hence, the stastistical approach may not be applicable for this energy regime in ^{128}Te and ^{130}TE. In addition, one may note that the model that describes the data best compared to the others is the EXPflat. This $E1$-PSF model is composed of experimentally determined values above 5 MeV and an extrapolation to low γ-ray energies modeled by an exponential function. Due to the latter extrapolation, the low-energy part is strongly suppressed in comparison to the SLO model. The SLO, however, is commonly used in stastistical model calculations for the correction of experimental data to extract average quantities, such as photoabsorption cross sections (see, e.g. [66, 72]). Moreover, it is applied in Hauser-Feshbach calculations [107] for astrophysical reaction scenarios (see, e.g. [115]). Indeed, further investigations are mandatory.

Furthermore, the discussion about $\langle b_{2_1^+} \rangle$ and $\langle b_{in} \rangle$ presented additional hints for the violation of the Brink-Axel hypothesis in ^{128}Te. In particular, in the region between 5.5 MeV and 6.5 MeV a different decay behavior of the 1^- states is observed indicating a different underlying structure of the states located in the region of the PDR.

6 Summary & Outlook

Within the scope of this thesis the low-lying dipole strength below the neutron separation threshold in ^{128}Te and ^{130}Te was studied exploiting photon-scattering experiments at DHIPS and at the novel γ-γ coincidence setup γ^3 at the HIγS facility. The investigation was separated into two approaches: A state-to-state analysis of dipole-excited states determining spin-parity quantum numbers and the $B(E1)\uparrow$ strength distribution for isolated levels. The other approach followed the analysis of average quantities, such as photoabsorption cross sections and average branching ratios. Of particular interest was the analysis of the γ-γ coincidence data obtained from the combination of the γ^3-setup with the quasi-monochromatic photon beam at HIγS. It allows to measure the direct population of the first excited 2_1^+ level as a function of the excitation energy via the $(\gamma,\gamma'\gamma'')$ coincidence method. Due to the varying detector positions a multipole decomposition of the associated average cross section is performed. Hence, a distinction of the set of states, i.e. $J^\pi = 1^-, 1^+$ or 2^+, that directly decay to the 2_1^+ level can be made.

The average branching ratios as well as the relative population intensities of low-lying 2^+ states were compared to calculations within the statistical model. A good agreement to the experimental results is found for excitation energies above $\sim$6.5 MeV. Below that energy, the statistical model fails in the description of the measured data indicating that it is not valid in this regime. In particular, in the energy region between 5.5 MeV and 6.5 MeV an enhanced population of the 2_1^+ state via direct transitions is observed relative to the total inelastic cross section. This points to a different underlying structure of the 1^- states compared to photo-excited states in other energy regions.

Furthermore, the photoabsorption cross section from the first excited 2_1^+ state in ^{128}Te was extracted and linked to the associated PSF. This is the first model-independent determination of the PSF build on an excited state from an NRF measurement. A comparison to the photon strength function on top of the ground state suggests that the Brink-Axel hypothesis is violated in ^{128}Te below the neutron separation energy. Instead, an enhanced ground-state transition probability is observed between 5.5 MeV and 8 MeV.

Open tasks

Further investigations of the decay behavior of dipole-excited states in the vicinity of the neutron separation threshold are crucial to learn more about the nature of the low-lying dipole strength in ^{128}Te. Experiments with complementary reactions, such as inelastic proton scattering have proven to be a useful tool to study decay properties of individual nuclear levels.

The SONIC@HORUS setup [156] at the tandem particle accelerator at University of Cologne is highly suited to investigate the single-particle structure of isolated excited states in $(p, p'\gamma)$ reactions. Exploiting $p-\gamma$ coincidences it is possible to extract even weak branching ratios to lower-lying excited states and, thus, probe the corresponding wave functions. Therefore, measurements of the decay behavior of 1^- states in ^{128}Te are of high interest, especially in the energy range between 5.5 MeV and 6.5 MeV, which exhibit an increased transition probability to the 2_1^+ state. The state-to-state analysis of the decay properties can help to identify excited 1^- states that might be attributed to the PDR and states that are assigned to other excitation modes, such as the IVGDR.

Another group of states that are interesting to study in detail using the $(p, p'\gamma)$ reaction are the positive-parity levels observed around 4 MeV excitation energy in ^{128}Te. It was predicted that if the nature of the PDR is connected to the neutron skin oscillation of the nucleus excitations with higher multipolarity are induced as well, namely the Pygmy Quadrupole Resonance (PQR) [191]. Recently, first experimental evidence of such PQR states were observed around 4 MeV in ^{124}Sn using the (^{17}O,^{17}O$'$) [86] and (α, α') [192] reactions, respectively. However, additional experimental information on potential PQR states is needed, in particular systematic studies throughout the nuclear chart. The observed positive-parity states at $\sim$4 MeV represent candidates for the PQR in ^{128}Te. The investigation of their decay pattern might provide useful information on wether they exhibit a collective or multiphonon character.

Improvement of the γ^3-setup

During the analysis of the data from the NRF measurements with ^{128}Te ideas for improvements of the γ^3-setup and of the experimental conditions evolved. Connected to the spin-parity assignments for the excited states it is apparent that a very good separation between 1^- states on the one hand and positive-parity states on the other hand is achieved. The sensitivity for the distinction between 1^+ and 2^+ levels, however, is not as good. Even though the main goal of this thesis is the investigation of the decay properties of 1^- states it might become important to improve the separation between positive-parity states for studies of other excitation modes, such as the scissors mode or the PQR. Therefore, the detector positions have to be adapted to increase the sensitivity for an unambiguous distinction between 1^+ and 2^+ states. This can be accomplished by comparison of the angular distributions for the three relevant ground-state transition characters, namely $E1$, $M1$ and $E2$ transitions (see Fig. 2.4). More appropriate positions can be found to improve substantially the experimental sensitivity for their separation.

In summer 2015, the γ^3-setup was extended by eight liquid scintillators for neutron detection with the aim to enable the measurement of $(\gamma, \gamma' n)$ reactions. The $\gamma - n$ coincidences allow for the investigation of γ-cascades following neutron emission. Thus, the photoabsorption cross section and the decay behavior of excited states above the neutron separation threshold can be studied in more detail than before. During an experimental campaign in 2015 first test measurements on ^{87}Rb were performed and are currently analyzed as part of the doctoral thesis of Philipp Erbacher.

Extreme light infrastructure for nuclear physics (ELI-NP)

A new photon facility in Europe is currently under construction, namely the extreme light infrastructure for nuclear physics, short ELI-NP, in Bucharest, Romania [193]. Up to now, the HIγS facility provides the most intense quasi-monochromatic photon beams available today via

intracavity laser Compton backscattering of FEL photons. At ELI-NP, photons from an external laser will be Compton backscattered creating γ-ray beams with a relative bandwidth of < 0.5 % (HIγS $\sim$ 1-10 %) and time-averaged spectral densities of $> 10^4$ γ/eVs (HIγS $< 10^3$ γ/eVs). The unique scale of the spectral bandwidth as well as the beam intensities on target will allow for investigations of stable nuclei on a whole new level exploiting the NRF reaction. Isotopes with very low natural abundances will be feasible to study via real-photon scattering due to the increased photon flux of one to two order of magnitudes in comparison to the HIγS beam. Furthermore, deformed nuclei exhibit very high level densities making a state-to-state analysis usually very sophisticated or even impossible. The extremely narrow width of the photon beam at ELI-NP will provide new opportunities to study substructures of a number of phenomena, such as the PDR and the IVGDR in greater detail than ever before.

A Appendix

A.1 Experimental settings

Table A.1: Target information on ^{128}Te and ^{130}Te.

	^{128}Te	^{130}Te
Target mass (mg)	2912.8(5)	1998.0(5)
Target diameter (cm)	2.0	2.0
Isotopic enrichment (%)	99.8	99.5
Chemical composition	metallic	metallic

Table A.2: Experimental properties of the NRF measurements with ^{128}Te at DHIPS.

Electron endpoint energy (MeV)	6.0	9.13
Target radiator material	Ag	Au
Target radiator thickness (mm)	2 + 5	1 + 2.5
Beam hardener material	Al (3 cm)	Al (3 cm)
Calibration standard	^{11}B	^{11}B
Calibration standard mass (mg)	302.7(5) + 339.4(5)	302.7(5) + 339.4(5)

Table A.3: Beam energy settings of the NRF measurements with ^{128}Te and ^{130}Te at HIγS.

	^{128}Te	^{130}Te
Beam energy (keV)	2765, 3105, 3185, 3820, 3910, 4030, 4200, 4330, 4460, 4590, 4730, 4870, 5020, 5170, 5320, 5480, 5640, 5820, 5960, 6190, 6400, 6640, 6900, 7160, 7440, 7720, 8000, 8280, 8560, 8920	5500, 5720, 5950, 6200, 6450, 6680, 6930, 7230, 7550, 7850, 8150, 8500

A.2 Results - ^{128}Te

Table A.4: Experimental results for J^π, I, Γ_0^2/Γ and reduced transitions probabilities of individual excited states in ^{128}Te.

E_γ (keV)	J^π	I (keV fm^2)	Γ_0^2/Γ (meV)	$B(E1)\uparrow$ 10^{-3} e^2 fm^2	$B(M1)\uparrow$ μ_N	$B(E2)\uparrow$ 10^3 e^2 fm^4
742.3(7)[a]	2^+	4.29(66)	1.2(2)			34.5(52)
2194.1(9)[a]	2^+	1.05(20)	2.6(5)			0.324(60)
2353.5(8)[a]	2^+	1.20(18)	3.5(5)			0.299(45)
2509.3(8)[a]	2^+	1.96(22)	6.4(7)			0.401(45)
2763.4(6)	1^+	3.04(21)	20.1(14)		0.247(17)	
2871.3(9)[b]	2^+	1.54(20)	6.6(9)			0.211(27)
3104.9(10)	1^+	0.62(13)	5.2(11)		0.045(9)	
3136.9(11)[a,b,c]	2^+	0.26(14)	1.3(7)			0.027(14)
3184.1(9)	1^-	1.01(14)	8.9(13)	0.79(11)		
3687.4(7)	1^-	2.66(14)	31.4(16)	1.79(9)		
3809.5(10)	1^+	1.15(19)	14.5(24)		0.068(11)	
3842.8(11)	2^+	1.45(25)	11.1(19)			0.082(14)
3975.9(9)	1^+	0.79(12)	10.9(17)		0.045(7)	
4027.5(11)	2^+	1.19(13)	10.1(11)			0.059(6)
4035.6(10)	1^+	1.98(13)	28.0(18)		0.110(7)	
4204.0(10)	1^+	1.86(14)	28.6(21)		0.100(7)	
4231.8(11)[c]	1^-	0.56(18)	8.7(28)	0.33(10)		
4298.6(12)	2^+	0.74(14)	11.9(22)		0.039(7)	
4314.2(14)	$(1,2)^+$	0.80(13)	12.9(21)		0.042(7)	32.3(53)
4319.5(11)	1^-	1.10(13)	17.8(21)	0.63(8)		
4353.8(9)	1^-	1.30(17)	21.4(28)	0.74(10)		
4383.2(13)	1^-	0.55(13)	9.1(22)	0.31(8)		
4412.4(14)[c]	$(1,2)^+$	0.33(9)	5.5(16)		0.017(5)	13.6(40)
4427.9(10)[c]	$(1,2)^+$	0.56(12)	5.7(12)		0.028(6)	20.9(45)
4447.2(13)[c]	1^-	1.96(45)	33.6(77)	1.09(25)		
4484.2(10)[c]	1^-	0.58(11)	10.1(18)	0.32(6)		
4516.3(14)[c]	1^-	0.53(11)	9.5(20)	0.29(6)		
4558.3(9)	1^-	1.34(13)	24.1(23)	0.73(7)		
4579.9(14)	1^-	0.78(12)	14.3(22)	0.43(6)		
4679.0(7)	1^-	3.33(18)	63.3(34)	1.77(9)		

Continued on next page

Table A.4 – *Continued from previous page*

E_γ (keV)	J^π	I (keV fm^2)	Γ_0^2/Γ (meV)	$B(E1)\uparrow$ 10^{-3} e^2 fm^2	$B(M1)\uparrow$ μ_N	$B(E2)\uparrow$ 10^3 e^2 fm^4
4747.3(10)	1^-	1.33(15)	26.0(29)	0.70(8)		
4758.9(13)	1^-	0.79(18)	15.6(35)	0.41(9)		
4770.9(13)	1^-	0.86(18)	17.0(35)	0.45(9)		
4842.8(12)	1^-	1.22(15)	24.8(30)	0.63(7)		
4884.8(11)	1^-	1.31(16)	27.1(33)	0.67(8)		
4889.2(10)	1^-	1.64(26)	34.1(53)	0.84(13)		
4912.5(12)^c	1^-	0.60(13)	12.5(27)	0.30(6)		
4969.8(14)^c	1^-	0.23(11)	4.9(23)	0.11(5)		
4989.2(9)	1^-	1.38(22)	29.9(48)	0.69(11)		
4997.4(14)	1^-	1.09(15)	23.6(32)	0.54(7)		
5027.8(10)^c	1^-	0.80(17)	17.6(37)	0.40(8)		
5128.6(12)	1^-	1.57(17)	35.9(38)	0.76(8)		
5143.3(14)	1^-	1.39(16)	32.0(36)	0.67(8)		
5151.1(11)^c	1^-	0.94(13)	21.7(30)	0.45(6)		
5204.9(11)^c	1^-	0.71(12)	16.6(28)	0.34(6)		
5260.1(14)^c	1^-	0.27(15)	6.6(36)	0.13(7)		
5291.2(15)	1^-	0.93(22)	22.5(53)	0.44(10)		
5327.5(10)	1^-	2.05(26)	50.5(65)	0.96(12)		
5373.2(21)^c	1^-	0.27(9)	6.8(23)	0.13(4)		
5382.6(15)	1^-	1.27(18)	32.0(45)	0.59(8)		
5421.9(14)^c	1^-	0.71(11)	18.0(28)	0.32(5)		
5434.6(15)	1^-	0.86(23)	22.1(59)	0.39(10)		
5459.3(13)	1^-	1.30(25)	33.6(65)	0.59(12)		
5467.8(16)^c	1^-	0.47(13)	12.2(33)	0.21(6)		
5471.1(21)^c	1^+	0.46(11)	11.9(29)		0.019(5)	
5492.8(8)	1^-	2.79(23)	72.9(60)	1.26(10)		
5502.8(10)	1^-	1.93(20)	50.7(54)	0.87(9)		
5512.1(10)	1^-	2.85(47)	75.1(124)	1.28(21)		
5516.1(10)	1^-	3.74(34)	98.7(90)	1.69(15)		
5522.9(13)	1^-	2.43(36)	64.3(97)	1.09(16)		
5539.6(9)	1^-	2.70(24)	71.9(64)	1.21(11)		
5546.7(12)^c	1^-	1.30(16)	34.8(43)	0.58(7)		
5557.9(14)	1^-	1.50(29)	40.1(79)	0.67(13)		

Continued on next page

Table A.4 – *Continued from previous page*

E_γ (keV)	J^π	I (keV fm^2)	Γ_0^2/Γ (meV)	$B(E1)\uparrow$ 10^{-3} e^2 fm^2	$B(M1)\uparrow$ μ_N	$B(E2)\uparrow$ 10^3 e^2 fm^4
5562.3(20)[c]	1^-	0.48(18)	12.9(49)	0.21(8)		
5572.4(19)[c]	1^-	0.77(22)	20.8(58)	0.35(10)		
5579.9(14)	1^-	1.86(38)	50.2(103)	0.83(17)		
5604.0(13)[c]	1^-	0.69(18)	18.9(49)	0.31(8)		
5612.2(10)[c]	1^-	0.96(20)	26.1(53)	0.42(9)		
5619.4(19)[c]	1^-	0.83(17)	22.7(46)	0.37(7)		
5636.0(13)[c]	1^-	0.85(16)	23.3(44)	0.37(7)		
5649.3(10)	1^-	2.60(26)	71.8(71)	1.14(11)		
5672.3(17)	1^-	1.18(32)	32.8(91)	0.51(14)		
5708.4(12)[c]	1^-	1.40(26)	39.6(73)	0.61(11)		
5715.8(17)	1^-	1.73(40)	49.1(112)	0.75(17)		
5722.7(11)	1^-	2.84(55)	80.6(156)	1.23(24)		
5729.6(16)	1^-	1.63(36)	46.5(102)	0.71(16)		
5760.2(14)	1^-	2.67(29)	76.8(83)	1.15(12)		
5764.0(15)[c]	1^-	2.36(48)	67.9(139)	1.02(21)		
5769.2(20)[c]	1^-	0.75(22)	21.8(62)	0.33(9)		
5780.1(8)	1^-	5.93(38)	172(11)	2.55(16)		
5794.4(12)	1^-	2.46(31)	71.7(90)	1.06(13)		
5804.4(14)[c]	1^-	0.80(18)	23.5(53)	0.34(8)		
5813.0(10)	1^-	2.80(39)	82.1(114)	1.20(17)		
5826.0(20)[c]	1^-	0.81(19)	23.8(56)	0.35(8)		
5839.7(16)[c]	1^-	1.10(24)	32.4(72)	0.47(10)		
5845.6(13)	1^-	4.50(49)	133(14)	1.91(21)		
5850.4(20)	1^-	3.55(46)	105(14)	1.51(20)		
5859.4(15)[c]	1^-	1.46(24)	43.6(71)	0.62(10)		
5871.0(10)	1^-	2.18(41)	65.1(121)	0.92(17)		
5885.2(8)	1^-	3.48(44)	105(13)	1.47(19)		
5897.6(19)[c]	1^-	1.52(22)	46.0(67)	0.64(9)		
5907.7(8)	1^-	4.41(44)	134(13)	1.86(18)		
5911.7(20)[c]	1^-	1.37(28)	41.4(86)	0.57(12)		
5928.6(16)[c]	1^-	2.53(27)	77.2(82)	1.06(11)		
5933.4(10)	1^-	8.03(67)	245(21)	3.37(28)		
5940.0(9)	1^-	8.55(70)	262(21)	3.58(29)		

Continued on next page

Table A.4 – *Continued from previous page*

E_γ (keV)	J^π	I (keV fm^2)	Γ_0^2/Γ (meV)	$B(E1)\uparrow$ 10^{-3} e^2 fm^2	$B(M1)\uparrow$ μ_N	$B(E2)\uparrow$ 10^3 e^2 fm^4
5948.6(8)	1^-	8.76(56)	269(17)	3.66(23)		
5957.5(12)	1^-	2.03(42)	62.5(129)	0.85(17)		
5967.4(13)	1^-	2.53(50)	78.1(154)	1.05(21)		
5975.3(7)	1^-	10.38(70)	321(22)	4.32(29)		
5985.9(6)	1^-	16.93(80)	526(25)	7.03(33)		
5999.3(10)[c]	1^-	2.17(29)	67.9(90)	0.90(12)		
6007.3(10)	1^-	4.47(46)	140(14)	1.85(19)		
6011.1(9)[c]	1^-	4.03(36)	126(11)	1.67(15)		
6033.9(13)	1^-	2.66(47)	84.1(147)	1.10(19)		
6053.1(14)	1^-	4.30(52)	137(16)	1.77(21)		
6058.3(15)[c]	1^-	2.68(49)	85.3(156)	1.10(20)		
6065.8(8)	1^-	10.25(65)	327(21)	4.20(26)		
6085.1(11)	1^-	5.79(61)	186(20)	2.37(25)		
6098.6(9)	1^-	9.24(66)	298(21)	3.77(27)		
6107.4(9)	1^-	10.12(70)	327(23)	4.12(29)		
6116.4(14)	1^-	3.88(51)	126(17)	1.58(21)		
6158.7(11)	1^-	4.15(50)	137(17)	1.67(20)		
6169.5(11)	1^-	3.91(53)	129(17)	1.58(21)		
6179.2(8)	1^-	10.77(69)	357(23)	4.33(28)		
6191.0(14)	1^-	2.90(49)	96.4(162)	1.16(20)		
6208.4(13)[c]	1^-	1.72(28)	57.4(95)	0.69(11)		
6216.4(16)[c]	1^-	1.44(28)	48.4(94)	0.58(11)		
6224.5(10)	1^-	4.59(54)	154(18)	1.83(22)		
6234.2(11)	1^-	4.46(53)	150(18)	1.78(21)		
6247.2(13)[c]	1^-	2.34(37)	79.3(124)	0.93(15)		
6254.9(12)	1^-	5.48(88)	186(30)	2.18(35)		
6268.3(12)[c]	1^-	5.01(55)	171(19)	1.99(22)		
6277.0(12)[c]	1^-	4.44(56)	152(19)	1.76(22)		
6289.0(8)	1^-	10.15(65)	348(22)	4.01(26)		
6300.7(13)	1^-	2.88(49)	99.2(169)	1.14(19)		
6314.4(10)	1^-	5.85(62)	202(21)	2.30(24)		
6323.3(12)	1^-	3.94(58)	137(20)	1.55(23)		
6340.0(9)	1^-	5.38(58)	188(20)	2.11(23)		

Continued on next page

Table A.4 – *Continued from previous page*

E_γ (keV)	J^π	I (keV fm^2)	Γ_0^2/Γ (meV)	$B(E1)\uparrow$ 10^{-3} e^2 fm^2	$B(M1)\uparrow$ μ_N	$B(E2)\uparrow$ 10^3 e^2 fm^4
6366.1(17)[c]	1^-	1.63(25)	57.2(89)	0.64(10)		
6380.1(8)	1^-	9.45(71)	334(25)	3.68(28)		
6390.9(16)	1^-	3.94(62)	140(22)	1.53(24)		
6400.3(9)	1^-	8.49(70)	302(25)	3.30(27)		
6408.0(14)[c]	1^-	3.22(33)	115(12)	1.25(13)		
6416.2(8)	1^-	8.12(66)	290(23)	3.15(25)		
6439.9(10)[c]	1^-	3.19(31)	115(11)	1.23(12)		
6449.4(13)[c]	1^-	2.68(31)	96.9(113)	1.03(12)		
6464.5(10)	1^-	4.32(56)	157(20)	1.66(22)		
6476.2(12)	1^-	4.01(59)	146(21)	1.54(23)		
6483.3(28)[c]	1^-	6.89(51)	251(19)	2.64(20)		
6486.0(6)	1^-	25.53(118)	931(43)	9.78(45)		
6503.4(15)	1^-	10.05(98)	369(36)	3.84(38)		
6508.0(19)[c]	1^-	3.49(74)	128(27)	1.33(28)		
6520.8(16)[c]	1^-	2.82(41)	104(15)	1.08(16)		
6524.9(14)	1^-	3.22(54)	119(20)	1.23(21)		
6542.8(13)	1^-	4.10(57)	152(21)	1.56(22)		
6551.2(12)	1^-	4.66(58)	173(21)	1.77(22)		
6566.1(14)	1^-	2.90(52)	108(20)	1.10(20)		
6580.9(10)	1^-	8.53(70)	320(26)	3.22(27)		
6588.9(14)	1^-	5.45(68)	205(25)	2.06(25)		
6595.9(13)	1^-	6.47(66)	244(25)	2.44(25)		
6605.4(14)	1^-	3.64(59)	138(22)	1.37(22)		
6616.1(12)	1^-	8.09(76)	307(29)	3.04(28)		
6621.9(15)	1^-	5.23(70)	199(27)	1.96(26)		
6639.7(22)[c]	1^-	2.03(38)	77.8(147)	0.76(14)		
6642.9(11)	1^-	5.32(61)	204(23)	1.99(23)		
6650.4(11)	1^-	6.97(74)	267(28)	2.60(27)		
6666.0(17)[c]	1^-	1.61(34)	61.9(130)	0.60(13)		
6681.0(14)[c]	1^-	2.87(42)	111(16)	1.07(16)		
6683.4(13)	1^-	4.01(58)	155(22)	1.49(22)		
6699.6(19)[c]	1^-	1.50(39)	58.5(152)	0.56(14)		
6718.0(14)[c]	1^-	2.78(51)	109(20)	1.03(19)		

Continued on next page

Table A.4 – *Continued from previous page*

E_γ (keV)	J^π	I (keV fm^2)	Γ_0^2/Γ (meV)	$B(E1)\uparrow$ 10^{-3} e^2 fm^2	$B(M1)\uparrow$ μ_N	$B(E2)\uparrow$ 10^3 e^2 fm^4
6722.0(12)	1^-	5.22(70)	205(28)	1.93(26)		
6736.7(8)	1^-	10.04(72)	395(28)	3.71(26)		
6758.1(11)	1^-	6.80(79)	270(31)	2.50(29)		
6770.9(19)^c	1^-	6.54(74)	260(29)	2.40(27)		
6773.3(11)	1^-	18.15(180)	722(72)	6.66(66)		
6781.5(21)	1^-	8.02(148)	320(59)	2.94(54)		
6806.5(8)	1^-	9.56(71)	384(29)	3.49(26)		
6833.1(23)	1^-	1.98(54)	80.3(219)	0.72(20)		
6836.3(16)^c	1^-	2.27(46)	92.0(187)	0.83(17)		
6844.2(19)^c	1^-	1.38(43)	56.0(176)	0.50(16)		
6853.4(12)^c	1^-	4.04(50)	164(20)	1.46(18)		
6860.7(11)^c	1^-	5.57(52)	227(21)	2.02(19)		
6874.2(7)	1^-	15.40(90)	631(37)	5.57(32)		
6895.1(11)	1^-	6.83(74)	282(30)	2.46(27)		
6909.4(10)^c	1^-	4.85(51)	201(21)	1.75(18)		
6916.8(8)^c	1^-	12.89(73)	535(30)	4.63(26)		
6926.8(13)	1^-	4.02(78)	167(32)	1.44(28)		
6935.4(18)	1^-	3.93(78)	164(33)	1.41(28)		
6944.7(21)	1^-	6.56(135)	274(56)	2.35(48)		
6952.0(17)	1^-	4.07(74)	170(31)	1.45(26)		
6966.2(14)^c	1^-	5.83(74)	245(31)	2.08(26)		
6971.4(13)^c	1^-	10.74(90)	453(38)	3.83(32)		
6976.6(12)	1^-	6.83(84)	288(36)	2.43(30)		
6990.5(39)	1^-	3.00(59)	127(25)	1.07(21)		
7017.8(19)^c	1^-	1.94(85)	82.9(361)	0.69(30)		
7021.9(9)	1^-	13.38(98)	572(42)	4.74(35)		
7045.6(14)^c	1^-	3.73(66)	161(28)	1.32(23)		
7060.1(17)^c	1^-	2.51(56)	109(24)	0.88(20)		
7071.2(12)	1^-	4.21(66)	183(29)	1.48(23)		
7084.6(14)	1^-	4.35(66)	190(29)	1.53(23)		
7090.0(12)^c	1^-	5.04(57)	220(25)	1.77(20)		
7099.6(9)	1^-	8.83(75)	386(33)	3.09(26)		
7118.4(12)	1^-	4.17(79)	183(35)	1.46(27)		

Continued on next page

Table A.4 – *Continued from previous page*

E_γ (keV)	J^π	I (keV fm^2)	Γ_0^2/Γ (meV)	$B(E1)\uparrow$ 10^{-3} e^2 fm^2	$B(M1)\uparrow$ μ_N	$B(E2)\uparrow$ 10^3 e^2 fm^4
7123.2(26)[c]	1^-	4.19(56)	185(25)	1.46(20)		
7126.3(16)	1^-	4.75(80)	209(35)	1.66(28)		
7135.8(12)	1^-	4.44(84)	196(37)	1.55(29)		
7148.6(19)[c]	1^-	4.21(52)	187(23)	1.46(18)		
7150.1(10)	1^-	7.39(77)	328(34)	2.57(27)		
7165.2(22)[c]	1^-	0.96(37)	42.8(163)	0.33(13)		
7171.4(17)	1^-	4.92(117)	219(52)	1.71(41)		
7178.4(17)	1^-	5.11(118)	228(53)	1.77(41)		
7195.9(19)[c]	1^-	2.08(47)	93.3(212)	0.72(16)		
7205.3(10)[c]	1^-	4.30(58)	194(26)	1.49(20)		
7214.8(12)	1^-	2.78(71)	126(32)	0.96(24)		
7234.1(10)	1^-	5.82(69)	264(31)	2.00(24)		
7265.1(12)	1^-	5.74(69)	263(32)	1.96(24)		
7279.2(20)[c]	1^-	3.66(89)	168(41)	1.25(30)		
7288.5(11)	1^-	6.37(77)	293(35)	2.17(26)		
7298.0(11)	1^-	7.02(81)	324(37)	2.39(27)		
7307.2(12)	1^-	5.26(75)	244(35)	1.79(25)		
7312.3(35)[c]	1^-	4.61(85)	214(40)	1.57(29)		
7323.7(13)	1^-	3.96(65)	184(30)	1.34(22)		
7338.3(12)	1^-	4.52(72)	211(34)	1.53(25)		
7347.7(19)	1^-	5.04(91)	236(43)	1.70(31)		
7355.3(18)	1^-	4.56(95)	214(45)	1.54(32)		
7363.7(16)[c]	1^-	2.58(55)	121(26)	0.87(19)		
7392.5(14)[c]	1^-	2.26(48)	107(23)	0.76(16)		
7405.0(17)[c]	1^-	2.18(48)	104(23)	0.73(16)		
7413.9(14)[c]	1^-	2.31(48)	110(23)	0.78(16)		
7425.0(11)	1^-	6.90(77)	330(37)	2.31(26)		
7433.8(12)	1^-	6.65(74)	319(36)	2.22(25)		
7439.3(12)[c]	1^-	6.51(65)	312(31)	2.17(22)		
7458.5(14)	1^-	4.94(92)	238(45)	1.65(31)		
7466.5(20)[c]	1^-	3.31(60)	160(29)	1.10(20)		
7476.3(19)[c]	1^-	2.44(51)	118(25)	0.81(17)		
7494.2(15)	1^-	2.88(63)	140(31)	0.95(21)		

Continued on next page

Table A.4 – *Continued from previous page*

E_γ (keV)	J^π	I (keV fm^2)	Γ_0^2/Γ (meV)	$B(E1)\uparrow$ 10^{-3} e^2 fm^2	$B(M1)\uparrow$ μ_N	$B(E2)\uparrow$ 10^3 e^2 fm^4
7507.0(16)[c]	1^-	1.51(60)	73.8(293)	0.50(20)		
7512.1(17)	1^-	3.08(63)	151(31)	1.02(21)		
7532.7(17)[c]	1^-	3.31(72)	163(35)	1.09(24)		
7543.5(11)	1^-	4.68(69)	231(34)	1.54(23)		
7582.5(15)	1^-	3.35(70)	167(35)	1.10(23)		
7596.7(16)	1^-	2.99(65)	150(33)	0.98(21)		
7625.6(13)[c]	1^-	3.08(51)	155(26)	1.00(17)		
7638.3(18)[c]	1^-	2.27(47)	115(24)	0.74(15)		
7643.6(11)	1^-	14.95(196)	757(99)	4.86(64)		
7665.2(15)	1^-	2.57(70)	131(36)	0.83(23)		
7677.3(15)	1^-	2.46(70)	126(36)	0.80(23)		
7703.6(18)	1^-	2.67(75)	137(39)	0.86(24)		
7713.8(16)	1^-	4.63(82)	239(42)	1.49(26)		
7722.5(9)	1^-	11.72(115)	606(59)	3.77(37)		
7736.4(17)[c]	1^-	1.85(40)	95.9(210)	0.59(13)		
7747.0(18)[c]	1^-	1.56(39)	81.4(205)	0.50(13)		
7764.9(18)	1^-	3.42(73)	179(38)	1.10(23)		
7778.6(18)[c]	1^-	2.28(48)	120(25)	0.73(15)		
7788.9(16)[c]	1^-	2.93(53)	154(28)	0.94(17)		
7799.0(12)	1^-	5.35(79)	282(42)	1.70(25)		
7811.9(20)	1^-	2.64(73)	140(38)	0.84(23)		
7824.1(17)	1^-	3.39(74)	180(39)	1.08(23)		
7853.3(13)	1^-	6.20(81)	332(43)	1.96(26)		
7868.1(20)[c]	1^-	3.99(102)	215(55)	1.26(32)		
7872.8(16)	1^-	5.33(86)	287(46)	1.68(27)		
7891.5(15)[c]	1^-	3.09(80)	167(43)	0.97(25)		
7904.3(15)	1^-	6.56(97)	356(52)	2.06(30)		
7912.6(12)	1^-	11.66(136)	633(74)	3.66(43)		
7922.7(16)	1^-	4.44(80)	242(44)	1.39(25)		
7935.3(20)	1^-	3.01(72)	164(39)	0.94(22)		
7964.5(12)[c]	1^-	4.29(70)	236(39)	1.34(22)		
7974.9(18)[c]	1^-	4.05(68)	223(37)	1.26(21)		
7984.9(20)	1^-	3.69(77)	204(42)	1.15(24)		

Continued on next page

Table A.4 – *Continued from previous page*

E_γ (keV)	J^π	I (keV fm^2)	Γ_0^2/Γ (meV)	$B(E1)\uparrow$ 10^{-3} e^2 fm^2	$B(M1)\uparrow$ μ_N	$B(E2)\uparrow$ 10^3 e^2 fm^4
8011.6(17)[c]	1^-	2.38(63)	132(35)	0.74(19)		
8019.6(18)[c]	1^-	3.01(66)	168(37)	0.93(20)		
8035.9(11)	1^-	7.26(92)	407(52)	2.25(29)		
8051.3(14)[c]	1^-	7.50(101)	422(57)	2.32(31)		
8062.6(13)[c]	1^-	4.76(83)	269(47)	1.47(26)		
8081.0(20)	1^-	3.65(77)	207(44)	1.12(24)		
8092.1(17)	1^-	3.35(85)	190(49)	1.03(26)		
8108.1(18)[c]	1^-	2.17(94)	124(54)	0.66(29)		
8132.9(15)	1^-	4.79(83)	275(48)	1.46(25)		
8150.7(13)	1^-	6.25(87)	360(50)	1.91(26)		
8172.2(16)	1^-	4.70(88)	272(51)	1.43(27)		
8183.5(22)	1^-	3.82(89)	222(52)	1.16(27)		
8193.5(14)[c]	1^-	5.52(68)	321(40)	1.67(21)		
8204.0(17)[c]	1^-	3.89(59)	227(35)	1.18(18)		
8213.8(17)[c]	1^-	3.18(56)	186(33)	0.96(17)		
8221.1(39)	1^-	3.25(87)	190(51)	0.98(26)		
8230.4(22)[c]	1^-	3.17(59)	186(35)	0.96(18)		
8246.8(20)[c]	1^-	2.14(45)	126(26)	0.65(13)		
8258.3(22)[c]	1^-	1.45(41)	85.6(242)	0.44(12)		
8271.6(15)[c]	1^-	3.63(52)	215(31)	1.09(16)		
8294.5(16)	1^-	4.00(84)	239(50)	1.20(25)		
8316.3(14)[c]	1^-	3.76(55)	226(33)	1.12(16)		
8329.4(14)[c]	1^-	4.27(59)	257(35)	1.28(18)		
8340.3(15)[c]	1^-	3.54(59)	213(36)	1.05(18)		
8355.9(23)[c]	1^-	3.52(65)	213(39)	1.05(19)		
8365.5(27)[c]	1^-	2.94(67)	179(41)	0.87(20)		
8374.1(26)[c]	1^-	2.14(65)	130(39)	0.64(19)		
8411.1(20)[c]	1^-	3.98(82)	244(50)	1.18(24)		
8437.7(19)[c]	1^-	3.52(122)	217(75)	1.04(36)		
8475.4(23)[c]	1^-	4.39(133)	274(83)	1.29(39)		
8483.0(16)	1^-	9.36(128)	585(80)	2.74(38)		
8499.3(18)[c]	1^-	5.33(130)	334(81)	1.56(38)		
8516.0(16)[c]	1^-	6.83(136)	430(86)	1.99(40)		

Continued on next page

Table A.4 – *Continued from previous page*

E_γ (keV)	J^π	I (keV fm^2)	Γ_0^2/Γ (meV)	$B(E1)\uparrow$ 10^{-3} e^2 fm^2	$B(M1)\uparrow$ μ_N	$B(E2)\uparrow$ 10^3 e^2 fm^4
8530.4(23)	1^-	5.22(121)	329(76)	1.52(35)		
8547.7(17)	1^-	7.53(134)	477(85)	2.19(39)		
8552.3(25)[c]	1^-	5.38(137)	341(87)	1.56(40)		
8567.5(19)[c]	1^-	4.72(121)	300(77)	1.37(35)		
8589.4(25)[c]	1^-	4.34(126)	278(80)	1.26(36)		
8605.2(23)	1^-	5.66(129)	363(83)	1.63(37)		
8640.9(24)[c]	1^-	5.69(158)	368(102)	1.64(45)		
8708.5(20)	1^-	7.59(158)	499(104)	2.17(45)		
8723.6(16)[c]	1^-	8.52(177)	562(117)	2.43(50)		
8754.7(21)[c]	1^-	5.76(127)	383(85)	1.64(36)		
8765.8(25)[c]	1^-	4.82(124)	321(83)	1.37(35)		
8778.3(19)[c]	1^-	6.27(127)	419(85)	1.78(36)		
8836.2(21)[c]	1^-	3.40(81)	230(55)	0.96(23)		

[a] Excited state already known in Ref. [178].

[b] Excited state already known in Ref. [179].

[c] Observed at HIγS, only.

Table A.5: Experimental results for average cross sections determined in ^{128}Te in single γ-ray spectroscopy measurements.

E_{beam} (MeV)	$\sigma^{p}_{\gamma\gamma,HPGe}$ (mb)	$\sigma_{\gamma\gamma,HPGe}$ (mb)	$\sigma_{\gamma\gamma,LaBr}$ (mb)	$\sigma_{\gamma\gamma}$ (mb)	$\sigma_{\gamma\gamma'}$ (mb)	σ_{γ} (mb)
2.765	0.280(35)	-	-	0.280(35)	-	0.280(35)
3.105	0.064(24)	-	-	0.064(24)	-	0.064(24)
3.185	0.081(16)	-	-	0.081(16)	-	0.081(16)
3.910	0.054(10)	-	-	0.054(10)	0.305(88)	0.359(88)
4.030	0.219(37)	-	-	0.219(37)	-	0.219(37)
4.200	0.181(61)	-	-	0.181(61)	0.48(18)	0.66(19)
4.330	0.202(16)	0.220(18)	0.158(11)	0.176(10)	-	0.176(10)
4.460	0.155(22)	0.170(25)	0.170(5)	0.170(5)	0.237(57)	0.407(57)
4.590	0.182(28)	0.235(37)	0.208(6)	0.209(5)	-	0.209(5)
4.730	0.226(48)	0.274(58)	0.241(8)	0.242(8)	-	0.242(8)
4.870	0.259(16)	0.371(23)	0.317(8)	0.322(8)	-	0.322(8)
5.020	0.159(41)	0.281(73)	0.212(7)	0.213(7)	0.346(98)	0.559(98)
5.170	0.180(21)	0.323(38)	0.409(6)	0.407(6)	0.450(65)	0.857(65)
5.320	0.219(21)	0.318(31)	0.346(5)	0.345(5)	0.327(43)	0.673(43)
5.480	1.019(65)	1.366(87)	1.610(7)	1.609(7)	0.767(73)	2.376(73)
5.640	1.126(70)	1.422(88)	1.588(8)	1.587(8)	0.807(85)	2.393(85)
5.820	1.72(11)	2.10(13)	2.538(10)	2.535(10)	1.254(85)	3.789(85)
5.960	3.67(22)	4.72(29)	4.958(15)	4.958(14)	1.75(13)	6.71(13)
6.190	3.52(22)	4.67(29)	4.972(15)	4.971(15)	2.64(17)	7.61(17)
6.400	3.42(14)	5.24(22)	4.780(14)	4.782(14)	2.302(98)	7.084(99)
6.640	4.96(25)	7.49(38)	7.265(15)	7.265(15)	3.99(20)	11.25(20)
6.900	4.67(27)	8.47(49)	8.855(16)	8.855(16)	5.92(33)	14.78(33)
7.160	3.43(23)	6.68(45)	7.127(20)	7.126(20)	6.19(39)	13.31(39)
7.440	2.68(29)	5.75(46)	5.980(16)	5.980(16)	7.57(55)	13.55(55)
7.720	1.98(14)	4.13(29)	4.632(17)	4.630(17)	6.62(41)	11.25(42)
8.000	2.68(29)	6.30(69)	6.694(22)	6.694(22)	12.8(13)	19.4(13)
8.280	1.98(19)	4.98(49)	4.680(15)	4.680(15)	11.2(10)	15.9(10)
8.560	2.11(34)	7.0(12)	7.948(39)	7.947(39)	26.8(40)	34.7(40)
8.920	0.73(13)	2.45(45)	2.525(17)	2.525(17)	9.6(16)	12.1(16)

Table A.6: Experimental results for $\langle b_0 \rangle$, $\langle b_{2_1^+} \rangle$, $\langle b_{in} \rangle$ and λ in ^{128}Te.

E_{beam} (MeV)	$\langle b_0 \rangle$	λ (MeV^{-1})	$\langle b_{2_1^+} \rangle$	$\langle b_{in} \rangle$
4.030	-	-	0.152(86)	-
4.200	-	-	1.31(49)	0.49(20)
4.330	-	-	0.56(10)	-
4.460	-	-	0.493(90)	0.36(11)
4.590	-	-	0.255(61)	-
4.730	-	-	0.477(69)	-
4.870	-	-	0.389(62)	-
5.020	0.448(40)	-	0.366(60)	0.225(73)
5.170	0.418(29)	-	0.275(33)	0.249(46)
5.320	0.493(29)	-	0.291(34)	0.307(54)
5.480	0.640(18)	-	0.164(10)	0.343(39)
5.640	0.638(22)	-	0.143(9)	0.281(35)
5.820	0.627(11)	-	0.199(12)	0.401(36)
5.960	0.730(8)	2.27(10)	0.204(7)	0.578(46)
6.190	0.639(7)	2.07(10)	0.273(8)	0.513(36)
6.400	0.695(5)	2.243(28)	0.160(4)	0.332(17)
6.640	0.653(5)	2.09(12)	0.154(4)	0.281(16)
6.900	0.588(5)	2.129(91)	0.205(6)	0.307(19)
7.160	0.519(7)	2.118(91)	0.268(7)	0.308(21)
7.440	0.432(8)	2.047(50)	0.291(10)	0.230(19)
7.720	0.384(8)	2.006(54)	0.298(11)	0.208(15)
8.000	0.331(8)	1.970(39)	0.286(12)	0.150(17)
8.280	0.308(8)	1.985(63)	0.268(9)	0.112(11)
8.560	0.207(10)	1.950(61)	0.298(13)	0.088(14)
8.920	0.204(13)	2.017(43)	0.283(21)	0.075(13)

Table A.7: Multipole decomposition of direct population of the 2_1^+ state considering primary excited 1^- and 1^+ states.

E_{beam} (MeV)	$\sigma_{1^-\to 2_1^+}$ (mb)	$\sigma_{1^+\to 2_1^+}$ (mb)	χ^2_{red}	$\sigma_{1^-\to 2_1^+}$ (mb)	$\sigma_{1^+\to 2_1^+(\delta=100)}$ (mb)	χ^2_{red}
5.820	0.405(67)	0.039(60)	2.39	0.349(57)	0.112(59)	1.75
5.960	0.551(82)	0.196(75)	9.49	0.738(51)	0.00(4)	10.90
6.190	1.09(12)	0.11(10)	3.00	1.190(79)	0.00(4)	3.23
6.400	0.605(31)	0.106(20)	7.20	0.709(34)	0.00(2)	7.84
6.640	0.95(11)	0.01(18)	5.11	0.928(54)	0.038(35)	5.09
6.900	1.85(11)	0.00(24)	10.4	1.52(15)	0.37(12)	8.51
7.160	1.71(12)	0.00(2)	7.43	1.71(12)	0.00(2)	7.43
7.440	1.028(88)	0.608(63)	4.50	1.61(13)	0.00(8)	8.58
7.720	0.886(68)	0.311(44)	1.67	1.181(82)	0.00(26)	3.22
8.000	1.80(20)	0.00(9)	5.42	1.68(18)	0.132(66)	5.31
8.280	1.04(16)	0.15(12)	4.93	1.11(15)	0.11(12)	5.11
8.560	2.19(34)	0.00(48)	0.66	2.14(40)	0.06(28)	0.65

Table A.8: Multipole decomposition of direct population of the 2_1^+ state considering primary excited 1^- and 2^+ states.

E_{beam} (MeV)	$\sigma_{1^-\to 2_1^+}$ (mb)	$\sigma_{2^+\to 2_1^+}$ (mb)	χ^2_{red}	$\sigma_{1^-\to 2_1^+}$ (mb)	$\sigma_{2^+\to 2_1^+(\delta=100)}$ (mb)	χ^2_{red}
5.820	0.401(51)	0.050(47)	2.25	0.410(92)	0.033(85)	2.45
5.960	0.592(68)	0.172(61)	9.24	0.59(12)	0.16(12)	10.53
6.190	1.075(73)	0.141(39)	2.66	1.090(74)	0.101(35)	3.15
6.400	0.655(33)	0.063(22)	7.49	0.709(34)	0.00(6)	7.84
6.640	0.749(84)	0.276(92)	3.22	0.961(55)	0.00(6)	5.11
6.900	1.377(88)	0.590(60)	4.56	1.77(24)	0.08(21)	10.39
7.160	1.71(12)	0.000(62)	7.43	1.71(12)	0.00(3)	7.43
7.440	1.26(10)	0.415(58)	5.79	0.80(22)	0.82(21)	5.28
7.720	1.006(74)	0.204(43)	2.12	0.84(17)	0.35(17)	2.30
8.000	1.47(21)	0.41(16)	4.11	1.49(34)	0.30(30)	5.22
8.280	0.89(13)	0.39(12)	2.62	1.20(12)	0.00(185)	5.28
8.560	2.03(36)	0.21(23)	0.50	2.19(34)	0.00(123)	0.66

Table A.9: Multipole decomposition of direct population of the 2_1^+ state considering primary excited 1^-, 1^+ and 2^+ states.

E_{beam} (MeV)	$\sigma_{1^-\rightarrow 2_1^+}$ (mb)	$\sigma_{1^+\rightarrow 2_1^+}$ (mb)	$\sigma_{2^+\rightarrow 2_1^+}$ (mb)	χ^2_{red}
5.820	0.387(69)	0.018(64)	0.045(51)	2.80
5.960	0.527(83)	0.113(89)	0.122(72)	11.14
6.190	1.06(12)	0.03(14)	0.130(99)	3.32
6.400	0.598(67)	0.089(68)	0.028(55)	8.93
6.640	0.749(84)	0.00(5)	0.276(91)	4.03
6.900	1.38(13)	0.00(3)	0.59(12)	5.70
7.160	1.71(12)	0.00(3)	0.00(7)	9.29
7.440	0.97(16)	0.48(16)	0.22(13)	4.90
7.720	0.87(13)	0.24(14)	0.10(11)	1.87
8.000	1.47(21)	0.00(5)	0.41(17)	5.14
8.280	0.88(16)	0.02(28)	0.39(12)	3.27
8.560	2.03(36)	0.00(22)	0.21(23)	0.62

Table A.10: Experimental results for $f(E_\gamma)$ and $f_{E1}(E_\gamma)$ build on the ground state and the I_{M1}/I_{E1} ratio in ^{128}Te.

E_γ (MeV)	$f(E_\gamma)$ (10^{-7} MeV^{-3})	$f_{E1}(E_\gamma)$ (10^{-7} MeV^{-3})	I_{M1}/I_{E1}
5.020	0.097(17)	0.087(15)	0.109(18)
5.170	0.144(11)	0.137(10)	0.052(12)
5.320	0.110(7)	0.104(7)	0.0561(85)
5.480	0.376(12)	0.349(11)	0.0777(25)
5.640	0.368(13)	0.353(13)	0.0436(23)
5.820	0.565(13)	0.550(12)	0.0272(18)
5.960	0.976(18)	0.959(18)	0.0177(13)
6.190	1.067(24)	1.053(23)	0.0133(14)
6.400	0.960(13)	0.945(13)	0.0164(13)
6.640	1.470(26)	1.401(24)	0.0492(12)
6.900	1.858(42)	1.742(39)	0.0662(8)
7.160	1.613(48)	1.544(46)	0.0444(15)
7.440	1.580(64)	1.492(61)	0.0590(17)
7.720	1.264(47)	1.144(42)	0.1055(23)
8.000	2.11(14)	1.95(13)	0.0801(21)
8.280	1.66(11)	1.58(11)	0.0541(16)
8.560	3.52(41)	3.32(38)	0.0608(28)
8.920	1.18(15)	1.07(14)	0.1014(50)

Table A.11: Experimental results for $\sigma_{\gamma}^{2_1^+}$, $f^{2_1^+}(E_\gamma)$ and $f_{E1}^{2_1^+}(E_\gamma)$ build on the first excited 2_1^+ state in ^{128}Te.

E_γ (MeV)	$\sigma_{\gamma}^{2_1^+}$ (mb)	$f^{2_1^+}(E_\gamma)$ (10^{-7} MeV^{-3})	$f_{E1}^{2_1^+}(E_\gamma)$ (10^{-7} MeV^{-3})
4.277	0.048(15)	0.049(15)	0.049(15)
4.427	0.073(12)	0.071(12)	0.071(12)
4.577	0.055(9)	0.052(8)	0.052(8)
4.737	0.110(10)	0.101(9)	0.101(9)
4.897	0.094(9)	0.083(8)	0.083(8)
5.077	0.211(17)	0.180(15)	0.155(31)
5.217	0.362(25)	0.301(21)	0.208(36)
5.447	0.549(37)	0.437(29)	0.381(59)
5.657	0.282(14)	0.216(10)	0.181(24)
5.897	0.435(24)	0.320(18)	0.234(28)
6.157	0.775(49)	0.546(34)	0.382(35)
6.417	0.915(63)	0.618(43)	0.618(49)
6.697	0.997(82)	0.645(53)	0.377(61)
6.977	0.880(67)	0.547(42)	0.394(66)
7.257	1.41(16)	0.840(95)	0.658(97)
7.537	0.984(99)	0.566(57)	0.39(11)
7.817	2.75(45)	1.52(25)	1.38(30)
8.177	0.84(16)	0.443(84)	0.443(84)

A.3 Results - ^{130}Te

Table A.12: Experimental results for the average cross sections, $\langle b_0 \rangle$ and λ in ^{130}Te.

E_{beam} (MeV)	$\sigma^{p}_{\gamma\gamma,HPGe}$ (mb)	$\sigma_{\gamma\gamma,HPGe}$ (mb)	$\sigma_{\gamma\gamma'}$ (mb)	σ_{γ} (mb)	$\langle b_0 \rangle$	λ (MeV^{-1})
5.500	0.90(12)	0.92(13)	0.46(11)	1.38(20)	0.666(51)	-
5.720	3.61(38)	3.75(40)	0.79(15)	4.54(47)	0.827(27)	-
5.950	3.63(28)	3.50(27)	1.18(14)	4.68(36)	0.747(19)	-
6.200	4.75(36)	5.81(45)	2.06(19)	7.86(59)	0.739(15)	2.06(16)
6.450	7.23(41)	8.85(50)	2.62(17)	11.47(63)	0.771(9)	2.74(38)
6.680	9.9(10)	10.9(11)	6.29(62)	17.2(16)	0.633(14)	2.15(27)
6.930	9.93(61)	10.10(62)	8.55(48)	18.7(10)	0.542(11)	2.14(10)
7.230	6.17(49)	7.68(61)	6.86(47)	14.6(10)	0.528(13)	2.14(15)
7.550	5.30(79)	7.5(11)	11.2(15)	18.6(26)	0.399(16)	2.03(5)
7.850	7.3(12)	9.9(17)	13.4(22)	23.3(38)	0.424(14)	2.11(9)
8.150	2.81(57)	4.81(97)	8.7(17)	13.5(26)	0.356(15)	1.99 (6)
8.500	0.47(14)	0.47(14)	1.10(20)	1.56(24)	0.30(14)	-

List of Figures

List of Tables

Bibliography

[1] J. Thomson, Phil. Mag. Ser. 5 **44**, 293 (1897).

[2] J. Thomson, Phil. Mag. Ser. 6 **7**, 237 (1904).

[3] H. Becquerel, C. R. Acad. Sci. Paris **122**, 501 (1896).

[4] P. Curie, M. Curie, and G. Bémont, C. R. Acad. Sci. Paris **127**, 1215 (1898).

[5] H. Geiger and E. Marsden, Proc. R. Soc. Lond. A **82**, 495 (1909).

[6] E. Rutherford, Phil. Mag. Ser. 6 **21**, 669 (1911).

[7] N. Bohr, Phil. Mag. **26**, 1 (1913).

[8] E. Schrödinger, Annalen der Physik **385**, 437 (1926).

[9] W. Heisenberg, Zeitschrift der Physik **43**, 172 (1927).

[10] E. Rutherford, Phil. Mag. Ser. 6 **37**, 537 (1919).

[11] J. Chadwick, Proc. R. Soc. Lond. A **136**, 692 (1932).

[12] T. I. N. C. inch (http://personal.ph.surrey.ac.uk/ phplic/Programs/Inch/inch.html, as at March 2016).

[13] M. N. Harakeh and A. van der Woude, *Giant Resonances* (Oxford University Press, 2001).

[14] W. Bothe and W. Gentner, Z. Phys. **71**, 236 (1937).

[15] G. C. Baldwin and G. S. Klaiber, Phys. Rev. **71**, 3 (1947).

[16] A. Migdal, J. Phys. (USSR) **8**, 331 (1944).

[17] W. Kuhn, Z. Phys. **33**, 408 (1925).

[18] F. Reiche and W. Thomas, Z. Phys. **34**, 510 (1925).

[19] F. R. Metzger, Prog. in Nucl. Phys. **7**, 53 (1959).

[20] U. Kneissl, H. H. Pitz, and A. Zilges, Prog. Part. Nucl. Phys. **37**, 349 (1996).

[21] W. Kuhn, Phil. Mag. **8**, 625 (1929).

[22] A. C. G. Mitchell and M. W. Zemansky, *Resonance Radiation and Excited Atoms* (Cambridge University Press, 1934).

[23] P. B. Moon, Proc. Phys. Soc. A **64**, 76 (1951).

[24] L. I. Schiff, Phys. Rev. **70**, 761 (1946).

[25] E. Hayward and E. G. Fuller, Phys. Rev. **106**, 991 (1957).

[26] J. S. O'Connell, P. A. Tippler, and P. Axel, Phys. Rev. **126**, 228 (1962).

[27] H. W. Kuehne, P. Axel, and D. C. Sutton, Phys. Rev. **163**, 1278 (1967).

[28] N. L. Iudice and F. Palumbo, Phys. Rev. Lett. **41**, 1532 (1978).

[29] N. L. Iudice and F. Palumbo, Nucl. Phys. A **326**, 193 (1979).

[30] A. Richter, in P. Blasi, R. A. Ricci, and ed., Proc. of the Int. Conf. on Nuclear Physics **Tipografica Compositori, Bristol, Vol. 2**, 189 (1983).

[31] D. Bohle, A. Richter, W. Steffen, and et al., Phys. Lett. B **137**, 27 (1984).

[32] K. Wienhard, R. K. M. Schneider, K. Ackermann, K. Bangert, U. E. P. Berg, and R. Stock, Phys. Rev. C **24**, 1363 (1981).

[33] R. Moreh, in R. Bergère, S. Costa, C. Schaerf, and eds., Intermediate Energy Nuclear Physics **World Scient. Pub. Co., Singapore**, 1 (1982).

[34] U. E. P. Berg, Jour. de Phys. **C4**, 359 (1984).

[35] U. Berg, K. Ackermann, K. Bangert, C. Blsing, W. Naatz, R. Stock, K. Wienhard, M. Brussel, T. Chapuran, and B. Wildenthal, Phys. Lett. B **140**, 191 (1984).

[36] U. Berg, C. Blsing, J. Drexler, R. Heil, U. Kneissel, W. Naatz, R. Ratzek, S. Schennach, R. Stock, T. Weber, et al., Phys. Lett. B **149**, 59 (1984).

[37] J. Beller, N. Pietralla, J. Barea, M. Elvers, J. Endres, C. Fransen, J. Kotila, O. Möller, A. Richter, T. R. Rodríguez, et al., Phys. Rev. Lett. **111**, 172501 (2013).

[38] J. Enders, P. von Neumann-Cosel, C. Rangacharyulu, and A. Richter, Phys. Rev. C **71**, 014306 (2005).

[39] K. Heyde, P. von Neumann-Cosel, and A. Richter, Rev. Mod. Phys. **82**, 2365 (2010).

[40] P. O. Lipas, Nucl. Phys. **82**, 91 (1966).

[41] P. Vogel, Nucl. Phys. A **176**, 33 (1971).

[42] R.-D. Herzberg, I. Bauske, P. von Brentano, T. Eckert, R. Fischer, W. Geiger, U. Kneissl, J. Margraf, H. Maser, N. Pietralla, et al., Nucl. Phys. A **592**, 211 (1995).

[43] W. Andrejtscheff, C. Kohstall, P. von Brentano, C. Fransen, U. Kneissl, N. Pietralla, and H. Pitz, Phys. Lett. B **506**, 239 (2001).

[44] D. Savran, T. Aumann, and A. Zilges, Prog. Part. Nucl. Phys. **70**, 210 (2013).

[45] G. A. Bartholomew, Annu. Rev. Nucl. Sci. **11**, 259 (1961).

[46] G. A. Bartholomew, E. D. Earl, A. J. Ferguson, J. W. Knowles, and M. A. Lone, Adv. Nucl. Phys. **7**, 229 (1973).

[47] R. Mohan, M. Danos, and L. C. Biedenharn, Phys. Rev. C **3**, 1740 (1971).

[48] P. Axel, K. K. Min, and D. C. Sutton, Phys. Rev. C **2**, 689 (1970).

[49] R. M. Laszewski and P. Axel, Phys. Rev. C **19**, 342 (1979).

[50] R. M. Laszewski, Phys. Rev. C **34**, 1114 (1986).

[51] R.-D. Herzberg, P. von Brentano, J. Eberth, J. Enders, R. Fischer, N. Huxel, T. Klemme, P. von Neumann-Cosel, N. Nicolay, N. Pietralla, et al., Phys. Lett. B **390**, 49 (1997).

[52] R.-D. Herzberg, C. Fransen, P. von Brentano, J. Eberth, J. Enders, A. Fitzler, L. Käubler, H. Kaiser, P. von Neumann˘Cosel, N. Pietralla, et al., Phys. Rev. C **60**, 051307 (1999).

[53] K. Govaert, F. Bauwens, J. Bryssinck, D. De Frenne, E. Jacobs, W. Mondelaers, L. Govor, and V. Y. Ponomarev, Phys. Rev. C **57**, 2229 (1998).

[54] A. Zilges, S. Volz, M. Babilon, T. Hartmann, P. Mohr, and K. Vogt, Phys. Lett. B **542**, 43 (2002).

[55] S. Volz, N. Tsoneva, M. Babilon, M. Elvers, J. Hasper, R.-D. Herzberg, H. Lenske, K. Lindenberg, D. Savran, and A. Zilges, Nucl. Phys. A **779**, 1 (2006).

[56] D. Savran, M. Elvers, J. Endres, M. Fritzsche, B. Löher, N. Pietralla, V. Y. Ponomarev, C. Romig, L. Schnorrenberger, K. Sonnabend, et al., Phys. Rev. C **84**, 024326 (2011).

[57] V. G. Soloviev, *Theory of Atomic Nuclei: Quasiparticles and Phonons* (Institute of Physics, Bristol, 1992).

[58] A. Jung, S. Lindenstruth, H. Schacht, B. Starck, R. Stock, C. Wesselborg, R. Heil, U. Kneissl, J. Margraf, H. Pitz, et al., Nucl. Phys. A **584**, 103 (1995).

[59] F. Bauwens, J. Bryssinck, D. De Frenne, K. Govaert, L. Govor, M. Hagemann, J. Heyse, E. Jacobs, W. Mondelaers, and V. Y. Ponomarev, Phys. Rev. C **62**, 024302 (2000).

[60] T. Hartmann, M. Babilon, S. Kamerdzhiev, E. Litvinova, D. Savran, S. Volz, and A. Zilges, Phys. Rev. Lett. **93**, 192501 (2004).

[61] J. Isaak, D. Savran, M. Fritzsche, D. Galaviz, T. Hartmann, S. Kamerdzhiev, J. H. Kelley, E. Kwan, N. Pietralla, C. Romig, et al., Phys. Rev. C **83**, 034304 (2011).

[62] H. Pai, J. Beller, N. Benouaret, J. Enders, T. Hartmann, O. Karg, P. von Neumann-Cosel, N. Pietralla, V. Y. Ponomarev, C. Romig, et al., Phys. Rev. C **88**, 054316 (2013).

[63] M. Scheck, V. Y. Ponomarev, T. Aumann, J. Beller, M. Fritzsche, J. Isaak, J. H. Kelley, E. Kwan, N. Pietralla, R. Raut, et al., Phys. Rev. C **87**, 051304 (2013).

[64] M. Scheck, V. Y. Ponomarev, M. Fritzsche, J. Joubert, T. Aumann, J. Beller, J. Isaak, J. H. Kelley, E. Kwan, N. Pietralla, et al., Phys. Rev. C **88**, 044304 (2013).

[65] P. M. Goddard, N. Cooper, V. Werner, G. Rusev, P. D. Stevenson, A. Rios, C. Bernards, A. Chakraborty, B. P. Crider, J. Glorius, et al., Phys. Rev. C **88**, 064308 (2013).

[66] R. Schwengner, G. Rusev, N. Benouaret, R. Beyer, M. Erhard, E. Grosse, A. R. Junghans, J. Klug, K. Kosev, L. Kostov, et al., Phys. Rev. C **76**, 034321 (2007).

[67] R. Schwengner, G. Rusev, N. Tsoneva, N. Benouaret, R. Beyer, M. Erhard, E. Grosse, A. R. Junghans, J. Klug, K. Kosev, et al., Phys. Rev. C **78**, 064314 (2008).

[68] N. Benouaret, R. Schwengner, G. Rusev, F. Dönau, R. Beyer, M. Erhard, E. Grosse, A. R. Junghans, K. Kosev, C. Nair, et al., Phys. Rev. C **79**, 014303 (2009).

[69] C. Romig, J. Beller, J. Glorius, J. Isaak, J. H. Kelley, E. Kwan, N. Pietralla, V. Y. Ponomarev, A. Sauerwein, D. Savran, et al., Phys. Rev. C **88**, 044331 (2013).

[70] D. Savran, M. Fritzsche, J. Hasper, K. Lindenberg, S. Müller, V. Y. Ponomarev, K. Sonnabend, and A. Zilges, Phys. Rev. Lett. **100**, 232501 (2008).

[71] A. P. Tonchev, S. L. Hammond, J. H. Kelley, E. Kwan, H. Lenske, G. Rusev, W. Tornow, and N. Tsoneva, Phys. Rev. Lett. **104**, 072501 (2010).

[72] R. Massarczyk, R. Schwengner, F. Dönau, E. Litvinova, G. Rusev, R. Beyer, R. Hannaske, A. R. Junghans, M. Kempe, J. H. Kelley, et al., Phys. Rev. C **86**, 014319 (2012).

[73] J. Isaak, D. Savran, M. Krtička, M. Ahmed, J. Beller, E. Fiori, J. Glorius, J. Kelley, B. Löher, N. Pietralla, et al., Phys. Lett. B **727**, 361 (2013).

[74] C. Romig, D. Savran, J. Beller, J. Birkhan, A. Endres, M. Fritzsche, J. Glorius, J. Isaak, N. Pietralla, M. Scheck, et al., Phys. Lett. B **744**, 369 (2015).

[75] P. Adrich, A. Klimkiewicz, M. Fallot, K. Boretzky, T. Aumann, D. Cortina-Gil, U. D. Pramanik, T. W. Elze, H. Emling, H. Geissel, et al., Phys. Rev. Lett. **95**, 132501 (2005).

[76] A. Klimkiewicz, N. Paar, P. Adrich, M. Fallot, K. Boretzky, T. Aumann, D. Cortina-Gil, U. D. Pramanik, T. W. Elze, H. Emling, et al., Phys. Rev. C **76**, 051603 (2007).

[77] O. Wieland, A. Bracco, F. Camera, G. Benzoni, N. Blasi, S. Brambilla, F. C. L. Crespi, S. Leoni, B. Million, R. Nicolini, et al., Phys. Rev. Lett. **102**, 092502 (2009).

[78] D. M. Rossi, P. Adrich, F. Aksouh, H. Alvarez-Pol, T. Aumann, J. Benlliure, M. Böhmer, K. Boretzky, E. Casarejos, M. Chartier, et al., Phys. Rev. Lett. **111**, 242503 (2013).

[79] G. Rusev, R. Schwengner, F. Dönau, M. Erhard, E. Grosse, A. R. Junghans, K. Kosev, K. D. Schilling, A. Wagner, F. Bečvář, et al., Phys. Rev. C **77**, 064321 (2008).

[80] R. Massarczyk, R. Schwengner, L. A. Bernstein, M. Anders, D. Bemmerer, R. Beyer, Z. Elekes, R. Hannaske, A. R. Junghans, T. Kögler, et al., Phys. Rev. C **92**, 044309 (2015).

[81] D. Savran, M. Babilon, A. M. van den Berg, M. N. Harakeh, J. Hasper, A. Matic, H. J. Wörtche, and A. Zilges, Phys. Rev. Lett. **97**, 172502 (2006).

[82] J. Endres, D. Savran, A. M. v. d. Berg, P. Dendooven, M. Fritzsche, M. N. Harakeh, J. Hasper, H. J. Wörtche, and A. Zilges, Phys. Rev. C **80**, 034302 (2009).

[83] J. Endres, E. Litvinova, D. Savran, P. A. Butler, M. N. Harakeh, S. Harissopulos, R.-D. Herzberg, R. Krücken, A. Lagoyannis, N. Pietralla, et al., Phys. Rev. Lett. **105**, 212503 (2010).

[84] V. Derya, D. Savran, J. Endres, M. Harakeh, H. Hergert, J. Kelley, P. Papakonstantinou, N. Pietralla, V. Ponomarev, R. Roth, et al., Phys. Lett. B **730**, 288 (2014).

[85] F. C. L. Crespi, A. Bracco, R. Nicolini, D. Mengoni, L. Pellegri, E. G. Lanza, S. Leoni, A. Maj, M. Kmiecik, R. Avigo, et al., Phys. Rev. Lett. **113**, 012501 (2014).

[86] L. Pellegri, A. Bracco, F. Crespi, S. Leoni, F. Camera, E. Lanza, M. Kmiecik, A. Maj, R. Avigo, G. Benzoni, et al., Phys. Lett. B **738**, 519 (2014).

[87] M. Krzysiek, M. Kmiecik, A. Maj, P. Bednarczyk, A. Bracco, F. C. L. Crespi, E. G. Lanza, E. Litvinova, N. Paar, R. Avigo, et al., Phys. Rev. C **93**, 044330 (2016).

[88] V. Derya, J. Endres, M. Harakeh, D. Savran, H. Wrtche, and A. Zilges, J. Phys. Conf. Ser. **366**, 012012 (2012).

[89] E. Litvinova, P. Ring, V. Tselyaev, and K. Langanke, Phys. Rev. C **79**, 054312 (2009).

[90] N. Paar, D. Vretenar, E. Khan, and G. Col, Rep. Progr. Phys. **70**, 691 (2007).

[91] E. Litvinova, private communication (????).

[92] D. Vretenar, N. Paar, P. Ring, and T. Nikšić, Phys. Rev. C **65**, 021301 (2002).

[93] N. Ryezayeva, T. Hartmann, Y. Kalmykov, H. Lenske, P. von Neumann-Cosel, V. Y. Ponomarev, A. Richter, A. Shevchenko, S. Volz, and J. Wambach, Phys. Rev. Lett. **89**, 272502 (2002).

[94] J. Piekarewicz, Phys. Rev. C **73**, 044325 (2006).

[95] A. Carbone, G. Colò, A. Bracco, L.-G. Cao, P. F. Bortignon, F. Camera, and O. Wieland, Phys. Rev. C **81**, 041301 (2010).

[96] C. J. Horowitz and J. Piekarewicz, Phys. Rev. Lett. **86**, 5647 (2001).

[97] J. Piekarewicz, Phys. Rev. C **83**, 034319 (2011).

[98] J. Piekarewicz, Phys. Rev. C **83**, 034319 (2011).

[99] B. Alex Brown, Phys. Rev. Lett. **85**, 5296 (2000).

[100] R. Furnstahl, Nucl. Phys. A **706**, 85 (2002).

[101] J. Piekarewicz, B. K. Agrawal, G. Colò, W. Nazarewicz, N. Paar, P.-G. Reinhard, X. Roca-Maza, and D. Vretenar, Phys. Rev. C **85**, 041302 (2012).

[102] M. Bender, P.-H. Heenen, and P.-G. Reinhard, Rev. Mod. Phys. **75**, 121 (2003).

[103] P.-G. Reinhard and W. Nazarewicz, Phys. Rev. C **81**, 051303(R) (2010).

[104] A. Tamii, I. Poltoratska, P. von Neumann-Cosel, Y. Fujita, T. Adachi, C. A. Bertulani, J. Carter, M. Dozono, H. Fujita, K. Fujita, et al., Phys. Rev. Lett. **107**, 062502 (2011).

[105] I. Poltoratska, P. von Neumann-Cosel, A. Tamii, T. Adachi, C. A. Bertulani, J. Carter, M. Dozono, H. Fujita, K. Fujita, Y. Fujita, et al., Phys. Rev. C **85**, 041304 (2012).

[106] A. Krumbholz, P. von Neumann-Cosel, T. Hashimoto, A. Tamii, T. Adachi, C. Bertulani, H. Fujita, Y. Fujita, E. Ganioglu, K. Hatanaka, et al., Phys. Lett. B **744**, 7 (2015).

[107] W. Hauser and H. Feshbach, Phys. Rev. A **87**, 366 (1952).

[108] S. Goriely, Phys. Lett. B **436**, 10 (1998).

[109] S. Goriely, E. Khan, and M. Samyn, Nucl. Phys. A **739**, 331 (2004).

[110] E. Litvinova, H. Loens, K. Langanke, G. Martnez-Pinedo, T. Rauscher, P. Ring, F.-K. Thielemann, and V. Tselyaev, Nucl. Phys. A **823**, 26 (2009).

[111] M. Arnould, Astron. & Astrophys. **46**, 117 (1976).

[112] M. Arnould and S. Goriely, Phys. Rep. **384**, 1 (2003).

[113] D. M. Brink, Ph.D. thesis **49**, Oxford University (1955).

[114] P. Axel, Phys. Rev. **126**, 671 (1962).

[115] T. Rauscher and F.-K. Thielemann, At. Data Nucl. Data Tables **75**, 1 (2000).

[116] A. Leprêtre, H. Beil, R. Bergère, P. Carlos, J. Fagot, A. de Miniac, A. Veyssière, and H. Miyase, Nucl. Phys. A **258**, 350 (1976).

[117] L. Henden, L. Bergholt, M. Guttormsen, J. Rekstad, and T. Tveter, Nucl. Phys. A **589**, 249 (1995).

[118] M. Guttormsen, R. Chankova, U. Agvaanluvsan, E. Algin, L. A. Bernstein, F. Ingebretsen, T. Lönnroth, S. Messelt, G. E. Mitchell, J. Rekstad, et al., Phys. Rev. C **71**, 044307 (2005).

[119] A. C. Larsen and S. Goriely, Phys. Rev. C **82**, 014318 (2010).

[120] H. K. Toft, A. C. Larsen, A. Bürger, M. Guttormsen, A. Görgen, H. T. Nyhus, T. Renstrøm, S. Siem, G. M. Tveten, and A. Voinov, Phys. Rev. C **83**, 044320 (2011).

[121] M. Guttormsen, A. C. Larsen, A. Görgen, T. Renstrøm, S. Siem, T. G. Tornyi, and G. M. Tveten, Phys. Rev. Lett. **116**, 012502 (2016).

[122] M. Wiedeking, L. A. Bernstein, M. Krtička, D. L. Bleuel, J. M. Allmond, M. S. Basunia, J. T. Burke, P. Fallon, R. B. Firestone, B. L. Goldblum, et al., Phys. Rev. Lett. **108**, 162503 (2012).

[123] M. Krtička, M. Wiedeking, F. Bečvář, and S. Valenta, Phys. Rev. C **93**, 054311 (2016).

[124] U. Kneissl, N. Pietralla, and A. Zilges, J. Phys. G **32**, R217 (2006).

[125] H. R. Weller, M. W. Ahmed, H. Gao, W. Tornow, Y. K. Wu, M. Gai, and R. Miskimen, Prog. Part. Nucl. Phys. **62**, 257 (2009).

[126] B. Löher, V. Derya, T. Aumann, J. Beller, N. Cooper, M. Duchłne, J. Endres, E. Fiori, J. Isaak, J. Kelley, et al., Nucl. Instr. and Meth. A **723**, 136 (2013).

[127] V. Derya, N. Tsoneva, T. Aumann, M. Bhike, J. Endres, M. Gooden, A. Hennig, J. Isaak, H. Lenske, B. Löher, et al., Phys. Rev. C **93**, 034311 (2016).

[128] B. Lher, D. Savran, T. Aumann, J. Beller, M. Bhike, N. Cooper, V. Derya, M. Duchłne, J. Endres, A. Hennig, et al., Phys. Lett. B **756**, 72 (2016).

[129] R. Schwengner, G. Winter, W. Schauer, M. Grinberg, F. Becker, P. von Brentano, J. Eberth, J. Enders, T. von Egidy, R.-D. Herzberg, et al., Nucl. Phys. A **620**, 277 (1997).

[130] N. Cooper, F. Reichel, V. Werner, L. Bettermann, B. Alikhani, S. Aslanidou, C. Bauer, L. Coquard, M. Fritzsche, Y. Fritzsche, et al., Phys. Rev. C **86**, 034313 (2012).

[131] G. Rusev, R. Schwengner, R. Beyer, M. Erhard, E. Grosse, A. R. Junghans, K. Kosev, C. Nair, K. D. Schilling, A. Wagner, et al., Phys. Rev. C **79**, 061302 (2009).

[132] K. Sonnabend, D. Savran, J. Beller, M. Bssing, A. Constantinescu, M. Elvers, J. Endres, M. Fritzsche, J. Glorius, J. Hasper, et al., Nucl. Instr. and Meth. A **640**, 6 (2011).

[133] J. A. Holmes, S. E. Woosley, W. A. Fowler, and B. A. Zimmerman, At. Data Nucl. Data Tables **18**, 305 (1976).

[134] M. Harris, Astrophys. Space Sci. **77**, 357 (1981).

[135] T. Rauscher, HTML Interface NON-SMOKER, Technical Report, University of Basel, http://www.nucastrodata.org/datasets.html (2001).

[136] A. Koning, S. Hilaire, and M. Duijvestijn, AIP Conference Series 769 **769**, 1154 (2005).

[137] F. Käppeler, R. Gallino, S. Bisterzo, and W. Aoki, Rev. Mod. Phys. **83**, 157 (2011).

[138] T. von Egidy and D. Bucurescu, Phys. Rev. C **72**, 044311 (2005).

[139] H. A. Bethe, Phys. Rev. **50**, 332 (1936).

[140] A. Gilbert and A. G. W. Cameron, Can. J. Phys. **43**, 1446 (1965).

[141] T. Ericson, Adv. Phys. **9**, 425 (1960).

[142] T. V. Egidy, H. Schmidt, and A. Behkami, Nucl. Phys. A **481**, 189 (1988).

[143] T. von Egidy and D. Bucurescu, Phys. Rev. C **80**, 054310 (2009).

[144] S. F. Mughabgha, *Atlas of Neutron Resonances, Resonance Parameters and Thermal Cross Sections Z=1100* (Elsevier Science, Amsterdam, 2006).

[145] Y. Kalmykov, T. Adachi, G. P. A. Berg, H. Fujita, K. Fujita, Y. Fujita, K. Hatanaka, J. Kamiya, K. Nakanishi, P. von Neumann-Cosel, et al., Phys. Rev. Lett. **96**, 012502 (2006).

[146] Y. Kalmykov, C. Özen, K. Langanke, G. Martínez-Pinedo, P. von Neumann-Cosel, and A. Richter, Phys. Rev. Lett. **99**, 202502 (2007).

[147] I. Usman, Z. Buthelezi, J. Carter, G. R. J. Cooper, R. W. Fearick, S. V. Förtsch, H. Fujita, Y. Kalmykov, P. von Neumann-Cosel, R. Neveling, et al., Phys. Rev. C **84**, 054322 (2011).

[148] I. Poltoratska, R. W. Fearick, A. M. Krumbholz, E. Litvinova, H. Matsubara, P. von Neumann-Cosel, V. Y. Ponomarev, A. Richter, and A. Tamii, Phys. Rev. C **89**, 054322 (2014).

[149] M. Blatt and V. F. Weisskopf, *Theoretical Nuclear Physics* (Wiley, New York, 1952).

[150] J. Kopecky and M. Uhl, Phys. Rev. C **41**, 1941 (1990).

[151] N. Rosenzweig, Nucl. Phys. A **118**, 650 (1968).

[152] S. Raman, O. Shahal, and G. G. Slaughter, Phys. Rev. C **23**, 2794 (1981).

[153] Z. Szefliski, G. Szefliska, Z. Wilhelmi, T. Rzaca-Urban, H. Klapdor, E. Anderson, K. Grotz, and J. Metzinger, Phys. Lett. B **126**, 159 (1983).

[154] S. Kahane, S. Raman, G. G. Slaughter, C. Coceva, and M. Stefanon, Phys. Rev. C **30**, 807 (1984).

[155] M. A. Islam, T. J. Kennett, and W. V. Prestwich, Phys. Rev. C **43**, 1086 (1991).

[156] L. Netterdon, A. Endres, S. Goriely, J. Mayer, P. Scholz, M. Spieker, and A. Zilges, Phys. Lett. B **744**, 358 (2015).

[157] H. A. Bethe and G. Placzek, Phys. Rev. **51**, 450 (1937).

[158] C. S. Wu, E. Ambler, R. W. Hayward, D. D. Hoppes, and R. P. Hudson, Phys. Rev. **105**, 1413 (1957).

[159] G. Breit and E. Wigner, Phys. Rev. **49**, 519 (1936).

[160] K. S. Krane, R. M. Steffen, and R. M. Wheeler, Nuclear Data Tables **11**, 351 (1973).

[161] R. M. Steffen and K. Alder, in *The Electromagnetic Interaction in Nuclear Spectroscopy*, edited by W. D. Hamilton (North-Holland Publishing Co., Amsterdam, 1975), chap. 12, pp. 505–582.

[162] L. W. Fagg and S. S. Hanna, Rev. Mod. Phys. **31**, 711 (1959).

[163] A. Richter, S. Myers (Ed.), Proc. of the 5th EPAC **Institute of Physics, Bristol**, 110 (1996).

[164] F. Hug, C. Burandt, and J. Conrad, Proc. of the 2011 Part. Acc. Conf. **New York, NY, USA**, 1999 (2011).

[165] Y. Fritzsche, Ph.D. thesis p. TU Darmstadt (2011).

[166] M. Knirsch, Ph.D. thesis p. TU Darmstadt (1991).

[167] D. Schüll, J. Foh, H.-D. Gräf, H. Miska, R. Schneider, E. Spamer, H. Theissen, O. Titze, and T. Walcher, Nucl. Instr. and Meth. **153**, 29 (1978).

[168] D. Savran, K. Lindenberg, J. Glorius, B. Löher, S. Müller, N. Pietralla, L. Schnorrenberger, V. Simon, K. Sonnabend, C. Wälzlein, et al., Nucl. Instr. and Meth. A **613**, 232 (2010).

[169] S. Agostinelli, J. Allison, K. Amako, J. Apostolakis, H. Araujo, P. Arce, M. Asai, D. Axen, S. Banerjee, G. Barrand, et al., Nucl. Instr. and Meth. A **506**, 250 (2003).

[170] T. J. Paulus and R. M. Keyser, Nucl. Instr. and Meth. A **286**, 364 (1990).

[171] M. A. Büssing, M. Elvers, J. Endres, J. Hasper, A. Zilges, M. Fritzsche, K. Lindenberg, S. Müller, D. Savran, and K. Sonnabend, Phys. Rev. C **78**, 044309 (2008).

[172] H. Essel and N. Kurz, Nuclear Science, IEEE Transactions on **47**, 337 (2000).

[173] M. Wojdyr and P. Zhang, xylib **http://xylib.sourceforge.net** (2013).

[174] K. Große, GSI Scientific Report 2010 [GSI Report 2011-1] **vol. 2011-1 of GSI Report**, wissenschaftlicher Ergebnisbericht der GSI, GSI Annual Report (GSI, Darmstadt, 2011), URL `http://repository.gsi.de/record/53521`.

[175] G. Knoll, *Radiation Detection and Measurement* (John Wiley & Sons, 2010), ISBN 9780470131480, URL `https://books.google.de/books?id=4vTJ7UDel5IC`.

[176] G. Gilmore, *Practical Gamma-ray Spectroscopy* (Wiley, 2011), ISBN 9781119964698, URL `https://books.google.de/books?id=S0Dy4hjkmmMC`.

[177] W. R. Inc., *Mathematica* (Version 10.3, Champaign, Illinois, 2016).

[178] Z. Elekes and J. Timar, Nucl. Data Sheets **129**, 191 (2015).

[179] S. F. Hicks, J. C. Boehringer, N. Boukharouba, C. Fransen, S. R. Lesher, J. M. Mueller, J. R. Vanhoy, and S. W. Yates, Phys. Rev. C **86**, 054308 (2012).

[180] N. Pietralla, P. von Brentano, and A. Lisetskiy, Prog. Part. Nucl. Phys. **60**, 225 (2008).

[181] F. R. Metzger, Phys. Rev. **103**, 983 (1956).

[182] J. Isaak, *Kernresonanzfluoreszenz-Untersuchung der Dipolanregungsstärke im Kern Te-130* (Master thesis, Institut für Kernphysik, TU Darmstadt, 2012).

[183] V. Y. Ponomarev, private communication (2016).

[184] V. Y. Ponomarev, private communication (2012).

[185] C. T. Angell, S. L. Hammond, H. J. Karwowski, J. H. Kelley, M. Krtička, E. Kwan, A. Makinaga, and G. Rusev, Phys. Rev. C **86**, 051302 (2012).

[186] B. Löher, Ph.D. thesis pp. Johannes Gutenberg–Universität Mainz (2014).

[187] F. Bečvář, Nucl. Instr. and Meth. A **417**, 434 (1998).

[188] C. Porter and R. Thomas, Phys. Rev. **104**, 483 (1956).

[189] B. Singh, Nucl. Data Sheets **93**, 33 (2001).

[190] T. Belgya, O. Bersillon, R. Capote, T. Fukahori, G. Zhigang, S. Goriely, M. Herman, A. Ignatyuk, S. Kailas, A. Koning, et al., *Handbook for calculations of nuclear reaction data, RIPL-2.* (IAEA, Vienna, 2006).

[191] N. Tsoneva and H. Lenske, Phys. Lett. B **695**, 174 (2011).

[192] M. Spieker, N. Tsoneva, V. Derya, J. Endres, D. Savran, M. Harakeh, S. Harissopulos, R.-D. Herzberg, A. Lagoyannis, H. Lenske, et al., Phys. Lett. B **752**, 102 (2016).

[193] ELI-NP, *The White Book of ELI Nuclear Physics Bucharest-Magurele, Romania* (http://www.eli-np.ro/documents/ELI-NP-WhiteBook.pdf, 2013).

Publikation

Constraining nuclear photon strength functions by the decay properties of photo-excited states

Phys. Lett. B 727, 361 (2013)

DOI: 10.1016/j.physletb.2013.10.040

Physics Letters B 727 (2013) 361–365

Contents lists available at ScienceDirect

Physics Letters B

www.elsevier.com/locate/physletb

Constraining nuclear photon strength functions by the decay properties of photo-excited states

J. Isaak [a,b,*], D. Savran [a,b], M. Krtička [c], M.W. Ahmed [d,e,f], J. Beller [g], E. Fiori [a,b], J. Glorius [h], J.H. Kelley [i,f], B. Löher [a,b], N. Pietralla [g], C. Romig [g], G. Rusev [e,f,1], M. Scheck [g,2,3], L. Schnorrenberger [g], J. Silva [a,b], K. Sonnabend [h], A.P. Tonchev [e,f,4], W. Tornow [e,f], H.R. Weller [e,f], M. Zweidinger [g]

[a] ExtreMe Matter Institute EMMI and Research Division, GSI Helmholtzzentrum für Schwerionenforschung GmbH, 64291 Darmstadt, Germany
[b] Frankfurt Institute for Advanced Studies FIAS, 60438 Frankfurt, Germany
[c] Faculty of Mathematics and Physics, Charles University, Prague 8, Czech Republic
[d] Department of Mathematics and Physics, North Carolina Central University, Durham, NC 27707, USA
[e] Department of Physics, Duke University, Durham, NC 27708, USA
[f] Triangle Universities Nuclear Laboratory, Durham, NC 27708, USA
[g] Institut für Kernphysik, Technische Universität Darmstadt, 64289 Darmstadt, Germany
[h] Institut für Angewandte Physik, Goethe-Universität Frankfurt, 60438 Frankfurt, Germany
[i] Department of Physics, North Carolina State University, Raleigh, NC 27695, USA

ARTICLE INFO

Article history:
Received 29 August 2013
Received in revised form 15 October 2013
Accepted 16 October 2013
Available online 22 October 2013
Editor: W. Haxton

Keywords:
Photon strength function
Pygmy dipole resonance
Nuclear resonance fluorescence
Gamma-spectroscopy

ABSTRACT

A new approach for constraining the low-energy part of the electric dipole Photon Strength Function ($E1$-PSF) is presented. Experiments at the Darmstadt High-Intensity Photon Setup and the High Intensity $\vec{\gamma}$-Ray Source have been performed to investigate the decay properties of ^{130}Te between 5.50 and 8.15 MeV excitation energy. In particular, the average γ-ray branching ratio to the ground state and the population intensity of low-lying excited states have been studied. A comparison to the statistical model shows that the latter is sensitive to the low-energy behavior of the $E1$-PSF, while the average ground state branching ratio cannot be described by the statistical model in the energy range between 5.5 and 6.5 MeV.

© 2013 Elsevier B.V. All rights reserved.

1. Introduction

In complex quantum systems with high level density a statistical treatment is often used to describe average quantities of the system. In nuclear physics, e.g., this is the case for describing the nucleus at sufficiently high excitation energies within the so-called statistical model. In nuclear astrophysics this approach is used in Hauser–Feshbach calculations [1] to calculate reaction rates and properties of atomic nuclei relevant for the nucleosynthesis of the elements [2–4]. A crucial input in these statistical model calculations are Photon Strength Functions (PSF), that describe the average radiative transition probabilities between nuclear levels as a function of the γ-ray energy involved [5]. It has been shown, that the low-energy behavior of the $E1$-PSF may have an important impact on reaction rates in astrophysical calculations [6–8]. The statistical model is also used in the analysis of different experimental approaches, i.e. to correct for unobserved branching transitions [9], where the low-energy region of the PSF is of particular importance. However, so far very little experimental information is available in this energy region on the PSF or the validity of the statistical approach in general. In this Letter we present an experimental approach which is based on the method of Nuclear Resonance Fluorescence (NRF) [10] with quasi-monochromatic photon beams to constrain the low-energy dependence of the relevant PSF, exemplarily, for the case of ^{130}Te. In addition, we show that the decay properties of photo-excited states in the energy range from 5.5 to 6.5 MeV cannot be reproduced by the statistical model, which

* Corresponding author.
E-mail address: j.isaak@gsi.de (J. Isaak).
[1] Present address: Chemistry Division, Los Alamos National Laboratory, Los Alamos, New Mexico 87545, USA.
[2] Present address: School of Engineering, University of the West of Scotland, Paisley PA1 2BE, UK.
[3] Present address: SUPA, Scottish Universities Physics Alliance, Glasgow G12 8QQ, UK.
[4] Present address: Physics Division, Lawrence Livermore National Laboratory, Livermore, California 94550, USA.

0370-2693/$ – see front matter © 2013 Elsevier B.V. All rights reserved.
http://dx.doi.org/10.1016/j.physletb.2013.10.040

points to a violation of the Brink–Axel hypothesis [11]. Nuclear structure effects thus seem to play an important role in the description of the photoresponse of medium-heavy atomic nuclei even up to 6.5 MeV excitation energy.

Several approaches have been used in the past to determine the energy dependence of PSF at low γ-ray energies. While the photoabsorption cross section from NRF experiments probes the PSF in relation to transitions to the ground state and a few observed decays to lower-lying excited levels, other methods, based on the study of nuclear decay [12–15], provide an insight into the PSF between excited states. However, the results from different approaches are in some cases very contradictory [16].

The most relevant PSF is the $E1$-PSF, that is dominated at high γ-ray energies by the well-known Giant Dipole Resonance (GDR) [17–19]. In the last decades, at lower excitation energies another structure has been observed in NRF experiments [20,21,9,22–24], Coulomb Excitation experiments [25–27] as well as in decay spectroscopy experiments probing the $E1$-PSF [13,28,29]. This additional strength has been denoted as Pygmy Dipole Resonance (PDR) [30]. The results indicate that the extrapolation of the GDR using a Standard Lorentzian (SLO) parametrization do not offer an appropriate description of the $E1$-PSF at low γ-ray energies. However, at these energies experimentally verified information is very scarce, thus, input from experiments on the qualitative behavior of the relevant PSF is highly mandatory.

In this manuscript, we present a new approach which allows for constraining the low-energy behavior of the $E1$-PSF and testing the applicability of the statistical model by an analysis of the decay pattern from NRF experiments with continuous-energy bremsstrahlung and quasi-monochromatic photons.

2. Experiments

The first experiment took place at the Darmstadt High-Intensity Photon Setup (DHIPS) [31] using continuous-energy bremsstrahlung to determine the spin quantum numbers and the integrated cross sections of individual excited states relative to the calibration standard ^{11}B, see e.g. Refs. [9,23]. No information on parity quantum numbers and therefore on the transition character was accessible from this measurement. Hence, a second experiment was performed using a quasi-monochromatic, nearly 100% linearly polarized photon beam at the High Intensity $\vec{\gamma}$-Ray Source (HI$\vec{\gamma}$S) facility [32] at Triangle Universities Nuclear Laboratory. The linear polarization of the incoming photons enabled the assignment of parity quantum numbers to excited states [33] in the energy region from 5.5 MeV to 8.5 MeV. All observed states were assigned to have negative parity, thus, indicating that $E1$ strength is dominant in this energy regime. For the main part of this work we want to concentrate on average decay properties, which are essential for the statistical model.

3. Analysis and results

In the low-energy part of the measured spectra peaks originating from decays of the lowest 2^+ excited states are observed in the HI$\vec{\gamma}$S experiment. Since these states cannot be excited directly by the quasi-monochromatic photon beam, they can only be populated by decay cascades of the primary excited states. The feeding occurs through different cascades, each too weak to be observed. However, the lowest-lying excited states collect most of the total intensity of non-direct ground state transitions of photo-excited states, which, in the following, we denote as inelastic decay.

The analysis of the population intensities of these lowest excited states thus allows for measuring the average inelastic cross section $\sigma_{\gamma\gamma'}$ for each beam energy, which has been demonstrated

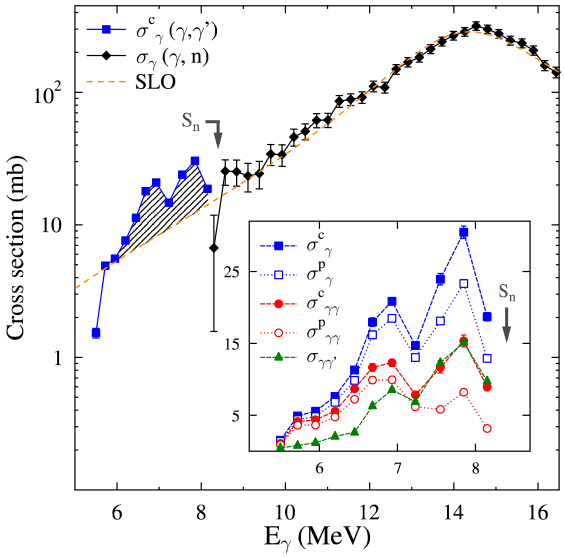

Fig. 1. (Color online.) Total photoabsorption cross sections from (γ,γ') and (γ,n) experiments [35]. Blue squares: total photoabsorption cross section; red dots: elastic cross section; green triangles: inelastic cross section. The hatched area corresponds to 0.83(6)% of the TRK sum rule. For details see text.

in Ref. [22]. Together with the elastic cross section $\sigma_{\gamma\gamma}$ the total photoabsorption cross section is given by $\sigma_\gamma = \sigma_{\gamma\gamma} + \sigma_{\gamma\gamma'}$.

Two different values for the elastic cross section are investigated: The cross section stemming from the analysis of resolved peaks in the spectra is denoted as $\sigma^p_{\gamma\gamma}$. The value indicated as $\sigma^c_{\gamma\gamma}$ takes into account the contribution of strength that might be hidden in the continuum of the spectra as pointed out earlier in [9,34]. This value is determined by integrating the total intensity observed in the spectra in the energy range between $E_b - 1\sigma_b$ and $E_b + 2\sigma_b$, where E_b is the mean photon beam energy and σ_b the standard deviation of the spectral photon flux distribution, respectively. An asymmetric energy range has been selected to minimize the effect of the detector response which has not been taken into account. This intensity has been corrected for cosmic background and converted into the cross section $\sigma^c_{\gamma\gamma}$ by normalizing to resolved transitions in this energy interval. Since no contribution of non-nuclear scattering processes and detector response have been subtracted the values of $\sigma^c_{\gamma\gamma}$ represent an upper limit of the cross section. In contrast, $\sigma^p_{\gamma\gamma}$ can be assigned to be a lower limit. Thus, the actual value of $\sigma_{\gamma\gamma}$ should be found between these two limits. The corresponding total photoabsorption cross sections are labeled as σ^p_γ and σ^c_γ, respectively.

Fig. 1 shows the photoabsorption cross section determined in the present experiments together with results from a former (γ,n)-experiment [35] above the neutron separation threshold S_n. An enhancement of the $E1$ strength below S_n compared to the SLO extrapolation of the GDR between 6 MeV and 8.5 MeV is apparent which corresponds to 0.83(6)% (1.82(5)%) of the Thomas–Reiche–Kuhn (TRK) sum rule [36,37] after (before) subtraction of the extrapolated SLO contribution. The additional strength shows two distinct maxima at 6.82 MeV and 7.85 MeV. Similar double structures of the low-lying $E1$ strength have been reported before in the neighboring $N = 82$ nuclei [38,22,39]. In experiments using the $(\alpha,\alpha'\gamma)$ method [40] different underlying structures could be assigned to the two accumulations of $E1$ strength in ^{140}Ce, ^{138}Ba [41,42] and ^{124}Sn [43,44].

Two additional observables have been extracted from the experimental data. Using the experimental cross sections the average ground state branching ratio $\langle b_0\rangle = \sigma_{\gamma\gamma}/\sigma_\gamma$ can be determined,

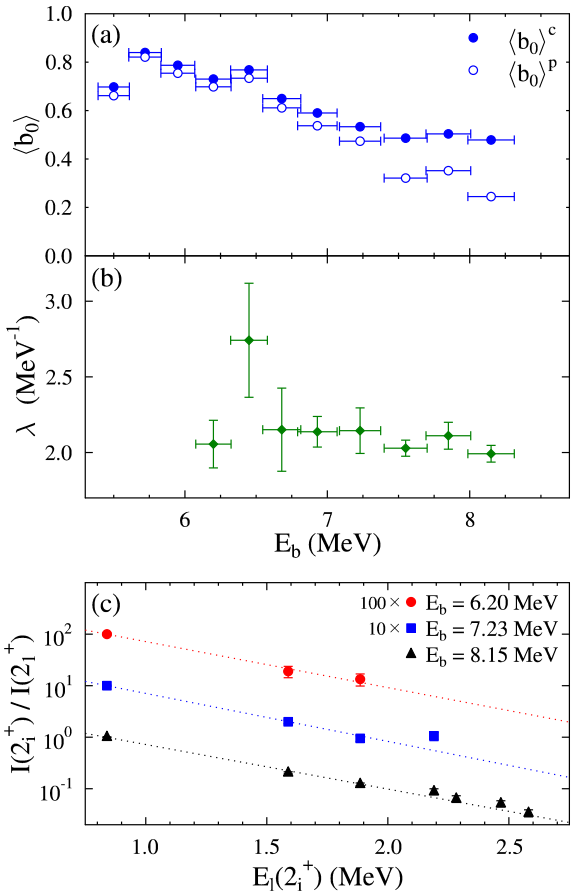

Fig. 2. (Color online.) (a): Average ground state branching ratios $\langle b_0\rangle^c$ and $\langle b_0\rangle^p$ using the corresponding cross section $\sigma^c_{\gamma\gamma}/\sigma^c_\gamma$ and $\sigma^p_{\gamma\gamma}/\sigma^p_\gamma$, respectively. (b): Exponential factor λ as a function of the photon beam energy E_b. (c): Relative population intensity of low-lying 2^+ states as a function of the level energy $E_l(2^+_i)$. For clarity reasons, the values for $E_b = 6.20$ MeV and $E_b = 7.23$ MeV are scaled by a factor of 100 and 10, respectively.

which is shown for the upper and lower limit of the corresponding cross sections ($\langle b_0\rangle^c$ and $\langle b_0\rangle^p$) in Fig. 2(a). The horizontal bars correspond to the FWHM of the incoming photon beam. By definition, $\langle b_0\rangle$ is connected to the decay properties of photo-excited states to excited states and the ground state. A second observable can be extracted from the present experiments, which will be called λ in the following. It can be derived from the pattern seen in the population intensities of low-lying 2^+ states as a function of their level energy $E_l(2^+_i)$. In Fig. 2(c) the behavior is shown exemplarily for three photon beam energies E_b. The population intensities are corrected for feeding by the other observed 2^+ states and are normalized to the intensity of the 2^+_1 excited state. Clearly, the intensities follow an exponential shape. Therefore, for each E_b an exponential as a function of E_l and λ ($\propto \exp(-\lambda \cdot E_l)$) can be obtained. As can be seen in Fig. 2(b), the value of λ is independent of the initial excitation energy. Furthermore, λ is also nearly independent of the involved level density (LD) since the populating cascades into the different low-lying 2^+ states pass similar intermediate excitation energy regions. The variation of the LD thus has similar effects to all cascades, which cancel in the ratios of the population intensities. Unlike $\langle b_0\rangle$ the parameter λ also exclusively depends on the decay properties to excited states. This leads to an independent sensitivity of λ to the low-energy behavior of the PSF as we show below.

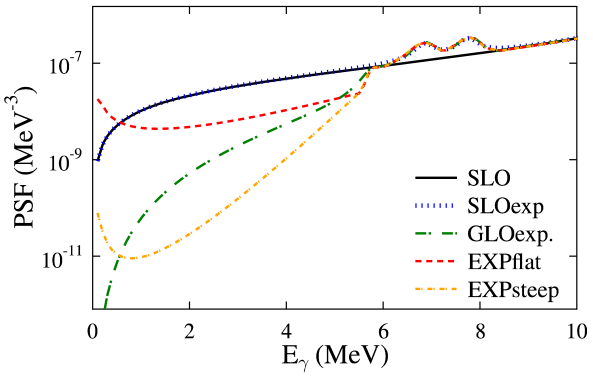

Fig. 3. (Color online.) $E1$-PSFs used for DICEBOX simulations. For details see text.

4. Comparison to statistical model calculations

To understand the dependence of $\langle b_0\rangle$ and λ on the PSF, detailed simulations in the framework of the statistical model were performed with the Monte Carlo-based DICEBOX code [45] which was modified to allow simulations of γ-ray cascades emitted in (γ,γ') reactions. The population of initial excited states in the code was simulated by generating the partial radiation widths to the ground state of all states and by knowing the spectral profile of the experimental photon flux. Below an excitation energy of $E_c = 2.62$ MeV the decay properties of ^{130}Te are taken from experimental data while above E_c the code simulates γ-decay using PSF models for $E1$, $M1$ and $E2$ transitions and an LD model. Expected Porter–Thomas fluctuations of partial radiation widths [46] are taken into account in the code.

For the $E1$-PSF several models were tested: the SLO and the SLO extended with data points derived from the experimental photoabsorption cross sections (SLOexp) as well as the Generalized Lorentzian including experimental results (GLOexp). The parameters for the Lorentzian based functions for the GDR are given by the energy of the maximum $E_0 = 14.38(5)$ MeV, the width $\Gamma_0 = 3.93(15)$ MeV and the maximum of the cross section $\sigma_0 = 286(9)$ mb. Another group of models is connected to an exponential behavior which was combined with experimental data (EXPflat and EXPsteep). The usage of an exponential behavior is based on the experimentally determined photoabsorption cross sections in this work and Refs. [22,39] which all show a strong decrease towards lower energies. Therefore, the cross section below 5.5 MeV was extrapolated by an exponential function $A \cdot \exp(B \cdot E_\gamma)$. The corresponding parameters are $A_{\text{flat}} = 2.5 \cdot 10^{-3}$ mb, $B_{\text{flat}} = 0.75$ MeV^{-1} and $A_{\text{steep}} = 5.3 \cdot 10^{-7}$ mb, $B_{\text{steep}} = 2.3$ MeV^{-1}. The $E1$-PSF models are shown in Fig. 3. For the $M1$-PSF and the $E2$-PSF the single-particle (SP) parametrization, which results in a constant value as a function of the γ-ray energy, as well as the SLO parametrization were used.

Since no experimental data for the LD in ^{130}Te are available the dedicated parameters were extrapolated from neighboring isotopes from Ref. [47]. For all simulations the Back-Shifted Fermi Gas (BSFG) model was used with the parameters $a = 12.36(25)$ MeV^{-1} and $E_1 = 1.16(11)$ MeV [47]. However, neither the variation of the parameters within their uncertainties nor the choice of another commonly used LD model [47] has a significant influence on the conclusion drawn below.

In the following the experimental results for $\langle b_0\rangle$ and λ are compared to the results of the DICEBOX simulations, which were analyzed in a consistent way to the experimental data.

For deciding which choice of the $E1$-PSF model describes all data in the best way one has to understand the influence of a given set of PSFs to the energy dependence of $\langle b_0\rangle$ and λ. Varying

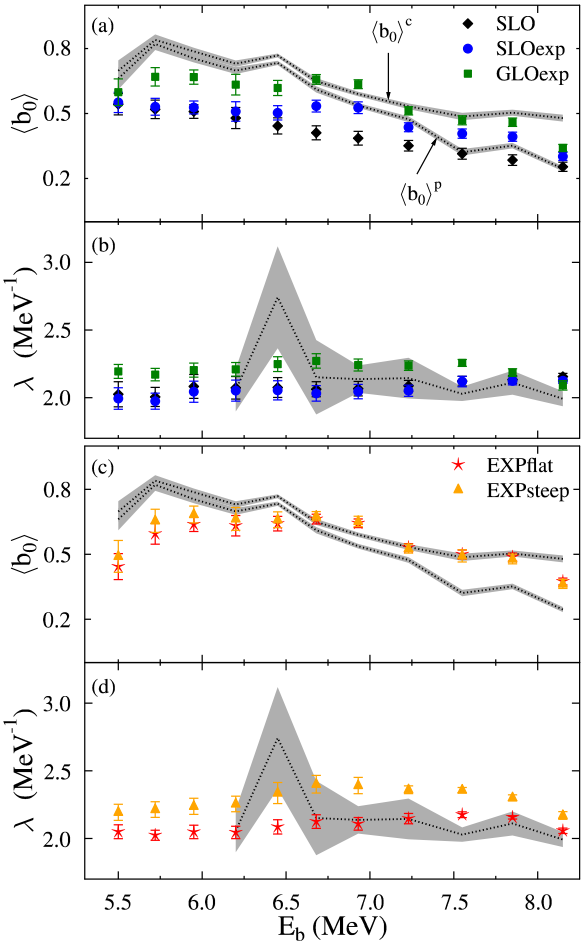

Fig. 4. (Color online.) Comparison of experimental results and simulation within the statistical model using DICEBOX. In panel (a) and (c) the upper and lower gray shaded band correspond to $\langle b_0\rangle^c$ and $\langle b_0\rangle^p$, respectively. For details see text.

the absolute value of the $M1$-PSF simply results in a shift of $\langle b_0\rangle$. The increase of the absolute value of the $M1$-PSF translates into a decrease of $\langle b_0\rangle$ at all E_b, because the probability for a $M1$ transition at a certain excitation energy is raised relative to the one for a $E1$ transition. The latter one, however, is crucial for the ground state decay of $J^\pi = 1^-$ states in an even–even nucleus like ^{130}Te. The opposite holds for a decrease of the $M1$-PSF. Consequently, any discrepancy of the observed to the simulated energy dependence cannot be removed in varying the $M1$-PSF. The behavior of λ is similar, although, the resulting shift depends also on the choice of the $E1$-PSF. Therefore, we conclude that any change in the energy dependence of $\langle b_0\rangle$ as well as λ can only be realized by choosing a different $E1$-PSF. The influence of this choice is demonstrated in Fig. 4. The two top panels (a and b) compare the simulated results for $\langle b_0\rangle$ and λ with the $E1$ models SLO, SLOexp and GLOexp to the experimental data while the two bottom panels (c and d) use the models EXPflat and EXPsteep.

The dotted lines in Fig. 4 represent the experimentally determined values with their corresponding uncertainties indicated as gray shaded bands. For $\langle b_0\rangle$, two values are available corresponding to the upper and lower limit of the elastic cross section determined by the analysis of the continuum of the spectra and the resolved peaks, respectively.

For each $E1$-PSF model the absolute value of the $M1$-PSF has been adjusted to achieve the best agreement between the simulated and experimental $\langle b_0\rangle^c$ at $E_b \gtrsim 6.5$ MeV. One can clearly see that the SLO and SLOexp models are in disagreement to the expected $\langle b_0\rangle^c$ values at most E_b, especially below 7 MeV, even if the $M1$ and the $E2$ strengths, which enhance the contribution of the inelastic scattering channels for $J^\pi = 1^-$ states, is completely neglected. Too low predicted $\langle b_0\rangle^c$ values indicate that the PSF at γ-ray energies $E_\gamma < E_b$ is too high. A suppression of its strength at very low E_γ is thus needed, which is the feature of the other $E1$-PSF models. All these models seem to be able to well reproduce $\langle b_0\rangle^c$ at $E_b > 6.5$ MeV. The GLOexp and EXPsteep models lead to a good agreement in $\langle b_0\rangle^c$ at $E_b > 6.5$ MeV, however, in contrast to the SLO models, they systematically overestimate the values for λ. An increase of this parameter can be expected for models with very low PSF values at low E_γ ($\lesssim$3 MeV), which favors transitions with high γ-ray energies. Thus $E1$-PSF models are required which do not show a too steep decrease down to $E_\gamma \to 0$. This shows, that the parameter λ offers a complementary constrain on the low-energy dependence of the $E1$-PSF compared to $\langle b_0\rangle$.

As a consequence, models similar to EXPflat result in a simultaneous description of λ and $\langle b_0\rangle^c$ for $E_b > 6.5$ MeV. However, within no parametrization $\langle b_0\rangle^c$ can be reproduced in the energy range below 6.5 MeV for the discussed family of PSFs. Therefore, we conclude that the statistical approach is not able to describe the decay behavior of ^{130}Te for the region below 6.5 MeV.

For a quantitative analysis of the disagreement a simple ansatz is used to separate σ_γ^c into two parts with different decay pattern: one part σ^{stat} decaying according to the statistical model and one part σ^{gs} decaying exclusively to the ground state. In the following, the relations $\sigma_\gamma^c = \sigma^{gs} + \sigma^{stat}$, and $\langle b_0\rangle^c = (\sigma_0^{gs} + \sigma_0^{stat})/\sigma_\gamma^c$, with $\sigma_0^{gs} = \sigma^{gs}$ and σ_0^{stat} being the corresponding elastic scattering cross sections are used. Furthermore, with $\langle b_0\rangle^{stat} = \sigma_0^{stat}/\sigma^{stat}$ being the simulated average ground state branching ratio, the fraction

$$\frac{\sigma^{gs}}{\sigma_\gamma^c} = \frac{\langle b_0\rangle^c - \langle b_0\rangle^{stat}}{1 - \langle b_0\rangle^{stat}}, \tag{1}$$

can be extracted from the data. Using this relation and the results of the simulation with PSF model EXPflat for $\langle b_0\rangle^{stat}$ in the energy region below 6.5 MeV, a ratio of $\sigma^{gs}/\sigma_\gamma^c = 0.42(4)$ is observed. This indicates that a large fraction of the $E1$ strength at this excitation energy region does not decay according to the statistical model, but may be influenced by additional mechanisms like nuclear structure effects.

5. Conclusion

In conclusion, this newly presented approach using the relative population intensity of low-lying excited states, expressed in the parameter λ together with the average ground state branching ratio $\langle b_0\rangle^c$ serves as a suitable tool to constrain the low-energy behavior of the $E1$-PSF involved. Furthermore, the comparison of the simulated results, using different classes of $E1$-PSFs, to the experimental data indicates that for the case of ^{130}Te below 6.5 MeV the ground state decay properties cannot be reproduced by the statistical model, but that a large fraction of the $E1$ strength is decaying strongly to the ground state. A similar observation has been made for the case of ^{94}Mo [48].

Thus, nuclear structure effects, such as deviations from the assumed Porter–Thomas fluctuations, seem to play an important role in the description of the decay pattern of low-lying $E1$ strength even up to energies of about 6.5 MeV. The discrepancy can in principal be solved by introducing an excitation energy dependent PSF which, however, is in contradiction to the assumptions of the Brink–Axel hypothesis [11] and the statistical model. To conclude on these statements, further experiments are needed to investigate the excitation energy dependence of PSFs, e.g. by using a new

γ-coincidence setup [49] to observe primary transitions of excited states to lower-lying excited states. Consequently, statistical models or concepts derived from them, such as the Brink–Axel hypothesis, seem to be inadequate tools for extracting the dipole PSF or estimating decay properties in that energy region.

Acknowledgements

The authors thank R. Schwengner and A. Zilges for stimulating discussions. This work was supported by the Alliance Program of the Helmholtz Association (HA216/EMMI), by the Deutsche Forschungsgemeinschaft (SFB 634 and SO907/2-1) and by the Grant No. 13-07117S of the Czech Science Foundation.

References

[1] W. Hauser, H. Feshbach, Phys. Rev. A 87 (1952) 366.
[2] J. Holmes, S. Woosley, W.A. Fowler, B. Zimmerman, At. Data Nucl. Data Tables 18 (1976) 305.
[3] J.J. Cowan, F.-K. Thielemann, J.W. Truran, Phys. Rep. 208 (1991) 267–394.
[4] T. Rauscher, F.-K. Thielemann, K.-L. Kratz, Phys. Rev. C 56 (1997) 1613.
[5] E. Litvinova, H. Loens, K. Langanke, G. Martínez-Pinedo, T. Rauscher, P. Ring, F.-K. Thielemann, V. Tselyaev, Nucl. Phys. A 823 (2009) 26.
[6] S. Goriely, Phys. Lett. B 436 (1998) 10.
[7] T. Rauscher, Phys. Rev. C 78 (2008) 032801(R).
[8] A.C. Larsen, S. Goriely, Phys. Rev. C 82 (2010) 014318.
[9] R. Schwengner, G. Rusev, N. Benouaret, R. Beyer, M. Erhard, E. Grosse, A.R. Junghans, J. Klug, K. Kosev, L. Kostov, C. Nair, N. Nankov, K.D. Schilling, A. Wagner, Phys. Rev. C 76 (2007) 034321.
[10] U. Kneissl, H.H. Pitz, A. Zilges, Prog. Part. Nucl. Phys. 37 (1996) 349.
[11] D. Brink, Ph.D. thesis, Oxford University, 1955.
[12] L. Henden, L. Bergholt, M. Guttormsen, J. Rekstad, T. Tveter, Nucl. Phys. 589 (1995) 249.
[13] A. Schiller, L. Bergholt, M. Guttormsen, E. Melby, J. Rekstad, S. Siem, Nucl. Instrum. Methods Phys. Res., Sect. A, Accel. Spectrom. Detect. Assoc. Equip. 447 (2000) 498.
[14] A. Chyzh, B. Baramsai, J.A. Becker, F. Bečvář, T.A. Bredeweg, A. Couture, D. Dashdorj, R.C. Haight, M. Jandel, J. Kroll, M. Krtička, G.E. Mitchell, J.M. O'Donnell, W. Parker, R.S. Rundberg, J.L. Ullmann, D.J. Vieira, C.L. Walker, J.B. Wilhelmy, J.M. Wouters, C.Y. Wu, Phys. Rev. C 84 (2011) 014306.
[15] M. Wiedeking, L.A. Bernstein, M. Krtička, D.L. Bleuel, J.M. Allmond, M.S. Basunia, J.T. Burke, P. Fallon, R.B. Firestone, B.L. Goldblum, R. Hatarik, P.T. Lake, I.-Y. Lee, S.R. Lesher, S. Paschalis, M. Petri, L. Phair, N.D. Scielzo, Phys. Rev. Lett. 108 (2012) 162503.
[16] G. Rusev, R. Schwengner, F. Dönau, M. Erhard, E. Grosse, A.R. Junghans, K. Kosev, K.D. Schilling, A. Wagner, F. Bečvář, M. Krtička, Phys. Rev. C 77 (2008) 064321.
[17] G.C. Baldwin, G.S. Klaiber, Phys. Rev. 71 (1947) 3.
[18] G.A. Bartholomew, E.D. Earl, A.J. Ferguson, J.W. Knowles, M.A. Lone, Adv. Nucl. Phys. 7 (1973) 229.
[19] M.N. Harakeh, A. van der Woude, Giant Resonances, Oxford University Press, 2001.
[20] R.-D. Herzberg, C. Fransen, P. von Brentano, J. Eberth, J. Enders, A. Fitzler, L. Käubler, H. Kaiser, P. von Neumann-Cosel, N. Pietralla, V.Y. Ponomarev, H. Prade, A. Richter, H. Schnare, R. Schwengner, S. Skoda, H.G. Thomas, H. Tiesler, D. Weisshaar, I. Wiedenhöver, Phys. Rev. C 60 (1999) 051307.
[21] A. Zilges, S. Volz, M. Babilon, T. Hartmann, P. Mohr, K. Vogt, Phys. Lett. B 542 (2002) 43.
[22] A.P. Tonchev, S.L. Hammond, J.H. Kelley, E. Kwan, H. Lenske, G. Rusev, W. Tornow, N. Tsoneva, Phys. Rev. Lett. 104 (2010) 072501.
[23] D. Savran, M. Elvers, J. Endres, M. Fritzsche, B. Löher, N. Pietralla, V.Y. Ponomarev, C. Romig, L. Schnorrenberger , K. Sonnabend, A. Zilges, Phys. Rev. C 84 (2011) 024326.
[24] M. Scheck, V.Y. Ponomarev, T. Aumann, J. Beller, M. Fritzsche, J. Isaak, J.H. Kelley, E. Kwan, N. Pietralla, R. Raut, C. Romig, G. Rusev, D. Savran, K. Sonnabend, A.P. Tonchev, W. Tornow, H.R. Weller, M. Zweidinger, Phys. Rev. C 87 (2013) 051304(R).
[25] P. Adrich, A. Klimkiewicz, M. Fallot, K. Boretzky, T. Aumann, D. Cortina-Gil, U.D. Pramanik, T.W. Elze, H. Emling, H. Geissel, M. Hellström, K.L. Jones, J.V. Kratz, R. Kulessa, Y. Leifels, C. Nociforo, R. Palit, H. Simon, G. Surówka, K. Sümmerer, W. Waluś, LAND-FRS Collaboration, Phys. Rev. Lett. 95 (2005) 132501.
[26] A. Tamii, I. Poltoratska, P. von Neumann-Cosel, Y. Fujita, T. Adachi, C.A. Bertulani, J. Carter, M. Dozono, H. Fujita, K. Fujita, K. Hatanaka, D. Ishikawa, M. Itoh, T. Kawabata, Y. Kalmykov, A.M. Krumbholz, E. Litvinova, H. Matsubara, K. Nakanishi, R. Neveling, H. Okamura, H.J. Ong, B. Özel-Tashenov, V.Y. Ponomarev, A. Richter, B. Rubio, H. Sakaguchi, Y. Sakemi, Y. Sasamoto, Y. Shimbara, Y. Shimizu, F.D. Smit, T. Suzuki, Y. Tameshige, J. Wambach, R. Yamada, M. Yosoi, J. Zenihiro, Phys. Rev. Lett. 107 (2011) 062502.
[27] O. Wieland, A. Bracco, Prog. Part. Nucl. Phys. 66 (2011) 374–378.
[28] U. Agvaanluvsan, A.C. Larsen, R. Chankova, M. Guttormsen, G.E. Mitchell, A. Schiller, S. Siem, A. Voinov, Phys. Rev. Lett. 102 (2009) 162504.
[29] H.K. Toft, A.C. Larsen, A. Bürger, M. Guttormsen, A. Görgen, H.T. Nyhus, T. Renstrøm, S. Siem, G.M. Tveten, A. Voinov, Phys. Rev. C 83 (2011) 044320.
[30] D. Savran, T. Aumann, A. Zilges, Prog. Part. Nucl. Phys. 70 (2013) 210.
[31] K. Sonnabend, D. Savran, J. Beller, M. Büssing, A. Constantinescu, M. Elvers, J. Endres, M. Fritzsche, J. Glorius, J. Hasper, J. Isaak, B. Löher, S. Müller, N. Pietralla, C. Romig, A. Sauerwein, L. Schnorrenberger, C. Wälzlein, A. Zilges, M. Zweidinger, Nucl. Instrum. Methods Phys. Res., Sect. A, Accel. Spectrom. Detect. Assoc. Equip. 640 (2011) 6.
[32] H.R. Weller, M.W. Ahmed, H. Gao, W. Tornow, Y.K. Wu, M. Gai, R. Miskimen, Prog. Part. Nucl. Phys. 62 (2009) 257.
[33] N. Pietralla, Z. Berant, V.N. Litvinenko, S. Hartman, F.F. Mikhailov, I.V. Pinayev, G.S.M.W. Ahmed, J.H. Kelley, S.O. Nelson, R. Prior, K. Sabourov, A.P. Tonchev, H.R. Weller, Phys. Rev. Lett. 88 (2002) 012502.
[34] D. Savran, M. Fritzsche, J. Hasper, K. Lindenberg, S. Müller, V.Y. Ponomarev, K. Sonnabend, A. Zilges, Phys. Rev. Lett. 100 (2008) 232501.
[35] A. Leprêtre, H. Beil, R. Bergére, P. Carlos, J. Fagot, A.D. Miniac, A. Veyssiére, H. Miyase, Nucl. Phys. 258 (1976) 350.
[36] W. Kuhn, Z. Phys. 33 (1925) 408.
[37] F. Reiche, W. Thomas, Z. Phys. 34 (1925) 510.
[38] S. Volz, N. Tsoneva, M. Babilon, M. Elvers, J. Hasper, R.-D. Herzberg, H. Lenske, K. Lindenberg, D. Savran, A. Zilges, Nucl. Phys. 779 (2006) 1.
[39] C.T. Angell, S.L. Hammond, H.J. Karwowski, J.H. Kelley, M. Krtička, E. Kwan, A. Makinaga, G. Rusev, Phys. Rev. C 86 (2012) 051302.
[40] D. Savran, A. van den Berg, M. Harakeh, K. Ramspeck, H. Wörtche, A. Zilges, Nucl. Instrum. Methods Phys. Res., Sect. A, Accel. Spectrom. Detect. Assoc. Equip. 564 (2006) 267.
[41] D. Savran, M. Babilon, A.M. van den Berg, M.N. Harakeh, J. Hasper, A. Matic, H.J. Wörtche, A. Zilges, Phys. Rev. Lett. 97 (2006) 172502.
[42] J. Endres, D. Savran, A.M.v.d. Berg, P. Dendooven, M. Fritzsche, M.N. Harakeh, J. Hasper, H.J. Wörtche, A. Zilges, Phys. Rev. C 80 (2009) 034302.
[43] J. Endres, E. Litvinova, D. Savran, P.A. Butler, M.N. Harakeh, S. Harissopulos, R.-D. Herzberg, R. Krücken, A. Lagoyannis, N. Pietralla, V.Y. Ponomarev, L. Popescu, P. Ring, M. Scheck, K. Sonnabend, V.I. Stoica, H.J. Wörtche, A. Zilges, Phys. Rev. Lett. 105 (2010) 212503.
[44] J. Endres, D. Savran, P.A. Butler, M.N. Harakeh, S. Harissopulos, R.-D. Herzberg, R. Krücken, A. Lagoyannis, E. Litvinova, N. Pietralla, V. Ponomarev, L. Popescu, P. Ring, M. Scheck, F. Schlüter, K. Sonnabend, V.I. Stoica, H.J. Wörtche, A. Zilges, Phys. Rev. C 85 (2012) 064331.
[45] F. Bečvář, Nucl. Instrum. Methods Phys. Res., Sect. A, Accel. Spectrom. Detect. Assoc. Equip. 417 (1998) 434.
[46] C.E. Porter, R.G. Thomas, Phys. Rev. 104 (1956) 483.
[47] T. von Egidy, D. Bucurescu, Phys. Rev. C 80 (2009) 054310.
[48] C. Romig, J. Beller, J. Glorius, J. Isaak, J.H. Kelley, E. Kwan, N. Pietralla, V.Y. Ponomarev, A. Sauerwein, D. Savran, M. Scheck, L. Schnorrenberger, K. Sonnabend, A.P. Tonchev, W. Tornow, H.R. Weller, A. Zilges, M. Zweidinger, Phys. Rev. C 88 (2013) 044331.
[49] B. Löher, V. Derya, T. Aumann, J. Beller, N. Cooper, M. Duchêne, J. Endres, E. Fiori, J. Isaak, J. Kelley, M. Knörzer, N. Pietralla, C. Romig, D. Savran, M. Scheck, H. Scheit, J. Silva, A. Tonchev, W. Tornow, H. Weller, V. Werner, A. Zilges, Nucl. Instrum. Methods Phys. Res., Sect. A, Accel. Spectrom. Detect. Assoc. Equip. 723 (2013) 136.